



UNIVERSITAT
POLITÈCNICA
DE VALÈNCIA

PROGRAMA DE DOCTORADO EN INGENIERÍA Y PRODUCCIÓN INDUSTRIAL

DOCTORAL THESIS

Analysis of tribocorrosion behavior
of biomedical powder metallurgy titanium alloys

Marie- Pierre Licausi

Supervisors

Anna Igual Muñoz

Vicente Amigó Borrás,

July 2017



UNIVERSITAT
POLITÈCNICA
DE VALÈNCIA

PROGRAMA DE DOCTORADO EN INGENIERÍA Y PRODUCCIÓN INDUSTRIAL

TESIS DOCTORAL

Análisis del Comportamiento Frente a la Tribocorrosión
de Aleaciones Biomédicas
de Titanio Pulvimetalúrgico

Marie- Pierre Licausi

Directores

Anna Igual Muñoz

Vicente Amigó Borrás,

Julio 2017

Memoria presentada por Marie-Pierre Licausi en la Escuela de Doctorado de la Universitat Politècnica de València, programa de Doctorado en Ingeniería y Producción Industrial, para optar al título de doctor.

Este trabajo ha sido desarrollado en el Instituto de Tecnología de Materiales, en el Departamento de Ingeniería Mecánica y de Materiales y el Departamento de Ingeniería Química y Nuclear de la Universitat Politècnica de València, mediante la ayuda del proyecto MAT2014-53764-C3-1-R del Ministerio de Economía y Competitividad de España y la beca de la Comunidad valenciana GRISOLIAP/2010/038.

To my family

Acknowledgments

The time has come to close an important stage of my life and it is of great importance to acknowledge all the people without whom this project would not have come to an end. I will try to summarize in a few lines the gratitude I have to all the people who have made this scientific and personal adventure come true.

First of all, I would like to thank my thesis directors for their help and guidance. You have shared your knowledge in materials, electrochemistry and love of science. Thanks for your encouragement, transmitting me your passion for research and your constant desire to innovate. You have been by my side throughout this long journey, which would have been impossible without you. You have given me strength to grow in all aspects of life. It has been a privilege and a great lesson to be able to count on you.

I would like to express my gratitude to Prof. Nuria Espallargas for welcoming me in the Department of Materials engineering at NTNU in Norway. It was a pleasure to work with you and your group, thanks for your help in my professional development. To all those who welcomed me during my stay in Norway, a special thought for Dani, my lab guide and friend.

Special thanks to the department of Microscopy at the UPV university: for your patience when we all go looking for you at the same time. To Manuel, José Luís, Merche, Ximo and Alicia..

I would like to thank the people who have been part of the group of research in both departments of Materials engineering and Chemical and Nuclear engineering: Mariado, Nelly, Rut, Juan, Jenny, Inma, Irma, Angelica, Virginia, Cristina, Ramon, Alba, Jordy, colleagues in research, some who have already reached the finish line and others who are walking the road. A special thought for Marga and Angels, who have not only been there to solve all the bureaucratic conundrum. Thank you for the support, the cheering up and the constant laughter. Your daily presence has meant so much to me.

To my “girls”. You are my family of heart and this journey would have been impossible without your presence by my side, distance means nothing.

To Dona Teresa, you have been there for me, always, I am so grateful to have you in my life.

Last but not least, to my family, for being always there at any time.

Many people have been present throughout the way in so many manners... Thank you all for everything.

ABSTRACT

Titanium and its alloys have been widely used in oral implantology due to their mechanical properties, corrosion resistance and biocompatibility. However, under in vivo conditions the implants are subjected to the tribocorrosion phenomenon, which consists in the degradation mechanisms due to the combined effect of wear and corrosion. This process contributes to limiting the life span of the implant and may generate clinical problems in patients as metallic ions are released. Another cause of dental implant failure may be the loosening of the implant as metal does not promote osseointegration. The powder-metallurgy process is a promising alternative to the traditional casting fabrication process of titanium alloys for bone implants design, as the porous structure would allow the bone to grow into the pores. This would result in a better fixation of the metal implant without the need of sandblasting /acid etching the surface.

The present Doctoral thesis aims at describing the corrosion and tribocorrosion behavior of titanium alloys and their degradation mechanisms when processed by powder metallurgy, as a possible alternative to standard casting for dental implant application. For this, model Ti6Al4V titanium alloy and possible substitute Ti6Al7Nb alloy, where Vanadium has been replaced by Niobium in order to avoid cytotoxicity of the resulting biomaterial, have been studied. Electrochemical and tribo-electrochemical characterization of the biomaterials have been carried out under different physico-chemical conditions with biological relevance (in artificial saliva (AS) with different fluoride content, pH and oxidising conditions) which noticeably influences the degradation mechanisms of the studied materials. A new tribocorrosion technique that allows measuring the galvanic potential and current between the wear track (anode) and the passive material (cathode) through Zero-Resistance Ammetry (ZRA) has been also used to elucidate tribocorrosion mechanisms of the model Ti6Al4V cast alloy in AS. The ZRA technique for tribocorrosion allowed predicting the real depassivated area and therefore, the deviation of the wear mechanisms from Archard wear law at Open Circuit Potential (OCP).

All alloys show passivity in artificial saliva although active dissolution occurs in presence of high fluoride concentration (1000 ppm) and acidic conditions, pH 3. The degradation mechanism of sintered alloys is mainly governed by the mechanical wear in AS and only determined by the active dissolution when fluorides are added to acidified artificial saliva (pH 3). Wear was found to be governed by the prevailing oxidizing condition (simulated by changes in the electrode potential).

Ti6Al4V alloy processed by powder metallurgy showed a similar tribocorrosion resistance when compared to commercially available cast alloy suggesting that powder metallurgy is a promising fabrication process for implant applications. The influence of the alloying elements, Al and Nb, on the corrosion and tribocorrosion behavior of different titanium alloys, Ti6Al7Nb, Ti7Nb and Ti6Al has been studied and in all cases, the corrosion resistance is improved when compared to pure titanium. Wear damage was found to be critically affected by the ductility of the material, thus by the alloying element. Ti6Al7Nb showed a better corrosion resistance and similar tribocorrosion behaviour when compared to Ti6Al4V.

The results of this thesis have shown that Ti6Al7Nb obtained by Powder metallurgy is a promising biomedical alloy for oral implants. Wear damage of sintered Ti alloys depends on the electrochemical potential and their tribocorrosion behaviour is critically affected by a high content of fluoride found in common daily dental health care products.

RESUMEN

El titanio y sus aleaciones han sido ampliamente utilizados en implantología oral debido a sus propiedades mecánicas, resistencia a la corrosión y biocompatibilidad. Sin embargo, bajo condiciones in vivo los implantes están sometidos al fenómeno de tribocorrosión, que consiste en mecanismos de degradación debido al efecto combinado de desgaste y corrosión. Este proceso contribuye a limitar la vida útil del implante y puede generar problemas clínicos en pacientes a medida que se liberan iones metálicos. Otra causa de fracaso del implante dental puede ser la pérdida de fijación del implante, ya que el metal no promueve la osteointegración. El proceso de metalurgia de polvos es una alternativa prometedora al proceso tradicional de fabricación por colada y forja de aleaciones de titanio para el diseño de implantes óseos, ya que la estructura porosa permitiría que el hueso crezca dentro de los poros. Esto daría lugar a una mejor fijación del implante metálico sin necesidad de arenado y/o grabado con ácido de la superficie.

La presente tesis doctoral pretende describir el comportamiento frente a la corrosión y tribocorrosión de las aleaciones de titanio y sus mecanismos de degradación cuando se procesan mediante metalurgia de polvos, como una posible alternativa a la colada estándar para la aplicación de implantes dentales. Para ello, se ha estudiado el modelo de aleación de titanio Ti6Al4V y posible sustitución por la aleación Ti6Al7Nb, donde el vanadio ha sido sustituido por niobio para evitar la citotoxicidad del biomaterial resultante. La caracterización electroquímica y tribo-electroquímica de los biomateriales se ha llevado a cabo en diferentes condiciones físico-químicas con relevancia biológica (en saliva artificial (AS) con diferente contenido de iones flúor, pH y condiciones oxidantes) que influye notablemente en los mecanismos de degradación de los materiales estudiados. También se ha utilizado una nueva técnica de tribocorrosión que permite medir el potencial galvánico y la corriente entre la pista de desgaste (ánodo) y el material pasivo (cátodo) a través de la ametría de resistencia cero (*Zero-Resistance Ammetry, ZRA*) para elucidar los mecanismos de tribocorrosión de la aleación de forja Ti6Al4V en AS. La técnica ZRA para tribocorrosión permitió predecir el área real despasivada y, por tanto, la desviación de los mecanismos de desgaste de la ley de desgaste de Archard en OCP.

Todas las aleaciones muestran pasividad en la saliva artificial, aunque la disolución activa se produce en presencia de alta concentración de fluoruro (1000 ppm) y condiciones ácidas, pH 3. El mecanismo de degradación de las aleaciones sinterizadas se rige principalmente por el desgaste mecánico en AS y sólo determinado por la disolución activa cuando se añaden fluoruros a la saliva artificial acidificada

(pH 3). Se encontró que el desgaste se rige por la condición oxidante predominante (simulada por cambios en el potencial de electrodo).

La aleación Ti6Al4V procesada por pulvimetalurgia mostró una resistencia similar a la tribocorrosión cuando se comparó con la aleación forjada comercial disponible, lo que sugiere que la metalurgia de los polvos es un prometedor proceso de fabricación para aplicaciones de implantes. Se ha estudiado la influencia de los elementos de aleación Al y Nb sobre el comportamiento de corrosión y tribocorrosión de diferentes aleaciones de titanio Ti6Al7Nb, Ti7Nb y Ti6Al y en todos los casos la resistencia a la corrosión se mejora en comparación con el titanio puro. Se encontró que el daño de desgaste está afectado críticamente por la ductilidad del material, por lo tanto, por el elemento de aleación. La aleación Ti6Al7Nb mostró una mejor resistencia a la corrosión y un comportamiento similar de tribocorrosión en comparación con la aleación Ti6Al4V.

Los resultados de esta tesis han demostrado que el Ti6Al7Nb obtenido por pulvimetalurgia es una prometedora aleación biomédica para implantes orales. El deterioro del desgaste de las aleaciones de Ti sinterizadas depende del potencial electroquímico y su comportamiento a tribocorrosión se ve afectado de manera crítica por un alto contenido de ion flúor que se encuentra en los productos diarios comunes de salud dental.

RESUM

El titani i els seus aliatges s'han utilitzat àmpliament en l'implantologia oral degut a les seves propietats mecàniques, resistència a la corrosió i biocompatibilitat. No obstant això, en condicions *in vivo* els implants són sotmesos al fenomen de tribocorrosió, que consisteix en els mecanismes de degradació causats per l'efecte combinat de desgast i corrosió. Aquest procés contribueix a limitar la vida útil de l'implant i pot generar problemes clínics en els pacients com l'alliberament d'ions metàl·lics. Una altra causa de fracàs de l'implant dental pot ser la pèrdua de fixació de l'implant, ja que el metall no promou l'osteointegració. El procés de pulvimetal·lúrgia és una alternativa prometedora al procés tradicional de fabricació per colada i forja d'aliatges de titani per al disseny d'implants ossis, ja que l'estructura porosa permetria que l'os creixca dins dels porus. Això donaria lloc a una millor fixació de l'implant metàl·lic sense necessitat de sorrejat i/o gravat amb àcid de la superfície.

La present tesi doctoral pretén descriure el comportament enfront de la corrosió i tribocorrosió dels aliatges de titani i els seus mecanismes de degradació quan es processen mitjançant pulvimetal·lúrgia, com una possible alternativa a la fabricació estàndard per forja per a l'aplicació d'implants dentals. Per a això, s'ha estudiat el model d'aliatge de titani Ti6Al4V i possible substitució per l'aliatge Ti6Al7Nb, on el vanadi ha estat substituït per niobi per evitar la citotoxicitat del biomaterial resultant. La caracterització electroquímica i tribo-electroquímica dels biomaterials s'ha dut a terme en diferents condicions fisicoquímiques amb rellevància biològica (en saliva artificial (AS) amb diferent contingut de ions fluor, pH i condicions oxidants) que influeix notablement en els mecanismes de degradació dels materials estudiats. També s'ha utilitzat una nova tècnica de tribocorrosió que permet mesurar el potencial galvànic i el corrent entre la pista de desgast (ànode) i el material passiu (cànode) a través de la ametria de resistència zero (Zero-Resistance Ammetry, ZRA) per elucidar els mecanismes de tribocorrosió de l'aliatge de forja Ti6Al4V en AS. La tècnica ZRA per tribocorrosió va permetre predir l'àrea real despassivada i, per tant, la desviació dels mecanismes de desgast de la llei de desgast de Archard en OCP.

Tots els aliatges mostren passivitat en la saliva artificial, tot i que la dissolució activa es produeix en presència d'alta concentració de fluorur (1000 ppm) i condicions àcides, pH 3. El mecanisme de degradació dels aliatges sinteritzats es regix principalment pel desgast mecànic en AS i només determinat per la dissolució activa quan s'afegixen fluorurs a la saliva artificial acidificada (pH 3). Es va trobar que el desgast es regix per la condició oxidant predominant (simulada per canvis en el potencial d'elèctrode).

L'aliatge Ti6Al4V processada per pulverimetal·lúrgia va mostrar una resistència similar a la tribocorrosió quan es va comparar amb l'aliatge forjada comercial disponible, el que suggerix que la pulverimetal·lúrgia és un prometedor procés de fabricació per a aplicacions d'implants. S'ha estudiat la influència dels elements d'aliatge Al i Nb sobre el comportament de corrosió i tribocorrosió de diferents aliatges de titani Ti6Al7Nb, Ti7Nb i Ti6Al i en tots els casos la resistència a la corrosió es millora en comparació amb el titani pur. Es va trobar que el dany de desgast està afectat críticament per la ductilitat del material, per tant, per l'element d'aliatge. L'aliatge Ti6Al7Nb va mostrar una millor resistència a la corrosió i un comportament similar de tribocorrosió en comparació amb l'aliatge Ti6Al4V.

Els resultats d'aquesta tesi han demostrat que el Ti6Al7Nb obtingut per pulverimetal·lúrgia és un prometedor aliatge biomèdic per a implants orals. El deteriorament del desgast dels aliatges de Ti sinteritzats depèn del potencial electroquímic i el seu comportament a tribocorrosió es veu afectat de manera crítica per un alt contingut de ió fluor que es troba en els productes diaris comuns de salut dental.

Index

ABSTRACT

RESUMEN

RESUM

CHAPTER 1: INTRODUCTION

| | |
|--|--------|
| 1.1 Titanium as biomaterial | ... 3 |
| 1.1.1 Titanium and its alloys in the biomedical field | ... 5 |
| 1.1.2 Titanium based Powder Metallurgy for biomaterials | ... 9 |
| 1.2 Electrochemical nature of corrosion | ... 13 |
| 1.2.1 Fundamentals of corrosion | ... 13 |
| 1.2.2 Corrosion mechanisms of titanium and titanium alloys | 14 |
| 1.2.3 Corrosion of titanium biomedical alloys in the oral environment | ... 15 |
| 1.2.4 Corrosion of porous material | ... 17 |
| 1.3 Tribocorrosion | ... 18 |
| 1.3.1 Concept and involved phenomena | ... 18 |
| 1.3.2 Tribocorrosion models | ... 25 |
| <i>1.3.2.1. Wear accelerated corrosion</i> | ... 25 |
| <i>1.3.2.2. Galvanic cell model for tribocorrosion at open circuit potential</i> | ... 26 |
| <i>1.3.2.3. Tribocorrosion of passive metals in the mixed lubrication regime</i> | ... 27 |
| 1.3.3 Tribocorrosion in the oral environment. | ... 29 |
| 1.3.5 Clinical impact | ... 30 |
| 1.4 Rational of the thesis | ... 32 |
| 1.5 References | ... 34 |

| | |
|---|---------|
| CHAPTER 2 : OBJECTIVES | ... 43 |
| CHAPTER 3: MATERIALS AND EXPERIMENTAL TECHNIQUES | |
| 3.1 Materials | ... 49 |
| 3.2 Electrochemical techniques | ... 51 |
| 3.2.1 Open-Circuit Potential (OCP) | ... 53 |
| 3.2.2 Potentiodynamic curves | ... 54 |
| 3.2.3 Potentiostatic tests | ... 60 |
| 3.2.4 Impedance | ... 62 |
| <i>3.2.4.1. Electrode response to a sinusoidal perturbation of the potential</i> | ... 62 |
| <i>3.2.4.2 Instrumentation</i> | ... 64 |
| <i>3.2.4.3. Interpretation of the impedance results and Equivalent Electrical</i> | ... 65 |
| 3.3 Tribocorrosion | 70 |
| 3.3.1 Tribocorrosion under Open Circuit Potential | ... 71 |
| 3.3.2 Tribocorrosion with applied potential | ... 72 |
| 3.3.3 Tribocorrosion under Open Circuit Potential using a ZRA | ... 74 |
| 3.4 Surface Analysis | ... 75 |
| 3.4.1 Optical and confocal microscopy | ... 75 |
| 3.4.2 Scanning electron microscope | ... 78 |
| 3.5 References | ... 79 |
| CHAPTER 4: CORROSION AND TRIBOCORROSION BEHAVIOUR OF Ti6Al4V BIOMEDICAL ALLOY IN ARTIFICIAL SALIVA | |
| 4.1 Influence of the fabrication process and fluoride content on the tribocorrosion behaviour of Ti6Al4V biomedical alloy in artificial saliva | ... 83 |
| 4.2 Tribocorrosion mechanisms of Ti6Al4V biomedical alloys in artificial saliva with different pHs | ... 109 |
| 4.3 Tribocorrosion mechanisms of Ti6Al4V in artificial saliva by zero-resistance ammetry (ZRA) technique | ... 135 |

**CHAPTER 5 : CORROSION AND TRIBOCORROSION BEHAVIOR OF
Ti6Al7Nb BIOMEDICAL ALLOY IN ARTIFICIAL SALIVA**

| | |
|---|---------|
| 5.1 Influence of the alloying element on the electrochemical behavior of Ti6Al7Nb obtained by powder metallurgy | ... 161 |
| 5.2 Influence of the alloying element (Al / Nb) and the potential on the tribocorrosion and electrochemical behavior of titanium biomedical alloys obtained by powder metallurgy | ... 181 |

CHAPTER 6: CONCLUSIONS AND FUTURE RESEARCH LINES

| | |
|----------------------------------|---------|
| 6.1 Conclusions | ... 209 |
| 6.2 Future research lines | ... 211 |

GLOSSARIES

| | |
|-----------------|---------|
| List of Tables | ... 215 |
| List of Figures | ... 217 |
| List of Symbols | ... 221 |

-Chapter 1-

Introduction

1.1 Titanium as biomaterial

In today's society, teeth are not only important for their vital role in the digestive process but are also important beauty criteria in the western world. This explains why, living in an era of longer life expectancy, oral implantology has become one of the most active and promising areas in dentistry and is a popular option for the oral rehabilitation of partially dentate or edentulous patients. In the past two decades the number of dental implant procedures has increased steadily worldwide. It is estimated that this number is above one million dental implantation annum [1]. According to NRC (National Research Canada) market research, 70 percent of Americans have at least one missing tooth and more than 18 million have no teeth. This not only affects the western world as for example in China the demand for dental implants is growing at about 25 percent per year [2]. Treating partially dentate patients with dental implants is nowadays considered a safe and predictable treatment, with a ten-year survival rate of over 93% [3]. In the early history of teeth replacements, natural materials such as minerals, re-sized animal bones and teeth were used to replace lost teeth. In the 20th century, the technological advances have enabled the use of metallic biomaterials as the usual material to replace the teeth lost by periodontal disease or injury.

A *biomaterial* has been defined by the European Society for Biomaterials as a “non viable material used in a medical device intended to interact with biological systems” [4].

The properties that should exhibit a biomaterial for successful application in total joint replacement are:

- **Biocompatible** chemical composition to avoid adverse tissue reaction which could lead to implant failure.
- **Corrosion resistance** to the body fluid.
- **Acceptable strength** to tolerate cyclic loading endured by the joint.
- **Low modulus** in order to minimize bone resorption.
- **High wear resistance** to limit wear debris generation.

The use of titanium for implant applications dates from the 1930s and it has been massively used in dentistry for over 30 years. The dental implant system was developed by Branemark [5] in 1952, and was first placed in the human body in 1965. Nowadays, dental implant can be divided into two main categories: the **endosteal** implant which is placed inside the jawbone and the **subperiosteal** implant which is placed above the jaw bone and under the gum. This type of implant may be used in patients who have a shallow bone [5]. The different parts of an implant are shown in **Figure 1.1**.

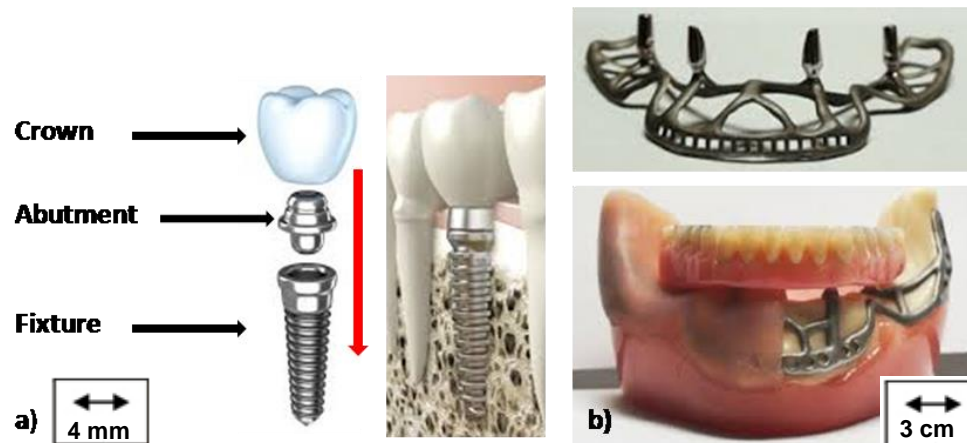


Figure 1.1. a) Endosteal and b) subperiosteal implants [6][7][8][9]

An endosteal implant system is composed of:

- **A crown** at the top part of a restoration in order to provide a biting surface and to give an aesthetic appearance.
- **An abutment** which provides support for the crown. It is also the interface between the crown and the implant.
- **An implant fixture** which is screwed into the bone of the jaw providing a fixed platform on which an abutment can be screwed.

In a dental implant, titanium and its alloys can either be used for the implant fixture, the abutment, metal-ceramic crowns, removable partial denture and overdenture [10].

To limit tribological damage an adequate fit between the crown-abutment and abutment-implant joint is crucial to ensure a more uniform adaptation and distribution of mastication forces. The orientation of stresses is very important on wear as axial loading promotes the transfer of stress through the dental implant to the bone [11] whereas oblique loads can overload the implant system and cause failure due to fatigue [12]

Overloading is not the only cause of dental implant failure. In literature, a mean interfacial discrepancy of about 49-60 μm in implant fixture-abutment gaps was reported [13]. Such microgaps favour the occurrence of micro-leakage which consists in the passage of fluids containing microorganisms and debris at the connection between the implant fixture and the abutment [14]. Guindy et al. [15] reported the failure of six dental implant systems caused by corrosion of the prosthetic superstructure. In that study, areas with clear signs of localized corrosion were detected by scanning electron microscopy on all implants and inner crown surfaces. As corrosive substances can

accumulate in the internal connection of dental implant systems, implant failure can be caused by corrosion and wear synergy along with the cyclic loading mechanism of the masticatory process [16]. If the formed debris remain in the contact due to a closed tribological system, it will originate a three body abrasion configuration [17]

1.1.1. Titanium and its alloys in the biomedical field

Since the intensive work accomplished by Branemark *et al.* (1987), titanium and its alloys have been the first choice materials for producing joint prosthesis [18] and prosthesis in oral rehabilitation. This is due to the properties of titanium and titanium alloys, as these combine low density (4.5 g/cm^3), high strength and exhibit an excellent corrosion resistance, as well as well as good biocompatibility. The two last properties are due to the ceramic-like surface caused by the high affinity of titanium for oxygen which results in the spontaneous formation of a dense oxide layer at the surface [19].

The main mechanical properties of CP titanium and titanium alloys are shown in **Table 1.1**. Titanium and titanium alloys show a lower elastic modulus compared to other currently used biomaterials for implants, which reduces the stress-shielding effect in bone implants. This effect is related to the mismatch between the elastic modulus of bone (about 1–20 GPa) and that of the implant material (around 100 GPa for titanium) causing the unsolicited bone tissue to degrade as most of the mechanical load will concentrate on the stiff implant. In the long term this may increase the risk of loosening of the implant. Even though the stiffness of titanium and its alloys is still largely greater than that of cortical bone, it is less than that of Co-Cr type alloys and stainless steels used for biomedical applications (240 and 210 GPa, respectively) [20].

The importance of the match of mechanical properties between materials used in implant systems is fundamental in rehabilitation and not only applies to the bone-metal pair but also to the different parts within the dental implant. It has been observed that in metal-ceramic restorations, prosthodontic alloys must possess a high elastic modulus to resist bending which might cause the fracture of the porcelain [21]. Moreover, if there is a large difference in hardness between abutment and implant fixture/crown the wear rate of the components can increase. Therefore, depending on the application, the dental implant material should possess specific mechanical, physical and chemical properties to insure a long term clinical performance

As mentioned before, titanium has an elastic modulus more similar to that of cortical bone and high biocompatibility when compared to other metallic alloys used in implants [10]. Apart from the CP titanium, titanium alloys such as Ti6Al4V, TiNi, Ti13Nb13Zr, Ti12Mo6Zr2Fe, are currently available on the market. The mechanical properties of Ti6Al4V are higher than for CP titanium which can be

explained by differences in microstructure and/or residual elements due to the alloying process [22]. In fact, the mechanical properties of titanium alloys depend on the amount, size, and morphology of α -titanium, and on the density of α/β interfaces [10].

Table 1.1. Mechanical properties of different biomaterials [22][20].

| Type of biomaterials | Density (g/cm ³) | Ultimate tensile strength (MPa) | Young's modulus (GPa) | Fatigue strength (MPa) | Elongation at fracture (%) |
|--------------------------------|------------------------------|---------------------------------|-----------------------|------------------------|----------------------------|
| Metals | | | | | |
| CrNi-steels | 7.8 | 490-690 | 200 | 200-250 | >40 |
| CoCr-alloys | 8.5 | 800-1200 | 230 | 550-650 | 8-40 |
| Cp-Ti | 4.5 | 390-540 | 100 | 150-200 | 22-30 |
| Ti6Al4V | 4.5 | 930-1140 | 105 | 350-650 | 8-15 |
| Ceramics | | | | | |
| Al ₂ O ₃ | 3.2 | 350 | 380-420 | - | <1 |
| ZrO ₂ | 3.5 | 350-400 | 150-208 | - | <1 |
| Polymer | | | | | |
| PMMA | 1.2 | 24-28 | 3.3 | 20-30 | <1 |
| UHMWPE | 1< | 37-46 | 0.9 | 16 | |
| Cortical bone | | | | | |
| | 1.6-2 | 80-150 | 7-30 | 23 | 1-2 |

Pure titanium (CP Ti) has an allotropic phase transformation from the lower temperature hexagonal close packed (*hcp*) phase (called α -alpha titanium) to the body centered cubic (*bcc*) phase (called β -beta titanium) at 882°C. Alloying elements can change phase transition temperature between α -titanium and β -titanium. **Figure 1.2** shows basic phase diagrams of Ti alloys depending on the alloying element. These alloying elements can be classified into 3 categories:

- **α stabilizers.** Elements such as O, Al, N and C increase the allotropic phase transformation temperature. Therefore these elements help to stabilize the alpha phase at room temperature.
- **β stabilizers.** Elements such as Mo, V, Nb, Ta (isomorphs) and Fe, W, Cr, Si, Co, Mn, H (β eutectoids) stabilize the β phase and therefore lower the allotropic transformation temperature are classified into two groups. The first group is known as β -eutectoid formers and includes elements such as Cu, Cr, W and Fe. The other group is known as isomorphous elements.
- **Neutral elements:** Zr and Sn

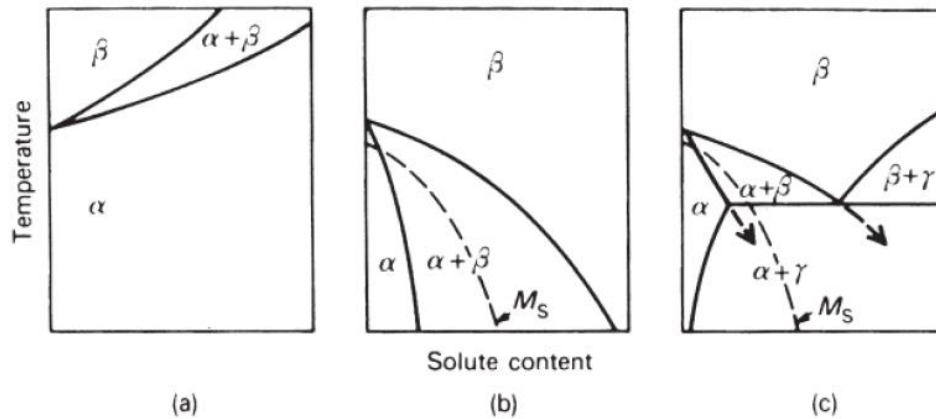


Figure 1.2. Basic phase diagrams for Ti alloys. The alloying elements affecting various phase diagrams are (a) Al, O, N, C; (b) Mo, W, V, Ta; (c) Cu, Mn, Cr, Ni, Fe. The dotted lines in (b) and (c) show the martensite starts (M_s) temperatures [23]

The microstructure of the thermo-mechanized alloys depend on the temperature of the process. A mixed $\alpha + \beta$ microstructure is obtained when the process takes place at a temperature below the β transition whereas above this limit a lamellar structure appears. The fraction and nature of the α and β phases are also affected by the chemical composition and the temperatures of thermal treatments and cooling. During fast cooling, the β phase can give rise to a martensitic structure or α' with retentions of the phase. However during a slow cooling, the β phase will almost completely be maintained. For metastable alloys, the β phase is maintained with cooling and very small structures precipitate at low temperature which increases the hardness of this type of alloy.

Depending on the resulting microstructure, the titanium alloy will be classified as **α /near α** alloys (only α microstructure), **$\alpha+\beta$** alloys (contain 10-30% of β microstructure) and **β** (metastable/stabilized) alloys which will influence the properties of the material. $\alpha+\beta$ microstructures will show an elevated hardness, lower ductility and an increased resistance to fatigue whereas β microstructures will exhibit lower Young's modulus. Hardness of the material tends to increase with the amount of β stabilizers. The microstructure obtained through different thermo-mechanical processes is shown in **Figure 1.3**.

Even though a material shows appropriate mechanical properties and corrosion resistance, the application of titanium alloys is also dictated by high biocompatibility requirements [21]. Possible cytotoxic effects associated to the presence of Al and V ions released from Ti6Al4V alloys have been reported in the literature [24]. Pan et al. [25]. studied the growth of endothelial cells *in vitro* on Ti6Al4V alloy and they verified a permanent oxidative stress of cells followed by a decrease of the metabolic activity, radical formation and antioxidant defense molecules production. These alloying elements are also suspected to be related to long-term health problems such as Alzheimer disease,

neuropathy and osteomalacia [26]. Extensive research is being done in order to develop new titanium alloys which better comply with biocompatibility and non toxicity requirements. Ti-6Al-7Nb, developed in the 80's, has nearly the same mechanical properties as Ti-6Al-4V Grade 5, but the toxic element vanadium is replaced by the biocompatible niobium. This alloy is currently being used as a replacement for Ti6Al4V. Another important line of research regarding medical implant material is the development of so-called metastable beta-titanium alloys. These alloys exhibit a lower elastic modulus down to 50–60 GPa, overcoming the issues related to stress shielding phenomena because it is more proximally to the bone modulus.

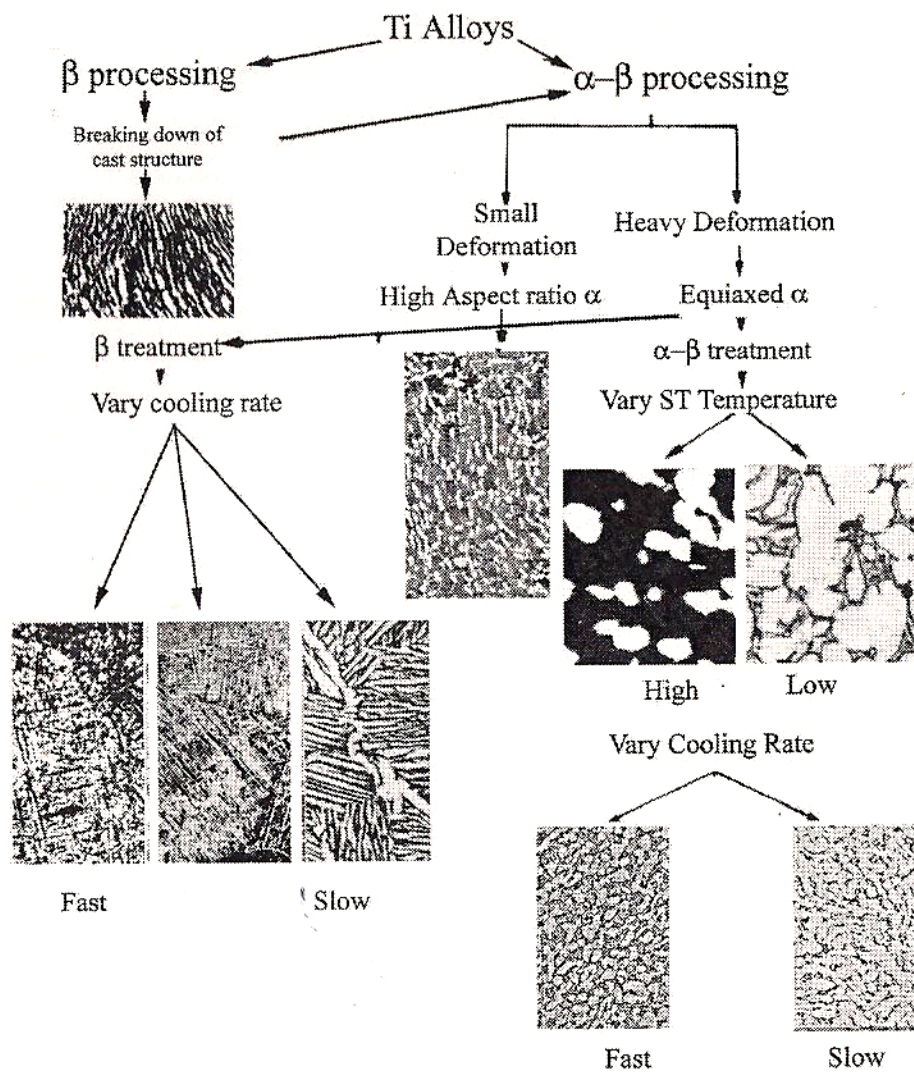


Figure 1.3. Influence of the thermal-mechanical process on the microstructure of the titanium alloy [27]

1.1.2. Titanium based Powder Metallurgy for biomaterials

In most cases, metallic implants are manufactured by ingot metallurgy which consists in first casting semi-finished parts, which means that the implant is formed from molten metal that is poured into a mold, followed by cold or hot working in order to improve the microstructure/mechanical properties and finally net-shaping by mechanical machining to obtain the final product [28]. Titanium production is hampered by the high cost in traditional manufacturing processes, and poor workability for complex shape production. This has led to numerous investigations of various potentially lower-cost processes. The **powder metallurgy** (PM) process is an attractive technique for the fabrication of implants due to its net or near-net shape capability [28]. The PM technique aims to transform metallic powders using pressure and heat. The thermal treatment referred to as *sintering* substitutes the classic melting and is carried out below the melting point of the most important metal. **Figure 1.4.** shows the general procedure of traditional powder metallurgy.

Up to date most Ti based implants are used in dense forms although it carries problems such as biomechanical mismatch of elastic constant and lack of biological anchorage. In general, implant failure is more likely due to aseptic loosening, after 10 years implantation, rather than to the mechanical failure of the material. Currently, implant research for orthopedic and dental use focuses on studies that address and enable a more reliable anchoring of the implant for a successful long-term performance and also a more rapid osseointegration of implants, in an attempt to reduce or even eliminate the period of bone healing free from functional load. Implant porosity has shown to improve bone neoformation. Studies focusing on porous metallic implants started in the late 1960s with Hirschhorn who reported on the fabrication of a porous CoCr alloy for use as an implant material [29], followed by Lueck et al. with a porous material consisting of pure Ti fibers [30]. During the early 1970s, porous coatings were first studied by Welsh, Galante, Pilliar and Cameron [31-34] with dual-structured implants. It consisted in a solid-machined or cast metallic core with a porous surface obtained using sintered metal powders or fibers. The powder metallurgy method can be used to manufacture porous implants or coatings.

Powder metallurgy offers the possibility of obtaining well-defined surface roughness or functional porosity, combining improved implant fixation (due to bone ingrowth) and adaptation of the elastic properties to the human bone reducing therefore the risk of stress shielding [28]. Another potential benefit would be to make dental implants less invasive. In fact, difficult implantation cases require bone grafts, with the increased friction of porous titanium smaller implants are needed reducing the need for graft surgery. Porous titanium has previously been used in orthopaedic applications, but hardly ever for dental implants even though its properties are ideal for this purpose. PM titanium

implants have been shown to be promising for biomedical applications, such as intervertebral discs, dental implants, or acetabular hip prostheses [35-37].

A titanium part can be made from powder using different methods. These include the traditional press-and-sinter or press-sinter-and-hot-work, extrusion or direct roll compaction of loose powders, hot-press-and-machine, hot isostatic pressing and metal-injection-moulding-and-sinter. The press-and-sinter route, which is the method used in this work, is technically the simplest and the most economically attractive.

The traditional powder metallurgy method shows several advantages [28]:

- Net or near-net shape capability, with no or very small amount of cutting and machining
- High utilization rate of materials, over 95%
- Small grain sizes and consistent and stable microstructure
- High strength and hardness
- Ability to produce complex or abnormal structural parts by mold forming which is difficult to be produced by other methods

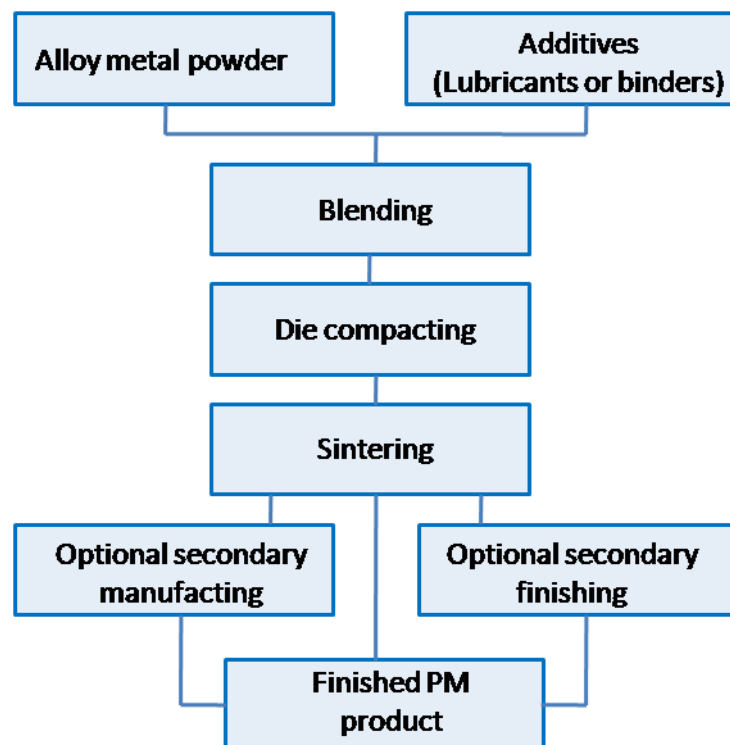


Figure 1.4. Simplified flowchart illustrating the sequence of operations in powder metallurgy

Production of the raw powder material:

The first major hurdle in PM is the availability of low-cost, low-impurity powder. Many processes of titanium and titanium alloy powders manufacture are known, these are: chemical reduction, hydrogenation/dehydrogenation, gas atomization, plasma-rotating electrode and plasma atomization.

Compaction:

Compaction of titanium mixture powders in closed steel dies, can be carried out with standard presses at room temperature, to obtain **green** compact similar to that of the final part, however, shrinkage will occur during the sintering phase of the manufacturing process. A pressure < 700 MPa is sufficient to ensure good green strength, which is essential for the safe and rapid ejection of green shapes from the die cavities and their subsequent handling prior to sintering.

Adding a lubricant to the metal powder prior to compaction is common for iron and aluminum but is avoided for titanium in order to limit possible contamination as it is a very reactive material [38]. However, it is possible to lubricate the die-wall in order to reduce both die wear and ejection force [19]. The typical commercial grade PM lubricants are zinc and lithium stearates and Acrawax [39].

In the case of biomedical applications, macropores (pore diameters in the range between $100\ \mu\text{m}$ to several mm) can be created using space holder materials [40], easily controlling porosity density, pore shape and pore sizes. Besides the macropores, residual micropores from the sintering process are observed. Both types of porosity are useful in implant applications since microporosity allows body fluid circulation and improves cell adherence, whereas macroporosity provides a scaffold for bone–cell colonization in combination with vascularization of blood vessels [41]. The space holders can be removed before or after the sintering step. Either thermally, prior to sintering, using a relatively low temperature to prevent any reaction with the host material. This temperature should be generally below 400°C for titanium. Or removal can be done by leaching out in a suitable solvent after sintering.

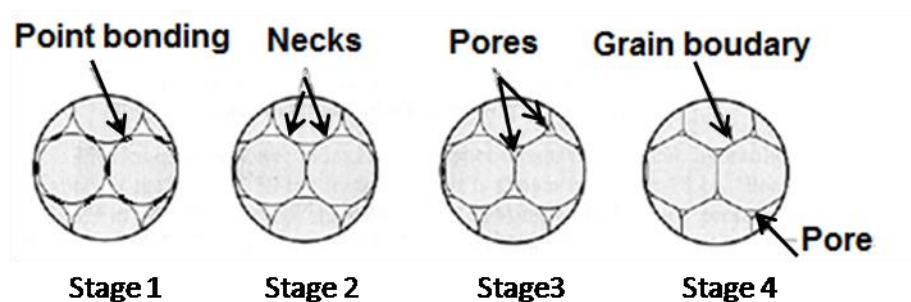


Figure 1.5. Sintering on a microscopic scale [28]

Sintering:

Green compacts need to be sintered because of their low strength. The purpose of sintering is that powder compacts achieve solid bonds among powder particles as illustrated in **Figure 1.5**, which shows on a microscopic scale the changes that occur during sintering of metallic powders. The sintering of powder materials follows a succession of heating ramps as shown on **Figure 1.6**. At approximately 550 °C, during the preheating phase, the oxide film on titanium powders disappears as it can diffuse into the titanium α phase [42] and therefore has little influence on the course of the sintering of titanium. Sintering of titanium-based materials takes place at temperatures below the melting point of the material, between 1200°C and 1500°C. It is therefore a critical step due to the possibility of oxygen and carbon contamination. This is due to the high temperatures involved, forcing the pick-up of interstitials.

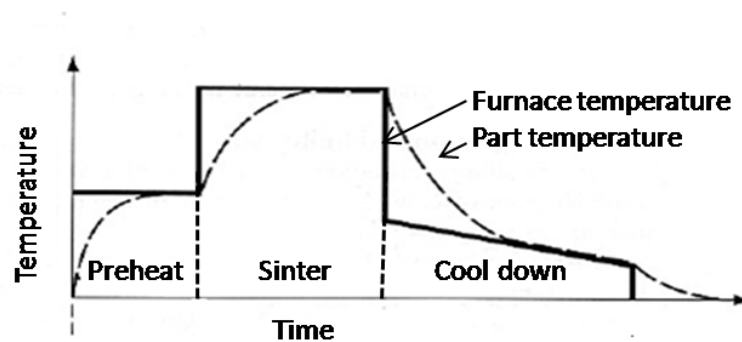


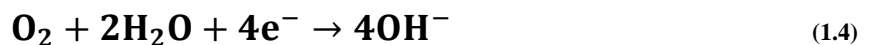
Figure 1.6. Typical heat treatment cycle in sintering [28]

In order to avoid such problem sintering has to be done under a controlled atmosphere. High-vacuum is the preferred sintering practice for titanium. However it is adapted for continuous production as large vacuum furnaces are usually difficult to operate at high temperatures from a production point of view due to leakage of oxygen and nitrogen from the surrounding atmosphere. Therefore Argon atmosphere, which was first used by Kroll [43], is the preferred atmosphere to prevent contamination and enable continuous production.

1.2. Electrochemical nature of corrosion

1.2.1 Fundamentals of corrosion

The **corrosion process** is an irreversible chemical or electrochemical reaction occurring at the interface of the material representing the spontaneous dissolution of the metal (M) by its reaction with the environment resulting in the loss of the material or in the dissolving of one of the constituents of the environment into the material [44]. The oxidation of the metal, **equation (1.1)**, is coupled to the reduction of the oxidizing agent (environment) which takes the electrons from the oxidation reaction. The **equations (1.2)** and **(1.3)** show the reduction reactions take place in acidic media, while the **equations (1.4)** and **(1.5)** are favored in neutral or alkaline media.



Corrosion reactions are not always detrimental to a metal as it can lead to the formation of protective reaction products such as in passive film. This **passivity** of metals consists in the spontaneous formation of a thin oxide layer on their surface which protects the metal from its environment. It is a physical barrier which limits cathodic and anodic reactions in taking place therefore lowering the corrosion rate.

The corrosion rate of a metal M is determined by the rate of reaction **(1.1)**, which is dependent on the electrode potential i.e. the electrical potential established across the metal/electrolyte interface. When under equilibrium conditions, reaction **(1.1)** is at kinetic equilibrium with the reduction reaction and the corresponding electrode potential is called corrosion potential. A metal may experience different corrosion potentials depending on the environmental conditions. Indeed under working conditions, the corrosion potential of a metal is influenced by a variety of factors such as the temperature, the rate of mass transport of the oxidizing agent or of anodic reaction products, kinetics of the reduction reaction, formation of passive surface films, galvanic contacts with other materials or externally imposed currents. Therefore, applying a well-defined potential to the metal offers the possibility to simulate the behaviour of a metal in a variety of practical corrosion situations [45].

1.2.2 Corrosion mechanisms of titanium and titanium alloys

Titanium and its alloys are classified as a passive material due to the formation of a thin titanium oxide film (TiO_2) when bare titanium is in contact with oxygen. In a bio-system this layer plays two important roles regarding corrosion and as a result biocompatibility [46].

The protectiveness of the passive film is determined by the rate of ion transfer through the film as well as the stability of the film against dissolution. Numerous factors can influence ion transport through the film, such as its chemical composition, structure, thickness and presence of defects. The nature and stability of a passive film on a particular metal or alloy depends on the environment conditions such as the chemical composition of the electrolyte, the redox conditions, the exposure time and temperature [37]. Many researchers have studied the electrochemical behavior of Ti based alloys in simulated physiological environments [47].

The composition of the passive film of Ti alloys presents high content in Ti (mainly TiO_2 with small amounts of suboxides TiO and TiO_3) and smaller amount of the alloying elements' oxides. In the case of the Ti6Al4V alloys, aluminium oxide Al_2O_3 and Vanadium oxides (V_2O_3 , V_2O_5) can be found. For Ti6Al7Nb , apart from Al_2O_3 oxides, niobium oxides (Nb_2O_5 , and NbO and/or NbO_2) can be incorporated in the passive layer. The Depth profiles of composition of surface oxide formed in simulated biological media of the Ti6Al4V and Ti6Al7Nb was studied by several authors. TiO and Ti_2O_3 are found to be closer to the metal/oxide interface. Concerning the alloying elements, oxidized Al is found at the top whereas the presence of Vanadium and Niobium oxides at the outermost surface is still ambiguous. Milosev et al. [47-48] observed a linear increase of the layer thickness of Ti6Al4V and Ti6Al7Nb with potential, up to a maximum of 9 nm approximately

The alloying elements play an important role in the electrochemical behavior of the alloy. Ti-6Al-7Nb alloy exhibits a broader passive range than Ti-6Al-4V alloy in simulated physiological solution [49, 50]. According to Metikoš-Huković et al. this increased corrosion resistance is due to the incorporation of Nb cations into the TiO_2 matrix [49]. The high protectiveness of the passive layer formed on Ti-6Al-7Nb alloy was also ascribed to the formation of a double oxide layer, a dense inner barrier layer and a porous outer layer [51].

1.2.3 Corrosion of titanium biomedical alloys in the oral environment

Saliva is produced by several glands (parotid, submaxilar, submandibular and oral mucosal) and has for goal to maintain the oral health. Human saliva is mainly composed of water (99%) with small amounts of organic and inorganic compounds. The main organic components are proteins (e.g. albumin), glycoproteins (e.g. mucin), amino acids (e.g. leucine), carbohydrates (e.g. glucose) and lipids (e.g. phospholipids). The inorganic components are mainly ions such as Ca^{2+} , PO_4^{3-} , Na^+ , K^+ and HCO_3^- [18].

The pH of saliva is usually found between 7-8. HCO_3^- binds to H^+ to form H_2CO_3 , H_2O and CO_2 , acting as the main buffering compound by maintaining the equi concentration of acid and base, i.e. $\text{H}_2\text{CO}_3/\text{HCO}_3^-$. The resulting increase in pH prevents teeth demineralization [52, 53]. However external factors (such as our diet and the presence of microbial metabolites) or internal factors (such as a dysfunction of the salivary glands) may affect the pH, making it vary from 3 to 8 [18]. In fact, the increase of lactic acid-producing bacteria is a critical factor in lowering of the pH which may happen during sleep due to a decrease in the salivary flow rate.

In order to study the corrosion behavior of biomaterials intended for dental applications several artificial saliva formulations have been used to mimic oral conditions [54, 55]. However, duplicating exactly human saliva properties is impossible due to the inconsistent and unstable nature of natural saliva, which makes the latter also inappropriate for use in standardized in vitro studies. Finding a good formulation is difficult to achieve as artificial saliva for in vitro tests should reproduce and react with the test material in a manner similar to natural saliva. Most of the reported synthetic saliva solutions are simplified version of what may actually occur in the oral cavity in terms of solubility of component, are organic-free and may even include unjustified components such as sulphide and pyrophosphate [54, 55]. Even though many formulations of artificial saliva are found in literature, Fusayama's solution has been largely used to study the electrochemical behavior of dental materials, including titanium and its alloys [56, 57]. In fact, results from corrosion studies using Fusayama's solution have shown to be consistent with the clinical experience of the materials, even though it should be noted that the formula deviates from natural saliva i.e. in the presence of sulphur and higher concentration of urea. In the present thesis a modified version of Fusayama's solution has been used corresponding to the following composition: 0.4 g NaCl, 0.4 g KCl, 0.6 g CaCl_2 , 0.58 g $\text{Na}_2\text{HPO}_4 \cdot 12\text{H}_2\text{O}$, 1 g urea, and distilled water 1 L. Similar results have been obtained when studying the electrochemical behavior of Ti and CoCrMo in this modified artificial saliva and fresh human saliva therefore validating the use of this solution when assessing the corrosion resistance of Titanium [58].

The TiO₂-film possesses a high corrosion resistance in various test solutions, such as artificial saliva, Ringer's solution, 0.9% NaCl solution, or physiological saline solution [57]. Schiff et al. [56], when measuring the corrosion potential of Ti6Al4V and CP-Ti, found good corrosion resistance in artificial saliva, enriched or not by lactic acid, although a slow decrease of corrosion potential was reached in the acidified solution. However, localized corrosion has been observed in solution with a lower pH and containing fluorides [59].

Fluoride therapy is now recognized as being one of the principal methods in preventing dental caries. It has been used for oral care in order to prevent demineralization and enhancing the remineralization of teeth [60]. Fluorides are present in toothpaste, mouth wash, and other dental hygiene products, most often added as the sodium salt, NaF, with concentrations ranging from 0.1% (1000 ppm) to 1% (10,000 ppm). Due to retaining mechanisms, such as the formation of CaF₂, traces can be found in the oral cavity even after their use. However, as early as 1957, awareness was raised on the possible deleterious effects of fluorides. For example, when found in an aqueous solution fluorides may have deleterious effects as it can form hydrofluoric acid (HF) from association between F⁻ and H⁺ [57]. Several studies have been undertaken on the combined effects of pH and concentration of fluoride ions on the solubility of TiO₂.

Only 3ppm of NaF in solution has been reported to be sufficient to tarnish the surface of Ti while autoclaving Ti implants [61]. While Horasawa and Marek [62] observed discoloration of Ti in a 1% NaCl solution occurs even at low concentrations (5–15 mg/cm²) of fluoride ions released from glass ionomer cements for dental use.

Nakagawa et al. [57] conducted immersion tests using different concentration of NaF and varying the pH. Their study revealed that the amount of fluorides needed to hinder the integrity of the passive film decreased with pH. While 0.4% of NaF (approximately 2000 ppm F⁻) was needed to observe the corrosive effect of fluoride ions for Ti, Ti6Al4V and Ti6Al7Nb at pH 5.5, they observed the destruction of the passive film of Ti in acidic artificial saliva solution with an HF concentration of only 30 ppm. The same observation was made for Ti6Al4V and Ti6Al7Nb in artificial saliva containing 200 ppm F⁻ at pH 4.2 and 3.7 respectively.

Al-Mayouf et al [63] also observed high corrosion rates in neutral solutions with high fluoride concentrations and in acidic solutions with low fluoride concentrations while studying the corrosion behavior of Ti, Ti6Al4V and Ti-30Cu-10Ag in artificial saliva varying pH (3-7) and NaF concentration (0, 0.01, 0.05 and 0.5 M). Boere [64] observed a large decrease in polarization resistance with increasing fluoride concentration at pH 4 while no change was observed at pH7.

Schiff et al. [56], reported a decrease of the corrosion potential of Ti6Al4V (and destruction of the protective layer) after a 24 h incubation period in fluoridated saliva (pH 2.5 - 1000ppm F⁻)

The presence of fluoride ions in the solution has been reported to alter the structure of the oxide layer causing it to be porous [63]. HF molecules can react on the titanium surface to give rise to titanium oxyfluorides in solid state. The lattice parameter of these compounds is such that they induce many structural defects in the oxide coating, whose protection is considerably loosened [63]. On the other hand Huang et al. have reported Na₂TiF₆ crystals at the surface of CP-Ti immersed for 8 h in 1% NaCl containing 1% NaF [65]. Fluoride ions in the electrolyte can form complex titanium-fluoride molecules which are very stable and soluble in the electrolyte solution. The titanium tri- and tetrahalides tend to form complexes with oxidizable atoms. The halide complexes [TiF₆]²⁻, [TiF₆]³⁻, [TiCl₅(H₂O)]⁻, [TiCl₆]²⁻ and [TiCl₅(H₂O)]²⁻ are known to be molecular species able to potentially form soluble salt with NH₄⁺ and alkaline metals. The formation of this type of salts thus explains the dissolution of titanium in the presence of HF and fluorides [66-68].

1.2.4. Corrosion of porous material

The sensitivity of corrosion to porosity is a reason of concern to maintain the integrity of the implants during their lifespan. Seah et al. [69] investigated the anodic polarisation behaviour of sintered pure titanium processed by powder metallurgy in 0.9% NaCl at 37°C. When compared to solid titanium, good passivation characteristics are exhibited however increased corrosion density and a narrower passivation region are observed. Larger current density for sintered titanium does not only result from the larger true surface area of the porous samples. Edwards and Higham [70] reported that surface area is not the only factor influencing corrosion and the type of porous structure had to be taken into account as crevices or restrictions to the flow of species can result in corrosion rates that are not proportional to the true surface area. Indeed, the anodic growth of titanium oxide obeys the high-field mechanism where film growth by ionic transport is controlled by the electric field across the film [71]. In porous structures, therefore, the limit of the influence of pore morphology on corrosion is not only dictated by the electrode potential but also by the supply of ionic species which ultimately, depend on pore morphology [71]. It was suggested that the highly porous compacts (produced under low compaction pressure), exhibiting wide open channels are narrow and isolated, thereby would provide a large number of sites capable of trapping liquid that eventually promote crevice corrosion. In low porosity compacts (produced under high compaction pressure), the high densification would promote pore closure during sintering, reducing the resultant number and size of crevices, causing these compacts to be more resistant to crevice corrosion attack [71]. Indeed, the study of the electrochemical properties of a selective laser sintered porous Ti-10Mo in a naturally aerated 0.9 wt % NaCl solution at 37°C showed the decrease of porosity caused the corrosion potential to move

towards positive direction, the corrosion current density reduced and the passivation range broadened, indicating an improvement in corrosion resistance [72]. Fojt et al. [73] studied the corrosion behaviour of porous Ti39Nb alloy processed by powder metallurgy and reported that up to 15 % of porosity samples exhibited similar corrosion behaviour to the dense samples, however, localized corrosion was observed above this porosity value.

However, the vulnerability of sintered titanium to localised corrosion was further studied by cyclic voltammetry and the final E_{corr} value was observed to decrease with decreasing porosity. Indeed in this case it was argued that small and isolated pores in the denser compacts promoted the trapping of electrolyte species and the exhaustion of oxygen supply which is crucial to the stability of the titanium oxide film. However in the more porous compacts, the interconnected structure enabled the species to flow freely and replenish the oxygen supply during the passivation [71]. Such studies highlight importance of porosity in corrosion resistance of porous structures.

1.3. Tribocorrosion

1.3.1. Concept and involved phenomena

Tribocorrosion can be defined as the material deterioration process which results from the combined effect of wear and corrosion that takes place in tribological contacts exposed to aggressive environment [74]. It is an irreversible transformation.

Many industrial sectors may be affected by this problem (such as transport industry, oil and gas, mining, biomedical engineering, food and textile industry) as tribocorrosion can affect a grand variety of devices where usually metallic components are at the same time in contact and in relative motion in a corrosive environment [74].

Material degradation due to the combination of mechanical and electrochemical solicitations may occur under a variety of conditions. A common tribocorrosion configuration is when two surfaces are in sliding movement either under two bodies or three bodies contact. Their relative movement can be unidirectional or reciprocating. In literature the term tribocorrosion is used most exclusively for sliding contacts. When the tribological contact consists of oscillatory micromovements so that the passive film is not rebuilt and the corrosion of the metal is continuously enhanced during the wear test, it is referred to as fretting corrosion [75]. Finally, when a particle impact or impingement attack is involved, which can also result in a combined mechanical, chemical, electrochemical attack of the material it is referred to as erosion corrosion.

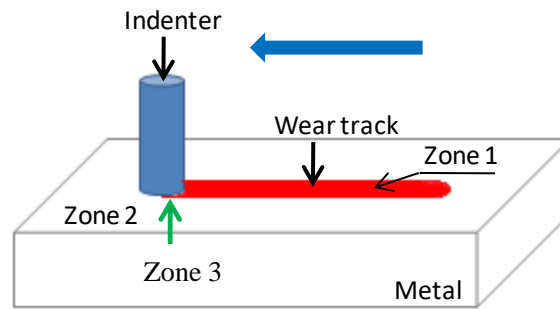


Figure 1.7. Model tribocorrosion situation

Figure 1.7 shows a model tribocorrosion situation where a chemically inert indenter is sliding against a passive metal plate. The whole contact is immersed in an aqueous solution. Three zones can be identified, which suffer three different tribocorrosion mechanisms:

- Zone 1: The worn surface. It undergoes depassivation (removal of the passive film and exposure of bare metal to the solution) due to the mechanical loading followed by repassivation. Thus corrosion rate increases due to the wear action. In this zone, wear **accelerated corrosion (WAC)** takes place.
- Zone 2: The mechanically unaffected metal surface which is only affected by corrosion. Under typical tribocorrosion conditions a galvanic coupling establishes between the depassivated area and unworn zone resulting in a shift toward lower potentials of the latter with a consequent change in corrosion rate.
- Zone 3: contact zone, where mechanical removal of material takes place due to the tribological contact between the indenter and the material. In this zone, **mechanical wear** takes place.

A tribocorrosion process can be affected by numerous parameters and interactions as shown in **Figure 1.8**

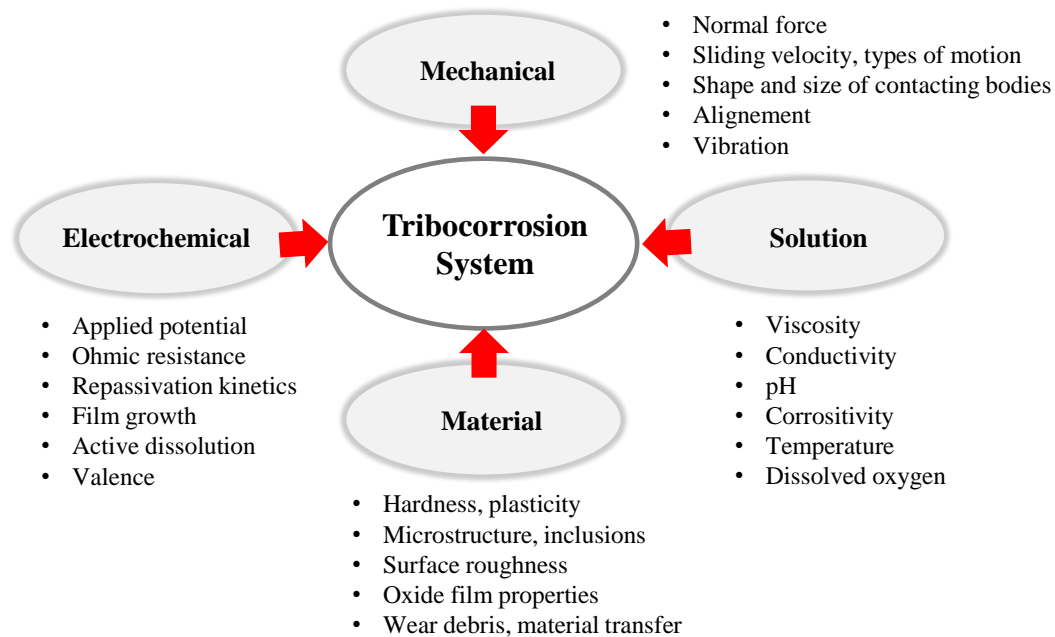


Figure 1.8 Factors influencing the tribocorrosion

The tribocorrosion mechanisms of passive metals sliding or interacting against an inert counterpart have been studied according to the following 4 different approaches:

The synergistic approach

The first attempt to model the quantitative effect of the synergism between wear and corrosion was proposed by Madsen et al [76]. According to these authors the total material loss due to tribocorrosion (T) can be expressed as the sum of three components according to the following equation:

$$T = W + C + S \tag{1.6}$$

Where W represents the material loss due to pure wear, C represents the material loss due to corrosion in absence of wear and S represents the synergistic factor which is the combined effect of wear and corrosion. This synergistic term (S) is defined as the sum of the change in corrosion rate due to wear (wear-accelerated corrosion, ΔC_w) and the change in wear rate due to corrosion (corrosion-accelerated wear, ΔW_c), using the following equation:

$$S = \Delta C_w + \Delta W_c \tag{1.7}$$

The mechanistic approach

First proposed by Uhlig (1954) [77], this approach takes into consideration two main contributions: the metal loss due to chemical or electrochemical oxidation also called wear-accelerated corrosion (V_{chem}) and the mechanical removal of metal particles (V_{mech}).

Therefore the total wear volume (V_{tot}), can be expressed as the sum of these two components using the following equation:

$$V_{\text{tot}} = V_{\text{mech}} + V_{\text{chem}} \quad (1.8)$$

In the case of passive metals, the corrosion in both the depassivated and passive areas contribute to V_{chem} , even though the latter is negligible.

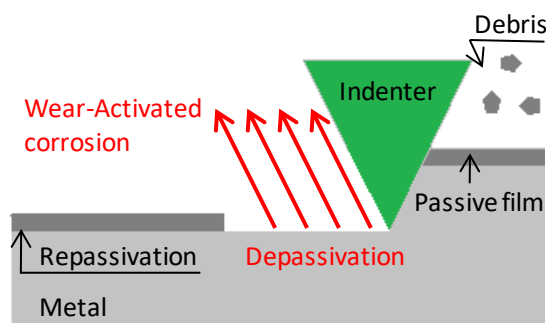


Figure 1.9. Illustration of the mechanistic approach [78]

For potentiostatic tribocorrosion experiments the amount of anodically oxidized metal (V_{chem}) can be determined from the measured current using Faraday's law:

$$V_{\text{chem}} = \frac{Q \cdot M}{n \cdot F \cdot \rho} \quad (1.9)$$

Where Q is the electric charge flowing in the wear track, M is the atomic mass of the metal, n is the charge number for the oxidation reaction (apparent valence), F is the Faraday constant and ρ is the density of the metal. This equation is only valid if the measured current mainly corresponds to the anodic partial current for metal oxidation and the charge number n for the oxidation reaction is known.

The total volume loss can be determined by profilometry of the wear track and the mechanical contribution is calculated by subtracting V_{chem} to V_{tot} .

The third body approach

The concept of third body particles in sliding contacts was introduced by Godet to describe the velocity of accommodation in tribological contacts due to the presence of particles [79, 80]. As evidenced by Landolt et al. [81], their role is critical as depending on their properties they might behave as an abrasive which accelerates wear, or a solid lubricant which might decrease friction and wear.

A tribocorrosion system involving a passive metal (first body), an inert counter body (second body) and a third body is presented in **Figure 1.10**. The arrows indicate the possible movement of material happening in the contact.

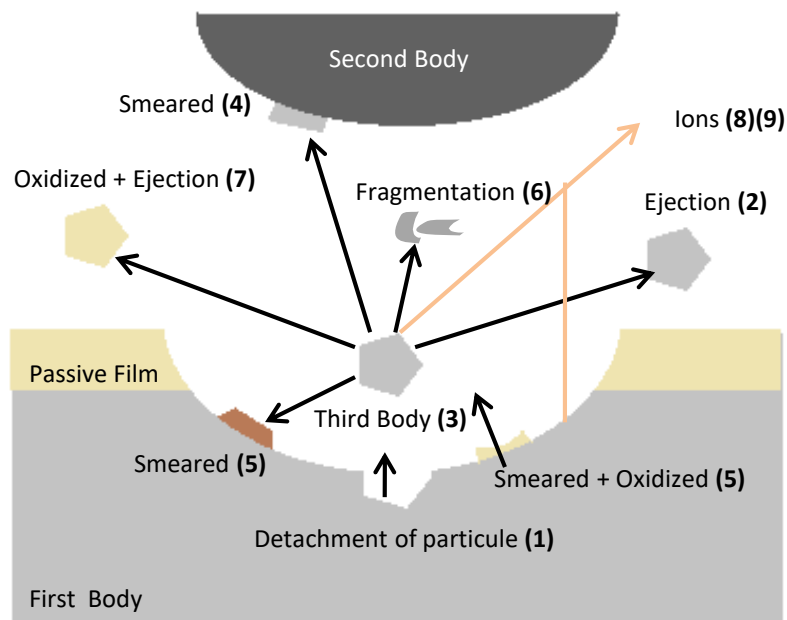


Figure1.10. The third body approach [75]

The antagonist (the second body) detaches wear particles from the metal (1) which can either directly be ejected from the contact (2) or remain in as a third body (3). The latter can adhere to the inert body (4) or to the metal (5) or further break into smaller particles (6). Once it has reached a critical size it can be ejected (7). Therefore corrosion can take place in 2 different locations, on the first body after detachment (9) or during fragmentation of the third body (8).

Depending on the physical properties of the third body wear can either be enhanced, if they can act as an abrasive, or lowered, if they behave as a solid lubricant diminishing friction and wear.

The subsurface deformation approach

This last approach introduces the subsurface deformation and the subsequent microstructural transformations (i.e. nanocrystalline layer formation) as determining factors in the wear behavior of sliding contacts.

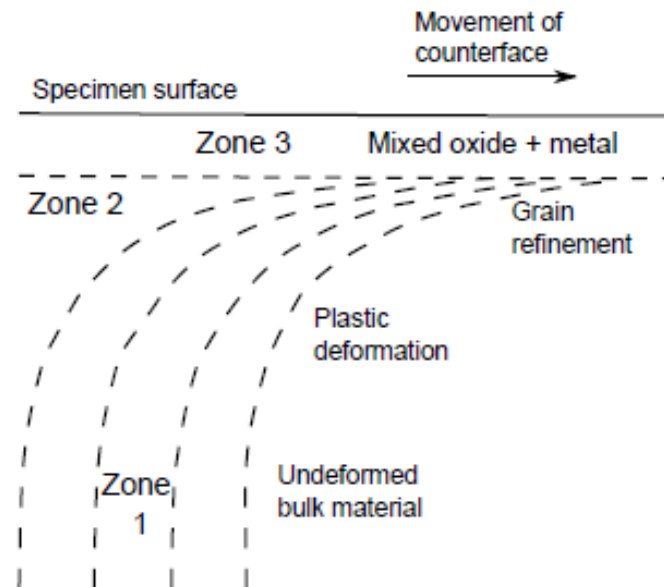


Figure 1.11. Cross-section scheme of the different regions beneath the worn surface of a metal-metal sliding contact [67]

Several authors have agreed on the following representation of the subsurface, first presented by Hutchings [82]. As shown in **Figure 1.11**, it is composed of 3 different zones:

- Zone 1: corresponds to the bulk material.
- Zone 2: corresponds to the plastically deformed area with a deformation gradient going from form the low strained bulk material (zone 1) to the highly strained material at the interface with the mechanically mixed layer (Zone 3)
- Zone 3: contains mixed material from the bulk and counterpart. Two layers can be distinguished: The tribochemical reaction layer, which is closer to the surface of the specimen and located on top of the nanocrystalline mixed layer.

Rigney [83] has published a review on the subsurface structural changes and associated wear mechanisms for ductile materials under sliding. The mechanism is thought to consist of two main steps:

- The formation of a nanocrystalline microstructure at the contact subsurface produced by the strain accumulation
- The wear generated by detachment of nano-grains

The occurrence of the nanocrystalline layer in tribocorrosion systems is due to the plastic deformation during the loaded sliding process. Under high plastic strains, dislocation cells form leading to dynamic recrystallization. Several authors have observed a larger deformation layer at passive applied potential than at cathodic potential. Perret et al [84] have suggested that the absence of the passive film at cathodic potentials would promote the annihilation process while at passive potentials the presence of a passive film can promote dynamic recrystallization by acting as a barrier to the displacement of dislocations.

The nanocrystalline layer is suspected to influence the wear of materials subjected to tribocorrosion due to the difference in the material properties from the bulk material. The following material properties of the mechanically mixed layer are expected to play a role:

- Increase in hardness which might result from the mixing with hard particles and chemical changes
- New crystalline structure may change the stress–strain response
- The mechanical mixing may also change the strain to failure, Young’s modulus and the coefficient of friction of the surface material.

1.3.2. Tribocorrosion models

Various models have been developed in order to predict the current transients in a tribocorrosion system and summarized below. The models can be separated into two main categories whether the approach is purely electrochemical or also takes into consideration mechanical parameters.

1.3.2.1. Wear accelerated corrosion model

Mischler et al. [85] and Landolt et al. [86] proposed a model for the prediction of the rate of wear accelerated corrosion in a two body sliding contact (passive metal and inert indenter and therefore not considering the third body) taking into account both the effect of normal load and the repassivation behavior of the metal.

During tribocorrosion of a passive metal mechanical wear causes the removal of the passive film, which will repassivate by oxidation of the underlying raw metal leading to an increase of the anodic partial current. Assuming that the anodic partial current is equal to the measured repassivation current I_p one can write:

$$I_p = R_{dep} Q_p \quad (1.10)$$

Where R_{dep} (m^2/s) is the rate of generation of depassivated area due to sliding and Q_p is the passivation charge density (C/m^2), i.e. the charge per surface area needed to form a new passive film on the abraded surface. The value of Q_p is potential dependent and can be experimentally determined by electrochemical tests using the following formula:

$$Q_p = \int_0^{\frac{1}{2}f} i_p dt \quad (1.11)$$

Where f is the frequency of rubbing. For a given metal–electrolyte combination the Q_p value depends on imposed potential. According to model [86], repassivation current I_p can be calculated using the following equation:

$$I_p = K_{st} v_s \left(\frac{F_n}{H_{wt}} \right)^b Q_p \quad (1.12)$$

where K_{st} is the proportionality factor including probability of depassivation of a contacting surface element, v_s is the sliding velocity, F_n applied normal load H_{wt} is the micro hardness in the wear track and b is a coefficient which value lies between 0.5 and 1 and depends on the type of contact.

Current increases with the applied normal load according to a square root or a linear relationship, which is expressed with the exponent b . The behavior of real systems is expected to lie somewhere in between the values of $b=0.5$ and 1. It depends on the dominant mechanism and the surface topography. The linear relationship between the repassivation current and applied normal load is predicted in the case of smooth hard body sliding on a rough ductile body. The exponent b takes the value of 0.5 for the contact between two rough bodies and when a hard rough body is sliding on a smooth ductile body. [86]

Barril et al. [87] showed the applicability of the models [85, 86], developed for the sliding contacts and based on cyclic depassivation-repassivation of the metal surface, in the fretting of Ti6Al4V. The effect of the normal load on the anodic current could be described using these models.

1.3.2.2. Galvanic cell model for tribocorrosion at open circuit potential

During tribocorrosion of a passive metal at OCP a galvanic coupling is established between the unworn passive surface (cathode) and the mechanically depassivated areas (anode) causing a cathodic shift of potential. The depassivated areas act therefore as an anode where metal oxidation is the dominating electrochemical reaction.

Vieira et al [88] proposed a model for the prediction of the anodic current passing through the wear track (i_a) at OCP, taking into account the cathodic kinetics and the corrosion potential of the alloys, the potential during sliding and the anode to cathode ratio.

Considering a galvanic cell, the anodic current I_a is equal to the absolute cathodic current I_c , one can write:

$$I_a = -I_c \Leftrightarrow i_a A_a = -i_c A_c \quad (1.13)$$

Where A_a and A_c correspond to the surface areas of the anode and cathode, respectively.

The difference between cathode potential E_c and anode potential E_a corresponds to the ohmic drop ($R_{ohm} \cdot I_a$) occurring in the solution according to:

$$E_a = E_c - R_{Ohm} I_a \quad (1.14)$$

Where R_{Ohm} is the ionic resistance of the solution located between cathode and anode.

Taking into account Tafel extrapolation of the linear part of the cathodic branch of the polarization curve this yields:

$$E_c = E_{\text{corr}} + a_a - b_c \log i_c \quad (1.15)$$

Where a_c and b_c are constants and E_{corr} the corrosion potential of the passivated metal. Combining **equations (1.13)** and **(1.15)** yields **equation (1.16)**:

$$E_c = E_{\text{corr}} + a_a - b_c \log(i_a) - b_c \log\left(\frac{A_a}{A_c}\right) \quad (1.16)$$

This model has been widely used in tribocorrosion literature in order to determine i_a and calculate the amount of anodically oxidized metal (V_{chem}) using Faraday's law (see **equation 1.9**)

1.3.2.3. Tribocorrosion of passive metals in the mixed lubrication regime

Cao et al. [89] developed a predictive wear model based on a mechanistic approach of tribocorrosion and lubrication taking into account clinical relevant parameters such as normal load, velocity and clearance.

Considering the mechanistic approach of tribocorrosion (**equation 1.8**), the mechanical wear rate V_{mech} can be determined using Archard's law which is a simple model used to describe sliding wear. It is based on the theory of asperity contact therefore contact of the surfaces is done only by a reduced number of asperities randomly distributed over the surface and these asperities have to withstand the load and the deformations in the elasticity domain.

It can be written as:

$$U_{\text{mech}} = K_m \left(\frac{F_n}{H}\right) v_s \quad (1.17)$$

Where U_{mech} is the mechanical wear rate according to the mechanistic approach of tribocorrosion. Other parameters are: k_m the wear coefficient depending on specific wear mechanism, F_n the normal load, v_s the sliding velocity, and H the hardness of the softer of the two materials in contact.

Considering the electrochemical model developed by Landolt et al, describing the extent of anodic current induced by sliding on passive metals, the chemical wear rate can be obtained by integrating the I_p (**Equation (1.12)**) into Faraday's law to obtain:

$$U_{\text{chem}} = K_{\text{st}} \frac{Q_p M v_s (F_n)^{0.5}}{n F \rho} \quad (1.18)$$

However **equations (1.12)** and **(1.17)** correspond to boundary lubricated contacts where the thickness of the hydrodynamic films is too small to provide any load bearing capacity and effective separation of the two contacting bodies. In the case of mixed lubricated contacts, part of the load F_n is carried out by the hydrodynamic fluid film and only a fraction of it acts as effective force F_{eff} at asperity contacts which generates mechanical wear and wear accelerated corrosion. The effective load in mixed lubrication regimes can be defined as.

$$F_{\text{eff}} = k_0 \frac{F_n}{h_{\text{min}}^{1.49}} \quad (1.19)$$

Where k_0 is a proportionality factor for effective load and h_{min} is the minimum film thickness.

Introducing F_{eff} as the effective load responsible for wear and depassivation of asperities in **equations (1.17)** and **(1.18)** and combining with **equation (1.12)** corresponding to mechanistic formalism yields a general equation for the tribocorrosion system degradation:

$$U_{\text{tot}} = K_m \left(\frac{F_{\text{eff}}}{H} \right) v_s + K_{\text{st}} \frac{Q_p M v_s (F_{\text{eff}})^{0.5}}{n F \rho} \quad (1.20)$$

The model correctly depicted wear rates observed in MoM hip joint simulators.

1.3.4. Tribocorrosion in the Oral environment.

The tribocorrosion of titanium in the oral environment is a complex system which depends on multiple factors. Several studies have been carried out to investigate the influence of the environment (artificial saliva composition, pH, fluorides) as well as surface treatments, which improve the wear and corrosion performance of the bulk material, on the tribocorrosion behavior of titanium alloys. Revathi et al has recently published a review article on the degradation mechanism which dental implants undergo after implantation [90]. The tribocorrosion of Ti alloys is found to be mainly due to the mechanical action and although independent of the pH, the addition of fluorides to acidified artificial saliva accelerates the corrosion process. Under sliding conditions at OCP, the dissolution of the oxide layer may take place due to the galvanic coupling formed between the worn area/anode and the unworn zone/cathode. The later depends on the surface treatment of the tested material, electrolyte and the contact pressure, load and frequency [90]. The influence of pH on the tribocorrosion behavior of commercially pure titanium in artificial saliva solutions was investigated by Vieira et al. [91]. Tests were carried out at OCP using the electrochemical noise technique which allows the fluctuations of both the corrosion current and potential to be monitored during sliding without disturbing the electrochemical state of the surface. The addition of citric acid to the artificial saliva resulted in an improvement of the tribocorrosion behavior, probably due to a lower corrosion rate during fretting. The tribolayers formed in the citric acid solution was more stable, resulting in lower corrosion currents and lower coefficient of friction. Souza et al [92] also studied the influence of fluoride on the tribocorrosion behavior at OCP of Ti in artificial under and reciprocating sliding. The Fluoride content ranged from 20 to 227 at pH 5.5 and 12300 ppm at pH 6.5. It was reported that, the total amount of material removed during the tribocorrosion test was significantly raised by the increased amount of fluoride. Nevertheless the OCP variation during sliding is almost negligible when the test is performed with very high amounts of fluoride (12300 ppm) which is due to an active state of titanium. In fact, the surface did not repassivate following the test. The registered coefficient decreased in the solution with high fluoride content probably due to the presence of reaction product layers

During implant operating conditions, alternative periods of movement and static conditions are produced. The effect of a latency period between the mechanical solicitations of pin on the worn surface has been studied by Dimah et al. [93]. They reported that the wear behaviour of the titanium alloy depends on the intermittent cycle imposed in the test. Indeed, increasing the intermittency (number of cycles pause/sliding), increased the removal of repassivated material compared to the continuous tests because in the pause period growth of the passive film took place.

Several authors studied the effect of small movements (fretting) on the degradation mechanisms of titanium and its alloys in saline solutions. For example, Barril et al. [94] studied the fretting corrosion of Ti6Al4V in 0.9 % NaCl solution and reported an increase of wear rate of titanium with the applied potential. The study revealed that the oxidation of debris significantly decreased the mechanical energy required for wear. In addition the strong influence of the electrode potential on the wear rate of titanium alloys has been attributed to the repassivation rate of the surface. Indeed, at anodic potential the repassivation rate of titanium, which consists in the formation of a new TiO₂ film immediately after mechanical destruction (depassivation), increases with potential causing the faster oxidation of third-body particles. Consequently the presence of these particles causes an increase in the contact pressure and therefore of wear.

1.3.4. Clinical impact

Despite the great benefits implants provide to patients there is a growing body of literature addressing the clinical issues of biomaterial degradation. **Figure 1.12** shows a scheme of the steps leading to body host reactions due to device implantation.

During their life span, implants subject to corrosion and/or wear can generate metallic ions and debris, respectively, which are released into the body. Higher contents of metal ions in surrounding bone tissue of retrieved implants was observed when compared to physiologic baseline values detected in healthy bones, was observed [15]. Metallosis i.e. deposition and build up debris in the soft tissues surrounding tissues of an implant has often been reported.

Degradation products can also be found in remote tissues. This distribution of foreign components to other tissues and organs is dependent on membrane diffusion into blood capillaries and lymph vessels. Metallic wear particles originating from prostheses have been detected in the vesicles of macrophage in the liver (0.1-10 µm in diameter), spleen, and para-aortic lymph nodes [95] showing a systemic particle distribution. Debris have been found in the paraorta lymph nodes in up to 70% of patients with total joint replacement. The large surface of debris is then available for further body-material interactions giving rise to further metallic ions release. The transport of metallic ions is facilitated by their bonding to blood components such as plasma protein, globulin and chylomicron (lipidic substance).

The presence of degradation products in human tissues can have biological effects on the surrounding tissues causing host reactions such as inflammation and foreign body reaction (FBR). FBR is the end-stage response of the inflammatory and wound healing responses following implantation of a medical device. It involves macrophages and foreign body giant cells. Enzyme and other bioactive molecules

associated with foreign body response may cause severe local tissue damage. Long term peri implant inflammations have been associated to osteolysis (bone resorption) causing failure of the implant due to loss of bone support [96]. Manaranche and Hornberger [97] classified the chemical corrosion of metallic materials in three classes based on the ion release per week: Class 1: $10 \mu\text{g}/\text{cm}^2$, Class 2: $10-100 \mu\text{g}/\text{cm}^2$ and Class 3: $100-1000 \mu\text{g}/\text{cm}^2$. Class 3 materials could stimulate an adverse biological response due the high release of ions.

Biomaterials can also cause immunologic toxicity. Dental materials in oral rehabilitation have been reported to cause immunological reactions such as gingivitis, mucosal inflammation and blistering. Vanadium has repeatedly been reported to be cytotoxic for human cells [24], explaining the growing effort to substitute this alloying element in new biomaterials. Ultrafine TiO_2 (UF- TiO_2) (<100 nm in diameter) particles have been reported to cause adverse biological reactions [98]. Garabrant et al. [18] reported that 50% of titanium metal production workers exposed to TiO_2 particles suffered from affected pulmonary function. Wang et al. have observed genotoxicity and cytotoxicity effects of UF- TiO_2 in cultured human cells.

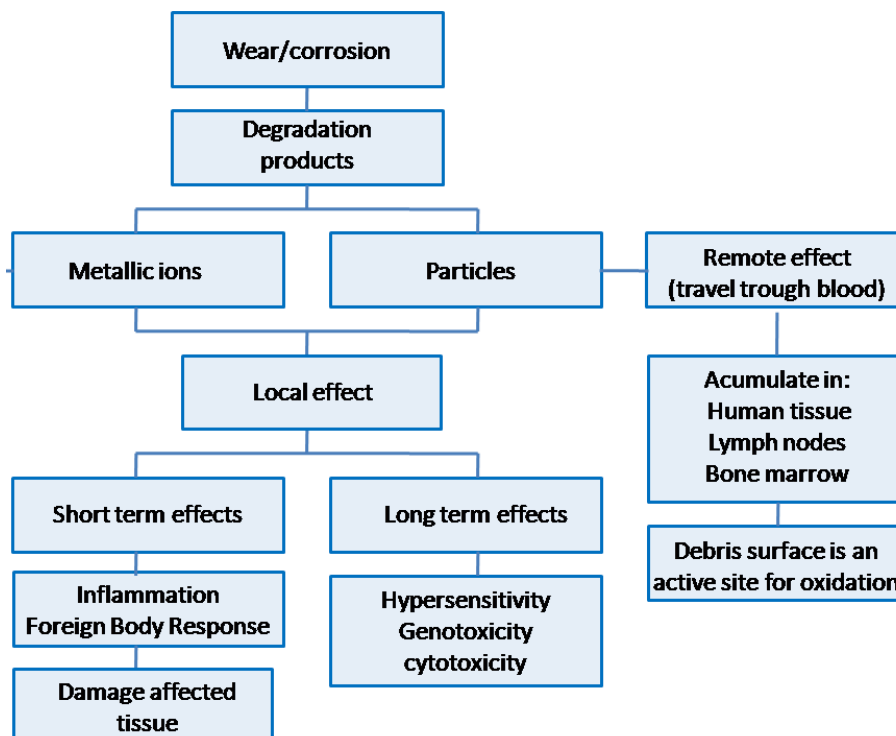


Figure 1.12. Scheme of body host reactions due to presence of metallic ions and debris

1.4 Rational of the thesis

Ti and its alloys are considered one of the most biocompatible biomaterials, however they cannot promote the very needed new bone growth at the early stage after implantation. Insufficient bone growth around the implanted biomaterial is one of the most frequent causes of implant failure. Therefore osseointegration is considered as a clinical predictor of success for dental implants. Over the last years surface modification techniques, such as etching, sandblasting or coatings have been studied in order to improve surface characteristics of titanium namely mechanical properties and biological functions. In this line of investigation powder metallurgy of titanium alloys is currently being researched for biomedical applications.

Over the last decades the worldwide dental implant market has had a global yearly growth rate of 10% starting from US\$ 3.4 billion in 2011 and expected to reach values around US\$ 6.6 billion in 2018 [99]. Despite the high overall success rate of dental implants a recent clinical study by Hujuel et al. [100] reported 4.3% and 8.2% of failures on two dental implant brands for porous oxidized surface and chemically altered surface respectively. The fulfilment of quick fixation of bone to implant is not the only requirement to avoid dental implant failure and tribocorrosion of prosthetic surfaces has to be evaluated.

The process of tribocorrosion consists in repetitive depassivation-repassivation cycles. The removal of titanium is affected by the kinetics of formation and thickness of the passive film, which depends on the chemical composition of the solution. In porous passive materials the film thickness is not only dictated by the electrode potential but also by the supply of ionic species which may depend on porosity. The sensitivity to pores in tribocorrosion titanium is therefore a cause of concern in implant resistance. However limited studies exist on the tribocorrosion behavior of porous metals. Understanding the tribocorrosion mechanisms of titanium processed by powder metallurgy has been therefore recognized and set as an objective of this PhD thesis.

When considering the environment around a dental implant the latter is subjected to variation of saliva pH depending on the diet and to high contents of fluorides in daily personal dental care products, due to the popularisation of fluoride therapy. Numerous studies have been carried out on the electrochemical corrosion of titanium and titanium based alloys in presence of fluorides and highlighted the deleterious effect of fluoride on the oxide film. However the literature survey shows limited number of studies have been focused on the tribocorrosion behavior of Ti6Al4V with these specific conditions. Moreover most studies have focused on the tribocorrosion response under Open circuit potential while it was found [86] that wear of titanium could be significantly increased when applying an anodic potential. This has led to the investigation of the tribocorrosion behavior of

Ti6Al4V in artificial saliva when varying the pH and the fluoride content of the solution. The influence of the potential was also studied as well as the influence of the fabrication process on the triboelectrochemical response by using cast Ti6Al4V as a reference material.

In the more realistic condition of operation tribocorrosion takes place at Open circuit potential. Under this condition the wear accelerated corrosion can only be quantified using the galvanic coupling model for tribocorrosion first proposed by Vieira et al. [88] However a new electrochemical technique developed by Espallargas et al. allows measuring the galvanic potential and current between the wear track (anode) and the passive material (cathode) through zero-resistance ammetry (ZRA). It was therefore of interest to extend the validation of the ZRA technique to other cast Ti6Al4V and to use it as a tool for investigating tribocorrosion mechanisms of this reference alloy at OCP under different contact pressures.

Finally, in recent years the increasing awareness of the cytotoxic effect of vanadium has led to the development of the Ti6Al7Nb, used as an alternate to the commercial Ti6Al4V alloy. In addition to avoiding cytotoxicity β and near β alloys have gained increased interest in order to avoid stress shielding. Thus, Ti alloys such as Ti–Nb alloys have been extensively developed due to their high biocompatibility, non-toxicity and low elastic modulus to avoid/limit bone resorption. The later has given rise to the study related to the corrosion and tribocorrosion behaviour Ti6Al7Nb processed by powder metallurgy as well as Ti7Nb and Ti6Al in order to observe the influence of the alloying elements on the wear and corrosion response of the Ti6Al7Nb alloy.

1.5 References

- [1] N. Eliaz. Degradation of implant materials. Springer. 2012
- [2] Titanium foam fills gap. Available on 2017
http://www.nrc-cnrc.gc.ca/eng/achievements/highlights/2008/titanium_foam.html?pedisable=true
- [3] B.E. Pjetursson, D. Thoma, R. Jung, M. Zwahlen, A. Zembic. A systematic review of the survival and complication rates of implant-supported fixed dental prostheses (FDPs) after a mean observation period of at least 5 years. *Clinical Oral Implants Research* 23(6) (2010) 22–38
- [4] D.F Williams. *Definitions in Biomaterials: proceedings of a consensus conference of the European Society for Biomaterials*. New york: Elsevier. 1987
- [5] H. Ananth, V. Kundapur, H. S. Mohammed, M. Anand, G. S. Amarnath and S. Mankar. A review on biomaterials in dental implantology. *International Journal of Biomedical Science* 11(3) (2015) 113–120
- [6] Central Florida periodontics and implantology. Available on 2017
<http://centralfloridaperio.com/dental-implants/>
- [7] Dr Hassan el Awour. Available on 2017
<https://drhassandental.ca/blog/types-dental-implants-endosteal-transosteal-subperiosteal>
- [8] Pearl dental clinic. Available on 2017.
<https://www.indiamart.com/proddetail/subperiosteal-implants-7130865930.html>
- [9] Life dental implants. Available on 2017
<http://lifedentalimplants.co.uk/subperiosteal-implants/>
- [10] J. Esquivel-Upshaw, K. J. Anusavice. *Dental Materials*. Elsevier (2005) 715-737
- [11] C.E. Misch. *Dental implant prosthetics*. Elsevier Mosby. 2005
- [12] D.G. Gratton, S.A. Aquilino, C.M. Stanford. Micromotion and dynamic fatigue properties of the dental implant-abutment interface. *Journal of Prosthetic Dentistry* 85 (2001) 47–52
- [13] A. Scarano, B. Assenza, M. Piattelli, G. Iezzi, G.C. Leghissa, A. Quaranta, P. Tortora, A. Piattelli. A 16-year study of the microgap between 272 human titanium implants and their abutments. *Journal of Oral Implant* 31 (2005) 269–275

- [14] R. Tsary, M. Kalbacova, U. Hempel, D. Scharnweber, R.E. Unger, P. Dieter, C.J. Kirkpatrick, K. Peters. Response of endothelial cells to oxidative stress on Ti6Al4 V alloy. *Biomaterials* 28 (2007) 806–813
- [15] J.S. Guindy, H. Schiel, F. Schmidli, J. Wirz. Corrosion at the marginal gap of implant-supported suprastructures and implant failure. *International Journal of Oral Maxillofacial Implants* 19 (2004) 826–831
- [16] M.G. Manda, P.P. Psyllaki, D.N. Tsiapas, P.T. Koidis. Clinical device-related article observations on an in-vivo failure of a titanium dental implant/abutment screw system: a case report. *Journal of Biomedical Material Research B* 89B (2009) 264–273
- [17] M. J. Neale. *The tribology handbook*. Butterworth-Heinemann. 2001
- [18] J. Souza, M. Henriques, W. Teughels, P. Ponthiaux, J.P. Celis, L. Rocha. Wear and Corrosion Interactions on Titanium in Oral Environment: Literature Review. *Journal of Bio Tribo Corrosion* (2015) 1:13
- [19] B.B. Panigrahi, M.M. Godkhindi, K. Das, P.G. Mukunda, P. Ramakrishnan. Sintering kinetics of micrometric titanium powder. *Materials Science and Engineering A* 396 (2005) 255–262
- [20] H. Dong. *Surface Engineering of Light Alloys : Aluminium, Magnesium and Titanium Alloys*, Woodhead Publishing. 2012
- [21] J.C. Wataha. Alloys for prosthodontic restorations. *Journal of Prosthetic Dental* 87 (2002) 351-362
- [22] W. Murphy, J. Black, G. Hastings. *Handbook of biomaterials properties*. Springer Nature. 2016
- [23] R. Boyer, E.W. Collings, and G. Welsch. *Materials Properties Handbook: Titanium Alloys*. ASM international. 1994
- [24] Y. Okazaki, S. Rao, Y Ito, T. Tateishi. Corrosion resistance, mechanical properties, corrosion fatigue strength and cytocompatibility of new Ti alloys without Al and V. *Biomaterials* 19 (1998) 1197-1215
- [25] J. Pan, H. Lia, C. Leygraf, D. Thierry, J. Li. Variation of oxide films on titanium induced by osteoblast-like cell culture and the influence of an H₂O₂ pre-treatment. *Journal of Biomedical Material Research* 40 (1998) 244–256

- [26] M. Nasab, M. Hassan. Metallic Biomaterials of Knee and Hip - A Review. Trends in Biomaterials and Artificial Organs 24 (1) (2010) 69-82
- [27] M. Geetha, A.K. Singh, R. Asokami, A.K. Gogia. Ti based biomaterials, the ultimate choice for orthopaedic implants – A review. Progress in Materials 54 (2008) 397-425
- [28] M. Bram, T. Ebel. Advances in powder metallurgy:18. Applications of powder metallurgy in biomaterials. Woodhead Publishing (2013) 520–554
- [29] J. S. Hirschhorn, J. T. Reynolds. Powder metallurgy fabrication of cobalt alloy surgical implant materials. Research in Dental and Medical Materials. Korostoff E. Ed. Plenum Press, New York, London (1969)137–150
- [30] R. Lueck, J. Galante, W. Rostoker, R.D. Ray. Development of an open pore metallic implant to permit attachment to bone. Surgical Forum 20 (1969) 456-7
- [31] R. Welsh, R. Pilliar, I. Macnab. Surgical implants. The role of surface porosity in fixation to bone and acrylic. Journal of Bone and Joint Surgery American 53 (5) (1971) 963-77
- [32] R. Pilliar, R. Cameron, I. Macnab. Porous surface layered prosthetic devices. Biomedical Engineering 10(4) (1975) 126-31
- [33] H. Cameron, I. Macnab, R. Pilliar. A porous metal system for joint replacement surgery. International Journal of Artificial Organs 1(2) (1978) 104-9
- [34] J. Galante, W. Rostoker, R. Lueck, R. Ray. Sintered fiber metal composites as a basis for attachment of implants to bone. Journal of Bone and Joint Surgery American 53 (1) (1971) 101-14.
- [35] A. laptev, M. Bram, H. Buchkremer, D. Stover. Study of production route for titanium parts combining very high porosity and complex shape. Powder metallurgy 47 (2004) 85-92,
- [36] H. Schiefer, M. BramH. P. Buchkremer, D. Stöver. Mechanical examinations on dental implants with porous titanium coating. Journal of Material Science: Material Medicine (2009) 20:1763.
- [37] Thomas Imwinkelried. Mechanical properties of open-pore titanium foam. Journal of Biomedical Material Research A. 81(4) (2007) 964-70
- [38] P.C. Eloff, M.R. Dustoor, V.S. Moxson. Properties of p/m titanium alloy produced from elemental blends—the current state of development. Progress in Powder Metallurgy 37 (1982) 267-277

- [39] S. Robinson and M. Paul. Debinding and sintering solutions for metals and ceramics. *Metal Powder Report* 56(6) (2001) 24-34
- [40] M. Bram, C. Stille, H.P. Buchkremer, D. Stöver, H. Baur. High-Porosity Titanium, Stainless Steel and Superalloy Parts. *Advanced Engineering Materials* 2 (2000) 196-199
- [41] T. Wintermantel, S. W. Ha. *Medical Life Science Engineering*. Springer Verlag. 2009
- [42] Bickerdike and Sutcliffe. The tensile strength of titanium at various temperatures. *Powder Metallurgy* 9 (1951) 153-9
- [43] W. Kroll. Malleable Alloys of Titanium *Z. Metallurgy* 29 (1937) 189-192.
- [44] D. Landolt. *Corrosion and surface chemistry of metals*. EPFL Press Editorial. 2007
- [45] S. Mischler. Triboelectrochemical techniques and interpretation methods in tribocorrosion: A comparative evaluation. *Tribology International* 41 (2008) 573–583
- [46] J. Kruger. Passivity. *Corrosion: Fundamentals and Protection. Testing*. ASM International. ASM Handbook (2003) 13A 61-67
- [47] I. Milosev, T. Kosec, H.H. Strehblow. XPS and EIS study of the passive film formed on orthopaedic Ti–6Al–7Nb alloy in Hank’s physiological solution. *Electrochimica Acta* 53 (2008) 3547-3558
- [48] I. Milosev, M. Metikos-Hukovich, H.H. Strehblow. Passive film on orthopaedic TiAlV alloy formed in physiological solution investigated by X-ray photoelectron spectroscopy. *Biomaterials* 21 (2000) 2103-2113
- [49] M. Metikos-Huković, A. Kwokal, J. Piljac. The influence of niobium and vanadium on passivity of titanium-based implants in physiological solution. *Biomaterials* 24 (21) (2003) 3765–3775
- [50] S. Tamilselvi, R. Murugaraj, N. Rajendran. Electrochemical impedance spectroscopic studies of titanium and its alloys in saline medium. *Materials and Corrosion* 58 (2007) 113-120
- [51] M. Aziz-Kerrzo, K. G. Conroy, A. Felon, S. Farrell, Carmel B. Breslin. Electrochemical studies on the stability and corrosion resistance of titanium-based implant materials. *Biomaterials* 22 (2001) 1531-1539
- [52] J.L. De Lorenzo. *Microbiologia para o estudante de Microbiologia*. São Paulo: Atheneu (2004) 151-62

- [53] A. Bardow, D. Moe, B. Nyvad, B. Nauntofte. The buffer capacity and buffer systems of human whole saliva measured without loss of CO₂, *Archives of Oral Biology* 45(2000) 1-12
- [54] VWH. Leung, BW. Darvell. Artificial saliva for in vitro studies of dental materials. *Journal of Dental Research* 25(1997) 475-484
- [55] J.Y. Gal, Y. Fovet, M. Adib-Yadzi. About a synthetic saliva for in vitro studies. *Talanta* 53 (2001) 1103-1115
- [56] N. Schiff, B. Grosogeat, M. Lissac, F. Dalard. Influence of fluoride content and pH on the corrosion resistance of titanium and its alloys. *Biomaterials* 23(9) (2002) 1995-2002
- [57] M. Nakagawa, S. Matsuya, T. Shiraishi, M. Ohta. Effect of fluoride concentration and pH on corrosion behavior of titanium for dental use. *Journal of Dental Research* 78(1999) 1568-1572
- [58] A. Mellado Valero. Estudio del comportamiento electroquímico y corrosión galvánica de aleaciones biomédicas para implantes dentales y supraestructuras. Universitat de Valencia. Spain. 2016
- [59] J.C.M Souza., S.L. Barbosa, E. Ariza, P. Ponthiaux, M. Henriques, W. Teughels, J-P. Celis, L.A. Rocha How do titanium and Ti6Al4V corrode in fluoridated medium as found in the oral cavity? An in vitro study. *Journal of Material Science and Engineering C* 47(2015) 384-393
- [60] E. Newbrun. Topical Fluorides in Caries Prevention and Management: A North American Perspective. *Journal of Dental Education* 65(2001) 1078-1083
- [61] J Lausma, B Kasemo, S Hansson. Accelerated oxide growth on titanium implants during autoclaving caused by fluorine contamination. *Biomaterials* 6 (1986) 23-27
- [62] N. Horasawa, M. Marek. Effect of fluoride from glass ionomer on discoloration and corrosion of titanium. *Journal of Dental Research* 80 (2001) 546
- [63] A.M. Al-Mayouf, A.A. Al-Swayih, N.A. Al-Mobarak, A.S. Al-Jabab. Corrosion behavior of a new titanium alloy for dental implant applications in fluoride media. *Materials Chemistry and Physics* 86 (2004) 320-329
- [64] G. Boere. Influence of fluoride on titanium in an acidic environment measured by polarization resistance technique. *Journal of Applied Biomaterials Winter* 6(4) (1995) 283-8
- [65] H.H. Huang. Effects of fluoride concentration and elastic tensile strain on the corrosion resistance of commercially pure titanium. *Biomaterials* 23 (2002) 59-63

- [66] M. Nakagawa, S. Matsuya, K. Udoh. Corrosion behavior of pure titanium and titanium alloys in fluoride-containing solutions. *Dental Materials Journal* 20 (2001) 305-314
- [67] M. Nakagawa, S. Matsuya, K. Udoh. Effects of fluoride and dissolved oxygen concentrations on the corrosion behavior of pure titanium and titanium alloys. *Dental Materials Journal* 21 (2002) 83-92
- [68] L. Reclaru, J.M. Meyer. Effects of fluorides on titanium and other dental alloys in dentistry. *Biomaterials* 19 (1998) 85-92
- [69] K.H.W. Seah, X. Chen. A comparison between the corrosion behaviour of sintered and unsintered porous titanium. *Corrosion Science* 34 (1993) 1841
- [70] B.J. Edwards, P. Higham. Anodic polarisation of porous coated vitalium alloy-effect of passivation. ASTM (1987) STP 953, 115-123
- [71] K.H.W. Seah, R. Thampuran, S.H. Teoh. The influence of pore morphology on corrosion. *Corrosion Science* 40(1998) 547
- [72] F.X. Xie, X.B. He, S.L. Cao, X. Lu, X.H. Qu. Structural characterization and electrochemical behavior of a laser-sintered porous Ti-10Mo alloy. *Corrosion Science* 67 (2013) 217-224
- [73] J. Fojt, L. Joska, J. Malek. Corrosion behaviour of porous Ti-39Nb alloy for biomedical applications. *Corrosion Science* 71(2013) 78-83
- [74] A.I. Munoz, N. Espallargas. Tribocorrosion mechanisms in sliding contacts, in: D. Landolt, S. Mischler (Eds). *Tribocorrosion of Passive Metals and Coatings*. EPFL Press Editorial. 2011
- [75] J. Geringer, M.T. Mathew. 2 - Tribocorrosion mechanisms in sliding contacts, in: J Paulo Davim (Ed.). *Synergism effects during friction and fretting corrosion experiments-focusing on biomaterials used as orthopaedic implants*. Woodhead publishing. 2013
- [76] B.W Madsen. Standard guide for determining amount of synergism between wear and corrosion. ASTM G119-93. Ann. Book ASTM standard. ASTM international. 1994
- [77] H. Ulich. Mechanism of fretting corrosion. *Journal of Applied Mechanisms* 21(4) (1954) 401-407.
- [78] G. Zambelli and L. Vincent, *Matériau et contact - Une approche tribologique*, presses polytechniques et universitaires romandes (1998) 277-284
- [79] M. Godet. Third-bodies in tribology. *Wear* 136 (1) (1990) 29-45

- [80] M. Godet, Y. Berthier, J. Lancaster and L. Vincent. Wear modelling: Using fundamental understanding or practical experience. *Wear* 149 (1-2) (1991) 325-340
- [81] D. Landolt, S. Mischler, M. Stemp, S. Barril. Third body effects and material fluxes in tribocorrosion systems involving a sliding contact. *Wear* 256 (5) (2004) 517-524
- [82] I. M. Hutchings. *Tribology - Friction and Wear of Engineering Materials*. Butterworth-Heinemann. 1992
- [83] D.A. Rigney: Transfer, mixing and associated chemical and mechanical processes during the sliding of ductile materials. *Wear* 245 (1-2) (2000)1-9
- [84] J. Perret, M. Cantoni, E. Boehm, A. Beaudouin, W. Chitty, J-Ph. Vernot, S. Mischler. EBSD, SEM and FIB characterisation of subsurface deformation during tribocorrosion of stainless steel in sulphuric acid. *Wear* 269 (2010) 383–393
- [85] S. Mischler, S. Debaud and D. Landolt. Wear-accelerated corrosion of passive metals in tribocorrosion systems. *Journal of The Electrochemical Society* 145 (3) (1998) 750-758
- [86] D. Landolt, S. Mischler and M. Stemp. Electrochemical methods in tribocorrosion: a critical appraisal. *Electrochimica Acta* 46 (24-25) (2001) 3913-3929
- [87] S. Barril, S. Mischler, D. Landolt. Influence of fretting regimes on the tribocorrosion behaviour of Ti6Al4V in 0.9 wt.% sodium chloride solution. *Wear* 256 (2004) 963-972
- [88] A.C. Vieira, L.A. Rocha, N. Papageorgiou, S. Mischler. Mechanical and electrochemical deterioration mechanisms in the tribocorrosion of Al alloys in NaCl and in NaNO₃ solutions. *Corrosion Science* 54 (2012) 26-35
- [89] S. Cao, S.G. Maldonado, S. Mischler. Tribocorrosion of passive metals in the mixed lubrication regime: theoretical model and application to metal-on-metal artificial hip joints. *Wear* 324-325 (2015) 55-63
- [90] A. Revathi, A. Dalmau Borrás, A. Igual Muñoz, C. Richard, G. Manivasagam. Degradation mechanisms and future challenges of titanium and its alloys for dental implant applications in oral environment. *Materials Science and Engineering C* 76 (2017) 1354-1368
- [91] A.C. Vieira, A.R. Ribeiro, L.A. Rocha, J.P. Celis. Influence of pH and corrosion inhibitors on the tribocorrosion of titanium in artificial saliva. *Wear* 261 (2006) 994-1001

- [92] M.K. Dimah, F. Devesa Albeza , V. Amigo Borrás, A. Igual Muñoz. Study of the biotribocorrosion behaviour of titanium biomedical alloys in simulated body fluids by electrochemical techniques. *Wear* 294–295 (2012) 409-418
- [93] J.C.M. Souza, S.L. Barbosa, E. Ariza, J.-P. Celis, L.A. Rocha. Simultaneous degradation by corrosion and wear of titanium in artificial saliva containing fluorides. *Wear* 292–293 (2012) 82-88
- [94] S. Barril. Electrochemical effects on the fretting corrosion behavior of Ti6Al4V in 0.9% sodium chloride solution. *Wear* 259 (2005) 282-291
- [95] R.M. Urban, J.J. Jacobs, M.J. Tomlinson, J. Gavrilovic, J. Black, M. Peoch. Dissemination of wear particles to the liver, spleen, and abdominal lymph nodes of patients with hip or knee replacement. *Journal of Bone and Joint Surgery American* 82 (2000) 457
- [96] D.R. Haynes, S.D. Rogers, D. Hay. The differences in toxicity and release of bone-resorbing mediators induced by titanium and cobalt-chromium wear particles. *Journal of Bone and Joint Surgery* 75-A (1993) 825-834
- [97] C. Manaranche, H. Hornberger. A proposal for the classification of dental alloys according to their resistance to corrosion. *Dental Materials* 23 (2007) 1428-1437
- [98] J.J. Wang, B.J.S. Sanderson, H. Wang. Cyto- and genotoxicity of ultrafine TiO₂ particles in cultured human lymphoblastoid cells. *Mutation Research* 628 (2007) 99-106
- [99] F.G. Oliveiraa, A.R. Ribeiro, G. Perez, B.S. Archanjo, C.P. Gouvea, J.R. Araújo, APC. Campos, A Kuznetsov, CM. Almeida, MM. Marud, C. Achete, P. Ponthiaux, JP. Celis, LA. Rocha. Understanding growth mechanisms and tribocorrosion behaviour of porous TiO₂ anodic films containing calcium, phosphorous and magnesium. *Applied Surface Science* 341 (2015) 1-12
- [100] P. Hujoel, W. Becker, B. Becker. Monitoring failure rates of commercial implant brands; substantial equivalence in question?. *Clinical Oral Implants Research* 24 (2013) 725-729

-Chapter 2-

Objectives

The objective of this doctoral thesis is to understand the electrochemical and tribocorrosion behavior of new titanium biomedical alloys (i.e. Ti6Al7Nb) obtained by powder metallurgy in simulated body fluids for dental implant applications.

A better understanding of the degradation mechanisms of titanium biomedical alloys (namely corrosion, wear and their combined effect) and the crucial parameters affecting the involved phenomena is needed to further develop predicting models and new materials for implant fabrication.

Experimental methods used to identify those degradation mechanisms include electrochemical and tribo-electrochemical techniques as well as surface analysis (SEM).

The Thesis is divided into eight chapters: introduction, objectives, materials and experimental methods, corrosion and tribocorrosion mechanisms of powder metallurgy Ti6Al4V in artificial saliva varying pH and fluorides content, corrosion and tribocorrosion behavior of Ti6Al7Nb biomedical alloy in artificial saliva and conclusions. **Figure 2.1** schematically shows the structure of the Doctoral Thesis indicating the main objectives of each chapter. These objectives can be summarized as follows:

- 1-** Understand the corrosion and tribocorrosion behavior of a model biomedical alloy Ti6Al4V in artificial saliva. The influence of the media (pH and fluoride content), applied potential and fabrication process (powder metallurgy and casting) was analyzed. Classical electrochemical techniques such as open circuit potential (OCP), potentiodynamic polarization curves and potentiostatic tests were used to characterize the electrochemical behavior of the Ti6Al4V alloy. Unidirectional sliding and reciprocating sliding tribocorrosion tests were carried out at OCP and at different applied potential followed by surface characterization by SEM. Some experimental part of this chapter was carried out at the Norwegian University of Science and Technology (NTNU) in Norway during three months.
- 2-** To compare the corrosion and tribocorrosion behavior of the non-toxic Ti6Al7Nb alloy as a possible substitute for the model Ti6Al4V. Analogously to the previous chapter, the same experimental techniques were used together with EIS analysis.

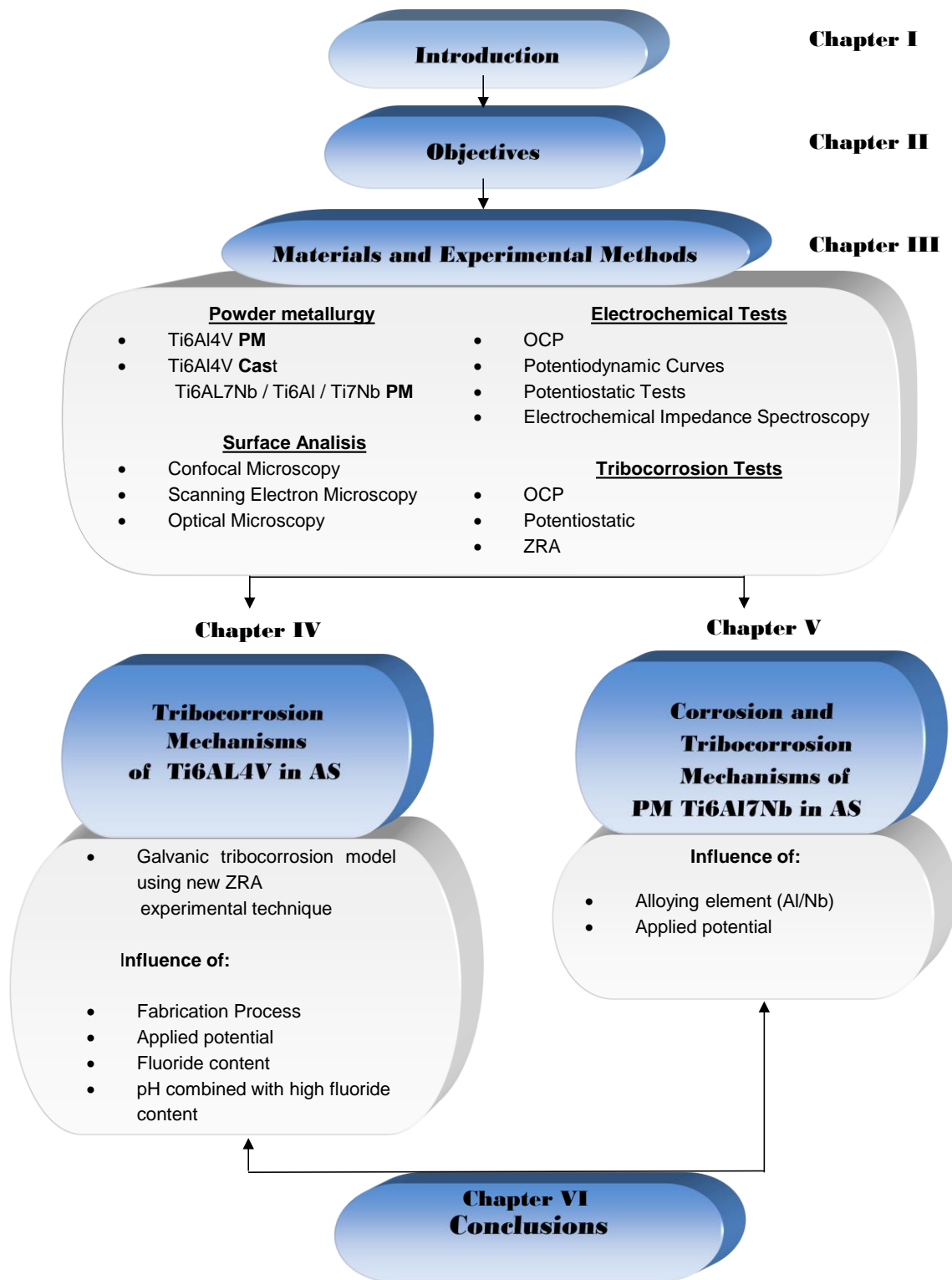


Figure 2.1. Scheme of the Doctoral Thesis structure

-Chapter 3-

Materials

and

Experimental techniques

3.1. Materials

The materials used in the present thesis are cast Ti6Al4V and powder metallurgy (PM) Ti alloys (Ti6Al4V, Ti6Al7Nb, Ti6Al and Ti7Nb). The cast material has been purchased and tested as received without prior treatment. The PM samples have been processed at the UPV.

The first step of the PM process consisted in obtaining the elemental mixture. Ti6Al, Ti7Nb and Ti6Al7Nb alloys were obtained mixing Ti, Al and Nb elemental powders in stoichiometric proportions in a turbula mixer (**Figure 3.1**), in order to have a homogenous distribution of the particles in the final powder. Each alloy has been mixed during 20min at a speed of 7/10. The Ti6Al4V alloy was purchased prealloyed from SE JONG™.

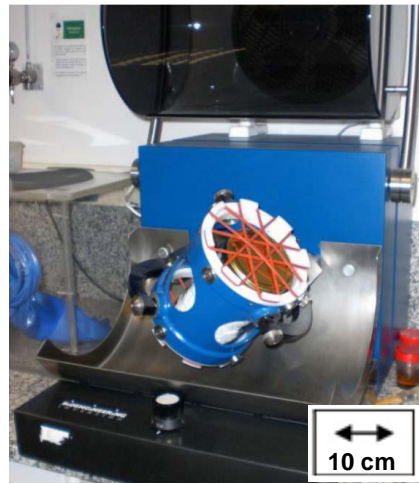


Figure 3.1. A turbula mixer

Compaction of the alloys has been carried out using a universal testing machine in order to monitor the process (Instron 432 with a load cell of 500 kN). **Figure 3.2** shows the set up used with a simple action cylindrical matrix. Compaction pressure used was 400MPa during 10 seconds with a speed of 5 mm/min.



Figure 3.2. Compaction system

Sintering was carried out in a high vacuum furnace (Cabolite model HVT 15/75/450) to prevent unwanted oxidation of the green samples. High vacuum (5×10^{-4} bars) was achieved after breaking down low vacuum 3 times in a row with argon. This is an inert gas which will prevent oxidation. **Figure 3.3** shows the sintering cycle used to sinter the samples. The first plateau of 30 min at 800°C is used to homogenize the oven and sample temperature. This will avoid samples from cracking due to a temperature gradient and prepare the allotropic change of the material at 882°C. The second plateau at 1250°C is the sintering temperature and is reached with a slow heating ramp of 10 °C/min, Sintering takes 2 hours followed by a controlled cooling of 10 °C/min to room temperature. Final sintered samples are shown in **Figure 3.4**.

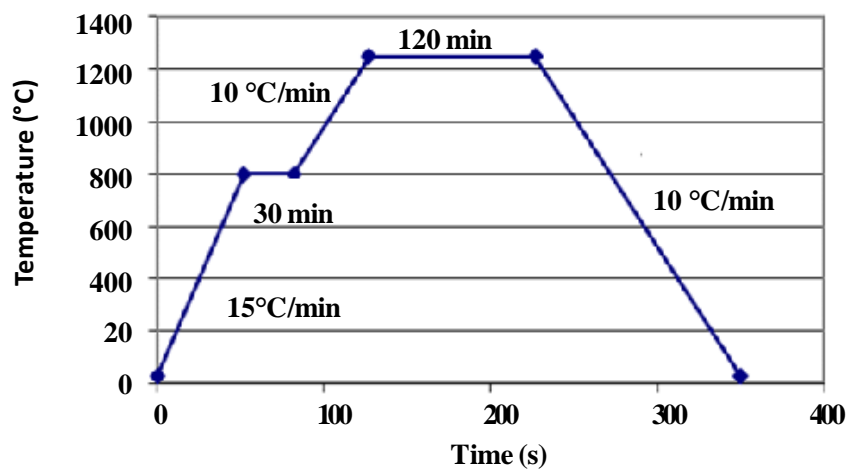


Figure 3.3. Heating cycle used to obtain the sintered samples



Figure 3.4. Sintered samples

3.2 Electrochemical techniques

The electrochemical measurements were carried out using a three-electrode configuration (**Figure 3.5**). The electrode system is formed by:

A **working electrode (WE)** which is the material tested. In our case the titanium alloys.

A **reference electrode which (RE)** is necessary to make potential measurements of the working electrode. The requirements are that the potential is reproducible and stable. The stability of the electrode potential is reached by employing a redox system with contact (buffer or saturated) concentrations of each participant of the redox reaction. Thus, a reference electrode should satisfy the following properties: reproducible potential value, thermodynamically well-defined reaction, non-polarizable (not sensible to current flow) and easy use [1]. The **silver/silver chloride electrode (Ag/AgCl)** was used in the present thesis (**Figure 3.5**).

A **counter electrode (CE)** which purpose is to supply the required current for controlling the potential of the working electrode. It is typically made from inert materials such as gold, platinum or graphite and it provides a highly reactive surface for the electrochemical reactions. The potential of the auxiliary electrode is usually not measured and is adjusted to balance the reaction occurring at the working electrode. This configuration allows the potential of the working electrode to be measured against a known reference electrode without compromising the stability of that reference electrode by passing current over it. The counter electrodes (**Figure 3.5**) employed in this experimental work is **platinum**.

The three electrodes are connected to the potentiostat which is essentially an electronic amplifier that regulates the current between the working and counter electrode and the potential between the working and reference electrode. Depending on the electrochemical test carried out, either the current or the potential is fixed and the other signal will be measured. The **Figure 3.5** schematically shows the electrodes and their connection to the potentiostat. In the present thesis, all electrochemical measurements (except EIS see **section 3.2.5**) were carried out using Solartron 1286.

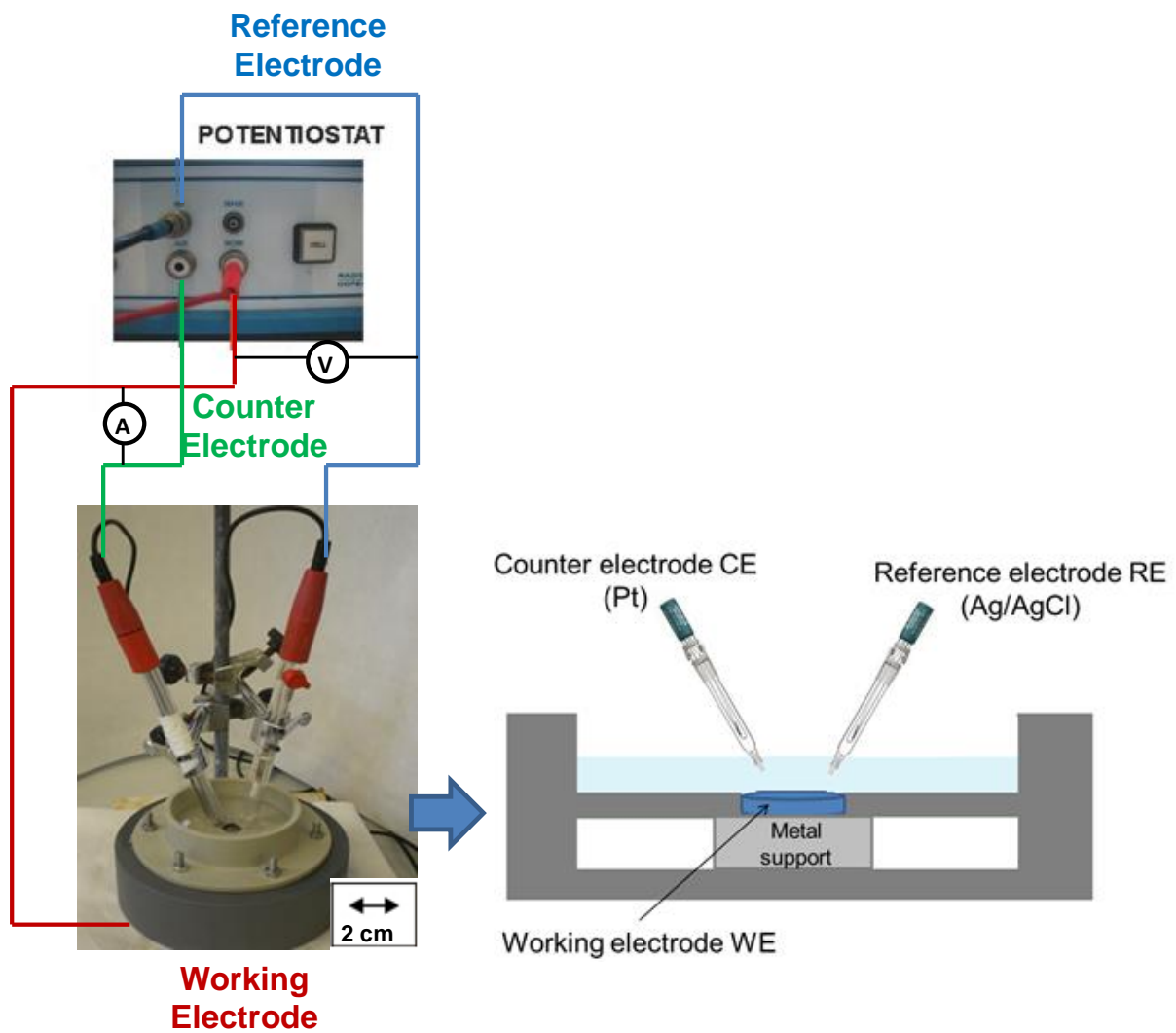


Figure 3.5. Flat electrochemical cell with electrodes

3.2.1. Open circuit

The open circuit potential (OCP) is the potential set up spontaneously by an electrode surface in absence of any external current. Under such condition the anodic and cathodic reactions occur simultaneously and at the same rate. Therefore, the total current flow is zero and cannot be directly measured.

In the case of a *single electrode*, i.e. when only one electrode reaction takes place at the metal surface, the open circuit potential corresponds with the equilibrium potential (E_{rev}) (**Figure 3.6 (a)**) according to **equation (3.1)**.



In the case of a mixed electrode i.e. when several electrode reactions take place simultaneously at the electrode/solution interface, the OCP is called corrosion potential and it has a value that lies in between the equilibrium potentials of the partial electrode reactions. This case is observed in metallic implants where oxidation of the metal takes place simultaneously with the reduction of oxygen present in the body fluids.

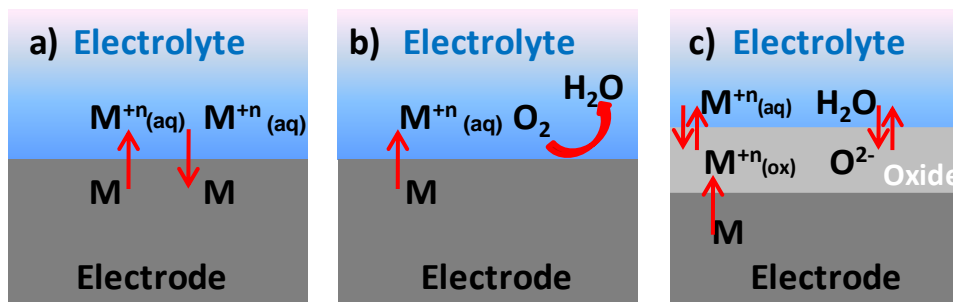


Figure 3.6. (a) Metal electrode in contact with its own ions (single electrode), (b) with aerated conditions (mixed electrode) and (c) passivation of the metal.

This technique is used for an initial characterization of the biomaterial in the system under study. It gives initial information about the surface state also referred to as nobility which enables a relative comparison between alloys in the same test situation. In practice, it is measured prior to polarization tests, until stabilization of the electrochemical conditions of the sample into the media reflected by a steady-state value. When studied over time the OCP can give information about the progress of possible chemical reactions taking place at the electrode surface such as the spontaneous formation of the oxide film or the breakdown of the passive film. The OCP depends on the experimental conditions i.e. mainly the media composition but also the temperature, the oxygen content of the electrolyte and the surface state of the metal.

3.2.2 Potentiodynamic

This method constitutes the first approach in a corrosion study as it enables to identify and determine the reactions taking place and their rates as well as the stability of the passive film. This technique consists in sweeping, at a selected rate, the potential of the working electrode and measuring the associated current density. The range of applied potentials of the polarization scan varies from cathodic to anodic values.

The total current density, i , measured during a polarization curve is given by the sum of the partial cathodic current density (i_c) and the partial anodic current density (i_a) as given by **equation (3.2)**. By convention, cathodic and anodic current densities are, respectively, negative and positive [1].

$$\mathbf{i = i_a + i_c} \quad (3.2)$$

The value of the total current density depends on the anodic and cathodic partial reactions taking place. For the oxidation and reduction reactions to take place, an activation energy threshold (one for each respectively) should be overcome. When an external potential is applied, shifting the electrode from its equilibrium situation, the transfer of charged species (ions and electrons) through the electrode/media interface is influenced and the activation energy barrier value changes. If the interfacial reaction is slower than the other reaction steps (mass transfer of reactions) the reaction rate is controlled by the **activation energy for the charge transfer**. In this case, the current potential relationship is described by the **Butler-Volmer equation**. The **Figure 3.7** shows the partial current densities and the total current density of a mixed electrode controlled by the rate of charge transfer at the electrode-electrolyte interface.

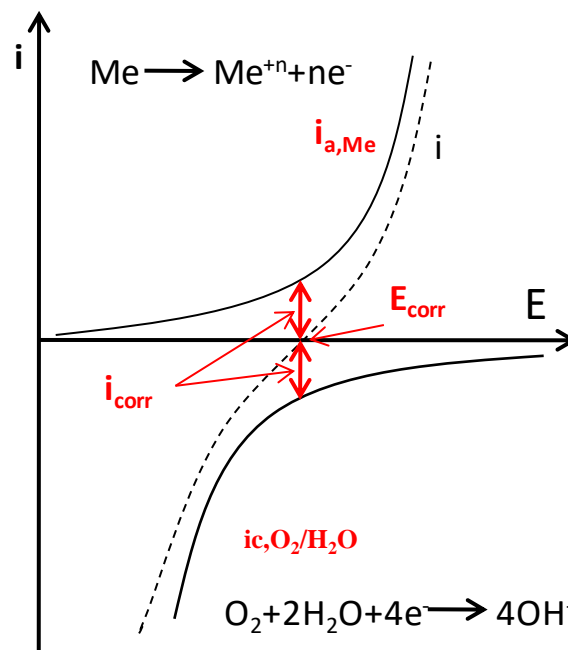


Figure 3.7. Partial current densities ($i_{a,Me}$ and $i_{c,O_2/H_2O}$ in solid lines) and total current density (i in dotted lines) of mixed electrode near the corrosion potential.

The Butler-Volmer equations for the anodic and the cathodic partial reaction are expressed by the **equations (3.3)** and **(3.4)** respectively [1]:

$$i_a = i_{\text{corr}} \exp\left(\frac{\alpha \cdot n \cdot F}{R \cdot T} \eta\right) \quad (3.3)$$

$$i_c = i_{\text{corr}} \exp\left(-\frac{(1-\alpha) \cdot n \cdot F}{R \cdot T} \eta\right) \quad (3.4)$$

In these expressions the proportionality constant α is the charge transfer coefficient and its value is situated between 0 and 1. This parameter indicates the fraction of the interfacial potential at an electrode/electrolyte interface that helps in lowering the free energy barrier for the electrochemical reaction. On the other hand, η is the polarization (overpotential) which expresses the difference between the potential of a mixed electrode subjected to anodic or cathodic polarization and its corrosion potential (E_{corr}).

Including the **equations (3.3)** and **(3.4)** into the **equation (3.2)** the most common form of Butler-Volmer equation for a mixed potential is obtained (**equation (3.5)**) [1]:

$$i = i_{\text{corr}} \left[\exp\left(\frac{\alpha \cdot n \cdot F}{R \cdot T} \eta\right) - \exp\left(-\frac{(1-\alpha) \cdot n \cdot F}{R \cdot T} \eta\right) \right] \quad (3.5)$$

The anodic and cathodic Tafel coefficients (β_a , β_c) are defined in the **equations (3.6)** and **(3.7)** respectively:

$$\beta_a = \frac{R \cdot T}{\alpha \cdot n \cdot F} \quad (3.6)$$

$$\beta_c = \frac{R \cdot T}{(1-\alpha) \cdot n \cdot F} \quad (3.7)$$

Thus, including the Tafel coefficients into the **equation (3.5)**, the Butler-Volmer equation becomes [1]:

$$i = i_{\text{corr}} \left[\exp\left(\frac{\eta}{\beta_a}\right) - \exp\left(-\frac{\eta}{\beta_c}\right) \right] \quad (3.8)$$

For relative high polarizations and depending on the η sign, one of both exponentials terms is negligible and therefore the **equation (3.5)** can be rewritten. The **anodic Tafel region** is the domain of potential corresponding to $\eta/\beta_a \gg 1$ [1].

$$i \cong i_a = i_{\text{corr}} \exp\left(\frac{\eta}{\beta_a}\right) \quad (3.9)$$

And taking the logarithms yields:

$$\eta = -\beta_a \ln i_{\text{corr}} + \beta_a \ln i \quad (3.10)$$

The **anodic Tafel line** is obtained converting the latter expression to base-10 logarithm, defining a_a and b_a as anodic Tafel constants:

$$\eta = \underbrace{-2.303\beta_a}_{a_a} \log i_{\text{corr}} + \underbrace{2.303\beta_a}_{b_a} \log|i| \quad (3.11)$$

On the other hand, the **cathodic Tafel region** corresponds to the potential domain where $\eta/\beta_c \ll -1$ is established [1].

$$i_T \approx i_c = -i_{\text{corr}} \cdot \exp\left(\frac{\eta}{\beta_c}\right) \quad (3.12)$$

Applying the logarithm in the expression:

$$\eta = \beta_c \ln i_{\text{corr}} - \beta_c \ln|i| \quad (3.13)$$

Thus, it is possible to define the Tafel equation of a cathodic reaction (**cathodic Tafel line**) using the cathodic Tafel constants a_c and b_c :

$$\eta = \underbrace{2.303\beta_c}_{a_c} \log i_{\text{corr}} - \underbrace{2.303\beta_c}_{b_c} \log|i| \quad (3.14)$$

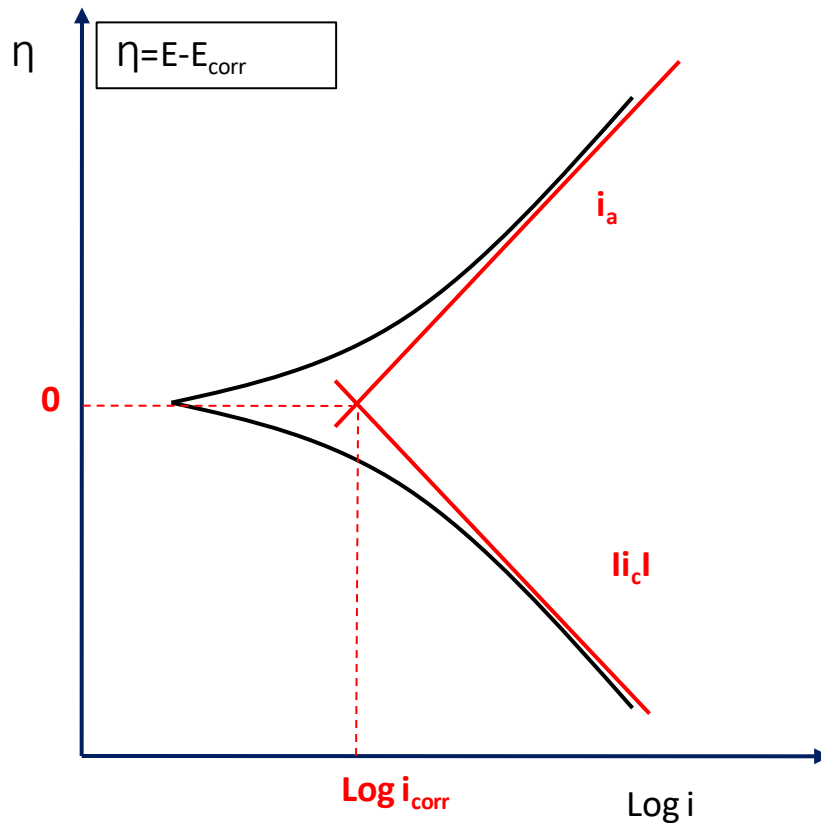


Figure 3.8. Evans diagram showing anodic and cathodic partial current densities and total current density of an electrode reaction on a logarithmic scale. Determination of i_{corr} from a η vs $\log i$ curve.

The **Tafel equations (3.11) and (3.14)** describe the anodic and cathodic limits of the Butler-Volmer equation. Representing the current density on a logarithmic scale against the overpotential will accentuate the linear relationship between both the logarithm of i and the overpotential, whenever the overpotential is large in absolute value (usually selected above 50 mV). It enables to determine experimentally the following kinetic parameters: The Tafel coefficients β_a and β_c can be extracted from the slopes of the Tafel lines and the corrosion current density (i_{corr}) and the corrosion potential (E_{corr}) is obtained experimentally from the crossing point of the cathodic and anodic Tafel slopes.

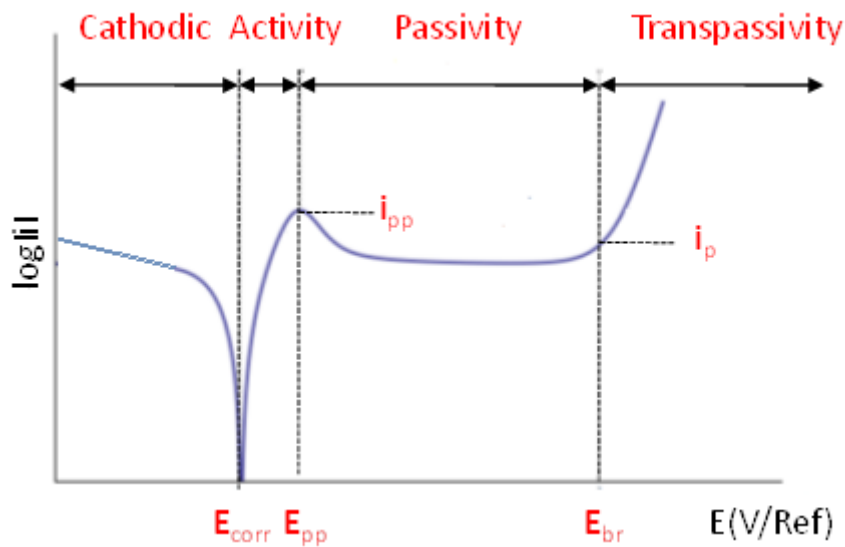


Figure 3.9. Evans diagram showing anodic and cathodic partial current densities and total current density of an electrode reaction on a logarithmic scale.

The potentiodynamic polarization curves are used to identify the electrochemical domains of a biomaterial in the body fluids solutions of interest (i.e. cathodic, active-passive transition, passive and transpassive domain). **Figure 3.9** represents the typical potentiodynamic curve for a passive metal. Four potential domains can be observed [2]:

- The *cathodic domain* includes potentials below the potential of corrosion E_{corr} . The current is determined by the reduction of water and dissolved oxygen for experiments carried out under aerated conditions.
- The *active region* includes potentials above the E_{corr} and is characterized by the dissolution of the metal in form of soluble ions (hydrated or complexed) and dissolved into the solutions.
- The *passive domain* includes potentials where the surface of the metal is covered by a thin protective layer which is formed by reacting the metallic cations with the anions coming from the solution (O_2^{2-} and OH^-).
- The *transpassive domain* is characterized by the increase in current. It is due to the uniform transpassive dissolution which results from both the oxidation of the passive film and the oxygen evolution due to water oxidation (whenever the potential is above the reversible potential of water oxidation). The transpassive dissolution can occur in some passive materials by pitting resulting from local film breakdown.

Relevant parameters are extracted from the curves:

- E_{corr} : The *corrosion potential* corresponds to the potential where the current changes from cathodic (negative) to anodic (positive).
- i_{corr} : The *corrosion current density*
- E_{pp} : The *passivation potential* separates the active from the passive potential region.
- i_{pp} : The *passivation current density* is the maximum current density corresponding to the passivation potential
- i_p : The *passive current density* characterizes the dissolution behavior of the metal in the passive potential region. It corresponds to the current density that flows through the metal electrode when the oxide film is formed onto the surface.
- E_{br} : The *pitting potential* also called the transpassivation potential or breakdown potential marks the end of the passive potential region and the transition from passive to transpassive behavior.

Theses parameters are useful to compare biomaterials and to pursue further experimentation.

3.2.3. Potentiostatic

The potentiostatic technique is used to observe anodic and cathodic behaviors of a metal surface in electrolytes. By varying the potential of the working electrode, different oxidation conditions at the electrode surface are achieved. The test consists in measuring the evolution of the current density when a selected potential E is imposed on the system, allowing to follow the evolution of the electrochemical kinetics of the involved reactions. In practice, the potentiostat maintains constant the potential between the working electrode and the reference electrode by adjusting the current flowing between the working electrode (biomaterial) and the counter electrode.

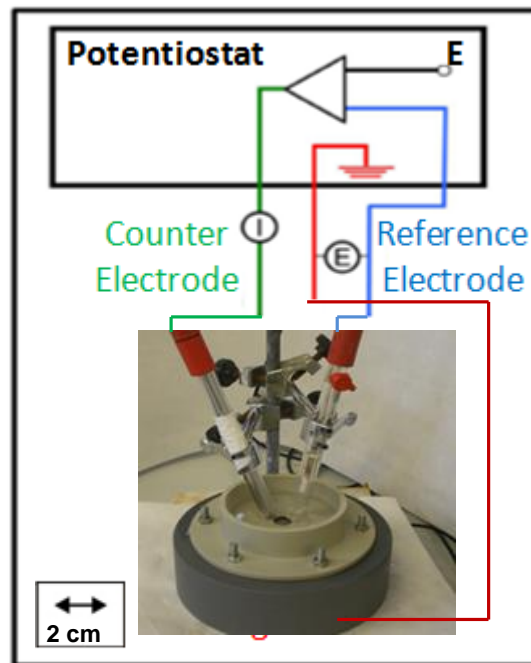


Figure 3.10. Experimental set up for potentiostatic measurements. Customized three electrode cell used for carrying out the electrochemical measurements.

The current measured during a potentiostatic test is equal to the sum of the anodic (i_a) and cathodic (i_c) currents related to the partial electrochemical reactions taking place on the electrode surface as described by the **equation 3.15** [2]:

$$i_{\text{measured}} = \sum i_{a,i} - \sum i_{c,i} \quad (3.15)$$

In contrast to an equilibrium situation, when a potential is imposed either anodic or cathodic reactions will be favored. A potential higher than the OCP indicates that an anodic current is crossing the interface electrode/electrolyte and that the oxidation of the metal is taking place whereas a potential lower than the OCP indicates that the dissolution rate of the metal is negligible and the measured current is determined by the kinetics of the cathodic reactions.

The electrochemical behavior of the biomaterial can be analyzed in the different potential domains by applying potentials within the cathodic, active, passive or transpassive regions. However the passive film characterization is of particular relevance when studying the electrochemical behavior of a biomedical alloy as the kinetics of formation and stability of this passive layer control the corrosion behavior of the implant. When applying a passive potential, the current density abruptly increases until a maximum value and then diminishes until reaching a constant value due to the oxide film formation, which generation reduces the transient of current density. When the material is passivated, the value of the current density remains constant and the final current density value, which is denoted as i_{pass} , gives information about the resistance of the oxide film formed.

Faraday's law (**equation (3.16)**) establishes a relationship between the mass loss of metal and the current in the exposed anodic area [2].

$$\mathbf{m} = \frac{\mathbf{I} \cdot \mathbf{M} \cdot \mathbf{t}}{\mathbf{n} \cdot \mathbf{F}} \quad (3.16)$$

where m is the metal oxidized during time t , I is the anodic current, F is the Faraday's constant (96500 C mol^{-1}), n is the oxidation valence and M is atomic mass of the metal. Therefore, the conversion of current into mass of oxidized metal can be determined by knowing the oxidation valence and if the metal oxidation is the prevailing contribution to the measured current.

3.2.4. Impedance

When applied under equilibrium corrosion, EIS is a non-destructive very sensitive technique which allows to characterize the interface electrolyte/biomaterial and to study the electrochemical properties of oxide film formed, even in low conductive media. This technique consists in measuring the response of an electrode to a sinusoidal potential modulation of small amplitude (typically 5-10 mV) at different frequencies. The alternative current (AC) modulation is superimposed either onto an applied anodic potential or cathodic potential or onto the corrosion potential [4].

3.2.4.1. Electrode response to a sinusoidal perturbation of the potential

An excitation sinusoidal signal $E(t)$ is superimposed onto the steady-state potential of an electrode, expressed as a function of time (t):

$$E(t) = E_0 \sin(\omega t) \quad (3.17)$$

where E_0 is the amplitude (in volts), ω is the radial frequency (in radians per second) defined also as $\omega=2\pi f$ and f is the frequency expressed in Hertz (Hz) and t the time in seconds. In order to maintain a linear response of the electrode the modulation amplitude must not exceed 10 mV.

The sinusoidal perturbation of the potential induces a sinusoidal current $I(t)$. The response signal $I(t)$ has a different amplitude and is shifted in phase with respect to the potential .

$$I(t) = I_0 \sin(\omega t - \varphi) \quad (3.18)$$

where I_0 is the amplitude (in amperes) and φ is the phase (in degrees).

The following equation defines the **electrochemical impedance** Z as the relation between the applied potential and the resulting intensity.

$$Z = \frac{E(t)}{I(t)} = \frac{E_0 \cdot \sin(\omega t)}{I_0 \cdot \sin(\omega t - \varphi)} = Z_0 \frac{\sin(\omega t)}{\sin(\omega t - \varphi)} \quad (3.19)$$

Using Euler's relationship (**equation (3.20)**) it is possible to represent these functions in the complex plane.

$$\exp(j\theta) = \cos \theta + j\sin\theta \quad (3.20)$$

where $j^2=-1$ is the imaginary number and θ is the angle.

The sinusoidal perturbation of the potential and the current response are represented therefore by two vectors in the complex plane. Thus, the impedance Z is represented by a vector sum of the real and the imaginary part (**equation (3.21)**) characterized by the modulus Z_0 and the phase shift φ .

$$Z = \frac{E_0 \cdot \exp(j\omega t)}{I_0 \cdot \exp(j\omega t - j\varphi)} = Z_0 \exp(j\varphi) = Z_0 (\cos \varphi + j \sin \varphi) \quad (3.21)$$

$$Z = Z_{\text{Re}} + Z_{\text{Im}} \quad (3.22)$$

The modulus (**equation (3.18)**) and the phase shift (**equation (3.19)**) can be calculated using Pythagoras' theorem and the adequate trigonometric relations:

$$|Z| = \sqrt{Z_{\text{Re}}^2 + Z_{\text{Im}}^2} \quad (3.23)$$

$$\varphi = \arctan \frac{Z_{\text{Im}}}{Z_{\text{Re}}} \quad (3.24)$$

Two graphical representations of the impedance results can be shown using two different graphical representations:

- **The Nyquist diagram:** Z is represented in the complex plane, where the real part is plotted on the x-axis and the imaginary part on the y-axis of a chart for different frequencies (see **Figure 3.11.a**).
- **The Bode plot:** Impedance in terms of modulus $|Z|$ in logarithmic scale and phase shift (φ) are represented on the same y-axis as functions of frequency on a logarithmic scale. (see **Figure 3.11.b**)

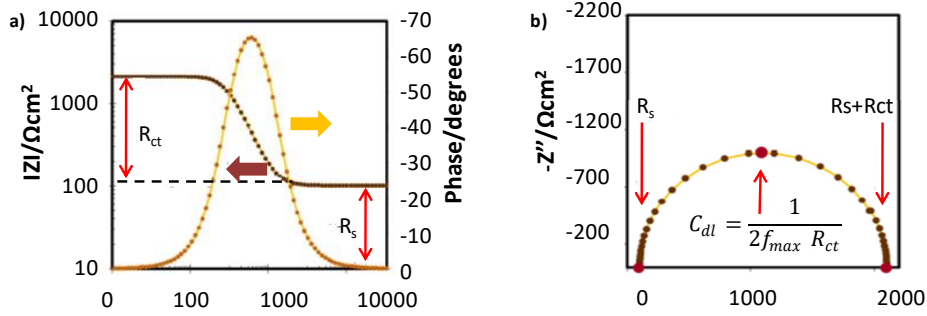


Figure 3.11. (a) Nyquist diagram and (b) Bode plot of impedance data for a simple equivalent circuit (Randles circuit with solution resistance (R_s) of $100 \Omega \cdot \text{cm}^2$, double layer capacitance (C_{dl}) of $1 \cdot 10^{-6} \text{ F cm}^{-2}$ and charge transfer resistance (R_{ct}) of $2000 \Omega \cdot \text{cm}^2$

3.2.4.2 Instrumentation

The conventional three-electrode cell configuration is used to carry out the EIS experiments. A potential (V) is applied between the working electrode (WE, i.e. titanium) and the reference electrode (RE, Ag/AgCl electrode) while the current (I) flowing through the working electrode and the counter electrode (CE, platinum) is measured.

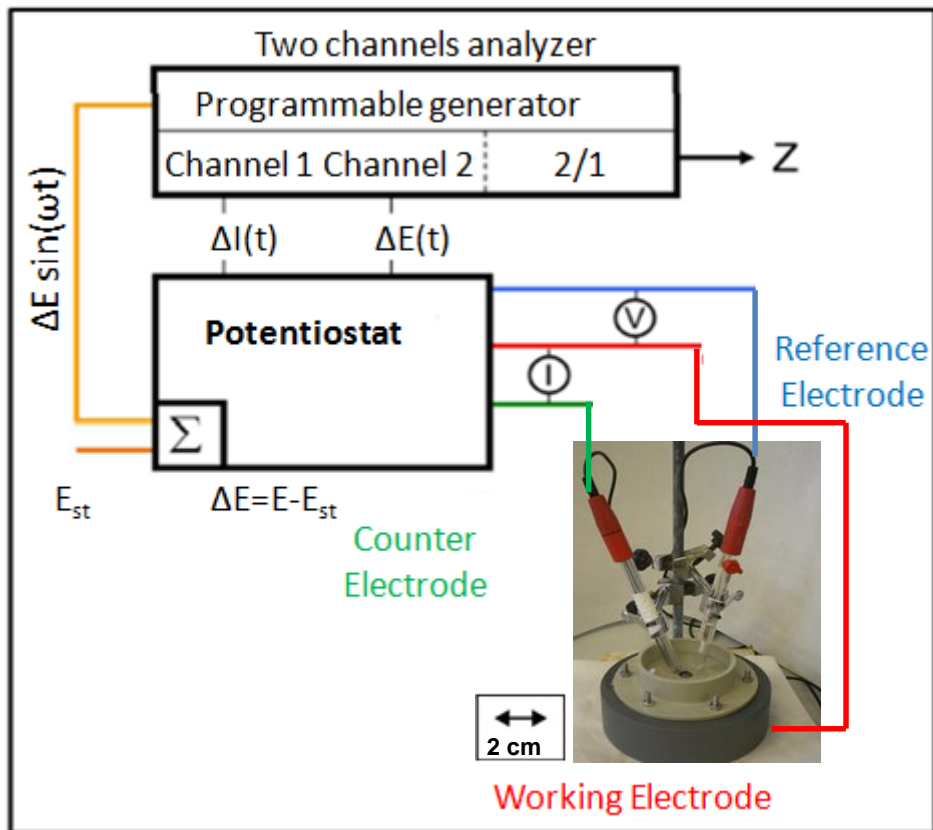


Figure 3.12 Experimental set up for impedance measurements using a transfer function analyser under potentiostatic control (a sinusoidal of weak amplitude $\Delta E = E - E_{st}$ is superimposed onto the steady state potential E_{st} of an electrode).

The basic electronic instrumentation that allows one to obtain the impedance spectra in electrochemical systems consists on a generator-analyser of functions denominated Frequency Response Analyzer (FRA) or “lock-in amplifier”. Metrohm Autolab was used in the present Thesis. The FRA can analyse and apply sinusoidal signals in a widespread frequencies range to the potentiostat with fast response and sensibility.

A potentiostat applies a sinusoidal signal (**equation (3.18)**) to the working electrode in the electrochemical cell. The latter is often built into a two-channel transfer function analyser, thus permitting simultaneously measurement of the potential and the current. The system responds with a signal (**equation (3.19)**) that differs from the **equation (3.18)** by its phase and amplitude. The response of the electrode, measured by the analyser, determines the impedance Z response of the electrochemical system and the phase shift corresponding to each frequency

3.2.4.3. Interpretation of the impedance results and Equivalent Electrical Circuits

The EIS data is commonly interpreted in terms of equivalent circuits. In this sense, the investigated parameters from the impedance experiments are common electrical elements (method used in the present Thesis). The interpretation of the impedance spectra requires the selection of an electric model that suitably fits the experimental data to a combination of electrical elements shown in **Table 3.1**. The selected model and associated properties thus give information about the electrochemical mechanisms and properties of the system. Common electrical elements and their corresponding meaning are described as follows [4]:

- **Resistance (R)**: describes some charge transfer across certain interface (i.e. metal/electrolyte). This resistance can be related to the resistivity present for one compound or dissolution to the charge transfer across them (solution resistance) or incorporated into one sub-circuit RC (electrical circuit formed by one resistance in parallel combination with one capacitance element) which corresponds to the transfer resistance or faradic resistance of the interface.

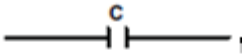
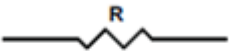
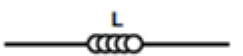
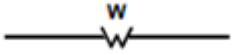
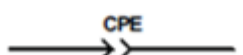
- **Capacitance (C)**: is characteristic to charge structures (double layers) considering these layers as parallel plate condenser. It is an element of easy interpretation since describes properly the charge distribution at the electrode/electrolyte interface which in the simplest case (Helmholtz model) describes the compensation of the surface excess charge by a monolayer of the opposite charge. When this element is included into one sub-circuit RC , the adsorption of an intermediary specie product of one process of faradic relaxation can be presented. Nevertheless, the main advantage of this element is the capability of evaluating the thickness of the physical layer that is considered into the selected

circuit. Generally, in real systems this element is corrected by a **constant phase element** (CPE) in order to take into account different aspects that can influence in its nonideality.

- **Inductance** (L): is associated with the adsorption-desorption process during the formation of passive films. This element is physically worthless because of it is difficult to assimilate the inductance element in the electrode/electrolyte interface. However, at lower frequencies the inductive semicircle generated can be attributed to the relaxation of intermediate species of the surface concentration. Typically, the inductance is associated with RL sub-circuit where R corresponds to the charge transfer resistance associated with desorption inductive process.

- **Warburg** (W): it represents linear diffusion under semi-infinite conditions. This also assumes the diffusion layer to possess an infinite thickness. The Warburg impedance is defined through an admittance Y_0 (fitting parameter that contains the diffusion coefficients and other parameters that depend on electrochemical properties of the system) and a diffusion parameter B . This electrical element corresponds to the solution of the second Fick's equation with one-dimension and infinite conditions of resolution.

Table 3.1 Impedance electrical symbols

| Element | Symbol |
|------------------------|--|
| Capacitance |  |
| Resistance |  |
| Inductance |  |
| Walburg |  |
| Constant Phase Element |  |

An Equivalent Electrical Circuit (EEC) is defined using a combination of electrical elements (resistance, capacitances and inductances) which will simultaneously describe the physical properties of the system and accurately fit the experimental data.

The general guidelines for the selection of the best-fit *EEC* are (i) to minimize the number of circuit elements employed to describe the electrochemical system, (ii) a low value of the Chi-squared value ($X^2 = 10^{-4}$) and (iii) the errors associated with each element must not exceed 5 % [5].

The impedance data has been analysed with the Zview 2.70 software package. Thus, the best fitting and the corresponding values of each element can be obtained. In addition, Chi-squared value and the error associated with each element is also acquired which allows to confirm the reliability of all them.

The Randles circuit is the simplest equivalent circuit used for fitting the experimental results (**Figure 3.13(a)**). In this case, the theoretical transference function is represented by means of parallel combination of the resistance R_{ct} (charge transfer resistance) and the capacitance C_{dl} (double layer capacitance related to the interactions in the electrode/electrolyte interface) both in series with the resistance R_s (electrolyte resistance).

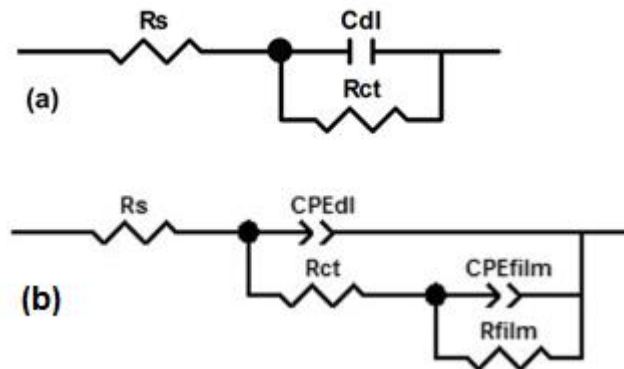


Figure 3.13 (a) Equivalent Electric Circuit (Randles) of the electrode-electrolyte interface and (b) Equivalent Circuit for the analysis of the impedance spectra of a Ti passive alloys.

The impedance spectrum obtained for the Randles circuit is represented in **Figure 3.11**. The higher frequency region is characterized by $\log|Z|$ which tends to a constant value with a phase shift close to 0° when the frequency increases. This corresponds to a resistive behaviour and the value of the impedance corresponds to R_s . This ohmic resistance is added in series to take into account the ohmic drop in the electrolyte between the working electrode and the reference electrode. The medium-lower frequencies range is characterized by a linear relationship between $\log|Z|$ and $\log f$. A slope of approximately -1 corresponds to this ideal capacitive behaviour. In this electrical circuit, the R_{ct} corresponds to the diameter of the semicircle represented in Nyquist diagram (**Figure 3.11 (a)**).

Metallic biomaterials such as titanium spontaneously passivate when in contact with body fluids resulting in the formation of an oxide film in contact with the biological environment. In the case of titanium when the oxide layer is chemically and physically stable and quite homogeneous, the impedance results are best fitted with the EEC proposed in **Figure 3.13 (b)**, where two R-C groups are adjusted as parallel circuits. Thus, two overlapped time constants can be considered in the impedance spectra, the first one related to the outer layer (attributed to the presence of inhomogeneous passive film and to the passive dissolution of the passive layer) and the second one

related to the oxide film formed on the passivated metallic biomaterial. One time constant is attributed to the charge transfer resistance (R_{ct})/double layer capacitance (C_{dl}) parallel combination, and the second is attributed to the film resistance (R_{film})/film capacitance (C_{film}) parallel combination. In this case, R_p (polarization resistance of the system) can be calculated as the sum of R_{out} and R_{in} after fitting the experimental results to the EEC.

Different authors used the same EEC on passive systems when two time constants were shown in the spectra assuming that the low-frequency time constants corresponded to the passive oxide film [6-7]. In the present thesis, the Randles circuit has been used instead of the previously presented EEC as it presented a better quality of the fit (evaluated firstly with the lower chi-square value, and secondly with the lower estimative errors (in %) for all the components).

Generally, the real systems present non-ideal capacitive behaviour in contrast with the ideal shown by the Randles Circuit. These real systems show certain modification from an ideal capacitance behaviour which remark mainly lower value of the slope and lower phase angles. A **constant phase angle element** (CPE) is introduced to replace the capacitance and to describe the non-ideal behavior which can be due to different physical phenomenon such as surface heterogeneity resulting from surface roughness, impurities, dislocations or grain boundaries [8]. These inhomogeneities are present on a microscopic level under the oxide phase and at the oxide electrolyte interface. Thus, *CPE* is defined in impedance representation as [4]:

$$\mathbf{Z}(\omega) = \mathbf{Z}_0(j\omega)^{-n} \quad (3.25)$$

where Z_0 is the CPE constant and n is the CPE exponent. Depending on n , CPE can represent resistance ($n=0$, $Z_0=R$), a capacitance ($n=1$, $Z_0=C$) or a Warburg impedance ($n=0.5$, $Z_0=W$). For $0.5 < n < 1$ the CPE describes a distribution of dielectric relaxation times in the frequency space.

The value of the capacitance can be used to determine the film thickness according to the **expression (3.26)** [9] which allows one to approximate, for anodic film growth, the dielectric behaviour of the oxide film with a plate capacitor [10,11].

$$\mathbf{C} = \frac{\epsilon\epsilon_0 A}{d} \quad (3.26)$$

where ϵ denotes the relative dielectric constant of the layer, ϵ_0 is the permittivity of the vacuum ($8.85 \cdot 10^{-14} \text{ F cm}^{-1}$), A the active area (in cm^2) and d the film thickness (in cm).

In order to use the previous expression and relate the capacitance with the thickness of the capacitor, the CPE must be converted into a pure capacitance (C) by means of the following equation [12]:

$$\mathbf{CPE = R^{n-1} \cdot C^n} \quad (3.27)$$

Therefore, the double layer capacitance (C_{dl}) and film capacitance (C_{film}) are given by the following equations [13]:

$$\mathbf{C_{dl} = \left(\frac{CPE_{dl}}{(R_s^{-1} R_{ct}^{-1})^{1-n_{dl}}} \right)^{\frac{1}{n_{dl}}}} \quad (3.28)$$

$$\mathbf{C_{film} = \left(\frac{CPE_{film}}{((R_s + R_{ct})^{-1} R_{film}^{-1})^{1-n_{film}}} \right)^{\frac{1}{n_{film}}}} \quad (3.29)$$

It should be noted that external conditions, such as applied potential and hydrodynamic effects, may generate ambiguous values of the capacitance since dielectric properties of the system (ϵ) can be altered [14-16]. Therefore, care has to be taken in order to obtain realistic values of layer thicknesses from capacitance values (**equation (3.26)**).

3.3. Tribocorrosion

The tribocorrosion technique enables to give insights on the material loss during wear in a corrosive media and to study the mechanisms which give rise to the synergetic/antagonistic effects of corrosion and wear. The tribocorrosion measurements are carried out using a tribocorrosion apparatus which consists in an electrochemical cell coupled with a tribometer. This coupling enables to carry out friction tests under well defined corrosion conditions. The rubbed metal is connected as the working electrode and immersed in the electrolyte of a cell equipped with a reference electrode and a counter electrode.

Two different configurations have been used in this thesis. The first is the Pin on Disk type which consists in a rotating working electrode onto which a pin or ball (in this study) is pressed at a constant normal force. Measurement of the normal force and of the angular momentum enables to determine the coefficient of friction. The second is a reciprocating set-up where the pin has a back-and-forth motion onto the working electrode. In this case the coefficient of friction is determined from the measurement of the normal and tangential loads.

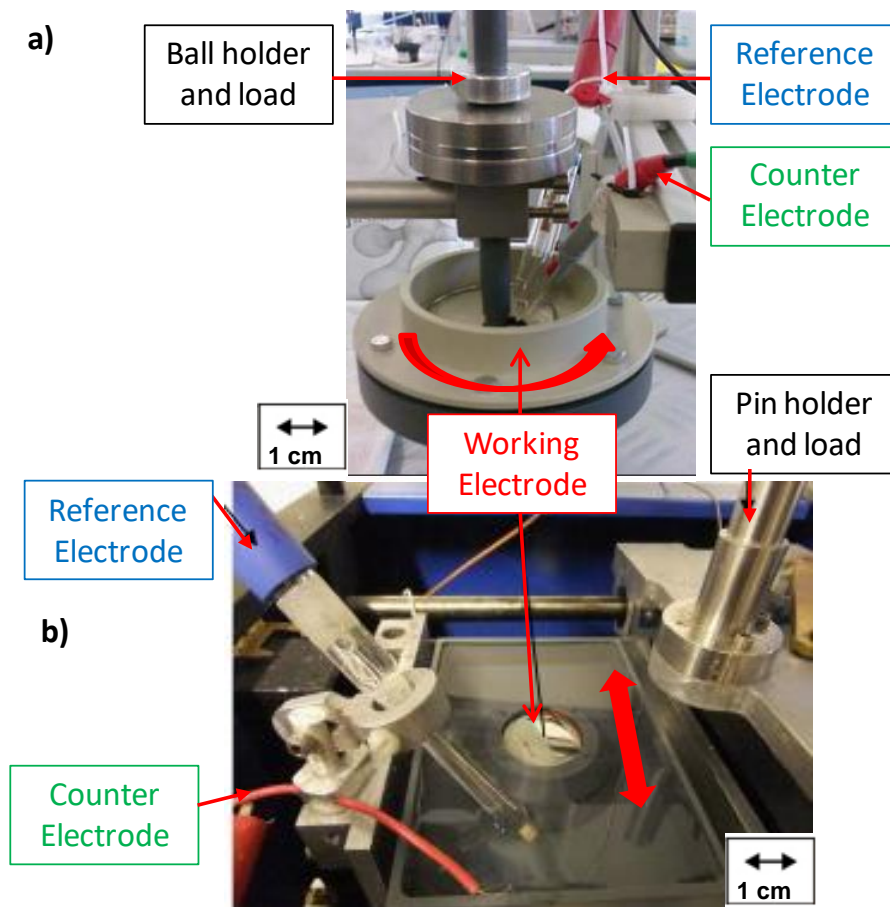
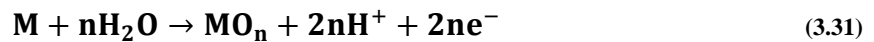


Figure 3.14. Tribocorrosion set-ups.
a) sliding and b) reciprocating configurations

In order to assess interactions between wear and corrosion two tests have been used: the first involves sliding wear under free corrosion potential and the second involves sliding wear under controlled potential.

3.3.1 Tribocorrosion under Open Circuit Potential

Tribocorrosion tests under OCP condition is the simplest method which consists in recording OCP before, during and after sliding. During sliding a mixed electrode potential condition is established between the worn and unworn surface due to the galvanic coupling between the worn area (inside the wear track) and the unworn area. Oxidation reactions take place in the wear track resulting in the formation of soluble ions and/or solid products as shown in **equation (3.30)** and **(3.31)**



Three coupled reduction reactions can take place:

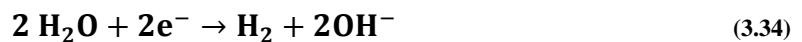
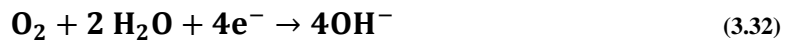


Figure 3.15 shows the evolution with time of the OCP during a tribocorrosion test. Prior to sliding, the potential reflects the presence of a passive film on the surface of the passive alloy. At the onset of sliding an abrupt decrease in potential is observed indicating a depassivation of the surface induced by the mechanical detachment of the passive film (depassivation), and the exposure of fresh active material which will oxidate and regenerate the passive layer. The depassivation/repassivation cycles will therefore cause accelerated corrosion wear. As sliding stops, the OCP increase suggests a repassivation of the surface.

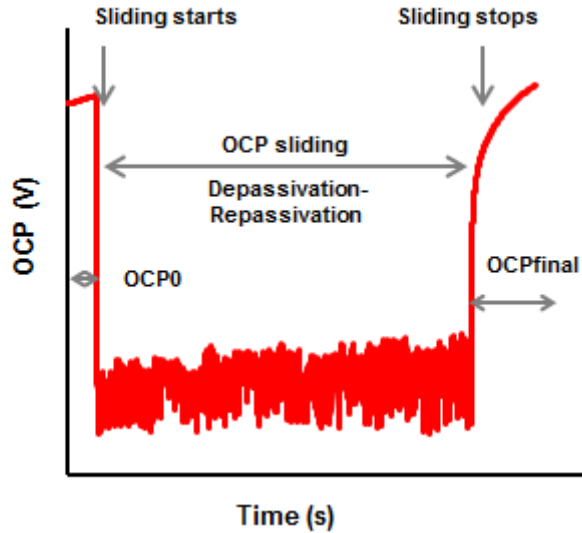


Figure 3.15. Evolution of potential vs time during a tribocorrosion test at OCP

The parameters extracted from tribocorrosion tests under equilibrium conditions are OCP_0 , $OCP_{sliding}$ and OCP_{final} . The total volume loss will also be determined using a confocal microscope (see **section 3.4.1**)

3.3.2 Tribocorrosion with applied potential

In the potentiostatic set up the potentiostat maintains the selected potential between working (WE) and reference (RE) electrodes. The current is recorded between the working (WE) and counter-electrodes (CE).

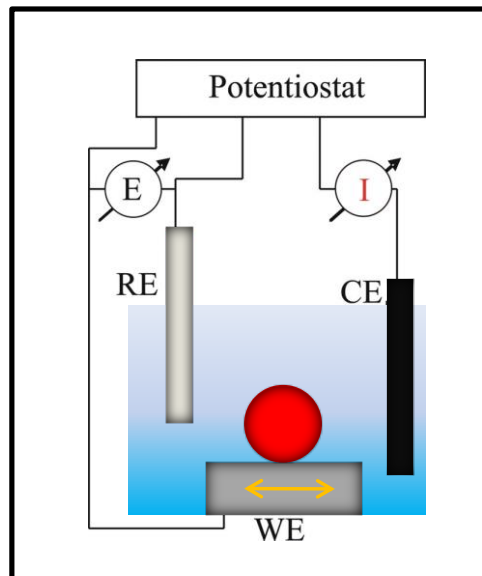


Figure 3.16. Scheme of potentiostatic set-up for tribocorrosion experiments.

Figure 3.16 shows the monitoring of the anodic current during a potentiostatic tribocorrosion test for a passive material. Before sliding the current is very low (μA) as the passive film covers the metal surface. During sliding the protective passive layer is removed leading to a significant increment in material dissolution causing the current to increase. As sliding stops the surface repassivates causing the current to drop back to low values. The parameters extracted from a tribocorrosion test at an applied potential are I_0 (prior to sliding), I_{sliding} (during sliding) and I_{final} (after sliding stops).

As mentioned previously (**chapter 1**) the total wear volume can be broken down into different contributions:

$$V_{\text{tot}} = V_{\text{chem}} + V_{\text{mech}} + V_{\text{corr}} \quad (3.35)$$

Where V_{tot} represents the total volume of removed material (wear track volume), V_{chem} is equal to the sum of oxidized metal during rubbing (wear accelerated corrosion), V_{mech} the mechanical wear volume (material removed mechanically) and V_{corr} the corrosion occurring on the overall surface exposed to the electrolyte (this component is considered negligible for passive alloys).

When experiments are carried out at an anodic applied potential, the amount of anodically oxidized metal is calculated using the parameter i_{sliding} , from the measured current using Faraday's law:

$$V_{\text{chem}} = \frac{I \cdot M \cdot t}{n \cdot F \cdot \rho} = \frac{Q \cdot M}{n \cdot F \cdot \rho} \quad (3.36)$$

Where M is the atomic mass of the alloy, n is the charge number for the oxidation reaction (valence of oxidation was assumed), Q is the electric charge flowing in the wear track (**Figure 3.17**), F is the Faraday constant (96500 C/mol), ρ is the density of the alloy and t is the duration of sliding. It may be mentioned that this equation is valid independent of whether anodic oxidation leads to formation of dissolved metal ions or of solid reaction products, such as oxide films.

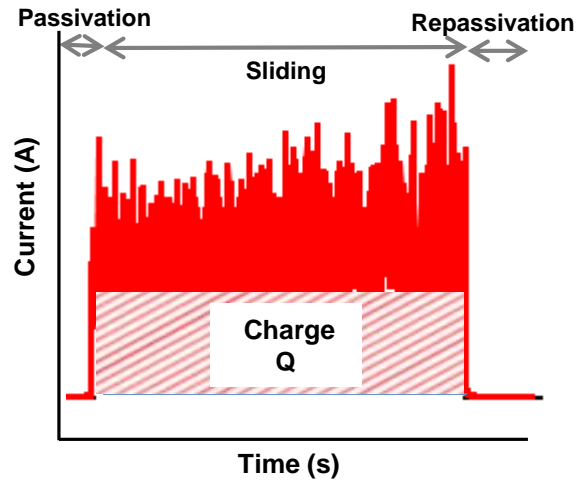


Figure 3.17. Evolution of current during a potentiostatic tribocorrosion test

The total wear volume, V_{tot} , is determined by measuring the volume of the wear track after an experiment using a confocal microscope (see 3.4.1). From the total wear volume, V_{tot} , and the chemical wear volume V_{chem} , calculated from the electric charge, the mechanical wear volume V_{mech} , which is the volume of metal removed mechanically, is obtained by subtraction:

$$V_{\text{mech}} = V_{\text{tot}} - V_{\text{chem}} \quad (3.37)$$

3.3.3 Tribocorrosion under Open Circuit Potential using a ZRA

Tribocorrosion at OCP gives limited information as it cannot provide quantitative information on the effect of wear on corrosion. However the galvanic current can be measured using the set up shown **Figure 3.18** as proposed by Espallargas et al. [17]. Two working electrodes of the same material are connected through a zero-resistance ammeter (ZRA) where electrode A (WE_A), the uncoated sample, consists in the cathode and electrode B (WE_B), the coated electrode consists in the anode. Before wear, the measured current is zero as electrode A is at equilibrium. As rubbing starts the coating on WE_B is removed, the worn area generates electrons due to metal oxidation, and the unworn area consumes the generated electrons by the cathodic reaction. Thus the potential of the sample is shifted and a galvanic cell is created between the WE_A and WE_B . This set up enables to measure both potential and current during rubbing. It is therefore possible to determine the chemical contribution to wear under equilibrium conditions.

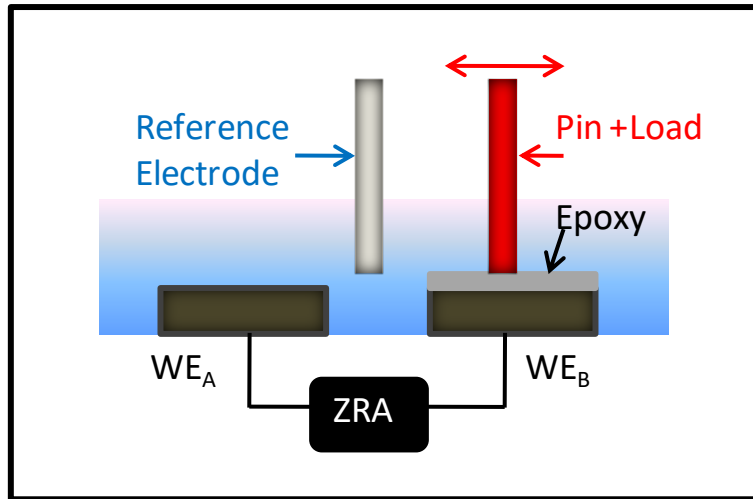


Figure 3.18. Scheme of the electrochemical measurements carried out through a Zero-Resistance Ammeter (ZRA) where WE_A is the cathode (unrubbed sample), WE_B is the anode (rubbed sample) and RE is the reference electrode.

3.4. Surface Analysis

A number of different methods can be used for the characterization of surface structure and topography depending on the scale of study i.e. whether it is microscopic or atomic to nanometer.

3.4.1. Optical and confocal microscopy

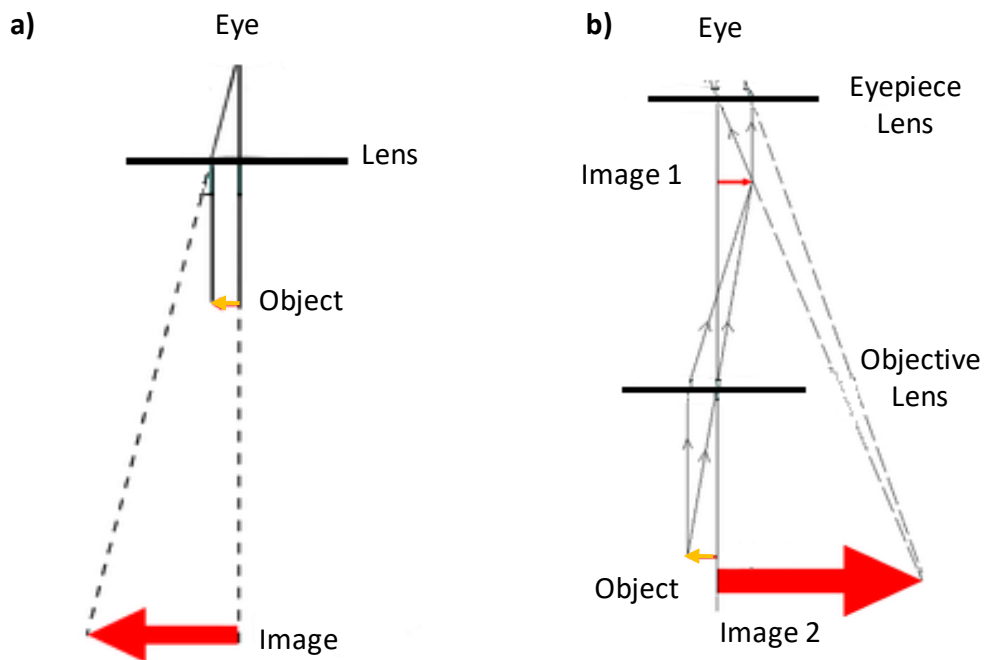


Figure 3.19. Schematic diagram of conventional optical microscope.
a) simple microscope and b) compound microscope

The conventional optical microscope has two basic configurations as **shown on Figure 3.19.a**: the simple microscope and the compound microscope more commonly used in research. A **simple microscope** uses a lens or set of lenses to enlarge an object through angular magnification alone, resulting in an erect enlarged virtual image. A **compound microscope combines objective/eyepiece for higher magnification**. The objective lens, close to the object, focuses a real image of the object inside the microscope (image 1). This image is then magnified by the eye piece lense(s) which gives the viewer an enlarged inverted virtual image of the object (image 2). The use of a compound objective/eyepiece combination allows for much higher magnification. In both configurations the lens/sample distance is adjusted in order to focus at different focal depths, and the width of field of view is set by the choice of a magnification objective.

The optical microscope was used in this thesis for the metallographic observation of the different materials.

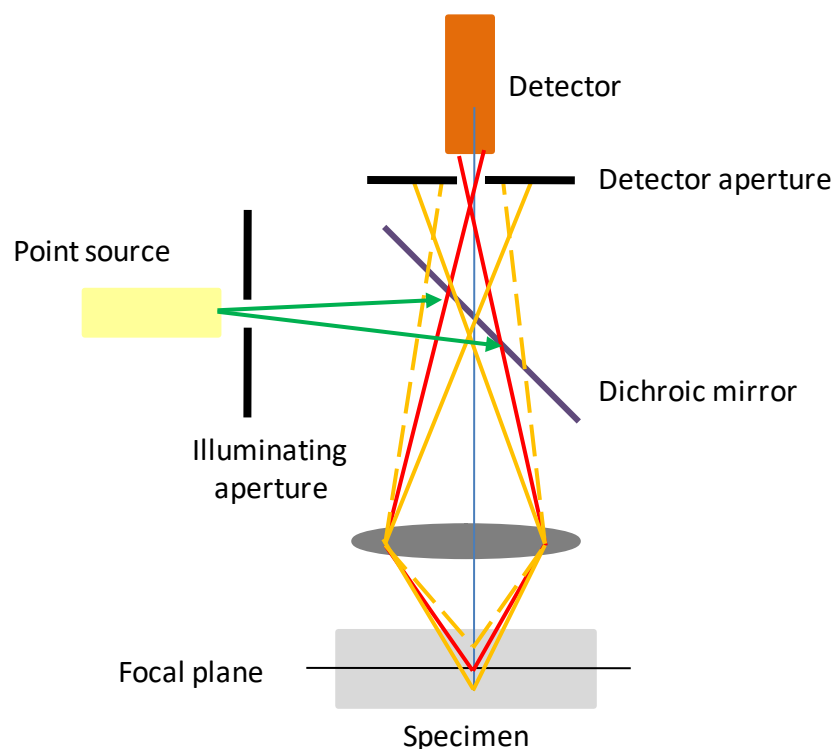


Figure 3.20. Schematic diagram of confocal microscope

In conventional light microscopy, the entire plane of focus is illuminated including the specimen above and below this point resulting in out-of-focus blur from these areas and a decreased resolution when the surface observed is not perfectly smooth.

In the confocal microscope, all out-of-focus structures are suppressed at image formation using spatial filtering techniques to eliminate out-of-focus light or glare in specimens whose thickness exceeds the immediate plane of focus. As shown on **Figure 3.20** a laser exciting light reflects off dichromatic mirrors which scan the laser across the sample. The emitted light passes through the mirror and is focused onto the pinhole. The light that passes through the pinhole is measured by a detector, i.e. a photomultiplier tube. The confocal instrument images only the one spot—rather than the entire field of view of the objective lens—onto the detector. To generate a complete image, the spot is moved over the specimen and the image built point by point. Because confocal microscopy allows for high-resolution measurements within thick specimens, it has spurred considerable development in optical sectioning and three-dimensional reconstruction.

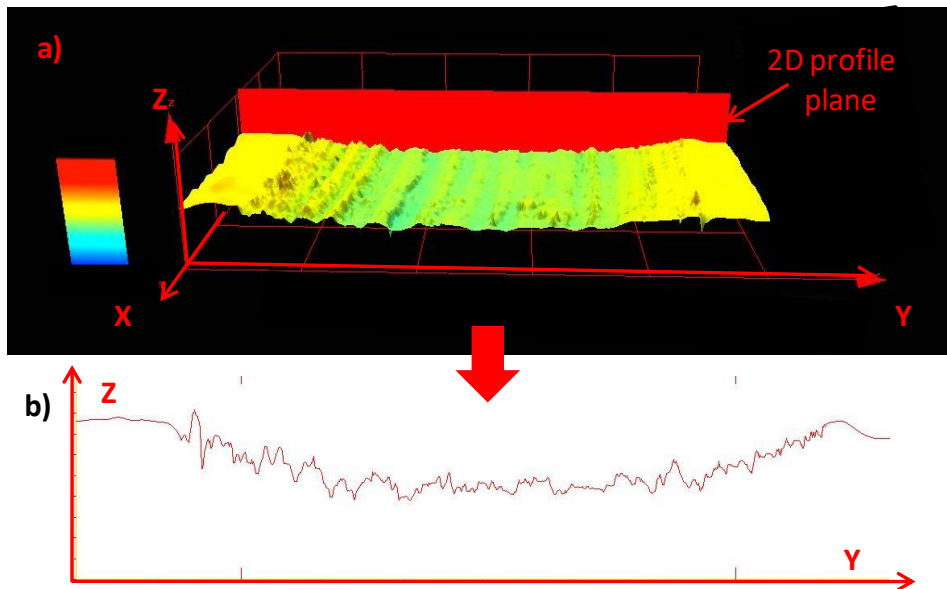


Figure 3.21. a) 3D section obtained with confocal microscope and b) associated 2D profile

In the present thesis, the confocal microscope was used to obtain the total wear volume following the tribocorrosion experiments. As shown in **Figure 3.21**. Cross sectional profiles were taken across the wear track for each sample. The area of each profile was calculated and the volume loss was then determined by multiplying the averaged area by the length of the track.

3.4.2. Scanning electron microscope

Scanning electron microscopy is used to characterize solid materials by giving information regarding morphology and composition of the surface. It is suited for the study of the micrometer or even millimeter scale surface.

The basic principle consists in a focused beam of high-energy electrons which generates a variety of electron-sample interactions at the surface of solid specimens.

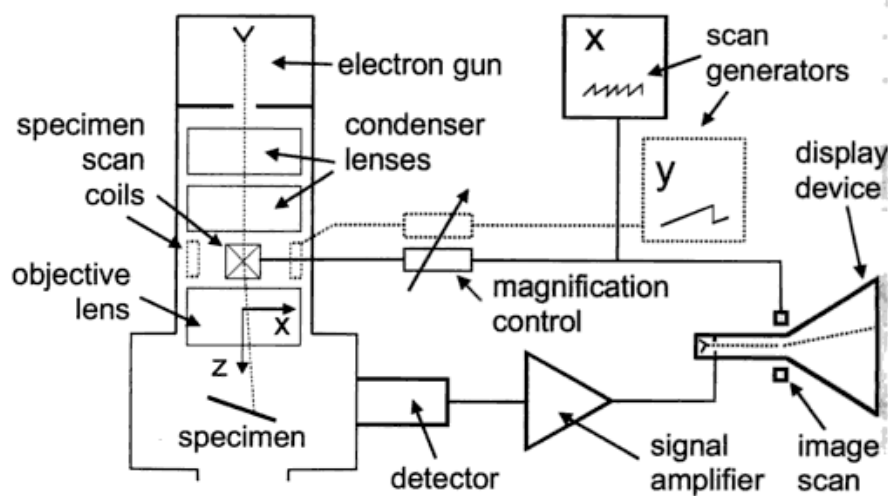


Figure 3.22. Schematic diagram of scanning electron microscope with CRT display [18]

A beam of electrons is generated by a suitable source, typically a tungsten filament or a field emission gun. The electron beam is accelerated through a high voltage (up to: 20 kV) and passes through a system of apertures and electromagnetic lenses to produce a thin beam of electrons. Scan coils enable to scan the surface of the specimen. The local electron flux depends on the angle created between the incident beam and the surface which is fixed by different lens and magnetic coils. The electrons that interact with the sample result in the reflection of high-energy electrons by elastic scattering, emission of secondary electrons by inelastic scattering and the emission of electromagnetic radiation, each being collected by a different suitably-positioned detector. Analyzed samples should be electrically conductive therefore gold coating can be necessary.

In the present thesis, following a tribocorrosion experiment, the wear track morphology was observed using the SEM technique in order to understand the wear mechanisms.

3.5. References

- [1] D. Landolt, Corrosion and surface chemistry of metals. EPFL Press. 2007
- [2] A.J. Bard and L.R. Faulkner. Electrochemical methods: fundamentals and application. John Wiley and Sons Ltd. 2001
- [3] P.H. Rieger. Electrochemistry. Chapman and Hall. 1994
- [4] Mansfeld, F.; Shih, H.; Greene, H., and Tsai, C.H. 1993. Analysis of EIS data for common corrosion processes. in: J.R. Scully, D. C. Silverman, and M. W. Kending (Eds). Electrochemical impedance. Analysis and interpretation. ASTM international. (1993) 37-53
- [5] M. Metikos-Hukovic, Z. Pilic, R. Babic, D. Omanovic. Influence of alloying elements on the corrosion stability of CoCrMo implant alloy in Hank's solution. Acta Biomaterialia 2 (2006) 693-700.
- [6] Y.J. Jo, C.M. Lee, H.S. Jang, N.S. Lee, J.-H. Suk, W.H. Lee. Mechanical properties of fully porous and porous-surfaced Ti–6Al–4V implants fabricated by electro-discharge-sintering. Journal of Materials. Processing Technology. 194 (2007) 121–125
- [7] B.A. Kolachev, A.A. Ilin, D.V. Ryndenkov. Structural diagrams of titanium alloys in the “molybdenum equivalent–aluminum equivalent” coordinates. Russian Metallurgy. (1997) 118–128
- [8] F. B. Growcock, R. J. Jasinski. Journal of the Electrochemical Society 136 (1989) 2310-2314
- [9] J. A. Helsen and H. J. Breme. Metals as biomaterials. John Wiley and Sons Ltd. 1998
- [10] P. Bommersbach, C. Alemany-Dumont, J. P. Millet, B. Normand. Formation and behaviour study of an environment-friendly corrosion inhibitor by electrochemical methods. Electrochimica Acta 51 (2005) 1076-1084
- [11] C.O. A. Olsson, D. Landolt. Anodisation of a Nb–Zr alloy. Electrochimica Acta 48 (2003) 3999-4011
- [12] N. P. Cosman, K. Fatih, S. G. Roscoe. Electrochemical impedance spectroscopy study of the adsorption behaviour of α -lactalbumin and β -casein at stainless steel. Journal of Electroanalytical Chemistry 574 (2005) 261-271

- [13] G.J. Brug, A.L.G. van den Eeden, M. Sluyters-Rehbach, J.H. Sluyters. The analysis of electrode impedances complicated by the presence of a constant phase element. *J. Electroanal. Chem. Interfacial Electrochem.* 176 (1984) 275–295
- [14] J. J. Gray, C. A. Orme. Electrochemical impedance spectroscopy study of the passive films of alloy 22 in low pH nitrate and chloride environments. *Electrochimica Acta* 52 (2007) 2370-2375
- [15] K.M. Ismail, S.S. El-Egamy, M.Abdelfatah. Effects of Zn and Pb as alloying elements on the electrochemical behaviour of brass in borate solutions. *Journal of Applied Electrochemistry* 31 (2001) 663-670
- [16] T. P. Cheng, J. T. Lee, W. T. Tsai. Passivation of titanium in molybdate-containing sulphuric acid solution. *Electrochimica Acta* 36 (1991) 2069-2076
- [17] N. Espallargas, R. Johnsen, C. Torres, A.I. Muñoz. A new experimental technique for quantifying the galvanic coupling effects on stainless steel during tribocorrosion under equilibrium conditions. *Wear* 307 (2013) 190-197.
- [18] Scanning electron microscopy. Available on (2017):
https://en.wikipedia.org/wiki/Scanning_electron_microscope

-Chapter 4-

**Corrosion and tribocorrosion behaviour
of Ti6Al4V biomedical alloy
in artificial saliva**

-Article 1-

**INFLUENCE OF THE FABRICATION PROCESS
AND FLUORIDE CONTENT
ON THE TRIBOCORROSION BEHAVIOUR
OF Ti6Al4V BIOMEDICAL ALLOY IN ARTIFICIAL SALIVA**

M.P. Licausi, A. Igual Muñoz, V. Amigó Borrás

Journal of the mechanical behavior of biomedical materials 20 (2013) 137–148

doi.org/10.1016/j.jmbbm.2013.01.019

INFLUENCE OF THE FABRICATION PROCESS AND FLUORIDE CONTENT ON THE TRIBOCORROSION BEHAVIOUR OF Ti6Al4V BIOMEDICAL ALLOY IN ARTIFICIAL SALIVA

M.P. Licausi^{1,2}, A. Igual Muñoz^{1*}, V. Amigó Borrás²,

1 UPV, Department of Chemical and Nuclear Engineering, Universitat Politècnica de València, camino de vera s.n., 46022 Valencia, Spain.

2 UPV, Institute of Materials Technology, Universitat Politècnica de València, camino de vera s.n.,

***Corresponding author**

Abstract

Titanium and its alloys are widely used as dental implants due to their low density, excellent biocompatibility, mechanical properties and corrosion resistance. However, during their lifetime Ti6Al4V biomedical alloys are subjected to different mechanical actions (i.e., sliding or fretting), thus resulting in a tribocorrosion system, which is an irreversible material degradation process due to the combined effect of corrosion and wear. In this study, the tribo-electrochemical behavior of cast and sintered (by powder metallurgy) Ti6Al4V alloy in artificial human saliva solution without and with fluoride additions of 100 ppm and 1000 ppm and in an average industrial mouth wash solution with a 112 ppm fluoride content have been investigated by different electrochemical techniques. The same tribocorrosion mechanisms were found in the cast and sintered titanium alloys, although slightly different wear debris behavior was observed. At low applied passive potentials, wear rates are similar to those obtained under equilibrium conditions (Open Circuit Potential). There exists a critical fluoride concentration above which corrosion and tribocorrosion rates increase.

Keywords: Tribocorrosion, Titanium, Wear, Powder metallurgy, Fluoride

1. Introduction

Titanium and the titanium-based alloy TiAl6V4 are chosen for dental implantology because of their resistance to corrosion and their biocompatibility (Assad et al., 1999; Strietzel, 1998; Zitter and Plenk, 1987). Nowadays, porous titanium has become a popular surgical implant material (Bundy and Luedemann, 1987; Lucas et al., 1987), since it has a low elastic modulus, that encourages regular bone growth, whilst its porosity enables bone in-growth. The corrosion behavior of titanium alloys depend on an oxide film mainly composed of TiO_2 , which spontaneously covers the titanium surface and its alloys in presence of oxygen (Kaneko et al., 2003). The chemical properties of the oxide layer play an important role in the biocompatibility of titanium implants and the surrounding tissues (Al-Mayouf et al., 2004). However, the passive layer of titanium possesses inferior mechanical properties and can be disrupted at very low shear stresses. Therefore, under wear conditions (fretting and sliding) the passive oxide layer can undergo fracture. When considering implants, the device suffers tribocorrosion, which is the deterioration that occurs at the interface of contacting surfaces, when surrounded by a corrosive medium, due to the existence of relative movement between them.

Nowadays, modular orthopedic implants imply the existence of contacts between their components which are exposed to corrosive body fluids. In dental implants, such contact zones appear between the implant/abutment or the abutment/ceramic crown. In such situations, debris and metal ion release can lead to toxicity, reddening and allergic reactions of the skin, inflammation of tissues, etc., which could cause the early failure of the implant. Tribocorrosion is, therefore, of increasing concern in orthopedic surgery.

Fluoride therapy is now recognized as being one of the main methods in preventing dental caries. In some commercial toothpastes and prophylactic gels the fluoride content can vary from 0.1–2.0 wt%. However, such a concentration may have some harmful results on the corrosion resistance of metallic implants, with possible clinical consequences. Thus, the presence of fluoride (F) ions in the electrolytic environment brings with it aggressiveness in the attack on titanium and its alloys, which has already been reported by several authors (Boere, 1995; Kononen et al., 1995; Lausmaa et al., 1985; Mimura and Miyagawa, 1996; Nakagawa et al., 1999, 2001, 2002; Oda et al., 1996; Probst et al., 1992; Reclaru and Meyer, 1998; Huang, 2002; Schiff et al., 2002; Siirila and Kononen, 1991; Toumelin-Chemla et al., 1996). According to their results, the oxide film reacts in fluoride solutions, resulting in the formation of complex titanium–Fluoride molecules which are very stable and soluble in the solution. The complexes which can be found on the surface of the alloy can either be of titanium fluoride, titanium oxide fluoride, or sodium titanium fluoride (Kaneko et al., 2003). The lattice parameter of these compounds induces many structural defects in the oxide layer, whose protection is considerably loosened. Hence, oxide films formed on the surface of metals undergo dissolution. The rate of the overall process depends on the rates of the following processes:

(i) formation of an oxide at the metal/oxide interface; (ii) transport of either metal or oxygen vacancies across the film; (iii) generation or consumption of vacancies at the oxide/ electrolyte interface; and (iv) chemical or electrochemical dissolution process (Frateur et al., 2000).

While numerous studies have been carried out on the electrochemical corrosion of titanium and titanium based alloys in presence of fluorides (Boere, 1995; Kononen et al., 1995; Lausmaa et al., 1985; Mimura and Miyagawa, 1996; Nakagawa et al., 1999, 2001, 2002; Oda et al., 1996; Probst et al., 1992; Reclaru and Meyer, 1998; Huang, 2002; Schiff et al., 2002; Siirila and Kononen, 1991; Toumelin-Chemla et al., 1996), few have taken into account the fabrication process and the combined influence of fluoride and the fabrication process on the tribocorrosion behavior of the titanium alloys

The aim of the present study is to examine the influence of fluoride and the fabrication process (forged and powder metallurgy) on the electrochemical and triboelectrochemical properties of the Ti6Al4V sintered and cast titanium alloy

2. Experimental

2.1. Materials and electrolytes

Cast titanium specimens, 20 20 2 mm³ in size, were cut from a sheet of commercially available Ti6Al4V (Grade 5) (chemical composition in wt% N: 0.02, C: 0.03, H: 0.011, Fe: 0.22, O: 0.16, Al: 6.12, and V: 3.93). Specimens were wet ground with 220–4000 grit silicon Carbide paper and further polished with OP-Chem polishing clothes using the OP-S colloidal silica suspension to a mirror like finishing (Ra=0.05 mm).

Care was taken during polishing to avoid any influence in the oxidation kinetic mechanisms, due to the extent of plastic deformation. After polishing, the samples were rinsed in deionized water and dried using a stream of compressed air.

The sintered titanium material was fabricated according to the following procedure: powder compression applying a compacting pressure of 400 MPa without the addition of any lubricant and sintering sequence consisting of a thermal cycle with specific heating and cooling ramps. The initial heating ramp consists of heating at 800 °C for 30 min in order to stabilize both the oven and the material at the same temperature and to avoid cracking due to thermal gradients. The sintering process lasts 2 h at 1250 °C in a vacuum tube oven.

The chemical composition of the sintered powder is the same as the cast alloy; therefore, both materials have the same alloying elements.

Before use, the sintered samples were cleaned with acetone in an ultrasonic bath in order to remove any existing particles from the pores. The samples were not polished and had a roughness of $R_a=1.7$ mm.

The sintered and cast titanium alloys have been tested in four different electrolytes which simulate the human saliva and fluoride containing solutions:

- 1) A modified Fusayama Meyer artificial saliva (AS) as the base electrolyte. The chemical composition of this solution, which closely resembles natural saliva, is (0.4 g NaCl, 0.4 g KCl, 0.6 g CaCl₂, 0.58 g Na₂HPO₄ 12H₂O, 1 g urea, and distilled water 1 L).
- 2) Base electrolyte (AS) + 100 ppm of NaF (AS+100F⁻).
- 3) Base electrolyte (AS) + 1000 ppm of NaF (AS+1000F⁻).
- 4) Commercial fluoridated mouth wash (MW) whose commercial fluoride content is 112 ppm.

All tests were carried out at $37\pm 1^\circ\text{C}$, under aerated conditions.

2.2. Microstructure characterization

Both cast and sintered specimens were mechanically polished with 1000 grit with SiC paper followed by a polishing with a 9 mm diamond suspension. Then they were etched with Kroll's reagent, consisting of 10 mL HF, 5 mL HNO₃ and 85 mL H₂O, and the revealed microstructure was examined by optical microscopy.

2.3. Active area determination for sintered alloys

The real active area of the sintered alloy was determined by optical microscopy measuring the average pore diameter and determining the percentage of pores per surface. The final active area was obtained by assuming that the pores are spherical, thus considering the area of a half sphere multiplied by the number of pores.

2.4. Electrochemical experiments

The electrochemical behavior of the titanium alloys was studied using a potentiostat (solatron1286) with three electrode configurations: a working electrode (the sample), a reference electrode (Ag/AgCl, 3 M KCl) and a platinum coiled wire acting as a counter electrode. All potentials were referred to the used reference electrode (205 mV versus Standard Hydrogen Electrode, SHE).

Potentiodynamic polarization curves of cast and sintered samples were carried out in all the electrolytes by scanning the potential from 1V to 3 V at a scan rate of 0.5 mV/s to assess the corrosion resistance by recording anodic and cathodic currents.

Several electrochemical parameters were calculated from the potentiodynamic curves: the corrosion potential (E_{corr}), the corrosion current density (i_{corr}) determined by the Tafel slope extrapolation and the corrosion passive current density (i_p), obtained by the measured current within the passive domain.

Potentiostatic tests were carried out by applying a constant potential of 0.2V within the passive domain of the alloys and measuring the response in current. The final passive current (i_{pass}) and the exchange charge (Q) was obtained from those experimental results.

2.5. Tribocorrosion experiments

The tribocorrosion tests were carried out, coupling the electrochemical cell to a ball on disk tribometer with the reference electrode no more than 1 cm away from the wear track. Only the upper surface of the samples (2.06 cm^2) was exposed to the electrolyte and the lower part was insulated and electrically connected to the potentiostat. The computer controlled tribometer applies a sliding motion through a ball (alumina ball 6 mm in diameter) on a flat disk (the titanium alloy). These tests were performed setting normal load, sliding velocity and sliding duration to 5 N (which corresponds to a maximum contact pressure of 960 MPa), 60 rpm and 1 h respectively.

Sliding tests were carried out either at Open Circuit Potential (OCP) of the titanium alloys, which is the difference in the electrical potential spontaneously established between the metal and the solution or at an applied passive potential of 0.2V. The experimental sequence consisted of:

- Cathodic cleaning by applying a potential of -1.1 V for 5 min.
- Applying potential (0.2 V) for 60 min or allowing the system to stabilize at OCP for 60 min.
- Sliding for 60 min while the polarization (0.2 V) is maintained or the OCP is measured.
- Sliding is stopped while the polarization (0.2 V) or the OCP is maintained for 20 min.

At the end of the tribocorrosion tests, the wear track and the alumina counterpart were examined using optical microscopy and Scanning Electron Microscopy (SEM). The wear track profile was acquired by profilometry (confocal microscope Olympus LEXT OLS3000).

3. Results

3.1. Microstructure and active area determination

The microstructure of Ti-6Al-4V alloy reveals $\alpha+\beta$ structure (**Figure 4.A1.1**). The casted microstructure consists of an elongated grain, the α -phase (light), and an intergranular β phase (outlined) (**Figure 4.A1.1a**). The sintered alloys show a lamellar microstructure with presence of pores (**Figure 4.A1.1b**). The average grain areas were 26 mm^2 and 176 mm^2 for the cast and sintered materials respectively.

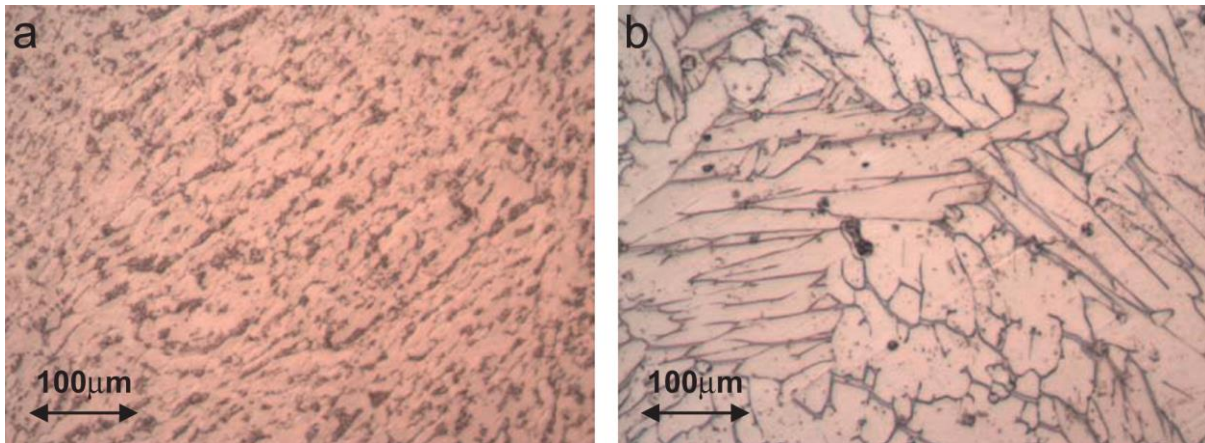


Figure 4.A1.1. Microstructure of the Ti6Al4V alloys: (a) casted and (b) sintered

The active area of the sintered samples is larger than of the cast ones. The total percentage of pores (5.7%) on the surface and the average diameter of a pore (0.11 mm) were determined and the active area was calculated assuming that the surface of a pore corresponds to half a sphere. Thus, the active area of the sintered alloy was 2.17 cm^2 , while the nominal area of the cast alloy is 2.06 cm^2 .

3.2. Potentiodynamic curves

The potentiodynamic curves of the cast and sintered Ti6Al4V are shown in **Figure 4.A1.2**. Four different domains were observed for the cast alloy (**Figure 4.A1.2a**). The cathodic domain includes potentials below 0.5 V, where the current is determined by the reduction of water and partially of dissolved oxygen. The domain between 0.5V and 0.2V is characterized by the transition from cathodic to anodic current at the corrosion potential. A large passive zone was found between the corrosion potential and 1V, where the current density remained approximately constant, except for the test carried out in the MW solution. Finally, a transpassive domain is observed in the tests carried out in the electrolytes with fluorides. The current density increases with the applied potential, at the highest applied potentials, due to the oxidation of water and oxides of the passive film.

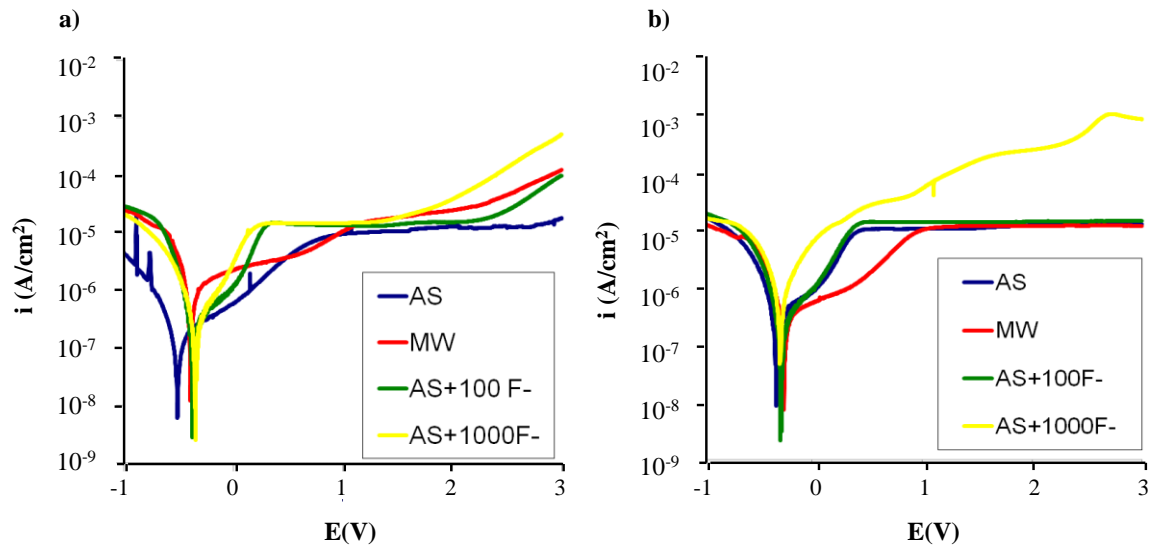


Figure 4.A1.2. Potentiodynamic curves for Ti6Al4V alloys: (a) casting and (b) PM in the studied solutions at 37 °C.

The sintered Ti6Al4V alloy only shows three potential domains in the potentiodynamic curves (**Figure 4.A1.2b**). All tests showed a cathodic domain at potentials below 0.5V, a transition from cathodic to anodic current at the corrosion potential around 0.3V and a large passive zone between 0.2 V to 3 V, where the current density remained constant. Only the sintered alloy in the AS+1000F⁻ solution shows a continuous increase in the current density with the applied potential from E_{corr} . No transpassive domain was observed in the PM alloy.

Table 4.A1.1- Electrochemical parameters for Ti6Al4V alloys in the studied solutions.

| Material | Solution | OCP(mV) | E_{corr} (mV) | i_{corr} ($\mu\text{A}/\text{cm}^2$) | i_p ($\mu\text{A}/\text{cm}^2$) |
|----------|-----------------------|---------------|------------------------|---|-------------------------------------|
| Cast | Saliva | -258 ± 50 | -512 ± 30 | 0.16 ± 0.05 | 18.1 ± 1 |
| | MW | -153 ± 8 | -394 ± 15 | 0.52 ± 0.1 | 23.1 ± 2 |
| | AS+100F ⁻ | -225 ± 20 | -365 ± 35 | 0.22 ± 0.07 | 39.4 ± 2 |
| | AS+1000F ⁻ | -186 ± 50 | -352 ± 50 | 0.30 ± 0.1 | 125 ± 5 |
| Sintered | Saliva | -267 ± 70 | -320 ± 50 | 0.42 ± 0.1 | 17.6 ± 1 |
| | MW | -108 ± 15 | -251 ± 25 | 0.39 ± 0.12 | 16.6 ± 1 |
| | AS+100F ⁻ | -84 ± 30 | -273 ± 30 | 0.33 ± 0.08 | 20.1 ± 2 |
| | AS+1000F ⁻ | -220 ± 60 | -284 ± 50 | 1.60 ± 0.1 | 1130 ± 4 |

Table 4.A1.1 shows the electrochemical parameters extracted from the potentiodynamic curves of the cast and sintered Ti6Al4V alloys. The cast alloy shows very similar E_{corr} values in all tested solutions, while the i_{corr} increases with the fluoride content and the highest i_{corr} values were found in the MW solution. Analogously, i_p values are higher in the fluoride containing solutions compared to the AS solution, which corresponds to a higher passive dissolution rate in presence of fluorides.

The corrosion potential of the PM alloys lies around 0.25 V in the fluoride containing solutions, while it is shifted towards lower values in the AS solution. With respect to the corrosion rates, the highest values were obtained in the AS solution. Small effect of fluoride content was observed in the i_{corr} of the sintered titanium alloys. The most important effect of fluorides on the electrochemical behavior of the sintered alloy was observed in the AS+100F⁻ solution, in which no passive plateau was detected.

E_{corr} of cast alloys are approximately 100 mV lower than the E_{corr} of sintered alloys, but the i_p values of the sintered alloys are slightly higher than the ones of the cast alloys.

3.3. Potentiostatic tests

Figure 4.A1.3 shows the current evolution versus time of the cast (**Figure 4.A1.3a**) and sintered (**Figure 4.A1.3b**) titanium alloys in the different solutions. In all cases an exponential decay in current with time was observed as the metal passivates, due to the oxide film growth. With respect to the fluoride effect, in the cast alloy, the increase in fluoride concentration increases the i_{pass} at the end of the potentiostatic tests, while they do not have a significant influence in the sintered alloy. In all cases, the test carried out in MW increases the electrochemical noise of the signal.

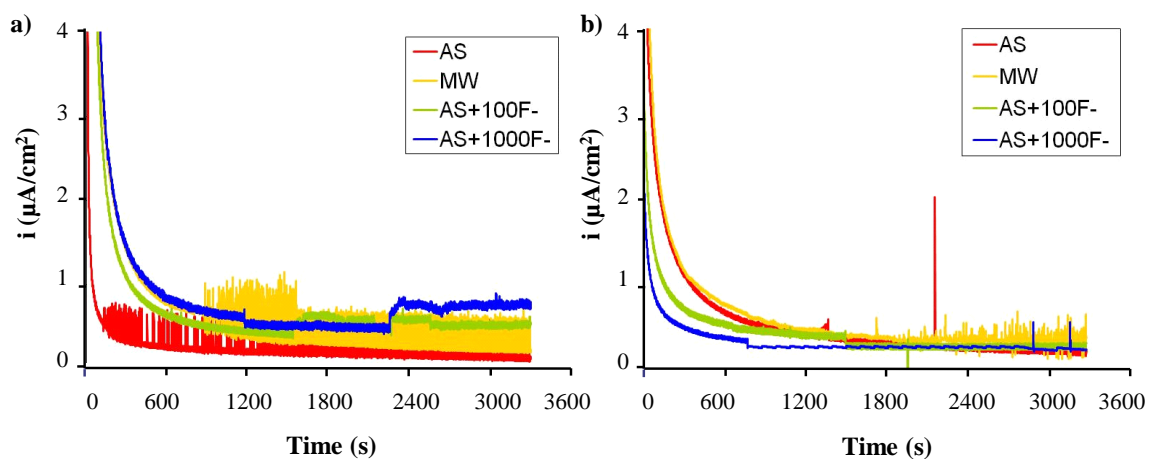


Figure 4.A1.3 Potentiostatic curves E0.2 V for Ti6Al4V alloys:
(a) casting and (b) PM in the studied solutions at 37 °C.

Table 4.A1.2 shows the Q and i_{pass} values obtained from the potentiostatic tests.

| Material | Solution | Q ($\text{C}/\text{cm}^2 \cdot 10^{-3}$) | i_{pass} ($\mu\text{A}/\text{cm}^2$) |
|----------|-----------------------|--|---|
| Cast | Saliva | 1.01 ± 1.4 | 0.13 ± 0.1 |
| | MW | 2.54 ± 1.2 | 0.20 ± 0.1 |
| | AS+100F ⁻ | 2.94 ± 1.7 | 0.55 ± 0.2 |
| | AS+1000F ⁻ | 4.80 ± 1.1 | 0.77 ± 0.1 |
| Sintered | Saliva | 3.25 ± 2.2 | 0.34 ± 0.2 |
| | MW | 3.55 ± 1.4 | 0.66 ± 0.1 |
| | AS+100F ⁻ | 3.48 ± 1.4 | 0.45 ± 0.2 |
| | AS+1000F ⁻ | 0.81 ± 1.9 | 0.36 ± 0.3 |

3.4. Tribocorrosion tests

The evolution of the open circuit potential (OCP) with time of the titanium alloys was monitored before, during and after the sliding and is shown in **Figure 4.A1.4**.

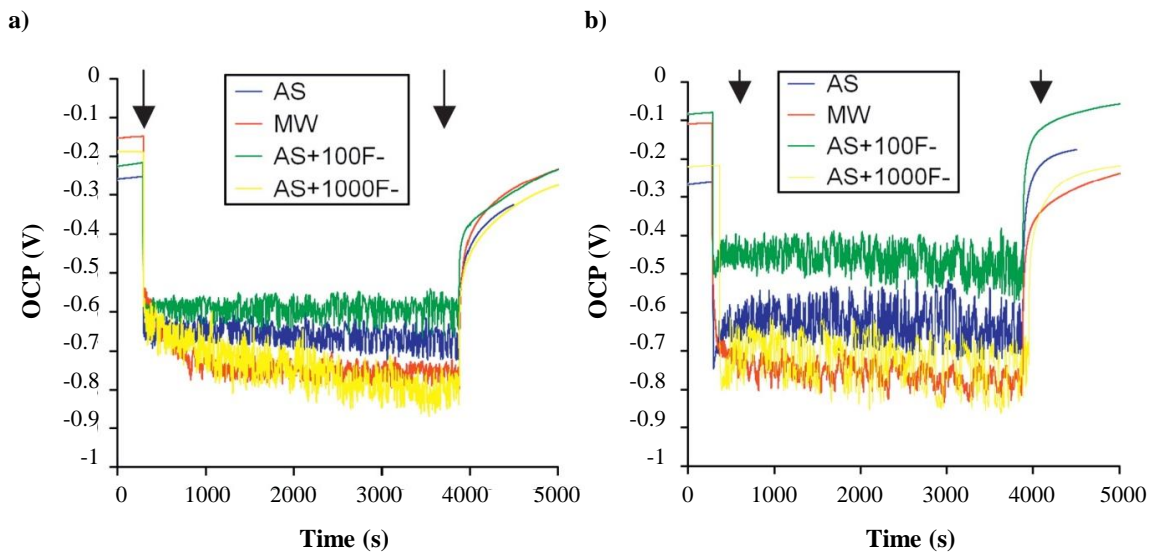


Figure 4.A1.4. OCP evolution with time during sliding of a smooth alumina ball against Ti6Al4V at OCP for (a) cast and (b) PM alloys. Arrows indicate the initiation and stop of sliding.

Before the initiation of sliding, the measured OCP reflects the presence of a passive film on the alloy surface in contact with the electrolytes. An abrupt decrease in potential is observed immediately after the initiation of the sliding, indicating a depassivation of the surface induced by the mechanical detachment of the passive film (depassivation), and the exposure of fresh active titanium to the lubricants.

During the sliding, the open circuit potential remains constant around the same low value, indicating that a depassivated state prevails in the wear track and that the alloy is not able to recover its passive state while mechanical perturbation is taking place. Indeed, in some cases (i.e., AS+100F⁻) OCP slightly decreases with time.

During the sliding period the potential shows transitions, with an amplitude of around 0.1 V for the cast samples and up to 0.2 V for the sintered samples, due to the establishment of a dynamic equilibrium between depassivation and repassivation mechanisms as a result of the periodic removal (depassivation) and growth (repassivation) of the passive film during the sliding

Finally, at the end of the sliding, the OCP exhibits an anodic shift, suggesting the occurrence of repassivation of the active area of the worn zone. Ideally, the corrosion potential recovers its original value established at the beginning of the test, or it is even slightly higher. This indicates that the newly formed passive film, grown after the removal of the original passive film during the sliding, has similar properties to the naturally formed film present on titanium before the mechanical action. However, the repassivation is not instantaneous and the initial OCP is only reached after longer rest times. It should be noticed that the recovery of the initial OCP values is faster in the sintered samples, except in the MW solution. None of the cast alloys recovered their original OCP at the end of the tribocorrosion tests, except in the AS+100F⁻ solution.

Table 4.A1.3 summarizes the average OCP values before, during and after the sliding. Initial values of the cast titanium alloy are lower than of the sintered alloy. The differences are more pronounced in the fluoride containing solutions. On the contrary, similar OCP values were established during sliding in both cast and sintered alloys, except in the AS+100F⁻ solution. Both materials show a slight increase in the OCPsliding with the fluoride content.

Table 4.A1.3 - Average values of the potential measured before (OCP₀), during (OCP_{sliding}) and after sliding (OCP_{final}) of the Ti6Al4V alloy sling against an alumina ball in diferent electrolytes. Normal force 5 N.

| Material | Solution | OCP ₀ (mV) | OCP _{sliding} (mV) | OCP _{final} (mV) |
|----------|-----------------------|--------------------------|--------------------------------|------------------------------|
| Cast | Saliva | -255±30 | -657±20 | -325±20 |
| | MW | -150±20 | -733±20 | -226±20 |
| | AS+100F ⁻ | -220±40 | -589±50 | -225±30 |
| | AS+1000F ⁻ | -188±20 | -742±30 | -268±30 |
| Sintered | Saliva | -264±10 | -627±8 | -176±30 |
| | MW | -108±20 | -754±10 | -232±40 |
| | AS+100F ⁻ | -81±20 | -459±20 | -54±50 |
| | AS+1000F ⁻ | -218±30 | -719±50 | -216±30 |

3.5. Anodic current during rubbing

Figure 4.A1.5 shows the current density evolution with time while sliding an alumina ball against cast and sintered Ti6Al4V disks in different lubricants at an applied constant potential. Before rubbing, the whole surface is passive and the anodic current (I_0) is low (below 1 mA). However, for both fabrication processes, there is a clear increase in the anodic current when the fluoride concentration in the electrolyte increases.

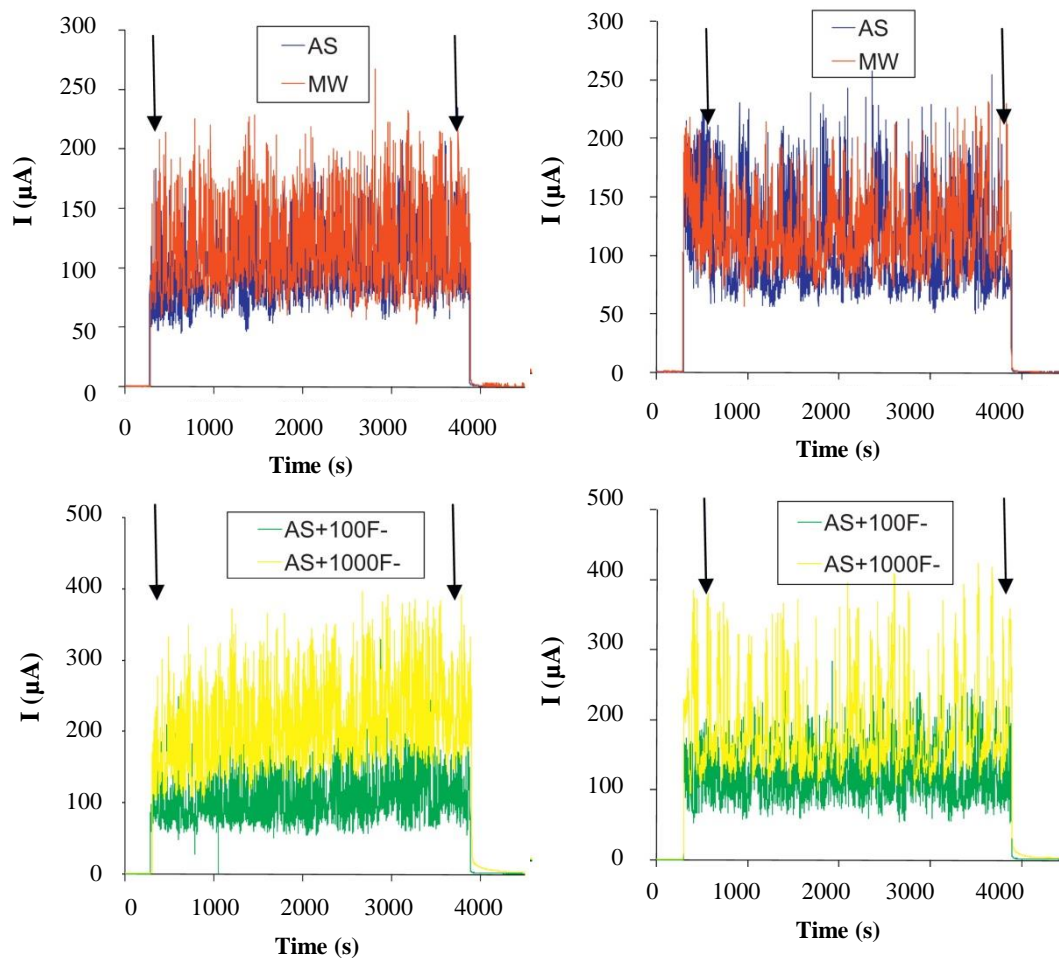


Figure 4.A1.5. Current evolution with time during sliding of a smooth alumina ball against Ti6Al4V alloys at imposed potential of 0.2 V for cast samples in (a) AS and MW, (b) AS+100F⁻ and AS+1000F⁻ and for sintered samples in (c) AS and MW, (d) AS+100F⁻ and AS+1000F⁻

At the onset of rubbing, the current exhibited a sharp increase and the steady state value was reached after a few seconds. After the first increase in current, arising from the mechanical removal of the passive film in the contact region when sliding starts, no significant variation in the current is observed during the tribocorrosion tests. The only exception to this behavior is the test carried out in the cast alloy in the AS+1000F⁻ electrolyte, which shows a slight current increase with time during sliding. The increase of the anodic current is much higher in the AS+1000F⁻ solution than in the other solutions, indicating that this lubricant has stronger corrosive action on fresh (depassivated) titanium surfaces than on the other ones, and that the alloy undergoes higher anodic dissolution. The current fluctuations are more visible in the AS+1000F⁻ solution. When the sliding is stopped, the current sharply decreased again to the value observed at the beginning of the tests, which suggests the occurrence of repassivation of the worn area of the sliding zone. It should be noticed that the recovery of the initial current density values is slower in the AS+1000F⁻ solution for both cast and sintered samples. Moreover, none of the samples recovered their original current density at the end of the tribocorrosion tests in the AS+1000F⁻ solution.

When the sliding is stopped, the current sharply decreased again to the value observed at the beginning of the tests, which suggests the occurrence of repassivation of the worn area of the sliding zone. It should be noticed that the recovery of the initial current density values is slower in the AS+1000F⁻ solution for both cast and sintered samples. Moreover, none of the samples recovered their original current density at the end of the tribocorrosion tests in the AS+1000F⁻ solution.

Table 4.A1.4 - Average values of the current density measured before (I_0), during ($I_{sliding}$) and after sliding (I_{final}) of the Ti6Al4V alloy sliding against an alumina ball in different electrolytes. Normal force 5 N.

| Material | Solution | $I_0(\mu A)$ | $I_{sliding}(\mu A)$ | $I_{final}(\mu A)$ |
|----------|-----------------------|--------------|----------------------|--------------------|
| Cast | Saliva | 0.42±0.1 | 132±12 | 0.68±0.2 |
| | MW | 0.55±0.1 | 114±5 | 0.89±0.3 |
| | AS+100F ⁻ | 1.11±0.3 | 102±6 | 1.41±0.4 |
| | AS+1000F ⁻ | 1.61±0.4 | 205±10 | 4.78±0.7 |
| Sintered | Saliva | 0.71±0.2 | 108±6 | 0.58±0.3 |
| | MW | 1.74±0.2 | 120±5 | 0.71±0.4 |
| | AS+100F ⁻ | 1.17±0.3 | 119±14 | 1.64±0.6 |
| | AS+1000F ⁻ | 2.27±0.2 | 179±21 | 4.35±0.7 |

Table 4.A1.4 summarizes the average values of the current density before, during and after the sliding in the tribocorrosion tests carried out at an applied passive potential. The current flowing in the wear track (I_{sliding}) was determined by subtracting from the current measured during sliding the value of the current measured before starting the sliding. The latter was assumed to correspond approximately to the current flowing through the area outside the wear track during sliding (the wear track area is much smaller than the total electrode area).

Fluoride ions increase the average values of the anodic current of both alloys during the sliding; however, it seems to be triggered from a minimum fluoride content of 100 ppm. Moreover, the I_{sliding} value is lower for the sintered alloy in the AS+1000F⁻ solution, which shows a higher resistance to the passive dissolution.

In a tribocorrosion system several mechanisms simultaneously take place generating material loss: wear accelerated corrosion (V_{chem}) and mechanical removal of particles (V_{mech}) in the wear track and corrosion (V_{corr}) outside the wear track. Therefore, the overall material loss can be expressed according to the following relationship:

$$V_{\text{tot}} = V_{\text{chem}} + V_{\text{mech}} + V_{\text{corr}} \quad (1)$$

Titanium alloys are passive and show very low passive dissolution rate and their material loss caused by corrosion outside the wear track can be neglected so that the overall material loss is simplified by the sum of the mechanical and wear accelerated corrosion volumes ($V_{\text{tot}} = V_{\text{mech}} + V_{\text{chem}}$).

The material loss removed by anodic oxidation in the wear track, V_{chem} was calculated from the measured current using Faraday's law:

$$V_{\text{chem}} = (I_{\text{sliding}} \times t \times M) / (n \times F \times \rho) \quad (2)$$

where M is the atomic mass of the alloy (46.64), n is the charge number for the oxidation reaction (valence of oxidation was assumed 4), F is the Faraday constant (96500 C/mol), ρ is the density of the alloy equal to 4.43 g/cm³ and t is the duration of sliding, 3600 s. The total wear volume, V_{tot} was determined geometrically by confocal microscopy through the measurement of five different profiles of the wear track. The area of an average cross section of the wear track multiplied by the length of the track gives one the V_{tot} .

The obtained V_{chem} values are listed in **Table 4.A1.5**, together with the mechanical wear volume (V_{mech}) and total wear volume (V_{tot}). V_{mech} , removed by tribocorrosion, is obtained by the difference between V_{tot} and V_{chem} .

Table 4.A1.5 - Average wear volumes ($\times 10^{-3}$) expressed in mm^3 .

| Electrolyte | Potential | Volume | Cast | Sintered |
|-----------------------|-----------|------------|--------|----------|
| AS | OCP | V_{tot} | 87±25 | 63±22 |
| | | V_{tot} | 97±22 | 108±26 |
| | 0.2V | V_{chem} | 12±1 | 11±2 |
| | | V_{mech} | 85±21 | 97±24 |
| MW | OCP | V_{tot} | 101±15 | 123± |
| | | V_{tot} | 205±21 | 132±20 |
| | 0.2V | V_{chem} | 11±1 | 12±1 |
| | | V_{mech} | 194±20 | 120±20 |
| AS+100F ⁻ | OCP | V_{tot} | 99±18 | 87±15 |
| | | V_{tot} | 119±28 | 105±25 |
| | 0.2V | V_{chem} | 9±1 | 12±2 |
| | | V_{mech} | 110±27 | 93±23 |
| AS+1000F ⁻ | OCP | V_{tot} | 120±24 | 127±22 |
| | | V_{tot} | 130±10 | 138±5 |
| | 0.2V | V_{chem} | 20±2 | 17±2 |
| | | V_{mech} | 110±10 | 121±5 |

At an applied potential, V_{tot} of both cast and sintered alloys are similar in the studied lubricants except in MW and show a slight increase with the fluoride concentration. With respect to the V_{chem} values, it only represents a small percentage of the total wear, in comparison to the mechanical wear in all electrolytes. In the AS solutions V_{chem} represents 5% of the total wear volume, in both cast and sintered alloys. With respect to the fluoride effect, in the cast alloy, the increase of fluoride concentration only increases the V_{chem} value up to 6.6% when adding 1000 ppm of fluoride, whereas it does not show any effect at lower fluoride contents. For the sintered alloys the increase of the V_{chem} depending on the fluoride concentration is higher. The V_{chem} is 5.5% and 8.4% of the V_{tot} in the electrolytes with 100 ppm and 1000 ppm of fluoride respectively. For both alloys V_{chem} noticeably increases for a fluoride concentration higher than 100 ppm.

At OCP, V_{tot} was also calculated by measuring the wear track profiles at the end of the tribocorrosion tests and multiplying them by the length of the wear track. Under those equilibrium conditions, no wear accelerated corrosion was measured; thus, V_{tot} is the total wear damage considered. At OCP, V_{tot} of cast and sintered alloys are similar in all media. V_{tot} slightly increases with the increase in the fluoride concentration. V_{tot} at OCP is smaller than at applied passive potential.

3.6. Wear morphology

The morphology of the wear tracks on the Ti6Al4V alloys were evaluated using optical and SEM microscopy. **Figure 4.A1.6** shows the SEM images of the wear tracks of the cast and sintered Ti6Al4V alloys at the end of the tribocorrosion tests in the different dissolutions. They show a predominant adhesive wear at OCP and applied anodic potential. Delamination was observed in presence of fluoride. A small amount of isolated wear debris is observed on all worn surfaces. The size and amount of particles on the track diminishes with the fluoride content, inside and outside the track (**Figure 4.A1.7 and 8**).

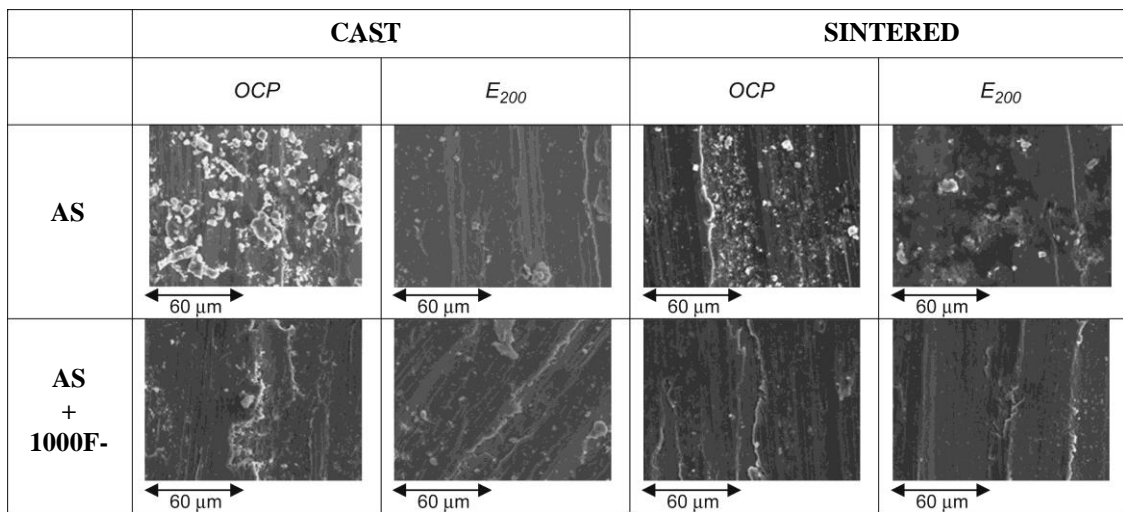


Figure 4.A1.6. SEM images of the center of the wear tracks in different electrolytes at OCP and E200. Normal load 5 N

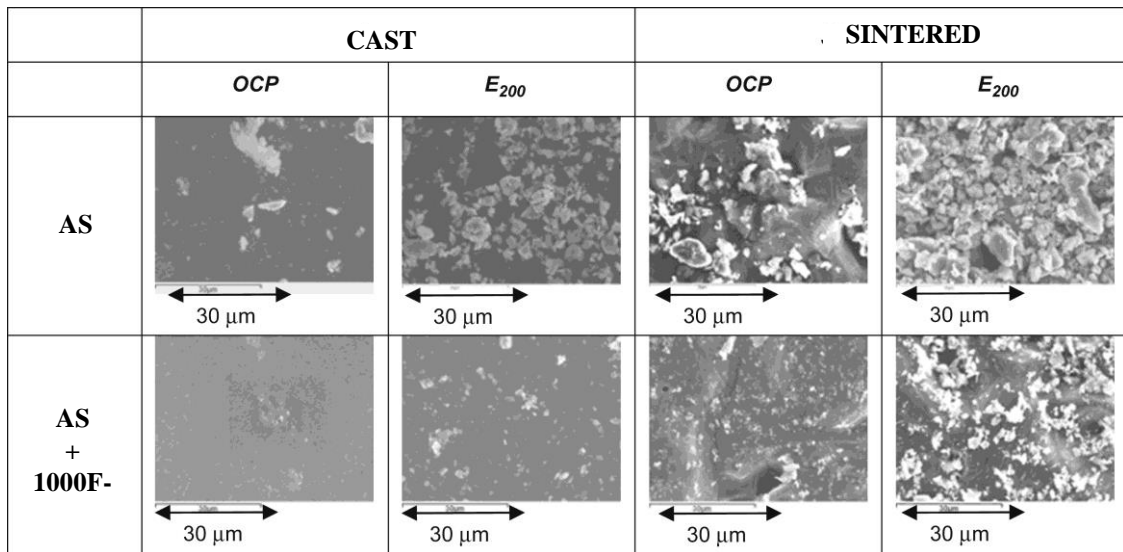


Figure 4.A1.7. SEM images outside the wear tracks in different electrolytes at OCP and E200. Normal load 5 N.

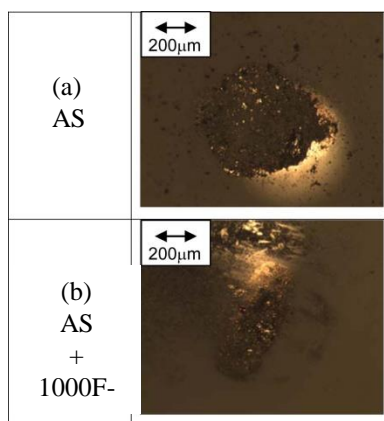


Figure 4.A1.8. Optical images of the alumina balls sliding against the Ti6Al4V alloy in (a) AS and (b) AS+1000F⁻

In all cases, the optical images of the alumina ball showed material transfer from the titanium samples. The material transfer diminishes in presence of fluorides.

4. Discussion

4.1. Effect of potential

At all studied potentials the metal surface suffers the same wear mechanism. The first step for the metal degradation consists of smearing of the material over the rubbed area, followed by the fragmentation of the smeared layer (third body) and formation of debris particles. These particles can be either smeared again or ejected from the contact.

However, the oxidation of the third body can affect this wear mechanism. The wear volumes measured in experiments at OCP and passive conditions are shown in **Table 4.A1.5**. These results show higher wear volumes at applied passive potential than at OCP. Barril (2005) suggested that the wear increases with potential. According to them, at anodic potential, the third body layer is formed of densely packed oxide particles, which gives the mechanical behavior resembling a solid film. When a critical thickness is exceeded, this third body oxide film can break away from the contacting surfaces, which would lead to ejection of oxidized wear debris from the contact (Barril, 2005). Milosev et al. (2000) studied the oxide film formation on Ti6Al4V in physiological solution and determined the film thickness as a function of the applied potential. From their results, a film thickness of 5 nm was measured at 0.2V, while at potentials below 0.25V (which corresponds to the average OCP values) titanium was mainly considered to be in its metallic state. Therefore, the difference in wear damage can be explained by the formation of a passive film which increases wear.

The OCP is measured when the net current flowing through the system is zero; however, under tribocorrosion conditions, when sliding starts, a galvanic pair is formed between the depassivated (wear track) and the rest of the passive area, which generates an acceleration of the corrosion processes taking place in the rubbed surface. A galvanic current flows from the anode (wear track) through the solution to the cathode, where the electrons are consumed by the reduction reaction. Vieira et al. (2012) proposed a simple model which relates the potential of the cathode (passive area) with electrochemical parameters (i.e., Tafel coefficients and corrosion potential) and the area ratio of the anode and the cathode. According to their model, the anodic current (i_a) can be estimated from **Eq. (3)** and thus the wear accelerated corrosion at OCP can be obtained.

$$\log i_a = (E_{\text{corr}} - E_c + a_c - b_c \log(A_a/A_c)) / b_c \quad (3)$$

where a_c and b_c are kinetic parameters of the reduction reaction (Tafel constants), A_a and A_c are the surface areas of the depassivated and passive zones respectively and i_a is the anodic current density (wear accelerated corrosion rate) established in the worn areas. Applying this approach to the titanium system, the calculated anodic current of the sintered alloys is between one or two orders of magnitude higher than the cast alloys. The loss of passivity caused by the mechanical removal of the passive film during sliding modifies the electrochemical conditions within the contact, generating a wear accelerated corrosion which depends on the solution chemistry and the material properties. Clearly, electrolytes with a fluoride content higher than 100 ppm accelerate the corrosion process, thus increasing the wear accelerated corrosion. However, this situation does not lead to a higher wear volume of the sintered alloys.

4.2. Effect of fluoride ions

Figure 4.A1.9 show the equilibrium diagrams of the fluoride species and the concentration of those compounds at different pH values according to the following equilibrium acidic constants (K_H) of the fluorhydric acid.



The assumption was made that the electrochemical reaction of fluorides on titanium is slower than the acid–base equilibriums. Consequently, the concentrations of the different fluoride species were supposed to be controlled by the acid–base equilibrium (expressed as dissociation reactions) and the corresponding acidic constant of deprotonation equilibrium is given in the following equation:

$$K_H = [\text{H}^+][\text{F}^-] / [\text{HF}] \quad (5)$$

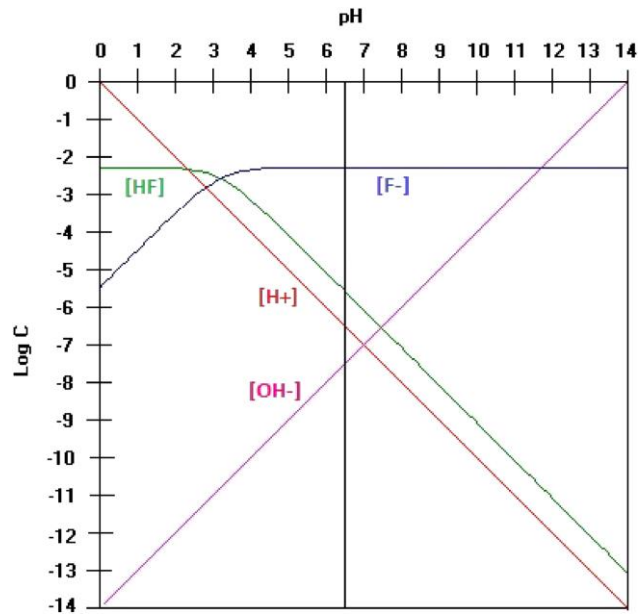


Figure 4.A1.9. Equilibrium diagram of the species in the NaF solutions at 52 different pH values, where C is the molar concentration.

According to the equilibrium and in the AS+100F⁻, the concentrations of the involved species are 3×10^{-7} M for [H⁺], 3×10^{-8} M for [OH⁻], 5.6×10^{-3} M for [F⁻] and 2.6×10^{-6} for [HF]. In AS+1000F⁻, the [F⁻] and the [HF] are 10 times higher. According to Nakagawa et al. (1999), in acidic conditions, 30 ppm of HF could lead to the destruction of the passive film on a titanium surface. Since the pH of the electrolyte used in the present study is 6.5, the concentration of HF is much lower than 30 ppm. Kwon et al. (2005) also confirmed that for the low HF concentrations the passive oxide layer on titanium alloys remains stable. The occurrence of active-passive transition in presence of 100, 112 and 1000 ppm of fluoride ions confirms the ability of the cast and sintered Ti6Al4V alloys to impart passivity. The spontaneous passivity in all the studied solutions is also observed by the OCP values. Cast and sintered alloys showed a shift in OCP to slightly more noble values as the fluoride content of the solution increases from 0 to 1000 ppm. This potential shift is attributable to the formation of a barrier film on the metal surface (Blackwood et al., 2000). This suggests that fluoride ions did not hinder the formation of oxide layer on the electrode surface, even for high fluoride concentration, as reported by Wigg et al. (1993). In the passive domain, i_p is found to increase from 18.1 to 125 mA/cm² and from 17.6 to 1130 mA/cm², with increase in fluoride ion concentration from 0 to 1000 ppm for cast and sintered samples respectively. The anodic current density in the passive region depends on the charge transfer resistance through the surface passive film, which may form spontaneously on corrosion resistant metals. A lower anodic current density represents higher charge transfer resistance through the passive film. Huang (2003) has also reported an increase of passive current density of Ti6A4V with the increase in fluoride ions in the electrolyte. According to Kumar and Sankara Narayanan (2008) and Kumar et al. (2010), the increase in i_p may be due to the dissolution of the alloying

element, induced by fluoride ions present in the medium and to the electro-chemical reaction of the sample in the electrolyte with the formation of a porous or defective oxide layer. Reclaru and Meyer (1998) have also reported that the dissolution of Ti in the presence of fluoride is due to the formation of the Ti-F complex, $[\text{TiF}_6]^{2-}$ that form soluble salts with alkaline metals. Huang (2003) has identified the formation of Na_2TiF_6 on the surface of the Ti6Al4V alloy immersed in acidic artificial saliva (pH: 5) containing 0.1 wt% of NaF, by XPS. Hence, it is evident that the addition of NaF to 0.15 M NaCl would lead to the incorporation of fluoride ions in the passive oxide layer of Ti and its alloys, resulting in the formation of a porous layer. Depending on the concentration of NaF and the pH, titanium fluoride, titanium oxyfluoride or sodium titanium fluoride could form on the surface of the titanium alloys (Huang, 2003; Nakagawa et al., 2001 and Reclaru and Meyer, 1998).

Under tribocorrosion conditions, the wear accelerated corrosion quantified through the measurement of the excess in current during rubbing at an applied passive potential was increased with the increase in the fluoride content, more significantly above 100 ppm. In the same sense, OCP values during sliding dropped to lower values in the AS+1000F⁻ solution. The average $\text{OCP}_{\text{sliding}}$ values were around 0.75 V in MW and AS+1000F⁻, between 0.1 and 0.2V lower than the $\text{OCP}_{\text{sliding}}$ values in AS and AS+100F⁻. This shift in potential leads to a higher wear accelerated corrosion in MW and AS+1000F. Therefore, fluoride content influences the wear accelerated corrosion of titanium alloys at very low fluoride concentrations and this effect is triggered from a minimum concentration of 100ppm in good agreement with the increase of the dissolution rate observed from the corrosion tests, potentiodynamic curves. These phenomena are related to the electrochemical behavior of the alloys in the active region, in which the fluoride reduces the charge transfer resistance (**Figure 4.A1.2**). The effect is higher in the cast alloy.

The wear volume has the same tendency of slightly increasing with the fluoride content for both tribocorrosion tests carried out at OCP and at the applied potential of 0.2V. The mechanical and chemical contributions to the total wear loss have been determined for the tests carried out at 0.2V and the mechanical volume is 90% of the total material loss, while the remaining 10% is due to the chemical contribution (**Table 4.A1.5**). In general, the higher the V_{chem} , the higher the VT.

A large number of debris are observed on the outside of the sliding zone for both Ti6Al4V alloys. This results from the grinding of trapped debris between contacting surfaces. However, a decrease in the amount of debris with the fluoride content is observed at the same time as a reduction of material transfer on the alumina ball. According to Sivakumar et al. (2011), it is due to a change in contact between the material and the alumina ball which decreases the extent of trapping and grinding of the wear debris. The lower size of wear debris observed when the fluoride ions concentration increases is correlated to the metal dissolution resulting from the presence of an increasing concentration of

fluoride in the electrolyte. This observation is in good agreement with previous results concerning the chemical volume loss and the subsequent increase in total wear volume in presence of fluorides.

4.3. Effect of the fabrication process

The fabrication process slightly affects the electrochemical behavior of the Ti6Al4V alloys in the different testing dissolutions. The electrochemical tests at an applied constant potential show a lower charge transfer (Q) and also a lower passive current density (i_{pass}) for the sintered alloys in all electrolytes with fluoride. This implies that the sintered alloy is more resistant to passive dissolution in a fluorinated media in comparison to the cast one. The potentiodynamic curves for the sintered material, showed on one hand a higher E_{corr} value in all the solutions and on the other hand a lower current density (i_p) in the solution with a fluoride content lower than 100ppm. According to Blackwood et al. (2000), the protective oxide film on porous specimens initially fails within the depths of the pores, as the oxide film is thinner. This would explain the absence of plateau and the i_p value six times higher than for cast in the solution with 1000 ppm of fluoride.

The fabrication process has also a small influence on the tribocorrosion behavior of titanium alloys and it also depends on solution chemistry and electrode potential. At OCP the sintered alloys show lower wear volume in the tests carried out in AS and AS+100F⁻ and higher wear accelerated corrosion in all solutions than the cast alloys. The constant sliding of the alumina ball over the material results in the formation of a tribolayer formed of the passive layer that is being removed as well as some bare (raw) underlying material. The sintered material has pores which walls (surface) are covered by a passive layer. On one hand, this implies that there is more passive layer incorporated in the tribolayer of the sintered material in comparison to the cast material. On the other hand, as the material is being removed, the underlying pores, which have a passive layer, are exposed to the test solution. Therefore, it could explain why the wear accelerated corrosion of the sintered material is higher than the cast alloys.

At an applied passive potential V_{mech} of sintered alloys are slightly higher than the material loss of the cast alloys due to the higher asperities obtained during the powder metallurgy.

5. Conclusions

Corrosion and tribocorrosion behavior of the Ti6Al4V alloy obtained by two different fabrication processes (cast and powder metallurgy) has been studied in artificial saliva (with and without fluorides) and the following conclusions can be extracted:

- Ti6Al4V alloy spontaneously passivates in all the electrolytes independently of the fluoride content, which only increases its passive dissolution at concentrations above 1000 ppm at pH 6.5.
- Wear damage is mainly due to the mechanical action and fluorides increase the wear accelerated corrosion at high concentrations, which produce an increase in the total wear damage.
- Potential increases the wear damage caused by the cyclic removal of the passive film.
- Sintered alloys show a promising behavior under tribocorrosion conditions for implant applications.

6. References

- A.M. Al-Mayouf, A.A. Al-Swayih, Al-Mobarak, N.A., Al-Jabab, A.S. Corrosion behavior of a new titanium alloy for dental implant applications in fluoride media. *Materials Chemistry and Physics* 86 (2004) 320–329.
- Assad, M., Lemieux, N., Rivard, C.H., Yahia, L.H., 1999. Comparative in vitro biocompatibility of nickel–titanium, pure nickel, pure titanium, and stainless steel: genotoxicity and atomic absorption evaluation. *Bio-Medical Materials and Engineering* 9, 1–12.
- Barril, S., 2005. Electrochemical effects on the fretting corrosion behavior of Ti6Al4V in 0.9% sodium chloride solution. *Wear* 259, 282–291.
- Blackwood, D.J., Chua, A.W.C., Seah, K.H.W., Thampuran, R., Teoh, S.H., 2000. Corrosion behavior of porous titanium–graphite composites designed for surgical implants. *Corrosion. Science* 42, 481–503.
- Boere, G., 1995. Influence of fluoride on titanium in an acidic environment measured by polarization resistance technique. *Journal of Applied Biomaterials* 6, 238–283.
- Bundy, K.J., Luedemann, R.E., 1987. Characterization of the corrosion behavior of porous biomaterials by A–C impedance techniques. In: Lemons, J.E. (Ed.), *Quantitative Characterization and Performance of Porous Implants for Hard Tissue Applications*. American Society for testing and Materials, Philadelphia, pp. 137–150 (ASTM STP 953).
- Frateur, I., Cattarin, S., Marco Musiani, M., Tribollet, B., 2000. Electrodeposition of Ti and p-Si in acidic fluoride media: formation ratio of oxide layers from electrochemical impedance spectroscopy. *Journal of Electroanalytical Chemistry* 482, 202–210.
- Huang, H.H., 2002. Effects of fluoride concentration and elastic tensile strain on the corrosion resistance of commercially pure titanium. *Biomaterials* 23, 59–63.
- Huang, H.H., 2003. Effects of fluoride and albumin concentration on the corrosion behavior of Ti 6Al–4V alloy. *Biomaterials* 24, 275–282.
- Kaneko, K., Yokoyama, K., Moriyama, K., Asaoka, K., Sakai, J., Nagumo, M., 2003. Delayed fracture of beta titanium orthodontic wire in fluoride aqueous solutions. *Biomaterials* 24, 2113–2120.
- Kononen, M.H., Lavonius, E.T., Kivilahti, J.K., 1995. SEM observations on stress corrosion cracking of commercially pure titanium in a topical fluoride solution. *Dental Materials* 11, 269–272.

Kwon, Y.H., Seol, H.J., Kim, H.I., Hwang, K.J., Lee, S.G., Kim, K.H., 2005. Effect of acidic fluoride solution on b-titanium alloy wire. *Journal of Biomedical Materials Research Part B Applied Biomaterials* 73, 285–290.

Kumar, Satendra, Sankara Narayanan, T.S.N., 2008. Corrosion behaviour of Ti–15Mo alloy for dental implant applications. *Journal of Dentistry* 36, 500–507.

Kumar, S., Sankara Narayanan, T.S.N., Saravana Kumarb, S., 2010. Influence of fluoride ion on the electrochemical behaviour of b-Ti alloy for dental implant application. *Corrosion Science* 52, 1721–1727.

Lausmaa, J., Kasemo, B., Hansson, S., 1985. Accelerated oxide grown on titanium implants during autoclaving caused by fluorine contamination. *Biomaterials* 6, 23–27.

Lucas, L.C., Lemons, J.E., Lee, J., Dale, P., 1987. In vitro corrosion of porous alloys. In: Lemons, J.E. (Ed.), *Quantitative Characterization and Performance of Porous Implants for Hard Tissue Applications*. American Society for testing and Materials, Philadelphia, pp. 124–136 (ASTM STP 953).

Milosev, I., Metikos-Hukovic, M., Strehblow, H.H., 2000. Passive film on orthopaedic TiAlV alloy formed in physiological solution investigated by X-ray photoelectron spectroscopy. *Biomaterials* 21, 2103–2113.

Mimura, H., Miyagawa, Y., 1996. Electrochemical corrosion behavior of titanium castings: part 1. Effects of degree of surface polishing and kind of solution. *The Journal of the Japanese Society for Dental Materials and Devices* 15, 283–285.

Nakagawa, M., Matsuya, S., Shiraishi, T., Ohta, M., 1999. Effect of fluoride concentration and pH on corrosion behavior of titanium for dental use. *Journal of Dental Research* 78, 1568–1572.

Nakagawa, M., Matsuya, S., Udoh, K., 2001. Corrosion behavior of pure titanium and titanium alloys in fluoride-containing solutions. *Dental Materials Journal* 20, 305–314.

Nakagawa, M., Matsuya, S., Udoh, K., 2002. Effects of fluoride and dissolved oxygen concentrations on the corrosion behavior of pure titanium and titanium alloys. *Dental Materials Journal* 21, 83–92.

Oda, Y., Kawada, E., Yoshinari, M., Hasegawa, K., Okabe, T., 1996. The influence of fluoride concentration on the corrosion of titanium and titanium alloys. *The Journal of the Japanese Society for Dental Materials and Devices* 15, 317–322.

Probster, L., Weili, L., Huttemann, H., 1992. Effect of fluoride prophylactic agents on titanium surfaces. *International Journal of Oral and Maxillofacial Implants* 7, 390–394.

Reclaru, L., Meyer, J.-M., 1998. Effects of fluorides on titanium and other dental alloys in dentistry. *Biomaterials* 19, 85–92.

Schiff, N., Grosgeat, B., Lissac, M., Dalard, F., 2002. Influence of fluoride content and pH on the corrosion resistance of titanium and its alloys. *Biomaterials* 23, 1995–2002.

Siirila, H.S., Kononen, M., 1991. The effect of oral topical fluorides on the surface of commercially pure titanium. *International Journal of Oral and Maxillofacial Implants* 6, 50–54.

Sivakumar, B., Kumar, S., Sankara Narayanan, T.S.N., 2011. Fretting corrosion behaviour of Ti–6Al–4V alloy in artificial saliva containing varying concentrations of fluoride ions. *Wear* 270, 317–324.

Strietzel, R., 1998. In vitro corrosion of titanium. *Biomaterials* 19, 1495–1499.

Toumelin-Chemla, F., Rouelle, F., Burdairon, G., 1996. Corrosive properties of fluoride-containing odontologic gels against titanium. *Journal of Dentistry* 24, 109–115.

Vieira, A.C., Rocha, L.A., N. Papageorgiou, N., S. Mischler, S., 2012. Mechanical and electrochemical deterioration mechanisms in the tribocorrosion of Al alloys in NaCl and in NaNO₃ solutions. *Corrosion Science* 54, 26–35.

Wigg, P., Ellingsen, J.E., Videm, K., 1993. Corrosion of titanium by fluoride. *Journal of Dentistry Research* 72, 195.

Zitter, H., Plenk, H., 1987. The electrochemical behavior of metallic implant materials as an indicator of their biocompatibility. *Journal of Biomedical Material Research* 21, 881–896.

-Article 2-

TRIBOCORROSION MECHANISMS OF Ti6Al4V BIOMEDICAL ALLOYS IN ARTIFICIAL SALIVA WITH DIFFERENT PHS

M.P. Licausi, A. Igual Muñoz, V. Amigó Borrás

Journal of Physics D: Applied Physics, **46** (2013) 404003 (10pp)

doi:10.1088/0022-3727/46/40/404003

TRIBOCORROSION MECHANISMS OF Ti6Al4V BIOMEDICAL ALLOYS IN ARTIFICIAL SALIVA WITH DIFFERENT PHS

M.P. Licausi¹; A. Igual Muñoz^{2*}, V. Amigó Borrás¹

1-Institute of Materials Technology, Universidad Politécnica de Valencia, P.O. BOX 22012, E-46071, Valencia, Spain

2-Institute for Industrial, Radio physical and Environmental Safety, Universidad Politécnica de Valencia, P.O. BOX 22012, E-46071, Valencia, Spain

*Corresponding author

Abstract

Titanium and its alloys has been widely used for the design of dental implants because of its biocompatibility, mechanical properties and corrosion resistance. The powder-metallurgy process is a promising alternative to the casting fabrication process of titanium alloys for bone implants design as the porous structure mimics the natural bone structures, allowing the bone to grow into the pores which results in a better fixation of the artificial implant. However, under in vivo conditions the implants are subjected to tribocorrosion phenomenon, which consists in the degradation mechanisms due to the combined effect of wear and corrosion. The aim of this study is to evaluate the tribocorrosion behaviour of cast and sintered Ti6Al4V biomedical alloy for dental applications using the cast material as reference. Titanium samples were tested in artificial human saliva solution with three different pHs (3, 6, 9) and in an acidic saliva with 1000 ppm fluorides (AS-3-1000F⁻) by different electrochemical techniques (potentiodynamic curves, potentiostatic tests and tribo-electrochemical tests). Cast and sintered titanium alloys exhibit the same tribocorrosion mechanisms in AS independently of the pH which consists in plastic deformation with passive dissolution, but the addition of fluorides to the acidified solution changes the degradation mechanism towards active dissolution of the titanium alloys.

Keywords: Tribocorrosion, titanium, wear, powder metallurgy, pH

Introduction:

Titanium has been widely used to design dental implants because of its biocompatibility and corrosion resistance [1–5]. Commercially pure titanium (CP-Ti) was initially used for biomedical applications [6, 7], however, due to its low strength, difficulty in polishing, and poor wear resistance [8] other titanium alloys were developed. Originally Ti6Al4V alloy was used as an aeronautical material and, because of its higher strength and better corrosion resistance when compared to CP-Ti, it was tested to substitute the pure metal [9] in other applications. One of the problems of the Ti6Al4V alloy for biomedical applications is that it has an elastic modulus much higher than the bone. Porous titanium obtained by powder metallurgy has become a popular surgical implant material [10, 11] since it has a low elastic modulus that encourages regular bone growth, whilst its porosity enables bone in-growth, when compared to the cast alloy.

Corrosion resistance of titanium alloys in aqueous media is due to the formation of a stable and tightly adherent thin protective titanium oxide layer on its surface [12–14] which spontaneously covers the metal surface and is around 1–4 nm thick [16–19]. The stability of the passive film depends on its composition and structure, which are also dependent on the conditions under which it is formed [12–15].

Despite these good corrosion properties, when placed in the mouth cavity, implants are in contact with the body tissues for years, thus long-term corrosion behaviour is of crucial importance because it can adversely affect the biocompatibility and the mechanical integrity of implants [12, 20, 21]. The oral bacteria metabolization and the utilization of fluoride in the oral solutions are two main factors that might affect the corrosion phenomenon. The local pH in the mouth can reach acidic values due to the production of fermentable carbohydrates (i.e. lactic, acetic or propionic acids) [22], and this influences the corrosion resistance of Ti and its alloys [23]. On the other hand fluoride therapy is now recognized as being one of the main methods in preventing dental caries. The combined effect of these two factors creates a local acidic fluoride environment and promotes the existence of hydrofluoric acid (HF) which may dissolve the protective oxide layer on the titanium surface and its alloys [24], thus enhancing corrosion.

The corrosive nature of the physiological environment and the action of movements between the metal components and the bone accelerate the material degradation leading to tribocorrosion [25], a situation where materials are exposed to the combined action of corrosion and wear [26]. Tribocorrosion can be defined as the degradation of a tribological contact which results from the combined effect of the metal removal by mechanical wear and by electrochemical oxidation. These simultaneous mechanical and electrochemical phenomena taking place in the contact zone do not act independently but depend on each other in a complex manner [27]. Namely, the mechanical disruption of surface films on passivating materials can enhance the corrosion rate of the uncovered

metal, while the presence of these passive films can affect the mechanical properties of the surface and the behaviour of third bodies in the contact [28]. The repeated removal of oxide films produces wear and corrosion products, i.e. wear debris and metal ions. Extensive release of ions from implants can result in adverse biological reactions, and can lead to mechanical failure of the device [12, 13, 29]. Also, the release of wear debris may lead to cellular damage, inducing inflammation or encapsulation of the implant by fibrous tissue [21]. A high wear resistance and an ability to repassivate at a high rate can minimize the alloys' susceptibility to tribocorrosion. A better insight into the tribocorrosion behaviour of metals in biological environments is a prerequisite for the biological compatibility of metallic implants. Therefore, an approach combining both electrochemistry and tribology is needed to study these complex phenomena and to screen candidate biomaterials [30].

In this study, the influence of the fabrication process (cast and powder metallurgy) on the corrosion and tribocorrosion behaviour of the Ti6Al4V titanium biomedical alloy in artificial saliva was investigated. The influence of the pH of the solution and the fluoride content in the acidic saliva was also studied.

1. Experimental

1.1 Materials and electrolytes

Cast titanium samples, $20 \times 20 \times 2 \text{ mm}^3$ in size, were cut from a sheet of commercially available Ti6Al4V (Grade5) (chemical composition in wt% N: 0.02; C: 0.03; H: 0.011; Fe: 0.22; O: 0.16; Al: 6.12; V: 3.93). Specimens were wet-ground with 220 to 4000 grit silicon carbide paper and further polished with OP-Chem polishing cloths using the OP-S colloidal silica suspension to a mirror like finishing ($R_a = 0.05 \pm 0.01 \mu\text{m}$).

Care was taken during polishing to avoid any influence in the oxidation kinetics/mechanism of the titanium samples due to the extent of plastic deformation. After polishing, the samples were rinsed in deionized water and dried using a stream of compressed air.

The sintered titanium material was fabricated by powder metallurgy according to the following procedure: powder compression, applying a compacting pressure of 400 MPa without the addition of any lubricant and sintering sequence consisting in a thermal cycle with specific heating and cooling ramps. The initial heating ramp consists in heating at $800 \text{ }^\circ\text{C}$ during 30 min in order to stabilize both the oven and the material at the same temperature and to avoid cracking due to thermal gradients. The sintering process lasts 2 h at $1250 \text{ }^\circ\text{C}$ in a vacuum tube oven.

The chemical composition of the sintered powder is the same as the cast alloy so that both final materials have the same alloying elements. Detailed microstructural characterization of the alloys was carried out in a previous paper [31].

Before use, the sintered samples were cleaned with acetone in an ultrasonic bath in order to remove any existing particle from the pores. The samples were not polished and had a roughness of $R_a = 1.7 \pm 0.2 \mu\text{m}$. The sintered and cast titanium alloys were tested in four different electrolytes which simulate the human saliva at different pHs.

(1) A modified Fusayama Meyer artificial saliva (AS) as the base electrolyte. The composition of this solution, which closely resembles natural saliva, is: 0.4 g NaCl, 0.4 g KCl, 0.6 g CaCl₂, 0.58 g Na₂HPO₄ 12H₂O, 1 g urea, distilled water at 1 L. The pH of the solution is 6.5.

(2) Base electrolyte (AS) + lactic acid with pH3 (AS-3).

(3) Base electrolyte (AS) + NaOH with pH9 (AS-9).

(4) Base electrolyte (AS) + lactic acid (to reach a solution pH of 3) and 1000 ppm of fluoride added in form of NaF (AS-3-1000F⁻).

All experimental determinations were carried out at $37 \text{ }^\circ\text{C} \pm 1 \text{ }^\circ\text{C}$, under aerated conditions

1.2 Electrochemical Experiments

The electrochemical behaviour of the titanium alloys was studied using a three-electrode electrochemical set-up: a working electrode (the sample), a reference electrode (Ag/AgCl) and a platinum coiled wire acting as a counter electrode. A potentiostat (solatron1286) was used for the electrochemical tests. All potentials were referred to the used reference electrode (205mV versus SHE).

Potentiodynamic polarization curves of cast and sintered samples were carried out in all the electrolytes by scanning the potential from -1 to 3V at a scan rate of 0.5mVs^{-1} , to assess the corrosion resistance by recording anodic and cathodic currents.

Several electrochemical parameters were calculated from the potentiodynamic curves: the corrosion potential (E_{corr}), the corrosion current density (i_{corr}), determined by the Tafel slope extrapolation and the corrosion passive current density (i_p), obtained by the measured current within the passive domain.

Potentiostatic tests were carried out by applying a constant potential of 0.2V within the passive domain of the alloys and measuring the response in current. The final passive current (i_{pass}) and the electrochemical charge (Q) were obtained from those experimental results.

1.3 Tribocorrosion Experiments

The tribocorrosion tests were carried out coupling the electrochemical cell to a ball-on-disc tribometer with the reference electrode no more than 1 cm away from the wear track. Only the upper surface of the samples (2.04 cm^2) was exposed to the electrolyte and the lower part was insulated and electrically connected to the potentiostat. The computer controlled tribometer applies a sliding motion through a ball (alumina ball 6mm in diameter) on a flat disc (the titanium alloy). These tests were performed setting normal load, sliding velocity and sliding duration to 5N (which corresponds to a maximum contact pressure of 960 MPa), 60 rpm and 1 h, respectively.

Sliding tests were carried out either at open circuit potential (OCP), which is the difference in electrical potential spontaneously established between the metal and the solution and at an applied passive potential of 0.2V. The experimental sequence consisted in:

- Cathodic cleaning by applying a potential of -1.1 for 5 min,
- Applied potential (0.2 V) for 60 min or allowing the system to stabilize at OCP during 60 min,
- Start the sliding for 60 min while the polarization (0.2 V) is maintained or the OCP is measured,
- Sliding is stopped while the polarization (0.2 V) or the OCP is maintained for 20 min.

At the end of the tribocorrosion tests the wear track and the alumina counterpart were examined using optical microscopy and scanning electron microscopy (SEM). The wear track profile was measured by confocal microscopy (Olympus LEXT OLS3000).

All electrochemical and tribocorrosion tests were repeated three times to check the reproducibility of the measurements.

2. Results

2.1 Potentiodynamic curves

The potentiodynamic curves of the cast and sintered Ti6Al4V are shown in **Figure 4.A2.1**. Two different behaviours can be observed in the cast and the sintered alloys depending on the presence of fluorides in the solution.

With respect to the potentiodynamic curves in the fluoride free solutions, the cast material (**Figure 4.A2.1a**) shows a cathodic domain at potentials below -0.5V , where the current is determined by the reduction of water and partially of dissolved oxygen. The transition from cathodic to anodic current at the corrosion potential comprises between -0.5 and -0.2V . A large passive zone is observed between the corrosion potential and 2.8V where the current density remains approximately constant. Finally at the highest applied potentials, a transpassive domain is observed in AS-3 and AS-9 where the current density increases with the applied potential, due to the oxidation of water and oxides of the passive film. The sintered Ti6Al4V alloy (**Figure 4.A2.1b**) also shows four potential domains in the potentiodynamic curves (**Figure 4.A2.1b**).

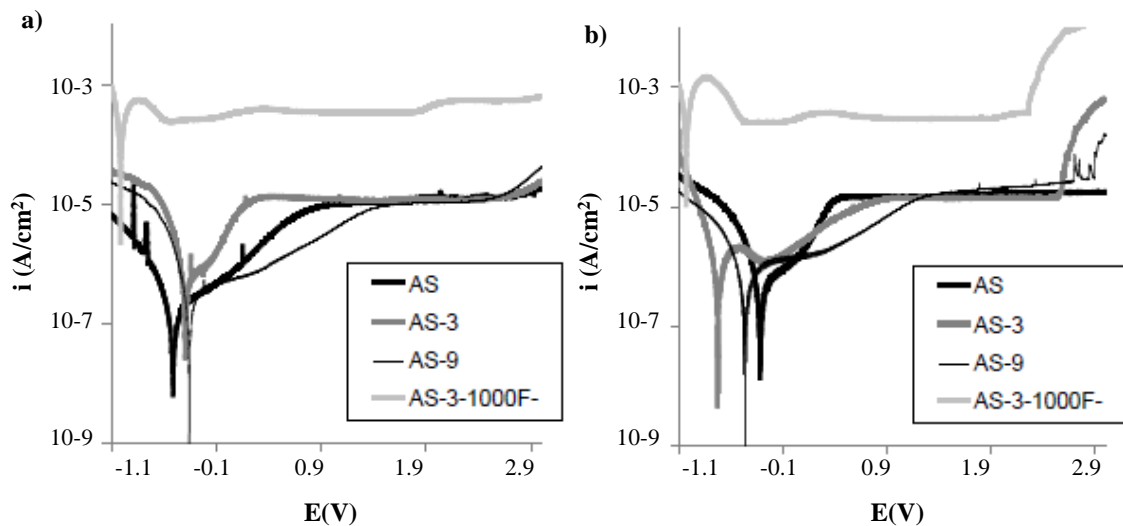


Figure.4.A2.1 Potentiodynamic curves for Ti6Al4V alloys: (a) Cast, (b) Sintered in the studied solutions at 37°C

Table 4.A2.1 shows the electrochemical parameters extracted from the potentiodynamic curves of the cast and sintered Ti6Al4V alloys. Concerning the OCP measurements, an ennoblement of the OCP value is observed with the increase of pH for the cast material. The sintered material shows higher OCP values in AS-3 and AS-9 when compared to the cast samples. The simultaneous effect of pH and fluorides reduces the OCP values of cast and sintered alloys towards very low values (~ 1 V).

Small effect of pH was observed on the E_{corr} of both sintered and cast alloys. However the i_{corr} is three times higher in the acidic media than in the neutral and basic ones for both cast and sintered alloys. The effect of pH is strongly enhanced when adding 1000 ppm of fluorides, in this case the corrosion rate increases three orders of magnitude with respect to the fluoride free solutions.

Table 4.A2.1 - Electrochemical parameters for Ti6Al4V alloys in the studied solutions.

| Material | Solution | OCP (mV) | E_{corr} (mV) | i_{corr} ($\mu\text{A}/\text{cm}^2$) | i_p ($\mu\text{A}/\text{cm}^2$) |
|----------|-------------------------|---------------|------------------------|---|-------------------------------------|
| Cast | AS | -258 \pm 8 | -512 \pm 6 | 0.21 \pm 0.1 | 12.2 \pm 2 |
| | AS-3 | -268 \pm 45 | -400 \pm 7 | 0.65 \pm 0.2 | 11.2 \pm 3 |
| | AS-9 | -304 \pm 30 | -358 \pm 10 | 0.36 \pm 0.1 | 10.5 \pm 2 |
| | AS-3-1000F ⁻ | -968 \pm 25 | -1003 \pm 13 | 178 \pm 6 | 243 \pm 73 |
| Sintered | AS | -268 \pm 10 | -318 \pm 8 | 0.31 \pm 0.1 | 17.6 \pm 4 |
| | AS-3 | -214 \pm 57 | -724 \pm 7 | 0.91 \pm 0.2 | 14.0 \pm 3 |
| | AS-9 | -219 \pm 80 | -465 \pm 11 | 0.38 \pm 0.1 | 25.5 \pm 4 |
| | AS-3-1000F ⁻ | -972 \pm 54 | -1017 \pm 28 | 414 \pm 14 | 291 \pm 19 |

Electrochemical behaviour of cast and sintered alloys in AS-3-1000F⁻ critically differs from the previous one. The cathodic anodic transition takes place at very low potential (around -1 V) and high passive dissolution is measured at potentials between -1 and 2 V. Transpassive dissolution was also observed in the sintered alloy above 2 V.

Table 4.A2.1 shows the electrochemical parameters extracted from the potentiodynamic curves of the cast and sintered Ti6Al4V alloys. An ennoblement of the OCP value is observed with the increase of pH in the cast material. The sintered material shows higher OCP values in AS-3 and AS-9 when compared to the cast samples. The simultaneous effect of pH and fluorides reduces the OCP values of cast and sintered alloys towards very low values (~ 1 V).

A small effect of pH was observed on the E_{corr} of both sintered and cast alloys. However the i_{corr} is three times higher in the acidic media than in the neutral and basic ones for both cast and sintered alloys. The i_p values of the sintered alloy are higher than the cast ones in all the electrolytes and it increases with pH. These i_p values strongly increase in the presence of fluorides.

2.2 Potentiostatic tests

Figure 4.A2.2 shows the current evolution versus time of the cast (**Figure 4.A2.2a**) and sintered (**Figure 4.A2.2b**) titanium alloys at an applied constant potential in the different electrolytes. In all cases the oxide film growth, due to the metal passivation, causes an exponential decay in current density with time. The pH of the dissolution does not have a significant influence on the charge (Q) or the passive current density (i_{pass}) values. In all electrolytes the charge is lower and the growth rate slower for the cast material when compared to the sintered one.

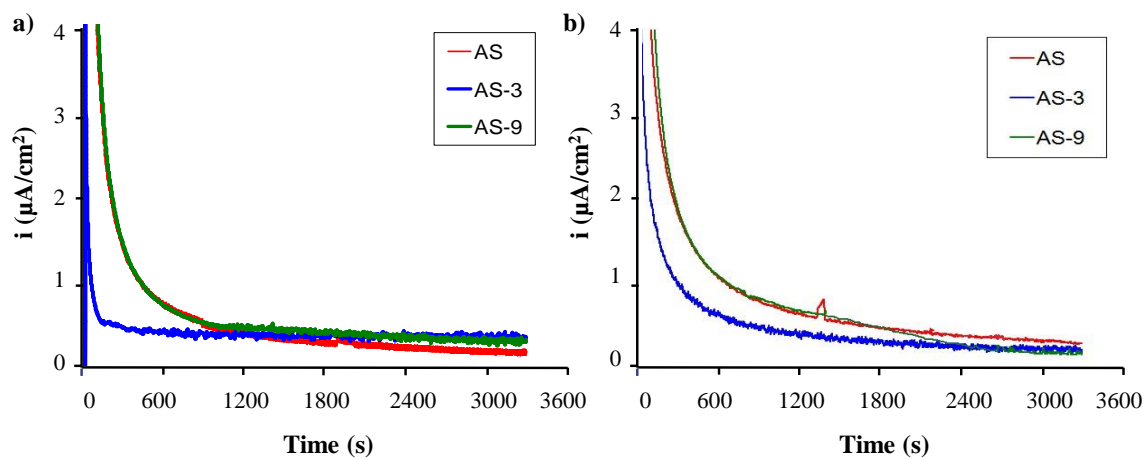


Figure.4.A2.2. Potentiostatic test at 0.2V for Ti6Al4V alloys: (a) Cast, (b) Sintered in the studied solutions at 37°C.

Figure 4.A2.3 shows the comparison between the current evolution with time of the cast and sintered alloys in AS-3-1000F⁻. In both cases the measured current is three orders of magnitude higher than in the fluoride-free solutions. The current evolution with time consists in an abrupt increase followed by a current recovery which remains above 100 $\mu\text{A}/\text{cm}^2$ during the whole test.

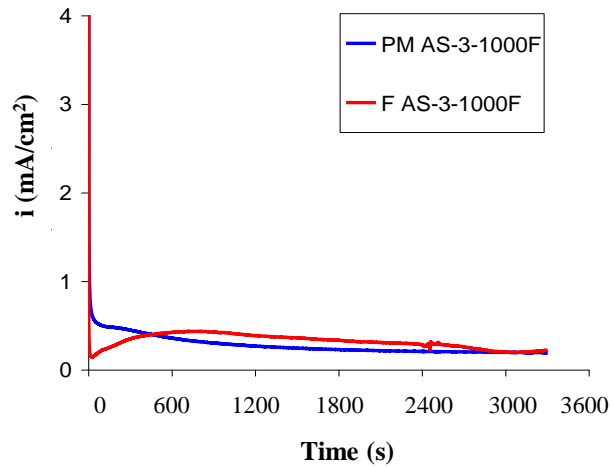


Figure.4.A2.3. Potentiostatic test at 0.2V for cast and sintered Ti6Al4V alloys in the AS-3-1000F- solution at 37°C.

Table 4.A2.2 shows the Q and i_{pass} values of the potentiostatic tests and the high passive dissolution rate in AS-3-1000F⁻ is clearly observed in both values.

Table 4.A2.2 - Electrochemical parameters of the Ti6Al4V alloys in the studied solutions

| Material | Solution | Q ($\text{C}/\text{cm}^2 \cdot 10^{-3}$) | i_{pass} ($\mu\text{A}/\text{cm}^2$) |
|----------|-------------|--|---|
| Cast | AS | 3.5 ± 0.7 | 0.31 ± 0.07 |
| | AS-3 | 1.69 ± 0.4 | 0.30 ± 0.1 |
| | AS-9 | 3.42 ± 1.2 | 0.24 ± 0.1 |
| | AS-3-1000F- | 1130 ± 70 | 266 ± 50 |
| Sintered | AS | 2.9 ± 1 | 0.40 ± 0.1 |
| | AS-3 | 1.98 ± 0.7 | 0.26 ± 0.1 |
| | AS-9 | 3.91 ± 1.7 | 0.22 ± 0.1 |
| | AS-3-1000F- | 715 ± 150 | 159 ± 30 |

2.3 Tribocorrosion tests

The evolution of the OCP with time of the titanium alloys is monitored before, during and after the sliding and it is shown in **Figure 4.A2.4**.

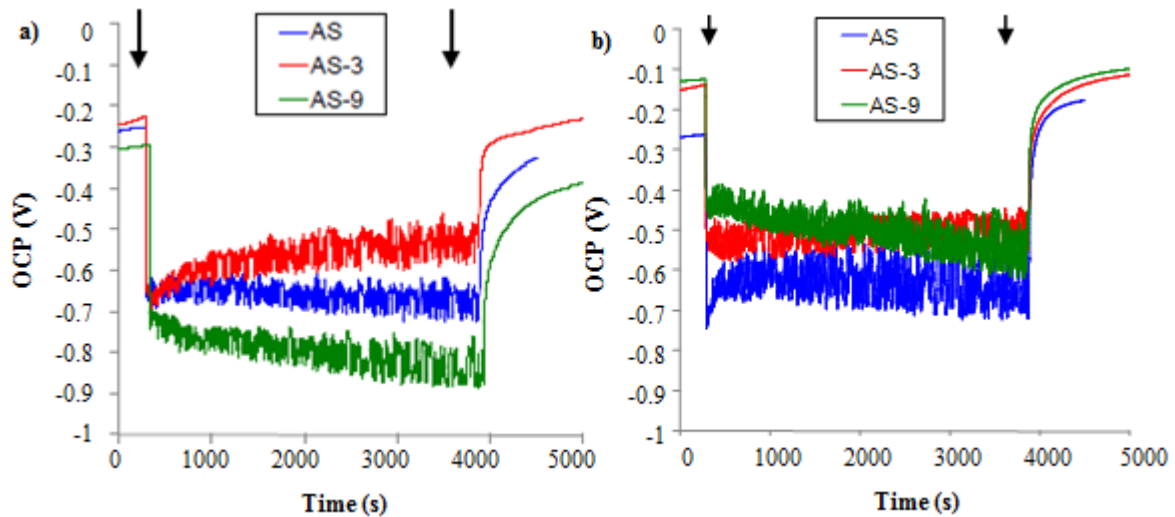


Figure.4.A2.4. Evolution with time of the OCP during sliding of a smooth alumina ball against Ti6Al4V for (a) Cast and (b) PM alloys

Before the initiation of sliding, the OCP value shows the existence of a passive film on the alloy surface. Immediately after the initiation of the sliding, an abrupt increase in potential is observed. This drop in potential is due to the mechanical detachment of the passive film (depassivation) and the exposure of the underlying raw, active titanium alloy to the solution.

During the sliding period, the potential shows transients of around 0.1V in amplitude in the cast samples and up to 0.2V in the sintered ones due to the establishment of a dynamic equilibrium between depassivation and repassivation mechanisms as a result from the cyclic removal (depassivation) and growth (repassivation) of the passive film during the sliding.

At the end of the sliding, the OCP shows an anodic shift due to the repassivation of the active area. If the potential recovers its initial value, or is greater than the value before the tests, it indicates that the newly formed passive film has similar properties as the naturally formed film present on the titanium samples before the mechanical action. The recovery of the initial OCP values is faster in the sintered samples, except in the acidic solution. None of the cast alloys recovered their original OCP at the end of the tribocorrosion tests, except in the acidic solution.

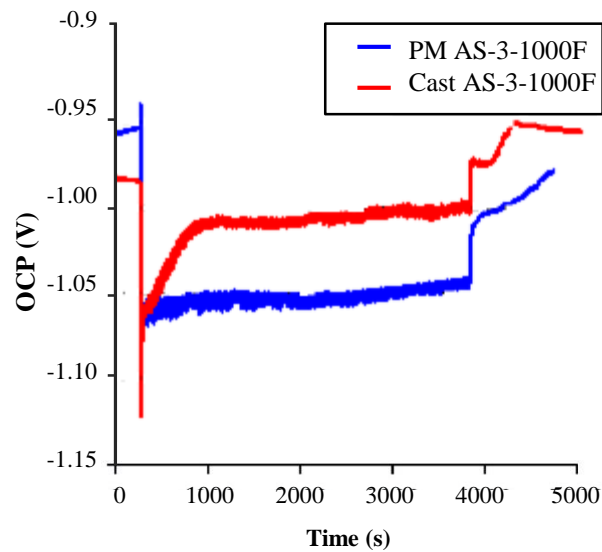


Figure 4.A2.5. Evolution with time of the OCP during sliding of a smooth alumina ball against Ti6Al4V alloys in the AS-3-1000F- at 37 °C. 1000

In the acidified solution in the presence of fluorides, **Figure 4.A2.5**, the OCP at the beginning of the test is very low and it only decreases around 10mV when sliding initiates in both cast and sintered alloys. This decrease is due to the movement of the electrolyte and the enhancement of mass transfer at the interface biomaterial/electrolyte. Electrochemical tests without the application of the normal load through the alumina ball were carried out at a rotation rate of 60 rpm and the same drop in potential was registered.

Table 4.A2.3 summarizes the average OCP values before (OCP_0), during ($OCP_{sliding}$) and after (OCP_{final}) the sliding. OCP values of the cast titanium alloy are higher than of the sintered alloy.

Table 4.A2.3 - Average values of the potential measured before (OCP_0), during ($OCP_{sliding}$) and after sliding (OCP_{final}) of the Ti6Al4V alloy sling against an alumina ball in different electrolytes. Normal force 5N

| Material | Solution | OCP_0 (mV) | $OCP_{sliding}$ (mV) | OCP_{final} (mV) |
|----------|--------------------------|-----------------|-------------------------|-----------------------|
| Cast | AS | -256±30 | -678±62 | -325±70 |
| | AS-3 | -236±44 | -559±50 | -255±39 |
| | AS-9 | -299±40 | -673±110 | -427±35 |
| | AS-3-1000F ⁺⁺ | -980±16 | -974±17 | -993±4 |
| Sintered | AS | -264±45 | -596±34 | -176±17 |
| | AS-3 | -147±7 | -504±10 | -137±11 |
| | AS-9 | -127±27 | -498±47 | -118±30 |
| | AS-3-1000F ⁺⁺ | -960±24 | -1050±25 | -952±17 |

Anodic current during rubbing.

Figure 4.A2.6 shows the current density evolution with time during sliding of an alumina ball against the cast and sintered Ti6Al4V discs in different AS solutions at an applied constant potential. Before rubbing, the whole surface is passive and the anodic current (I_0) is low (below $1\mu\text{A}$).

At the onset of rubbing, the current exhibits a sharp increase. After a few seconds the steady state value is reached. When the sliding stops, the current sharply decreases again to the initial value observed before the sliding which suggests the repassivation of the worn area.

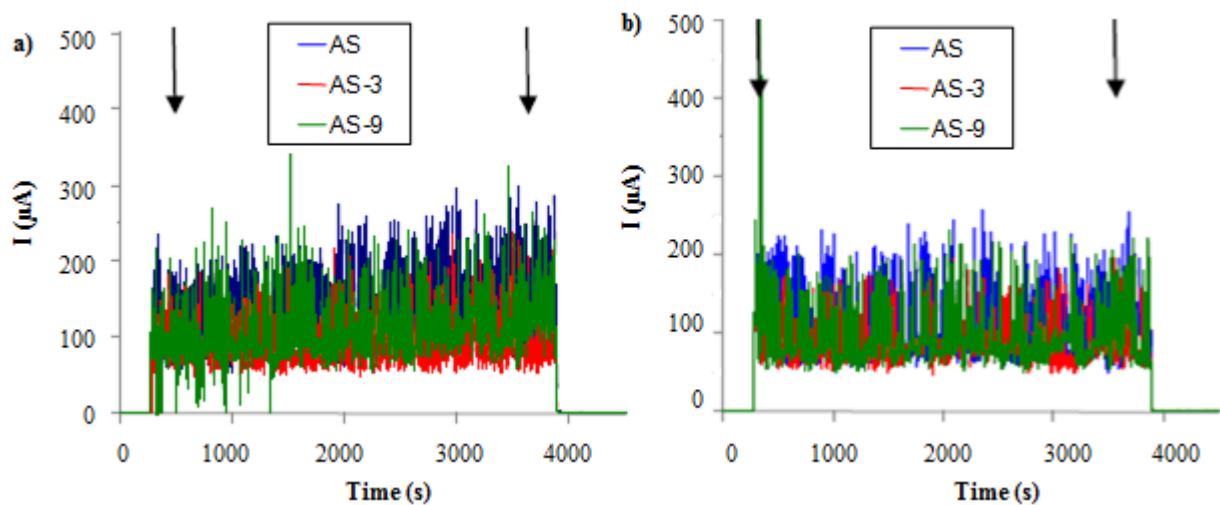


Figure 4.A2.6 Evolution with time of the current during sliding of a smooth alumina ball against Ti6Al4V alloys at imposed potential of 0.2 V for (a) cast material, and (b) sintered material.

Figure 4.A2.7 shows the current evolution of both alloys in AS-3-1000F-. The current slightly increases when sliding initiates and slowly recovers the initial values at the end of the sliding. The high dissolution rate of the titanium alloys in this solution modifies the prevailing tribocorrosion mechanisms as will be discussed later.

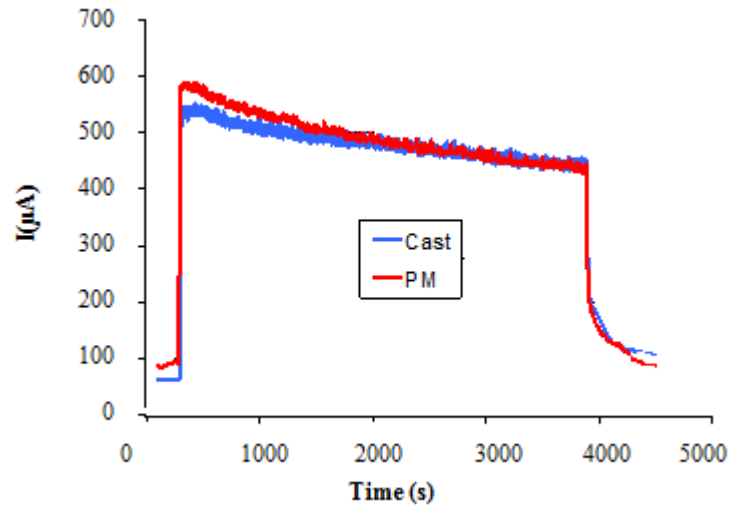


Figure 4.A2.7 Evolution with time of the current during sliding of a smooth alumina ball against Ti6Al4V alloys at imposed potential of 0.2 V in AS-3-1000F- at 37 °C.

Table 4.A2.4 summarizes the average values of the current density before (I_0), during (I_{sliding}) and after (I_{final}) the sliding in the tribocorrosion tests at 0.2V. The current flowing in the wear track (I_{sliding}) was determined by subtracting from the current measured during sliding the value of the current measured before starting the sliding. The latter was assumed to correspond approximately to the current flowing through the area outside the wear track during sliding (the wear track area is much smaller than the total electrode area). In the case of the tests carried out in the AS-3-1000F⁻ solution, the current during rubbing (I_{rubbing}) corresponds to the total current measured during the sliding, which has been used to determine the damage produced by the corrosion mechanism.

The pH has no significant influence on the anodic current, except in the presence of fluorides. The I_{sliding} value is similar for both alloys in all solutions. The most important influence of the electrolyte in the current measured during sliding was observed in the AS-3-1000F⁻ solution.

Table 4.A2.4 - Average values of the current density measured before (I_0), during (I_{sliding}) and after sliding (I_{final}) of the Ti6Al4V alloy sliding against an alumina ball in different electrolytes. Normal force 5N.

| Material | Solution | I_0 (μA) | I_{sliding} (μA) | I_{rubbing} (mA) | I_{final} (μA) |
|----------|-------------------------|-------------------------|--|---------------------------|--------------------------------------|
| Cast | AS | 0.42±0.6 | 96±8 | - | 0.68±0.4 |
| | AS-3 | 0.93±0.8 | 92±6 | - | 1.75±1.4 |
| | AS-9 | 2.09±1.2 | 111±4 | - | 0.58±0.5 |
| | AS-3-1000F ⁻ | 566±60 | - | 4.8±0.5 | 1180±98 |
| Sintered | AS | 0.71±0.4 | 108±12 | - | 0.58±0.3 |
| | AS-3 | 0.53±0.4 | 88±7 | - | 0.51±0.2 |
| | AS-9 | 0.45±0.2 | 96±10 | - | 0.84±0.7 |
| | AS-3-1000F ⁻ | 645±65 | - | 4.4±0.4 | 853±30 |

According to Bazzoni et al [32], three main mechanisms contribute to the overall material loss, the material removal by tribocorrosion in the sliding surface (wear-accelerated corrosion, V_{chem} , and mechanical wear, V_{mech}) and the corrosion, occurring in the overall surface exposed to the electrolyte (V_{corr}). The total degradation taking place under tribocorrosion system can be quantified by the sum of the three contributions, **equation (1)**.

$$V_{\text{tot}} = V_{\text{chem}} + V_{\text{mech}} + V_{\text{corr}} \quad (1)$$

In a passive alloy, V_{corr} can be considered negligible, thus overall volume loss can be expressed as the sum of the wear accelerated corrosion and mechanical wear inside the wear track, **equation (2)**.

$$V_{\text{tot}} = V_{\text{chem}} + V_{\text{mech}} \quad (2)$$

The volume, V_{chem} removed by anodic oxidation in the wear track was calculated from the measured current using Faraday's law:

$$V_{\text{chem}} = \left((I_{\text{sliding}} \cdot t \cdot M) / (n \cdot F \cdot \rho) \right) \quad (3)$$

where M is the atomic mass of the alloy (46.64 g mol^{-1}), n is the charge number for the oxidation reaction (4), F is the Faraday constant (96500 C mol^{-1}), ρ is the density of the alloy (4.43 g cm^{-3}) and t is the duration of sliding (3600 s). The total wear volume, V_{tot} was determined geometrically by confocal microscopy, through the measurement of five different profiles of the wear track. The area of an average cross section of the wear track multiplied by the length of the track gives one the V_{tot} . The obtained V_{chem} values are listed in **Table 4.A2.5**, together with the mechanical wear volume (V_{mech}) and total wear volume (V_{tot}). V_{mech} removed by tribocorrosion is obtained by the difference between V_{tot} and V_{chem} . Finally, in the AS-3-1000F⁻ solution, wear-accelerated corrosion does not take place and the only two contributions to the overall damage are V_{corr} and V_{mech} , obtained from the current during sliding (**equation (4)**) and the measure of the material loss in the wear track (area of the wear track), respectively.

$$V_{\text{corr}} = \left((I_{\text{rubbing}} \cdot t \cdot M) / (n \cdot F \cdot \rho) \right) \quad (4)$$

Table 4.A2.5 - Average wear volumes expressed in 10^{-3} mm^3 .

| Material | Solution | OCP | | E0.2V | | | |
|----------|-------------------------|------------------|-------------------|------------------|-------------------|-------------------|-------------------|
| | | V_{tot} | V_{mech} | V_{tot} | V_{chem} | V_{mech} | V_{corr} |
| Cast | AS | 87±11 | | 97±13 | 12±1 | 85±14 | |
| | AS-3 | 86±9 | | 82±11 | 8±1 | 73±12 | |
| | AS-9 | 97±8 | | 116±14 | 10±1 | 105±15 | |
| | AS-3-1000F ⁻ | | 85±10 | 602±23 | | 121±46 | 481±23 |
| Sintered | AS | 80±16 | | 128±18 | 11±1 | 97±19 | |
| | AS-3 | 46±10 | | 50±9 | 9±1 | 41±10 | |
| | AS-9 | 123±14 | | 120±15 | 9±1 | 111±16 | |
| | AS-3-1000F ⁻ | | 110±12 | 566±25 | | 106±58 | 460±34 |

At OCP, V_{tot} was also calculated by measuring the wear track profiles at the end of the tribocorrosion tests and multiplying it by the length of the track. Under those equilibrium conditions the wear-accelerated corrosion was measured according to the model proposed by Viera et al [33] which takes into account the cathodic kinetics and corrosion potential from **Figure 4.A2.1**, the potential during sliding (**Figure 4.A2.4**) and the anode to cathode ratio. However the contribution was negligible (below $1 \times 10^{-3} \text{ mm}^3$), thus, only V_{tot} is indicated in the table and corresponds to the mechanical wear volume. At OCP, V_{tot} of the cast alloys does not depend on the pH, while for the sintered material it slightly increases with the pH. V_{tot} at the applied potential is higher than V_{tot} at OCP.

The wear-accelerated corrosion only represents a small percentage (10%) of the total wear in all electrolytes. In AS-3-1000F⁻, the total volume is much higher than under passive conditions for both, cast and sintered alloys.

2.4 Wear morphology

Optical and SEM microscopy were used to evaluate the morphology of the wear tracks on the Ti6Al4V alloys. **Figure 4.A2.8** shows the SEM images of the wear tracks of the cast and sintered alloys at the end of the tribocorrosion tests in the different dissolutions. At OCP and applied anodic potential, the wear damage shows a predominant adhesive wear in AS-3 and AS. However, in the basic media the wear track shows an abrasive wear with signs of delamination. A small number of isolated debris particles are observed inside the worn surfaces in the alkaline media.

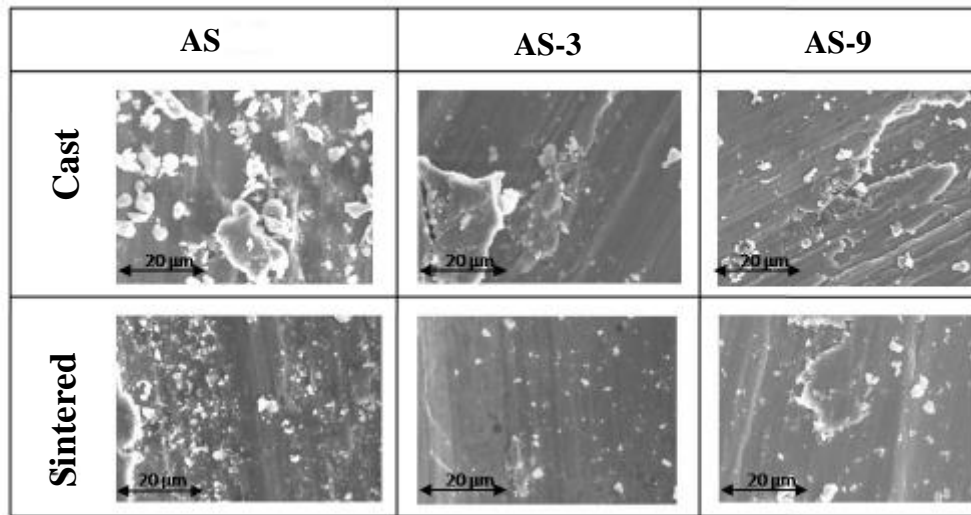


Figure 4.A2.8. SEM images for cast and sintered alloys of the center of the wear tracks in different electrolytes at E200. Normal load 5N

In the AS-3-1000F– the prevailing corrosion mechanism leads to more uniform surfaces (**Figure 4.A2.8**) in which a small amount of wear debris was observed and even grain boundaries were revealed in the sintered alloy.

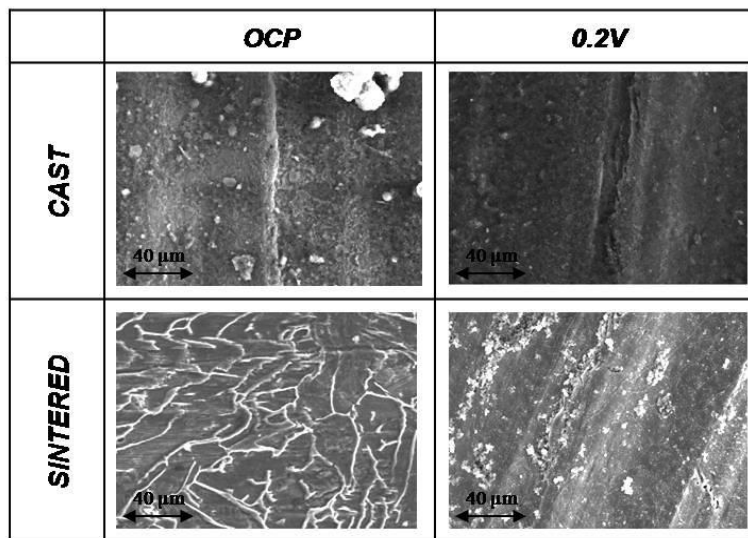


Figure 4.A2.9 SEM images for cast and sintered alloys of the center of the wear tracks in AS-3-1000F- at OCP and E200. Normal load 5N

In all cases the optical images of the alumina ball showed matter transfer from the titanium discs. The matter transfer diminishes in the electrolytes with fluorides.

3. Discussion

According to the equilibrium $\text{HF} \leftrightarrow \text{H}^+ + \text{F}^-$ and in the AS solution in the presence of fluorides, the concentration of the involved species $[\text{H}^+]$, $[\text{OH}^-]$, $[\text{F}^-]$ and $[\text{HF}]$ depends on the pH and the fluoride concentration. In the AS-1000F⁻, the concentration of HF corresponds to $2.6 \times 10^{-5} \text{ M}$ but when the pH is 3 that concentration changes to 0.15 M, a much higher value than the 30 ppm proposed by Nakagawa [24] as the limit concentration for the destruction of the titanium passive film.

Figure 4.A2.10 shows the potentiodynamic curves of the cast and sintered alloys in AS with pH 3 and different fluoride concentrations (from 0 to 1000 ppm). A fluoride content higher than 100 ppm actively dissolves both titanium alloys. Kwon et al [34] also confirmed that in low HF concentrations the passive oxide layer on titanium alloys remains stable.

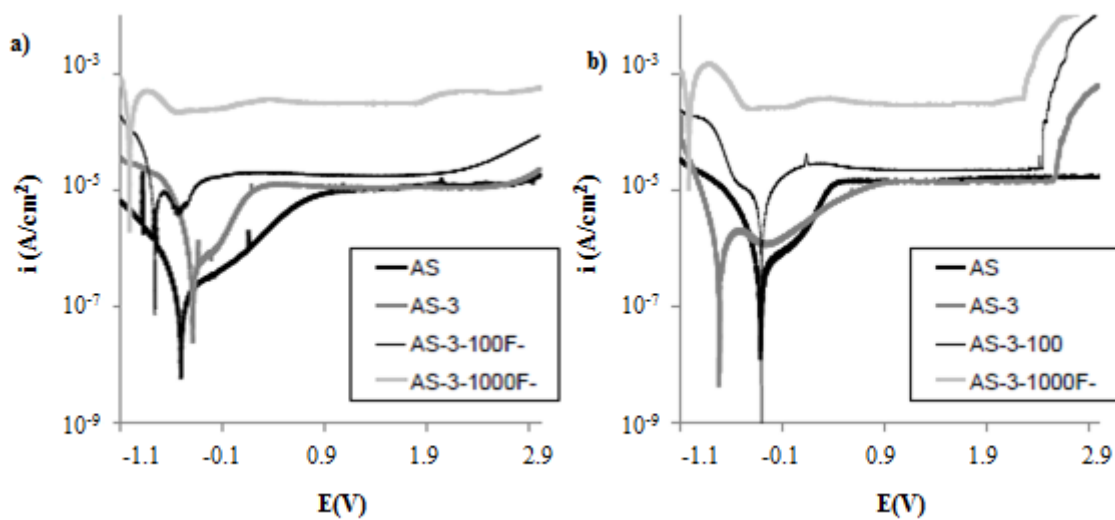


Figure 4.A2.10. Potentiodynamic curves for Ti6Al4V alloys: (a) Cast and (b) PM in AS and AS-3 with different fluoride content at 37°C.

As referred to previously, according to Bazzoni et al [32] tribocorrosion systems usually consist in three mechanisms which lead to the degradation of the material: wear-accelerated corrosion (V_{chem}), mechanical wear (V_{mech}) and the corrosion occurring in the overall surface exposed to the electrolyte (V_{corr}). Ti6Al4V is a passive metal and the main contribution to the tribocorrosion degradation is mechanical wear. The morphological features of the worn zone indicate adhesive wear in all AS solutions, independently of the pH, which has been confirmed by the presence of material transfer on the alumina ball. However in the basic solution, AS-9, the wear track shows sliding marks with few plastically deformed grooves, thus meaning that the tribocorrosion proceeds from an abrasive wear mechanism. Moreover, the tests carried out in the AS-9 electrolyte show a wider track width at OCP and at 0.2V. This indicates an increasing contact area between the alumina ball and the sample during

sliding confirmed by the increase in current and decrease in OCP with time during sliding (**Figures 4.A2.4 and 6**, respectively).

On the other hand, a higher amount of wear debris is observed in the wear track of the samples tested in AS-9, whereas there is only a little in the samples tested in AS-3 and AS. This may be attributed to the influence of the oxidation and reduction reactions occurring in the contact area during sliding, depending on the chemical composition of the test solution leading to ejection of oxidized wear debris from the contact. It is well known that wear particles have an influence on wear by a surface-damage mechanism [35]. Therefore, the presence of particles and their grinding between the alumina ball and track surface enhances the wear of the material. When a critical thickness is exceeded, this third-body oxide film can break away from the contacting surfaces, which would lead to the ejection of oxidized wear debris from the contact [36].

The presence of debris in the wear track could also change the contact. In fact, the alumina balls showed higher contact surface at OCP than at 0.2V, which implies that the pressure on the surface of the alloys tested at OCP is smaller than at the applied potential. According to Landolt *et al* [37] at low anodic potentials the metallic particles formed by mechanical wear completely dissolved in the electrolyte, while at higher potentials the repassivation rate is sufficiently fast to allow them to repassivate and to form a third body. Apparently the presence of the third body in these experiments attenuated the pressure distribution in the contact. This observation would explain the higher volume loss at 0.2V due to the higher pressure and to the hard debris that acts like abrasive particles during sliding.

This is the case of the experiments carried out in AS without the addition of fluoride, however in the AS-3-1000F⁻ solution the system also includes overall corrosion as the main degradation mechanism. At OCP the microstructure of the cast and sintered alloys was revealed after the tribocorrosion tests, both in the worn and unworn areas. This appearance is due to the aggressiveness and concentration of HF⁻ formed in AS-3-1000F⁻, which leads to a continuous dissolution of the material resulting in an active state of the titanium surface.

Even though the presence of material transfer on the alumina ball suggests that the material suffers adhesive wear. At 0.2V the smooth surface morphology barely showed abrasion marks for the cast material and none were noticed for the sintered material, which confirms once more that the main mechanism is corrosion.

4. Conclusions

In this work, the influence of pH in artificial saliva on the tribocorrosion behaviour of a Ti6Al4V alloy obtained by two different fabrication processes (cast and powder metallurgy) was investigated. The following conclusions were drawn.

- Ti6Al4V alloy spontaneously passivates in AS regardless of the pH and only in acidified AS solution with fluorides (AS-3-1000F⁻) does the alloy actively corrode.
- Independently on the pH, wear damage is mainly due to the mechanical action in AS. When fluorides are added to acidified artificial saliva (pH 3) the main degradation mechanism corresponds to corrosion and it generates material loss one order of magnitude higher than in the rest of the solutions.
- Differences in corrosion and tribocorrosion mechanisms and degradation extent between both fabrication processes for the titanium alloys are not significant

5. Acknowledgements

We wish to express our gratitude to the Ministerio de Ciencia e Innovación of the Spanish government for the financial support under the project MAT2011-22481.

6. Bibliography

- [1] D. Paul, P.D. Bianco, M.C. John. Titanium serum and urine levels in rabbits with a titanium implant in the absence of wear. *Biomaterials* 17 (1996) 1937–42
- [2] D. Steinberg, A. Klinger, D. Kohavi, M.N. Sela. Adsorption of human salivary proteins to titanium powder: I. Adsorption of human salivary albumin. *Biomaterials* 16 (1995) 1339–43
- [3] Z. Cai, H. Nakajima, M. Woldu, A. Berglund, M. Bergman, T. Okabe. In vitro corrosion resistance of titanium made using different fabrication methods. *Biomaterials* (1999) 20183–90
- [4] M.A. Khan, R.L. Williams, D.F. Williams. In-vitro corrosion and wear of titanium alloys in the biological environment. *Biomaterials* 17(1996) 2117–26.
- [5] M. Koike, H. Fujii .The corrosion resistance of pure titanium inorganic acids. *Biomaterials* 22 (2001) 2931–627
- [6] K. Ida, Y. Tani, S. Tsutsumi, T. Togaya, T. Nambu, K. Suese, T. Kawazoe, M. Nakamura, H. Wada. Clinical application of pure titanium crowns. *Dent Mater J* 4 (1985) 191–5
- [7] B. Bergman, C. Bessing, G. Ericson, P. Lundquist, H. Nilson, M. Andersson. A 2-year follow-up study of titanium crowns. *Acta Odontol Scand* 48 (1990) 113–7
- [8] T. Hirata, T. Nakamura, F. Takashima, T. Maruyama, M. Taira, J. Takahashi. Studies on polishing of Ag–Pd–Cu–Au alloy with five dental abrasives. *J Oral Rehab* 28 (8) (2001) 773–7
- [9] D. Iijima, T. Yoneyama, H. Doi, H. Hamanaka, N. Kurosaki. Wear properties of Ti and Ti–6Al–7Nb castings for dental prostheses. *Biomaterials* 24 (2003) 1519–1524
- [10] L.C. Lucas, J.E. Lemons, J. Lee, P. Dale. 1987 Lemons (Ed.), *Quantitative Characterization and Performance of Porous Implants for Hard Tissue Applications*, ASTM STP 953, American Society for Testing and Materials, Philadelphia, 137

- [11] K.J. Bundy, R.E. Luedemann, 1987 J.E. Lemons (Ed.), Quantitative Characterization and Performance of Porous Implants for Hard Tissue Applications, ASTM STP 953, American Society for Testing and Materials, Philadelphia, p. 137
- [12] C.E.B. Marino, L.H. Mascaró. EIS characterization of a Ti-dental implant in artificial saliva media: dissolution process of the oxide barrier *J. Electroanal. Chem.* 568 (2004) 115–120
- [13] A.W.E. Hodgson, Y. Mueller, D. Forster and S. Virtanen. Electrochemical characterization of passive films on Ti alloys under simulated biological conditions *Electrochim. Acta* 47(2002) 1913–23
- [14] A.K. Shukla, R. Balasubramaniam, S. Bhargava. Passive Film Behaviour of CP Titanium, Ti-6Al-4V and Ti-13.4Al-29Nb alloys in Simulated Human Body Conditions. *Intermetallics* 13 (2005) 631–637
- [15] A.C. Vieira, A.R. Ribeiro, L.A. Rocha, J.P. Celis. Influence of pH and corrosion inhibitors on the tribocorrosion of titanium in artificial saliva. *Wear* 261 (2006) 994–1001
- [16] Schmidt H, Stechemesseur G, Witte J, Farshi MS. Depth distributions and anodic polarization behaviour of ion implanted Ti6Al4V. *Corros. Sci.* 40 (1998) 1533-45
- [17] Z. Cai, T. Shafer, I. Watanabe, M.E. Nunn, T. Okabe. Electrochemical characterization of cast titanium alloys. *Biomaterials* 24 (2003) 213
- [18] L. Thair, U.K. Mudali, S. Rajagopalan, R. Asokamani, Raj B. Surface characterization of passive film formed on nitrogen ion implanted Ti-6Al-4V and Ti-6Al-7Nb alloys using SIMS. *Corros. Sci.* 45 (2003) 1951-67
- [19] T. Hanawa, M. Ota. Characterization of surface-film formed on titanium in electrolyte using XPS. *Appl. Surf. Sci.* 55 (1992) 269-76
- [20] X. Liu, P.K. Chu, C. Ding. Surface modification for titanium, titanium alloys and related materials for biomedical applications. *Mater. Sci. Eng. R* 47(2004) 49–121.
- [21] F.H. Jones. Teeth and bones: applications of surface science to dental materials and related biomaterials. *Surf. Sci. Rep.* 42 (2001) 75–205.
- [22] J.D. Featherstone, B.E. Rodgers. The effect of acetic, lactic and other organic acids on the formation of artificial carious lesions. *Caries Res.* 15 (1985) 377-85

- [23] M. Nakagawa, Y. Matono, S. Matsuya, K. Udoh, K. Ishikawa. The effect of Pt and Pd alloying additions on the corrosion behavior of titanium in fluoride-containing environments. *Biomaterials* 26 (2005) 2239–2246
- [24] M. Nakagawa, S. Matsuya, T. Shiraishi, M. Ohta. Effect of fluoride concentration and pH on corrosion behavior of titanium for dental use. *J. Dent.Res.* 78 (1999) 1568-72
- [25] D.W. Hoepfner, V. Chandrasekaran. Fretting in orthopaedic implants: A review. *Wear* 173 (1994) 189–197
- [26] S. Barril, N. Debaud, S. Mischler, D. Landolt. A tribo-electrochemical apparatus for in vitro investigation of fretting–corrosion of metallic implant materials. *Wear* 252 (2002) 744–754
- [27] N. Diomidis, J-P Celis, P. Ponthiaux, F. Wenger. Tribocorrosion of stainless steel in sulfuric acid: identification of corrosion–wear components and effect of contact area. *Wear* 269 (2010) 93–103
- [28] N. Diomidis, S. Mischler, N.S. More, M. Roy, S.N. Paul. Fretting–corrosion behavior of β titanium alloys in simulated synovial fluid. *Wear* 271 (2011) 1093–1102
- [29] K. Merritt, S.A. Brown, 1983 Biological effects of corrosion products from metals, in: A.C. Fraker, C.D. Griffin (Eds.), *Corrosion and Degradation of Implant Materials*, ASTM STP 859, Philadelphia, PA, 195–207
- [30] Cohen J 1979 *Metal implants—historical background and biological response to implantation* *Biomaterials in Reconstructive Surgery* (St Louis, MO: C.V. Mosby) 46–61
- [31] MP. Licausi, A. Igual Munoz, V. Amigo´ Borrás. Influence of the fabrication process and fluoride content on the tribocorrosion behaviour of Ti6Al4V biomedical alloy in artificial saliva. *journal of the mechanical behavior of biomedical materials* 20 (2013) 137–148
- [32] A. Bazzoni, S. Mischler, N. Espallargas. Tribocorrosion of Pulsed Plasma-NitridedCoCrMo Implant Alloy. *Tribology Letters* 4 (1) (2013) 157-167
- [33] A.C. Vieira, L.A. Rocha, N. Papageorgiou, S. Mischler. Mechanical and electrochemical deterioration mechanisms in the tribocorrosion of Al alloys in NaCl and in NaNO₃ solutions. *Corrosion Science* 54 (2012) 26–35

[34] Y.H. Kwon, H.J. Seol, H.I. Kim, K.J. Hwan, S.G. Lee, K.H. Kim. Effect of acidic fluoride solution on b-titanium alloy wire. *Journal of Biomedical Materials Research Part B Applied Biomaterials*. 73 (2005) 285–290

[35] S. Barril, S. Mischler, D. Landolt. Electrochemical effects on the fretting corrosion behaviour of Ti6Al4V in 0.9% sodium chloride solution *Wear* 259 (1–6) (2005) 282–291

[36] D. Landolt, S. Mischler, M. Stemp, S. Barril. Third body effects and material fluxes in tribocorrosion systems involving a sliding contact. *Wear* 256 (5) (2004) 517–524

-Article 3-

TRIBOCORROSION MECHANISMS OF Ti6Al4V IN ARTIFICIAL SALIVA BY ZERO-RESISTANCE AMMETRY (ZRA) TECHNIQUE

M.P. Licausi, A. Igual Muñoz, V. Amigó Borrás, Espallargas Nuria

Journal of Bio Tribo Corrosion (2015) 1: 8.

doi: 10.1007/s40735-015-0008-x

The final publication is available at link.springer.com

TRIBOCORROSION MECHANISMS OF Ti6Al4V IN ARTIFICIAL SALIVA BY ZERO-RESISTANCE AMMETRY (ZRA) TECHNIQUE

M.P. Licausi^{1,2}, A. Igual Muñoz^{1*}, V. Amigó Borrás², N. Espallargas³

1-UPV, Department of Chemical and Nuclear Engineering, Universitat Politècnica de València, camino de vera s.n., 46022 Valencia, Spain.

2-UPV, Institute of Materials Technology, Universitat Politècnica de València, camino de vera s.n., 46022 Valencia, Spain.

3-NTNU, Faculty of Engineering Science and Technology, Dept. Engineering Design and Materials, Tribology Lab. N-7491 Trondheim, Norway.

*** Corresponding author**

Abstract

Degradation mechanisms of biomedical alloys involve two different phenomena, corrosion and wear, which simultaneously act and may cause the failure of implants and prosthesis. In this work, tribocorrosion of Ti6Al4V biomedical alloy in artificial saliva is studied at open circuit potential (OCP) by a new electrochemical technique that allows measuring the galvanic potential and current between the wear track (anode) and the passive material (cathode) through zero-resistance ammetry. The experimental set-up was conceived for physically separating the depassivated area from the passive material, thus allowing to quantify the mechanically activated corrosion at OCP. Two different counterparts, SiC and Al₂O₃, were used against the Ti6Al4V alloy in order to analyse the influence of the initial contact pressure on the tribocorrosion mechanisms. A galvanic model based on the cathodic reaction kinetics can describe the current and the potential evolution with time during sliding. It has been observed that at the highest initial contact pressures, wear follows the Archard law, while at lower contact pressures, third body appeared and wear can not be described by the Archard law. Quantification of the evolution of the depassivated wear track with time was obtained and the deviation from the Archard predictions was analysed.

Keywords: biotribocorrosion, corrosion, Ti6Al4V, Zero Resistance Ammetry, galvanic model.

1. Introduction

Titanium and its alloys are widely used in the biomedical field due to their excellent properties: low density, high hardness, good corrosion resistance, inactivity with the biological environment, low elastic modulus and high capacity to attach to tissue and bone, thus making titanium a good choice as a biomaterial [1, 2, 3]. Commercially pure titanium (α alloy) and the Ti6Al4V alloy ($\alpha + \beta$ alloy) have been the most employed alloys for dental implants during years, although they exhibit prolonged use limitations such as high elastic modulus compared to the bone, and low wear resistance [4, 5]. Ti6Al4V was also found to be toxic due to the release of aluminium and vanadium ions [6, 7]. All these adverse effects are related to the degradation mechanisms of the alloy under operating conditions, which are typically the combined effect of corrosion and wear. The corrosion behaviour of titanium alloys depends on an oxide film formation mainly composed of TiO_2 , which spontaneously covers the titanium surface in the presence of oxygen [8]. The chemical properties of the oxide layer play an important role in the biocompatibility of titanium implants and the surrounding tissues, but typically its chemical and electrochemical stability is known to be very good. On the contrary, the mechanically activated corrosion and the wear resistance of titanium alloys are very dependent on the mechanical [7, 9, 10] and electrochemical conditions [7, 11], which also may change during sliding. Several authors [7, 9, 12] observed potential and current transitions during different tribocorrosion tests carried out on titanium alloys. Those transitions were explained through changes in wear mechanisms. Komotori et al. [9] observed a transition from abrasive to adhesive wear when increasing the scratching rate of the tests; Moore et al. [7] observed a change in the depassivation/repassivation rate caused by the decrease in contact pressure during wear and Runa et al. [12] explained the decrease in current during rubbing by the formation of a tribolayer. In all cases, there is not a clear understanding of the mechanisms that cause the transitions in the electrochemical signals. The development of new triboelectrochemical techniques is, therefore, needed for identifying critical parameters determining the different tribocorrosion mechanisms during wear and for predicting and quantifying the involved phenomena.

Tribocorrosion testing of passive metals has been a topic of interest since late 1970s for investigating the synergistic effects of corrosion on wear and vice versa [13]. Measuring the combined action of wear and corrosion is not an easy task and it requires the use of electrochemical techniques and tribometers. Typically, the electrochemical techniques used in tribocorrosion (summarized in Ref. [14]) have been the measurement of the open circuit potential (OCP) while rubbing, potentiodynamic techniques (i.e. the variation of potential with time during rubbing and the measurement of current) and potentiostatic techniques (i.e. the application of a constant electrode potential while rubbing and the measurement of current). These techniques have allowed the proposal of tribocorrosion mechanisms and models [13, 14]. The use of electrochemical techniques is necessary for advancing in

tribocorrosion modelling and more accurate techniques focusing onto the passivation/depasivation kinetics of passive metals are necessary in the field.

Recently, a new electrochemical technique for measuring currents during OCP has been proposed [15]. This technique physically separates the anode and the cathode in a tribocorrosion system and uses a zero-resistance ammeter (ZRA) for measuring the cathodic potential and the anodic current. The ZRA-tribocorrosion technique has allowed the experimental validation of the galvanic coupling model for tribocorrosion first proposed by Vieira et al. [16] for Aluminium alloys and later expanded by Papageorgiou and Mischler [17] for Co- and Ti-based alloys and by Papageorgiou et al. [18] for Ni-based alloys. The galvanic coupling model for tribocorrosion simulates the evolution of OCP with time during a tribocorrosion experiment assuming an anodic current density (i_a) that is used as a fitting parameter. The ZRA-tribocorrosion technique experimentally determines i_a and therefore allows to accurately model the potential evolution with time and eliminates the need of using fitting parameters. So far this experimental technique has been only validated with a Fe-based alloy where a good correlation between the model using a fitting parameter and the experimental results was obtained at high loads. However, when the load was decreased, a constant decay in current and an increase in potential with time were obtained causing a deviation from the model using a fitting parameter [15]. This can be explained by the fact that the mechanical aspects of the system played a role, i.e. a deviation from the Archard wear law happened, which led to a different triboelectrochemical response. Therefore, the ZRA technique can be used as a tool for explaining tribocorrosion mechanisms.

The aim of this work has been to extend the validation of the ZRA technique to other passive alloys and to use it as a tool for investigating tribocorrosion mechanisms at OCP, which typically corresponds to a more realistic condition of operation. Specifically, in this work, a biomedical Ti6Al4V cast alloy immersed in artificial saliva (AS) has been chosen for this purpose, and it has been tested at different applied contact pressures to study the influence of the mechanical conditions on the potential and current responses.

2. Experimental procedure

2.1. Materials and electrolyte

The metal alloy used in this work was an as-cast Titanium alloy, Ti6Al4V Grade 5, with a chemical composition in wt% N: 0.02; C: 0.03; H: 0.011; Fe: 0.22; O: 0.16; Al: 6.12; V: 3.93. The sample was cut from a plate of commercially available Ti6Al4V, thus specimens $25 \times 25 \times 5 \text{ mm}^3$ were obtained.

Specimens were wet-ground with 220 – 4000 grit silicon carbide paper and further polished with diamond suspension to a mirror-like finishing ($R_a = 0.05 \pm 0.01 \text{ }\mu\text{m}$). After polishing, the samples were rinsed in water and dried using a stream of compressed air.

The electrolyte used in this work was a modified Fusayama Meyer AS. The chemical composition of this solution, which closely resembles natural saliva, is 0.4 g NaCl, 0.4 g KCl, 0.6 g CaCl₂, 0.58 g Na₂HPO₄ 12H₂O, 1 g urea and distilled water 1 L. The electrolyte was used in the tests at 37 °C.

2.2. Electrochemical tests

Cathodic polarization tests were carried out in order to determine the cathodic kinetics of the alloy in the studied electrolyte. For these experiments, an electrochemical cell with a three-electrode configuration (an Ag/AgCl/KCl_{sat} as reference electrode, a Pt wire as counter electrode and the titanium sample as working electrode) and a potentiostat (Autolab PGSTAT 302 N) were used. All potentials in this paper are given with respect to the Ag/AgCl/KCl_{sat} electrode (0.205 V vs SHE). The working electrode of each sample was fixed at the bottom of the electrochemical cell, exposing an area of 0.78 cm² to the solution. After the stabilization of the OCP, the cathodic polarization curves were recorded dynamically at a scan rate of 5 mV/min from the OCP towards -1V with respect to the OCP. Each measurement was carried out at least two times in order to check the repeatability of the experiments.

2.3. Tribocorrosion tests by Zero Resistance Ammetry

The tribocorrosion tests of this study were carried out coupling a ZRA to a ball-on-flat reciprocating tribometer (TriboCorr, Resmat Corporation, Canada) in a customized electrochemical cell with a physically separated cathode and anode of the same material described in detail elsewhere [15]. The ZRA allows one to measure the galvanic current between the passive (cathode) and depassivated (anode) areas of the sample during tribocorrosion testing at OCP. To do that, one of the samples (the anode) was covered by an organic coating thus after the first stroke the coating was removed and only

the depassivated area (anode) was exposed to the electrolyte. The second sample remained passive (cathode) and physically separated from the previous one (**Figure 4.A3.1**). The cathode area was 2.8 cm² for all experiments.

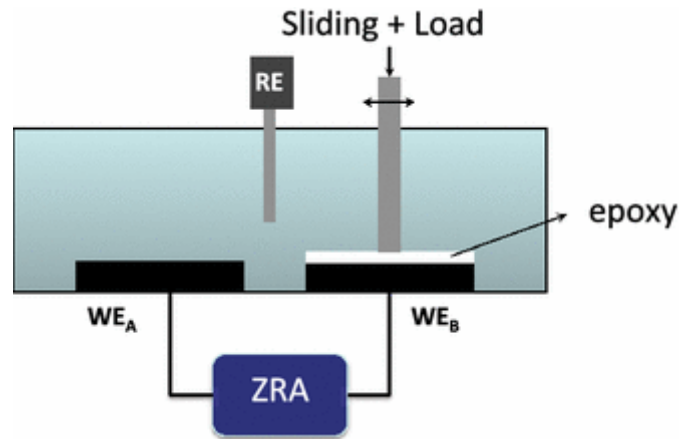


Figure 4.A3.1. Scheme of the electrochemical measurements carried out through a zero-resistance ammeter (ZRA) where WE_A is the cathode (unrubbed sample), WE_B is the anode (rubbed sample) and RE is the reference electrode

This experimental set-up enables on the one hand to measure the galvanic potential E_c , which is equivalent to the OCP measured in a standard tribocorrosion set-up [15] with no separation of cathode–anode and on the other hand to record the anodic current during the tribocorrosion experiment at OCP. The same reference electrode as the one used in the electrochemical tests was used for the tribocorrosion tests. Potential and current values were acquired simultaneously to the rubbing process.

The sliding was established by rubbing two different counter bodies, an alumina ball of 6 mm in diameter and a SiC pin, against the anode sample. The SiC pin was a cylinder of 1 cm diameter, which was ground axisymmetrically to a conical tip of 90° angle. The very end of the tip was microscopically rounded to a spherical finish with a diameter of 2.8 mm (blunt conical pin). **Figure 4.A3.2.** shows a sketch of the pin. In all cases, the frequency of the sliding pin was 1 Hz. The applied normal load used for the alumina ball was 3 N, which corresponded to an initial average contact pressure of 540 MPa. For the SiC pin, two normal loads of 2 and 10 N were used, which corresponded to initial average contact pressures of 830 and 1410 MPa, respectively. The yield strength of the alloy is 880 MPa. The potential, current and the frictional force were continuously monitored. Each measurement was carried out two times with new counterparts to check the repeatability of the experiments.

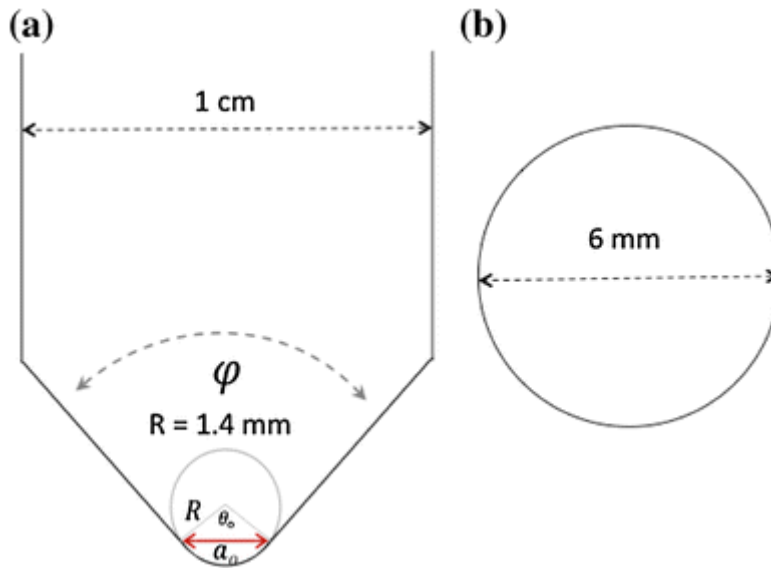


Figure 4.A3.2. Scheme of the a SiC pin and b alumina ball geometry used as counterpart for the tribocorrosion tests

The volume loss was quantified by means of confocal microscopy (IFM Alicona, Austria) at the end of the tests. Cross-sectional profiles were taken across the wear track for each sample. The width and depth of the wear track was measured from the wear track cross section taken at three positions along the wear track and measured twice at each position. By multiplying these by the length of the track, the volume loss was then calculated.

The wear track topography was analysed by scanning electron microscopy (SEM) JEOL6300)

3. Results

3.1. Cathodic behaviour

Figure 4.A3.3 shows the cathodic polarization curves of the cast Ti6Al4V alloy in AS. The current density linearly increases (negative sign) with the applied potential from around -0.4 to -0.8 V; thus, the cathodic Tafel equation can be used for describing the current evolution with the applied potential:

$$\eta = a_c - b_c \log i \quad (i)$$

where η is the overpotential ($E - E_{\text{corr}}$), a_c and b_c are the Tafel coefficients and i is the current density. By carrying out the linear regression the Tafel coefficients, $a_c = -2.2$ and $b_c = 0.23$, were obtained.

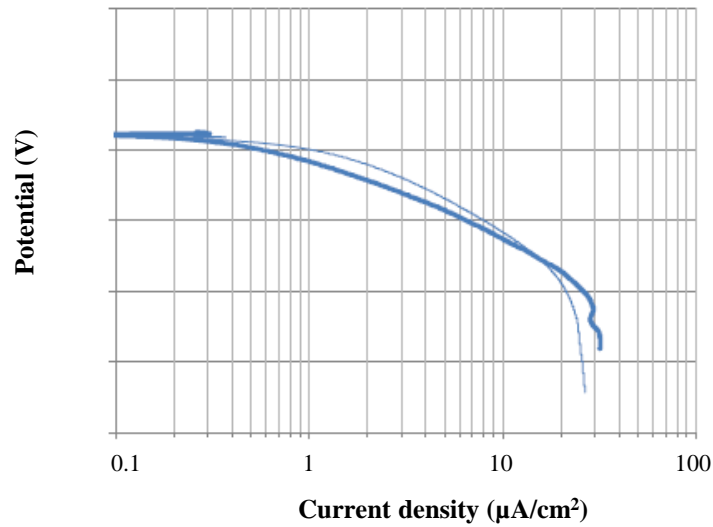


Figure 4.A3.3. Cathodic curves of the Ti6Al4V alloy in artificial saliva at 37 °C. Two repetitions are shown in the figure for checking repeatability

3.2. Tribocorrosion at OCP

Typical potential and current evolution with time in a tribocorrosion test carried out using the ZRA technique as described in Sect. 2.3 are shown in **Figure 4.A3.4**. The graphs show the electrochemical response for the Ti6Al4V at different contact pressures, achieved by applying different loads and changing the geometry and material of the counterpart. In all cases, at the onset of rubbing, the potential decays due to the galvanic coupling established between the anode and the cathode while the current abruptly increases due to the flow of electrons from the anode to the cathode.

The magnitude of the potential decay is mainly dependent on the counterpart geometry and thus on the initial contact pressure. There is a clear jump in potential decay between 540 MPa and the other two contact pressures, which indeed follows the yield strength of the material (880 MPa). In the case of the current evolution with time, surprisingly the highest current values are found for the smallest initial contact pressure. For the largest initial contact pressures, the current evolution with time is nearly the same analogously to the potential evolution with time.

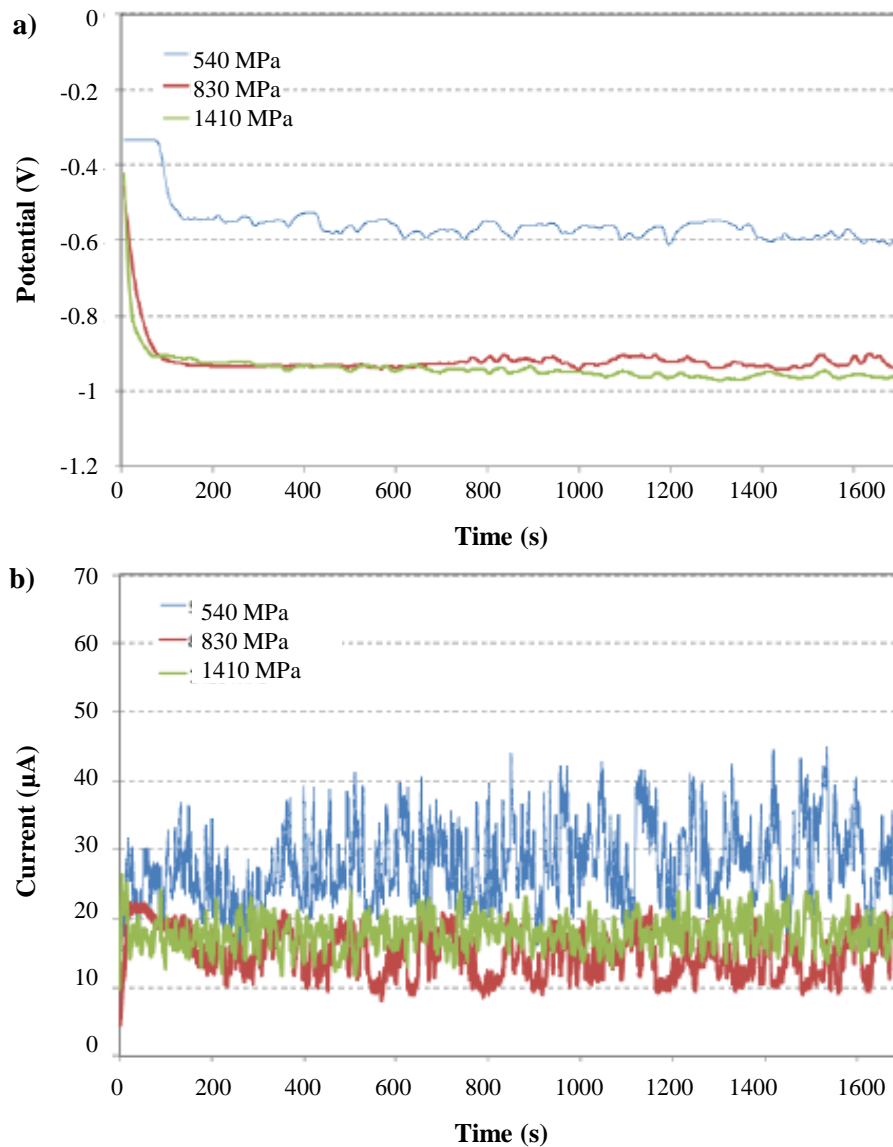


Figure 4.A3.4. (a) Potential and (b) current evolution with time for the Ti6Al4V alloy in artificial saliva at 37 °C. Only one test result is shown in the graphs for clarity however the repetition tests were successful.

3.3. Wear

The total volume loss (V_{tot}) was measured by non-contact profilometry (Alicona, IFM), and the chemical (V_{chem}) and mechanical (V_{mech}) contributions were quantified using the current obtained during rubbing after the tribocorrosion tests (**Figure 4.A3.4b**) and applying Faraday's law (**Equation 1**) and the mechanistic approach for tribocorrosion (**Equation 2**) [13]. The results are summarized in **Table 4.A3.1**. The chemical volume corresponds to the amount of material loss caused by wear accelerated corrosion and the mechanical volume is the difference between V_{tot} and V_{chem} .

$$V_{\text{chem}} = \frac{I \cdot t \cdot M}{n \cdot F \cdot \rho} \quad (1)$$

$$V_{\text{total}} = V_{\text{mech}} + V_{\text{chem}} \quad (2)$$

where V_{chem} is the volume loss due to the metal oxidation during time t , V_{total} is the total material loss in the wear track, V_{mech} is the mechanical volume loss, I is the anodic current measured during rubbing, F is the Faraday's constant (approximately 96,500 C/mol), n is the oxidation valence of the metal, M is the atomic mass of the metal and ρ is the density of the metal.

Table 4.A3.1 - Volume loss values (total, chemical and mechanical) after tribocorrosion tests at OCP using the ZRA set-up.

| Pressure (MPa) | Counterpart | V_{tot} ($\times 10^{-3}$)mm ³ | V_{chem} ($\times 10^{-3}$)mm ³ | V_{mech} ($\times 10^{-3}$)mm ³ |
|----------------|--------------------------------|---|--|--|
| 540 | Al ₂ O ₃ | 24±7 | 1.42±0.08 | 23.3±7 |
| 840 | SiC | 90±10 | 0.67±0.05 | 88.6±7 |
| 1410 | SiC | 130±7 | 0.84±0.08 | 129±7 |

The average friction during rubbing is also shown in the table

The wear topography of the Ti6Al4V alloy and the alumina counterpart after tribocorrosion testing in AS is shown in **Figures 4.A3.5 and 6**, respectively. For the tests performed against SiC pin (largest initial contact pressures), the surface appears smooth and plastically deformed. When the counterpart material changes to alumina ball (lowest initial contact pressure), wear debris is observed on the wear track surface. Material transfer and wear of the counterpart are also observed.

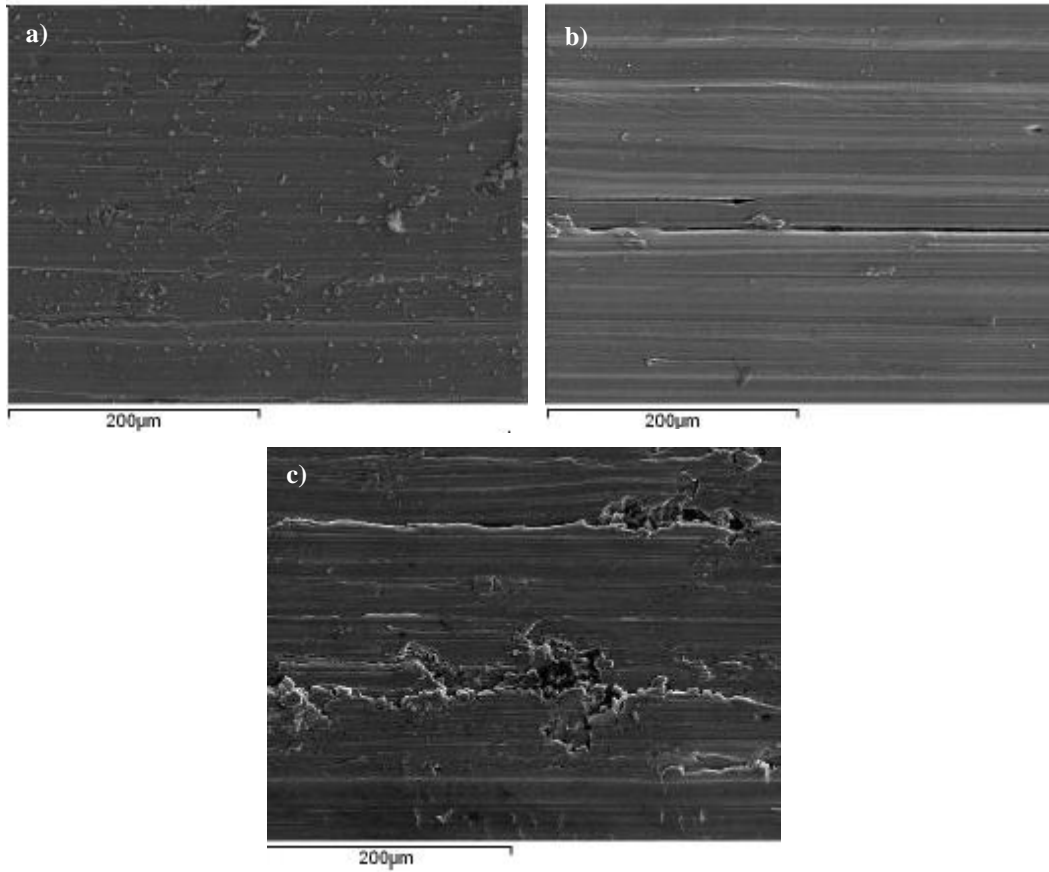


Figure 4.A3.5. SEM images of the center of the wear tracks after tribocorrosion testing in artificial saliva at OCP: (a) against alumina ball at 3 N normal load (540 MPa), (b) against SiC pin at 2 N normal load (830 MPa) and (c) against SiC pin at 10 N normal load (1,410 MPa).

The roughness of the wear tracks was 1 µm for a and b 1.5 µm for c.

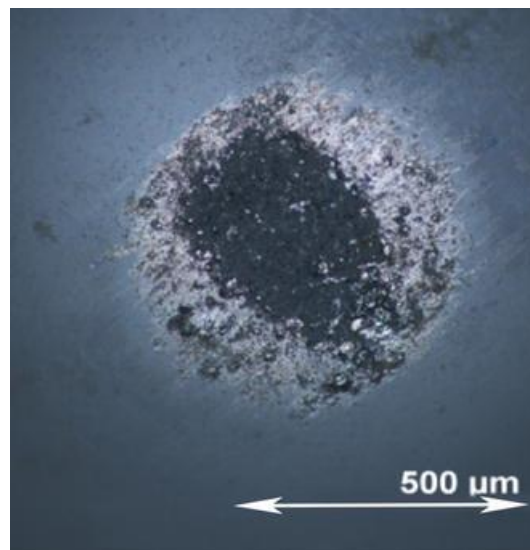


Figure 4.A3.6. Optical image of the alumina counterpart after tribocorrosion testing in artificial saliva at 3 N normal load

4. Discussion

4.1. Galvanic coupling model

4.1.1. Using i_a as fitting parameter

Vieira et al. developed a galvanic coupling model for tribocorrosion to interpreting and quantifying wear at OCP of aluminium alloys [16]. An electrochemical approach for representing the cathodic potential as a function of kinetic parameters (Tafel coefficients and corrosion potential) and anode to cathode area ratio (ratio between the depassivated area and passive area) was proposed according to the following equation:

$$E_c = E_{\text{corr}} + a_c - b_c \log i_a - b_c \log \frac{A_a}{A_c} \quad (3)$$

where E_c is the cathodic potential outside the wear track (the potential measured during tribocorrosion at OCP), a_c and b_c are constants calculated from Tafel equations, i_a is the anodic current density produced during the depassivation process inside the wear track, and A_a and A_c are the surface areas of the anode and the cathode, respectively.

The model is based on a simple galvanic coupling model used in corrosion, but adapted to tribocorrosion situations. The model requires not only kinetic parameters (which can be obtained from independent electrochemical tests such as cathodic potentiodynamic curves shown in **Figure 4.A3.3**) and the area ratios (which can be measured geometrically at the end of the test), but it also requires the anodic current (i_a), which was proposed as a fitting parameter. This fitting parameter should be constant for an experiment at a constant potential and during OCP testing it is expected to change as potential changes [17].

Figure 4.A3.7 shows the experimental evolution of the galvanic potential with time for the Ti6Al4V alloy sliding against SiC and Al₂O₃ at the different initial contact pressures along with the mathematical simulation of the model (**Equation 3**) using two different values for the fitting parameter ($i_a = 5$ and 0.5 mA/cm^2). The i_a value of 5 mA/cm^2 was previously used by Papageorgiou and Mischler when studying the tribocorrosion behaviour at OCP of pure Titanium in NaCl [17]. In this work, a similar fitting parameter could be expected since for different passive metals, i.e. Al, stainless steel and pure Ti values varying between 5 and 10 mA/cm^2 have been reported [16, 17].

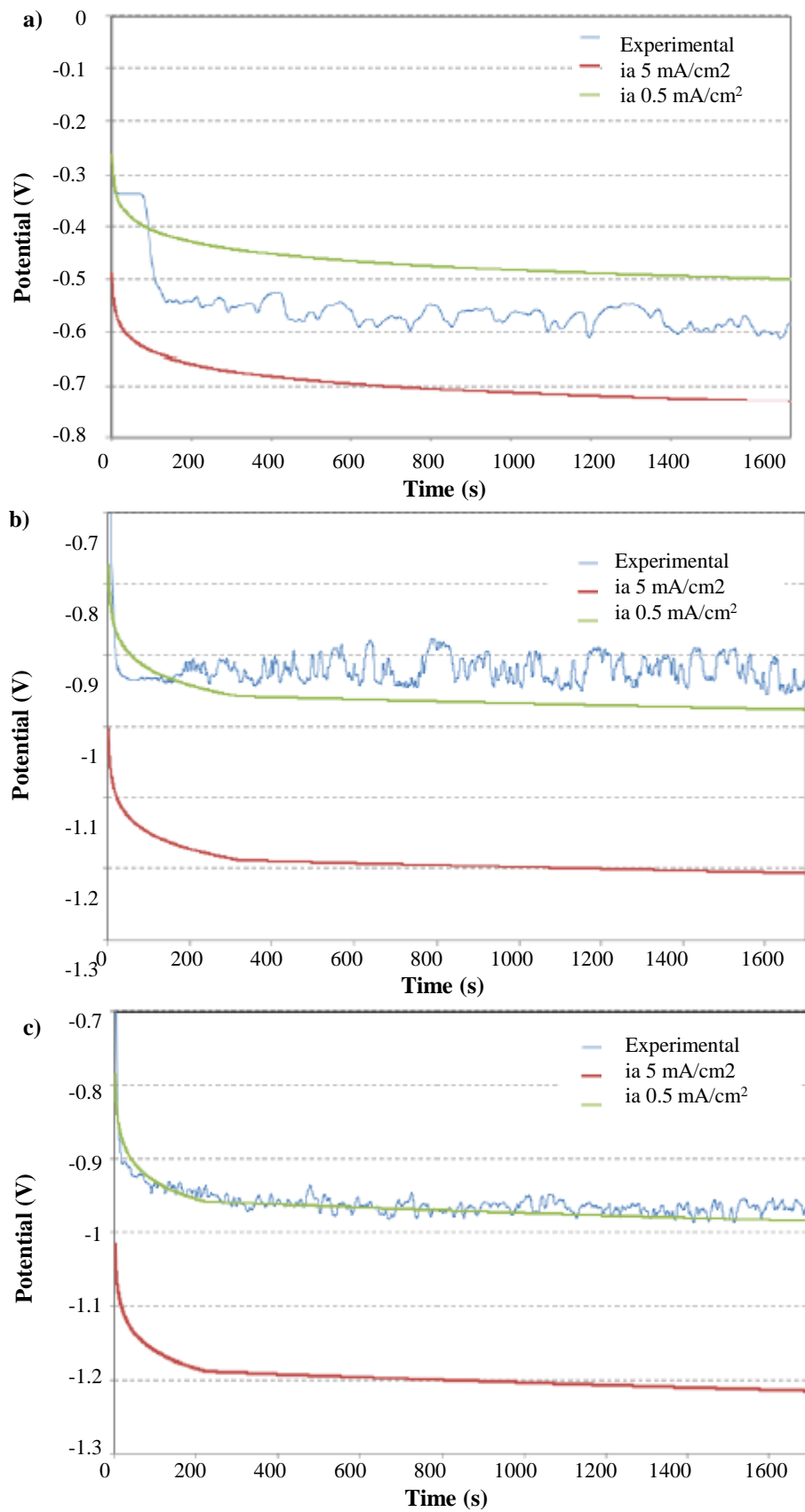


Figure 4.A3.7. Experimental potential evolution with time for the Ti6Al4 V against (a) Al₂O₃ 540 MPa, (b) SiC pin 843 and (c) 1,410 MPa measured by ZRA in artificial saliva at 37 C. The model OCP (mathematical simulation) is superimposed in all figures according to equation 3 using i_a as fitting parameter

When using 5 mA/cm^2 as fitting parameter, the modelled evolution of potential with time (red curve) is lower than the experimental values (blue curve) in all tribocorrosion tests. However, when changing the fitting parameter to one order of magnitude lower, 0.5 mA/cm^2 , the model perfectly fits for the largest initial contact pressure (1410 MPa), deviates slightly at 830 MPa and predicts a more positive potential at 540 MPa.

Clearly, using a fitting parameter for modelling, the potential evolution is not a very accurate method for the experimental results obtained in this work. Indeed, Vieira et al. [16] already anticipated that the quantification approach taken when using a fitting parameter neglects relevant effects such as the increase of the wear track area induced by the surface roughening or debris particles formation, the deviation from the Archard wear behaviour in the initial run-in and non homogeneous potential distribution on the sample surface.

4.1.2. Using experimental current density (ZRA)

For overcoming the limitations of using a fitting parameter for the galvanic coupling model, the experimental technique using a ZRA was proposed recently [15]. The ZRA technique allows measuring experimentally the galvanic potential and the anodic current (i_a) during rubbing by physically separating the wear track (anode) from the passive area (cathode) as shown in **Figure 4.A3.1**. **Equations 3** and **4** have been applied using the measured anodic current I_a ($I_a = i_a \cdot A_a$) and the potential evolution during rubbing at OCP, respectively. The results of the experimental and the simulated values using ZRA are shown in **Figure 4.A3.8**, which shows the accuracy of the ZRA technique for modelling the potential and current evolution during sliding.

$$\log i_a = \frac{E_{\text{corr}} + a_c - E_c - b_c \log \frac{A_a}{A_c}}{b_c} \quad (4)$$

Measuring experimentally the potential and current evolution with time at OCP and applying the galvanic model, the ZRA technique can be used for determining the evolution with time of the relationship between the depassivated area (anode) with the wear track area predicted by Archard wear law. Assuming that the anodic current density (i_a) in **Equation 3** equals the anodic current measured during rubbing at OCP divided the Archard wear area (A_{wt}), the relationship between the real depassivated area (A_a) and the Archard prediction (A_{wt}) can be determined using the following equation:

$$E_c = E_{\text{corr}} + a_c - b_c \log \frac{I_a}{A_{wt}} - b_c \log \frac{A_a}{A_c} \quad (5)$$

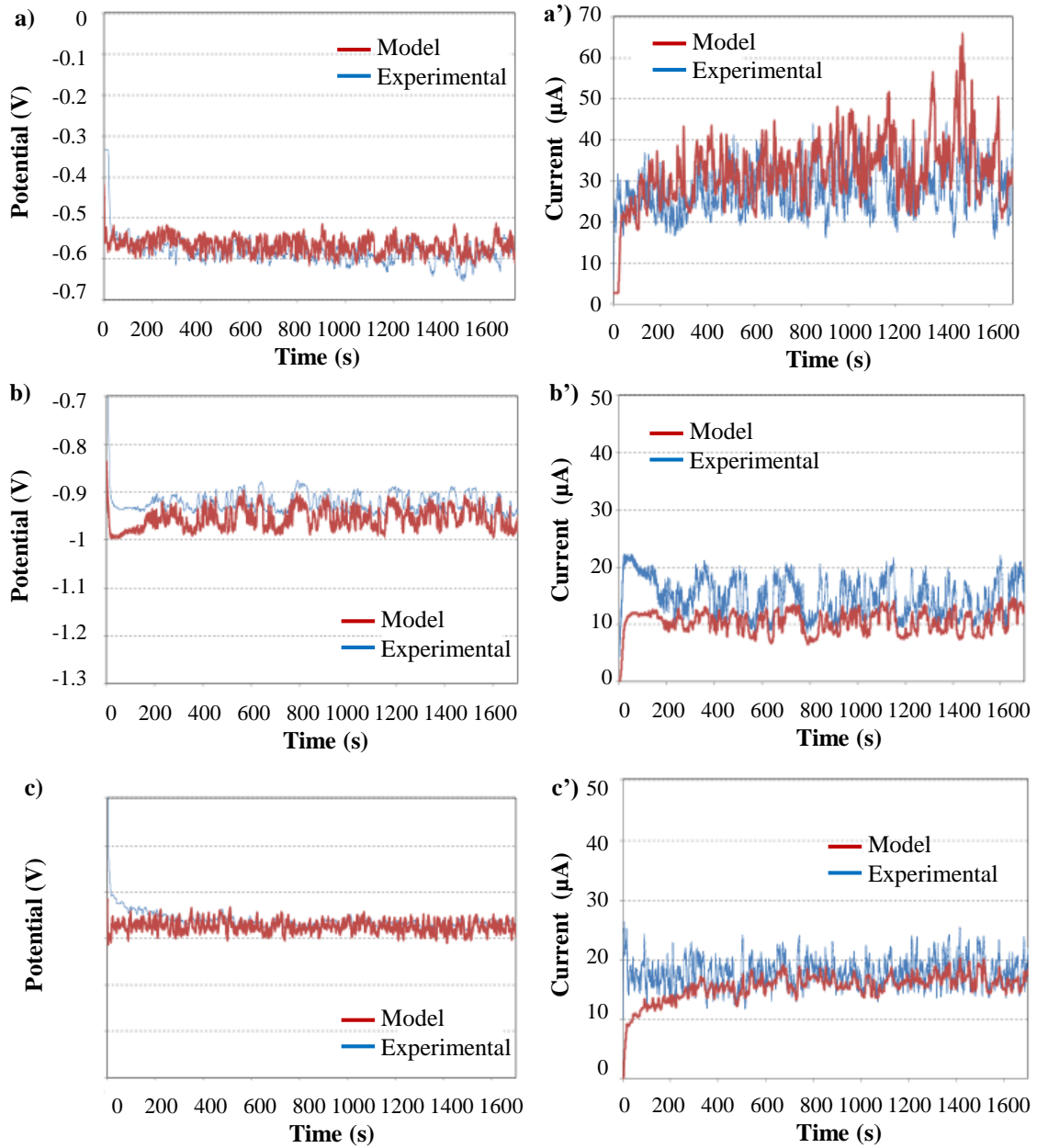


Figure 4.A3.8 Potential and current evolution with time of the Ti6Al4V rubbed against (a–a') Al₂O₃ ball at 540 MPa, (b–b') SiC pin at 830 MPa and (c–c') SiC pin at 1,410 MPa in artificial saliva at 37 °C. The blue curve corresponds to the experimental data, while the red one is the simulated response according to Eqs. 3 and 4.

The wear track area (A_{wt}) can be determined considering the Archard wear law and the linear relationship between wear volume (V_{tot}) and rubbing time (t), $V(t) = C_w t$, where C_w is a constant that can be calculated by dividing the wear track volume measured at the end of the tests (**Table 4.A3.1**) by the duration of rubbing. Depending on the geometry of the counterpart, the A_{wt} and the theoretical area of contact as predicted by Hertz ($A_{contact}$) can then be represented as a function of time [15, 17].

Figure 4.A3.9 shows the evolution of the theoretical (A_{wt}) and experimental depassivated area (A_a) as a function of rubbing time. In the same graph, the Hertzian area of contact ($A_{contact}$) has been also plotted for the different initial contact pressures. It is worth noticing that there is more than one order of magnitude difference between the Hertzian area of contact and the depassivated area of contact.

A good correlation between the wear track area and the depassivated area at the highest initial contact pressures was obtained (**Figures 4.A3.9b, c**). This correlation corresponds well with a clear plastic deformation of the wear tracks (**Figures 4.A3.5b, c**). In both cases, the area rapidly increases at the beginning of the test and after around 200s, the slope abruptly changes. This change in slope is purely geometrical and it corresponds with the indenter reaching the conical part as already discussed in a previous work [15]. At 830 MPa initial contact pressure, A_a is slightly lower than A_{wt} , which means that not all wear track area is depassivated. Indeed, the relation A_a/A_{wt} in this case is below 80 % after the first 200s, while for the initial contact pressure of 1410 MPa, it reaches 100 %. Assuming that depassivation occurs by plastic deformation of asperities, this is in good agreement with the SEM images that show less plastic deformation and small and isolated wear particles at 830 MPa, thus smaller A_a with respect to A_{wt} .

Figure 4.A3.9a shows the experimental results when the Ti6Al4V slides against an Al_2O_3 ball at an initial contact pressure of 540 MPa, which is well below the yield strength of the alloy thus no plastic behaviour is expected. In this case, A_a cannot be predicted by the Archard law as clearly shown in **Figure 4.A3.9a**, where A_{wt} is smaller than A_a ; therefore, the current is generated not only by the depassivation of the wear track but also by other wear mechanisms. Indeed, when observing the wear track after rubbing, a large amount of wear debris is present (**Figure 4.A3.5a**).

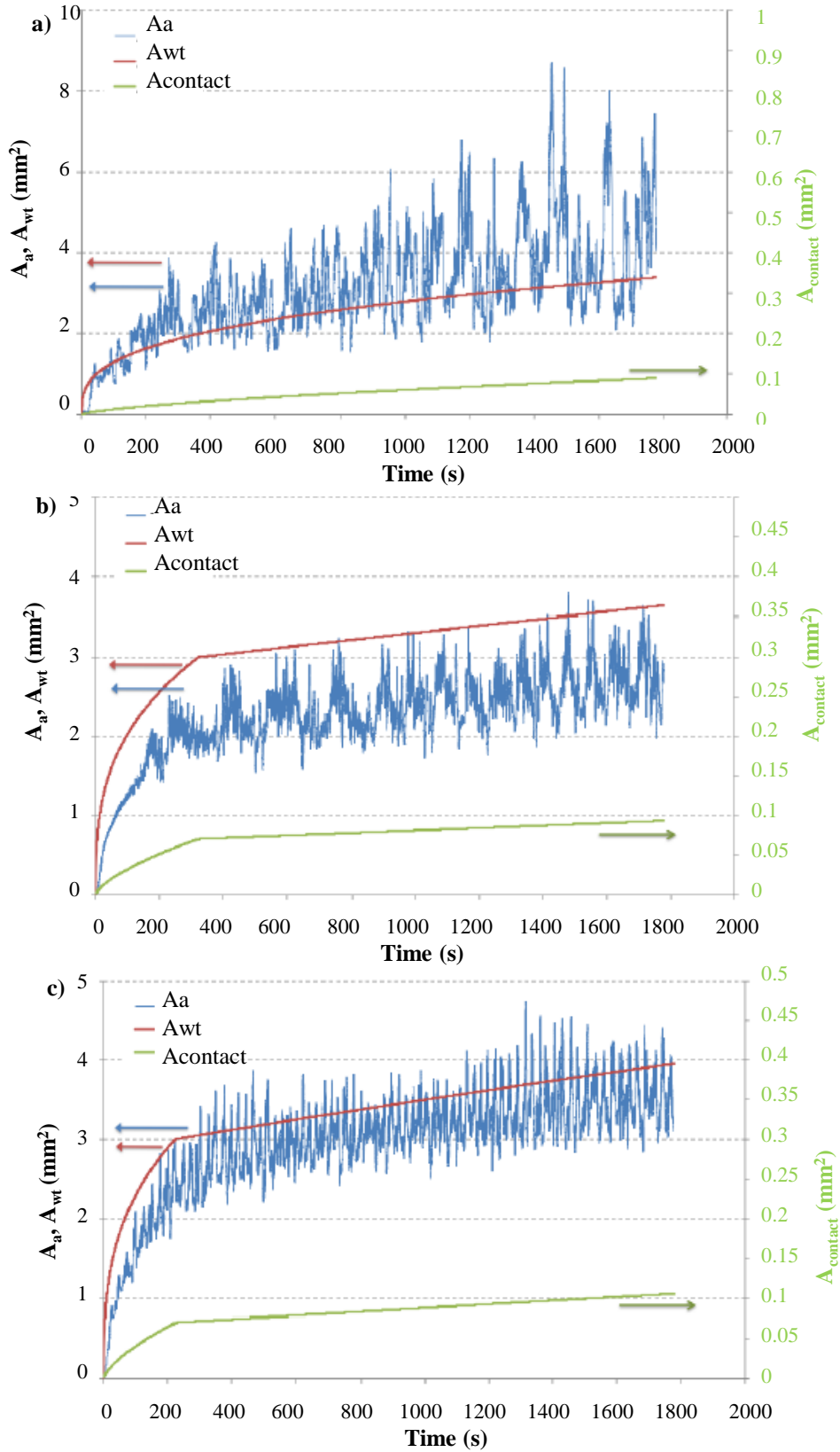


Figure 4.A3.9. Evolution of the depassivated (A_a) and Hertzian ($A_{contact}$) areas versus time from the potential and current values measured by ZRA. Superimposed the wear track area (A_{wt}) obtained by the Archard wear law and the geometry of the counterpart

4.2. Wear mechanisms

The ZRA-tribocorrosion technique allowed measuring both potential and current during rubbing at OCP. For the three tribocorrosion test conditions in this work, the highest current during rubbing was surprisingly obtained for the lowest initial contact pressure (540 MPa, using an alumina ball as counterpart). The image of the alumina counterpart (**Figure 4.A3.6**) shows that together with material transfer some particles or grains of alumina could have been pulled out from the ball, analogously to what was reported by Dearnley et al. [19]. This may cause an increase in the chemical dissolution of the titanium surface when sliding against the alumina ball. In addition, a deviation from the Archard wear equation in the depassivated area was also found. When using a SiC pin as counterpart material and increasing the initial contact pressure to 830 and 1410 MPa, the current evolution and the depassivated area of contact changed. At 1410 MPa, the depassivated area of contact followed well the Archard wear prediction as expected from a material experiencing large plastic deformation (**Figure 4.A3.5c**). In the other two tribocorrosion conditions, the initial contact pressure was below the yield strength of the alloy (880 MPa), and therefore, a deviation from the Archard prediction was found, which was clearly observed for the lowest initial contact pressure of 540 MPa (**Figure 4.A3.9a**).

When the initial contact pressure of the tribocorrosion test was well below the yield strength of the material, wear debris was observed on the wear track after testing (**Figure 4.A3.4a**). This wear debris formation and its oxidation in the electrolyte contributed to an increase in the anodic current measured (**Figure 4.A3.4a**). In this case, the wear mechanism is mainly governed by the presence of the third body, which could be detected by the ZRA technique. Indeed, an identical test performed on a Ti6Al4V alloy obtained by powder metallurgy showed a larger amount of debris formed after testing; in this case, the current during rubbing was the largest of all (**Figure 4.A3.10**).

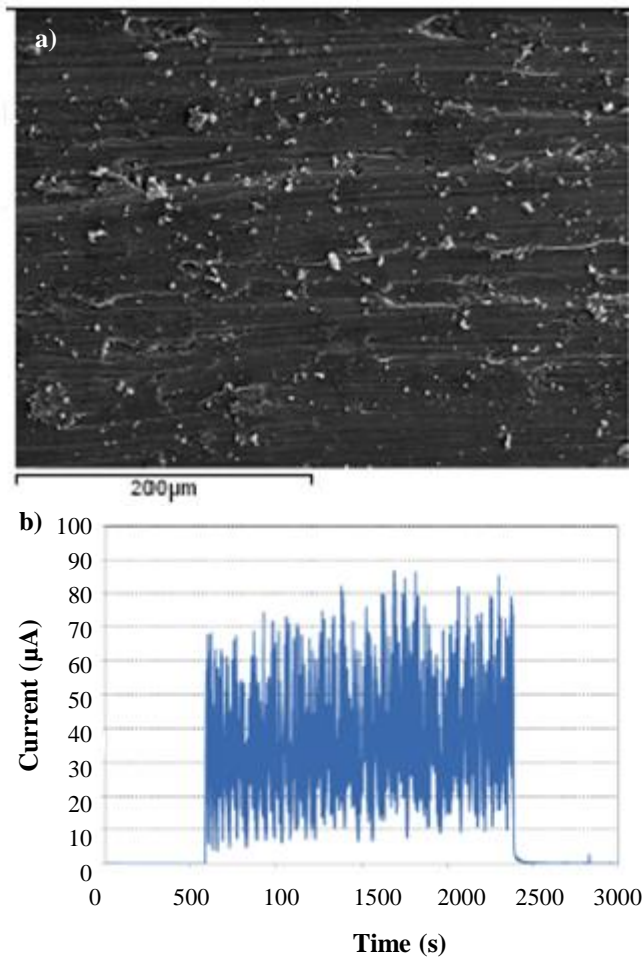


Figure 4.A3.10. (a) SEM image of the center of the wear track after tribocorrosion testing of a Ti6Al4V obtained by powder metallurgy in artificial saliva at OCP against alumina ball at 3 N normal load (540 MPa) and (b) current evolution with time measured by ZRA

5. Conclusions

In this work, the tribocorrosion mechanisms at OCP of a Ti6Al4V biomedical alloy in AS have been investigated by means of ZRA coupled to a triboelectrochemical cell. Different initial mechanical conditions have been tested, e.g. below, above and at the yield strength of the alloy. The following conclusions can be drawn:

- The ZRA technique for tribocorrosion has been used for studying the triboelectrochemical behaviour of a Ti-based biomedical alloy in AS at OCP by obtaining experimental values for the anodic current (wear accelerated corrosion during rubbing at different initial mechanical conditions).
- The experimental measurement of the anodic current and the galvanic potential of the wear track (anode) and the passive material (cathode) in a tribocorrosion test allowed for an accurate simulation of the current and potential during rubbing using the galvanic coupling model for tribocorrosion based on the kinetics of the cathodic reaction.
- The highest anodic current was obtained when the initial contact pressure was well below the yield strength of the alloy. This corresponded to a deviation of the wear behaviour from the Archard law caused by the presence of third bodies, as observed in the scanning electron microscopy analysis.
- The ZRA technique for tribocorrosion and the galvanic model allows predicting the real depassivated area and therefore, the deviation of the wear mechanisms from Archard wear law at OCP.

6. Acknowledgements

The authors would like to thank financial support from NTNU (project number 69450741) for performing the experiments of this work and Universitat Politècnica de Valencia VLC/Campus (PMIA-2013) for the mobility grant.

7. References

- [1] É. Martin, M. Azzi, G.A. Salishchev, J. Szpunar, Influence of microstructure and texture on the corrosion and tribocorrosion behaviour of Ti–6Al–4V. *Tribol. Int.* 43 (2010) 918–924
- [2] M. Nosonovsky, B. Bhushan, Green tribology: principles, research areas and challenges, *Philos. Trans. R. Soc. A Math. Physical Eng. Sci.* 368 (2010) 4677–4694
- [3] M. Geetha, A.K. Singh, R. Asokamani, A.K. Gogia. Ti based biomaterials, the ultimate choice for orthopaedic implants – A review, *Prog. Mater. Sci.* 54 (2009) 397–425
- [4] M. Niinomi, D. Kuroda, K. Fukunaga, M. Morinaga, Y. Kato, T. Yashiro, et al.. Corrosion wear fracture of new β type biomedical titanium alloys. *Mater. Sci. Eng. A.* 263 (1999) 193–199
- [5] D. Kuroda, M. Niinomi, M. Morinaga, Y. Kato, T. Yashiro. Design and mechanical properties of new β type titanium alloys for implant materials. *Mater. Sci. Eng. A.* 243 (1998) 244– 249
- [6] E. Eisenbarth, D. Velten, M. Müller, R. Thull, J. Breme. Biocompatibility of β -stabilizing elements of titanium alloys. *Biomaterials.* 25 (2004) 5705–5713
- [7] N.S. More, N. Diomidis, S.N. Paul, M. Roy, S. Mischler. Tribocorrosion behaviour of β titanium alloys in physiological solutions containing synovial components. *Mater. Sci. Eng. C.* 31 (2011) 400–408
- [8] I. Milošev, M. Metikoš-Huković, H.-H. Strehblow. Passive film on orthopaedic TiAlV alloy formed in physiological solution investigated by X-ray photoelectron spectroscopy. *Biomaterials.* 21 (2000) 2103–2113
- [9] J. Komotori, N. Hisamori, Y. Ohmori. The corrosion/wear mechanisms of Ti–6Al–4V alloy for different scratching rates. *Wear,* 263 (2007) 412-418

- [10] M.K. Dimah, F. Devesa Albeza, V. Amigó Borrás, A. Igual Muñoz. Study of the biotribocorrosion behaviour of titanium biomedical alloys in simulated body fluids by electrochemical techniques. *Wear*, 294–295 (2012) 409-418
- [11] M P Licausi, A Igual Muñoz, V Amigó Borrás. Tribocorrosion mechanisms of Ti6Al4V biomedical alloys in artificial saliva with different. pHs *J. Phys. D: Appl. Phys.* 46 (2013) 404003
- [12] M.J. Runa, M.T. Mathew, L.A. Rocha. Tribocorrosion response of the Ti6Al4V alloys commonly used in femoral stems. *Tribology International*, 68 (2013) 85-93
- [13] A.I. Munoz, N. Espallargas. Tribocorrosion mechanisms in sliding contacts in: D Landolt, S Mischler (Eds.). *Tribocorrosion of Passive Metals and Coatings* (2011)
- [14] S. Mischler. Triboelectrochemical techniques and interpretation methods in tribocorrosion: a comparative evaluation. *Tribology International* 41 (2008) 573–583
- [15] N. Espallargas, R. Johnsen, C. Torres, A.I. Muñoz. A new experimental technique for quantifying the galvanic coupling effects on stainless steel during tribocorrosion under equilibrium conditions. *Wear* 307 (2013) 190-197
- [16] A.C. Vieira, L.A. Rocha, N. Papageorgiou, S. Mischler. Mechanical and electrochemical deterioration mechanisms in the tribocorrosion of Al alloys in NaCl and in NaNO₃ solutions. *Corrosion Science* 54 (2012) 26–35
- [17] N. Papageorgiou, S. Mischler. Electrochemical Simulation of the Current and Potential Response in Sliding Tribocorrosion. *Tribology Letters* 48(3) (2012) 271-283.
- [18] N. Papageorgiou, A. von Bonin, N. Espallargas. Tribocorrosion mechanisms of NiCrMo- 625 alloy: An electrochemical modeling approach. *Tribology International* 73 (2014) 177-186

-Chapter 5-

**Corrosion and tribocorrosion behaviour
of Ti6Al7Nb biomedical alloy
in artificial saliva**

-Article 1-

INFLUENCE OF THE ALLOYING ELEMENT ON THE ELECTROCHEMICAL BEHAVIOR OF Ti₆Al₇Nb OBTAINED BY POWDER METALLURGY

M.P. Licausi, A. Igual Muñoz, V. Amigó Borrás

(Manuscript)

**INFLUENCE OF THE ALLOYING ELEMENT ON THE
ELECTROCHEMICAL BEHAVIOR OF Ti6Al7Nb OBTAINED BY
POWDER METALLURGY**

M.P. Licausi¹, V. Amigó¹, A. Igual Muñoz^{2*}

1- Universitat Politècnica de València, Instituto de Seguridad Industrial, Radiofísica y Medioambiental. Camí de Vera s/n, 46022València

2- Universitat Politècnica de València, Institut de Tecnologia de Materials. Camí de Vera s/n, 46022València.

***Corresponding author**

Abstract:

The electrochemical behavior of Ti6Al, Ti7Nb and Ti6Al7Nb processed by powder metallurgy has been investigated by different electrochemical techniques in order to study the influence of the alloying element and the applied potential on the corrosion mechanisms of these titanium alloys. All studied alloys show very low passive dissolution rate in a wide range of potentials in artificial saliva. At low potential the alloying element does not influence passive film thickness. However the addition of aluminium decreases corrosion resistance by increasing the passive dissolution rate. This effect is enhanced with the applied potential.

Keywords: Titanium alloys, powder metallurgy, corrosion, Electrochemical Impedance Spectroscopy, Surface analysis.

1. Introduction

Titanium and its alloys are commonly used as dental material for implants as a result of their good biocompatibility, mechanical properties and high corrosion resistance. The latter is mainly due to the spontaneous formation of a 3–7 nm thick amorphous [1] or crystalline passive titanium oxide (TiO_2) [2]. One of the most widely used alloy in the biomedical field is the Ti6Al4V (numbers indicate the wt% of the alloying elements in the titanium alloy) which contains Aluminium to increase its strength and decrease its density while Vanadium is used as an Aluminium scavenger to decrease corrosion [3]. Although the Ti6Al4V alloy exhibits excellent corrosion properties, Vanadium is known for its cytotoxicity and the metal ions released by corrosion and/or wear processes may cause allergic and adverse reactions in the human body [4]. During recent years a number of different Ti-based alloys [4] (Ti–Mo–Nb–Al, or Ti–Mo–Nb–Al–Cr–Zr alloys, and Ti–Zr–Nb, Ti–Al–Nb, or Ti–Zr–Nb–Ta–Pd) have been studied in order to replace the current Ti6Al4V alloy by alloying the titanium with other elements such as niobium. The Ti6Al7Nb alloy has been produced as an alternative $\alpha + \beta$ alloy exhibiting similar mechanical properties to those of Ti6Al4V alloy. Tamilselvi et al. [5] studied the electrochemical behaviour of Ti6Al4V and Ti6Al7Nb alloys in a saline solution (0.9% NaCl) and have reported an increased corrosion resistance than the former one. In fact, Nb_2O_5 is considered to be more stable, less soluble and more biocompatible oxide compared to V_2O_5 [6], thereby improving the biocompatibility of the Ti6Al7Nb alloy as well.

Besides biocompatibility, osseointegration is a key factor to predict the success of dental implants. Titanium such as other metals cannot promote bone growth. To add biofunctionality to metals, research has been focused on surface modification techniques with the goal to improve hard tissue compatibility or accelerate bone formation [7]. Indeed studies have shown that surface topography (roughness and porosity) play an important role in the biological response of implants as it influences osteoblastic proliferation, differentiation and extracellular matrix protein expressions [8]. Based on that, porous titanium alloys processed by powder metallurgy is of great interest in order to improve mechanical anchorage of the implant to the bone. Recently sintered Ti6Al7Nb has shown to have similar mechanical properties to its wrought equivalent material suggesting that it would be a promising alternative for biomedical applications [9]. However even though titanium exhibit good corrosion resistance due to the formation of a semiconductive oxide film, porosity has shown to affect the electrochemical behaviour of materials [10]. Some studies have reported corrosion due to the trapping of electrolyte species and the depletion of oxygen depending on the morphology of pores [11, 12]. Alves et al reported the formation of less protective oxide film in the pores when studying highly porous titanium [13].

Corrosion resistance is of main concern for implant material as it can lead to ion dissolution and harmful body reactions. The aim of this study is to electrochemically characterize Ti6Al7Nb obtained by powder metallurgy and to investigate the influence of the alloying element on its corrosion resistance.

2. Experimental

2.1. *Materials and electrolytes*

The materials used as working electrodes were Ti6Al, Ti7Nb and Ti6Al7Nb sintered titanium samples where the numbers indicate the weight percentage of the alloying elements. The sintered titanium material was fabricated by powder metallurgy according to the following procedure: powder compression, applying a compacting pressure of 400 MPa without the addition of any lubricant and sintering sequence consisting in a thermal cycle with specific heating and cooling ramps. The initial heating ramp consists in heating at 800 °C during 30 min in order to stabilize both the oven and the material at the same temperature and to avoid cracking due to thermal gradients. The sintering process lasts 2 hours at 1250 °C in a vacuum tube oven.

Before use, the sintered samples were cleaned with acetone in an ultrasonic bath in order to remove any existing particle from the pores and tested without any prior polishing.

The three different alloys were tested in the same electrolyte, a modified Fusayama Meyer artificial saliva (AS), which simulates the human saliva. The composition of this solution, which closely resembles natural saliva, is: 0,4g NaCl, 0,4gKCl, 0,6g CaCl₂, 0,58g Na₂HPO₄·12H₂O, 1g urea, distilled water at 1L. The pH of the solution is 6.5.

All tests were carried out at 37°C +/- 1°C, under aerated conditions and repeated three times for checking their reproducibility.

2.2. *Microstructure*

In order to observe the materials' microstructure the alloys were mechanically polished with 1000 grit with SiC paper followed by a polishing with 9µm diamond suspension. The samples were then etched with Kroll's reagent, consisting of 10ml HF, 5ml HNO₃ and 85ml H₂O. The revealed microstructure was examined by optical microscopy

2.3 Electrochemical Experiments

The electrochemical behavior of the titanium alloys was studied using a three-electrode electrochemical set-up: a working electrode (the titanium sample), a reference electrode (Ag/AgCl 3MKCl) and a platinum coiled wire acting as a counter electrode. A potentiostat (solatronTM1286) was used for the electrochemical tests. All potentials are given with respect to the reference electrode (205 mV vs SHE). The real surface area was determined following a previously reported procedure [14].

Potentiodynamic polarization curves of the 3 different sintered alloys were performed to assess corrosion resistance by recording anodic and cathodic currents. These tests were carried out in the AS by scanning the potential from -1V to 3V at a scan rate of 0.5 mV/s

From the potentiodynamic curves several electrochemical parameters were calculated: the corrosion potential (E_{corr}), the corrosion current density (i_{corr}), determined by the Tafel slope extrapolation and the corrosion passive current density (i_p), obtained by the measured current within the passive domain.

Potentiostatic tests were carried out, taking into account the potentiodynamic curves, by applying a constant potential of 0.2, 1 and 2V within the passive domain and -0.5 and -1V within the cathodic domain of the alloys and measuring the response in current. The final passive current (i_{pass}) and the electrochemical charge (Q) were obtained from those experimental results.

Electrochemical impedance spectroscopy (EIS) measurements were carried out on Ti, Ti6Al7Nb and Ti7Nb under potentiostatic conditions (at the constant passive potentials of 0.2, 1 and 2 V_{Ag/AgCl}). Impedance measurements were performed from 2 mHz to 10⁴ Hz with an amplitude of the sinusoidal wave of 10 mV. The impedance data were analysed with the Zview 2.70 software package and fitted to the corresponding equivalent circuit.

3. Results

3.1 Material characteristics

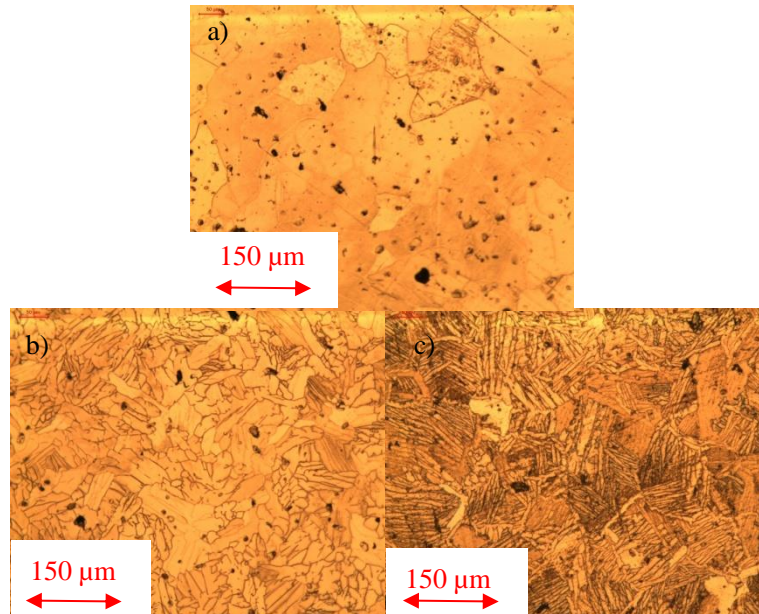


Figure 5.A1.1. Optical images of the microstructure of (a) Ti6Al, (b) Ti6Al7Nb and (c) Ti7Nb alloys

Microstructures of all samples are shown in **Figure 5.A1.1**. For the three alloys the grains have an equiaxial structure as the material has been sintered. Microstructure analysis shows two distinct structures. An alpha (α) microstructure is observed for the Ti6Al alloy whereas the two other alloys show an $\alpha+\beta$ microstructure due to the addition of niobium. The lighter areas correspond to the α phase, while the darker ones are the β phase. A coarser structure for the Ti7Nb alloy is observed.

3.2. Electrochemical tests

3.2.1. DC tests

The polarization curves of the titanium alloys in the artificial saliva are shown in **Figure 5.A1.2**. Three different domains were observed in all cases. First is the cathodic domain which includes potentials below -0.25 and -0.35 $V_{Ag/AgCl}$ for Ti6Al7Nb and Ti6Al/Ti7Nb respectively. In this zone the current is determined by the reduction of water and, partially, of dissolved oxygen. The domain comprised between the previous potentials and approximately $0.4V_{Ag/AgCl}$ is characterized by the transition from cathodic to anodic current at the corrosion potential. Finally a large passive zone was found between

0.5 V_{Ag/AgCl} and 2 V_{Ag/AgCl}, where the current density remained approximately constant. This domain is characterized by the presence of the passive film which reduces the corrosion rate by reducing the dissolution of the metal. No transpassive domain was observed for none of the alloys.

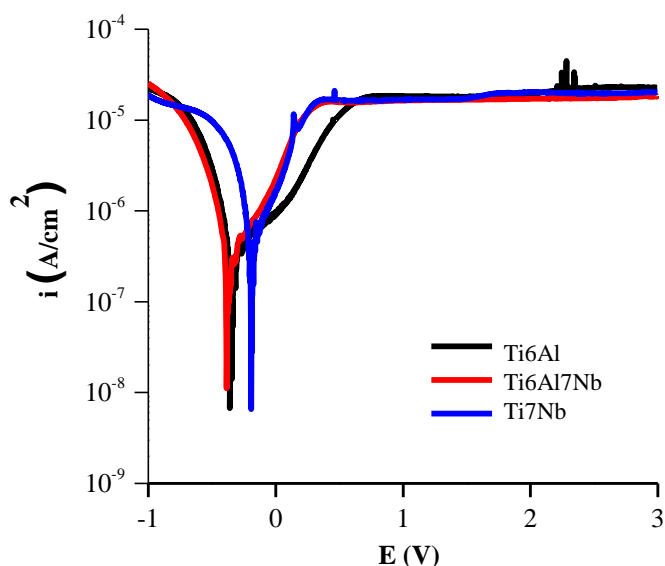


Figure 5.A1.2 Potentiodynamic curves in AS at 37±1°C

The electrochemical parameters extracted from the curves are summarized in **Table 5.A1.1**, including the OCP values obtained before the polarization curves. Ti6Al7Nb exhibits the lowest corrosion current density. The E_{corr} of Ti7Nb is approximately 100 mV lower than for Ti6Al and Ti6Al7Nb but the i_p is similar for all the materials regardless of the alloying element.

Table 5.A1.1 - Electrochemical parameters of Ti6Al, Ti7Nb and Ti6Al7Nb in AS.

| Material | OCP (mV) | E_{corr} (mV) | i_{corr} ($\mu\text{A}/\text{cm}^2$) | i_p ($\mu\text{A}/\text{cm}^2$) |
|----------|----------|------------------------|---|-------------------------------------|
| Ti6Al | 62±2 | -344±1 | 0.31±0.02 | 23.1±0.25 |
| Ti7Nb | -47±7 | -163±27 | 0.34±0.04 | 20.5±0.32 |
| Ti6Al7Nb | -169±1 | -359±26 | 0.25±0.01 | 17.3±0.91 |

In order to characterize the influence of the potential on the passivation kinetics of the titanium alloys, potentiostatic tests were carried out. **Figure 5.A1.3** shows the evolution of the current density during 1h at all potentials under study for all the titanium alloys. At -1 V (**Figure 5.A1.3a.**), the potential lies within the cathodic domain and the overall current is dominated by the cathodic reaction as consequence of reduction of water and dissolved oxygen. This explains the negative value of the current density from the beginning of the test. At the passive potentials (**Figure 5.A1.3b, c and d**) an exponential decay in the current with time was observed as the metal passivates due to the oxide film formation and growth.

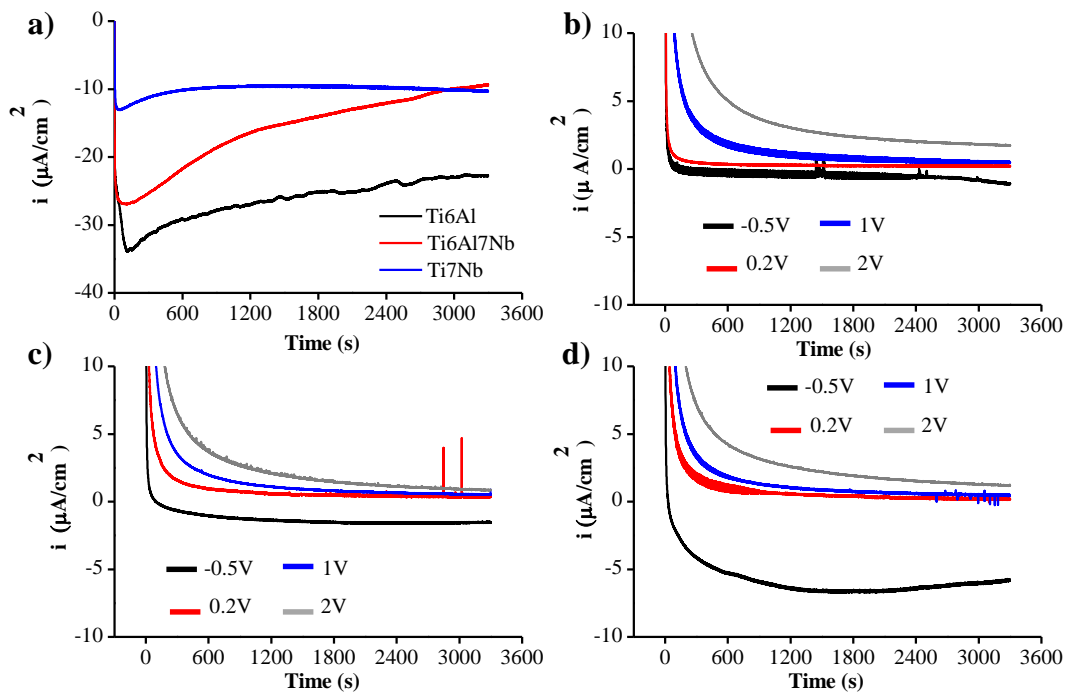


Figure 5.A1.3 Long term potentiostatic tests at a) -1V and -0.5, 0.2, 1 and 2V for b) Ti6Al, c) Ti7Nb and d) Ti6Al7Nb alloys in AS at 37°C.

When a passive potential is applied, metallic cations form and combine with oxygen to form a passive film. The charge (Q) which is proportional to the formed cations and the passivation current density (i_{pass}), which is a quantitative measure of the passive dissolution rate, can be extracted from the potentiostatic tests. **Table 5.A1.2** shows the values of the electrochemical parameters, i_{pass} and Q for all alloys at the different potentials. The charge increases with the applied potential for all materials and have similar values. The same trend was observed for the passivation current density.

Table 5.A1.2 - Electrochemical parameters extracted from the potentiostatic tests of Ti6Al, Ti7Nb and Ti6Al7Nb in AS.

| Material | Potential (V _{Ag/AgCl}) | Q(C/cm ² *10 ⁻³) | i _{pass} (μA/cm ²) |
|----------|-----------------------------------|---|---|
| Ti6Al | -1 | -116.61±7.7 | -20.53±2.0 |
| | -0.5 | -19.10±8.9 | -4.59±1.7 |
| | 0.2 | 1.47±0.6 | 0.16±0.1 |
| | 1 | 7.47±0.5 | 0.52±0.1 |
| | 2 | 24.27±0.4 | 1.61±0.1 |
| Ti7Nb | -1 | -71.83±21.3 | -13.71±3.3 |
| | -0.5 | -6.82±0.2 | -2.12±1.2 |
| | 0.2 | 3.97±0.4 | 0.41±0.1 |
| | 1 | 7.25±0.1 | 0.49±0.1 |
| | 2 | 16.33±0.6 | 0.81±0.1 |
| Ti6Al7Nb | -1 | -71.40±21.2 | -13.62±3.3 |
| | -0.5 | -31.93±12.6 | -6.40±2.9 |
| | 0.2 | 3.51±0.2 | 0.23±0.1 |
| | 1 | 9.01±0.1 | 0.45±0.1 |
| | 2 | 19.02±0.8 | 1.24±0.1 |

3.2.2. AC tests

Electrochemical impedance spectroscopy was employed to investigate the film/electrolyte-interface on the Ti6Al7Nb and Ti7Nb alloys in AS solution at different potentials. For comparison purposes pure sintered Titanium (Ti) was also tested under the same conditions.

Figure 5.A1.4 shows the impedance spectra (Bode plots) for the titanium alloys in AS at the different applied anodic potentials, 0.2, 1 and 2 V_{Ag/AgCl}. In order to interpret the electrochemical behavior of the materials under study, an equivalent electrical circuit (EEC) is used to model the experimental EIS data. Solid lines in **Figure 5.A1.4** correspond to the fitted model.

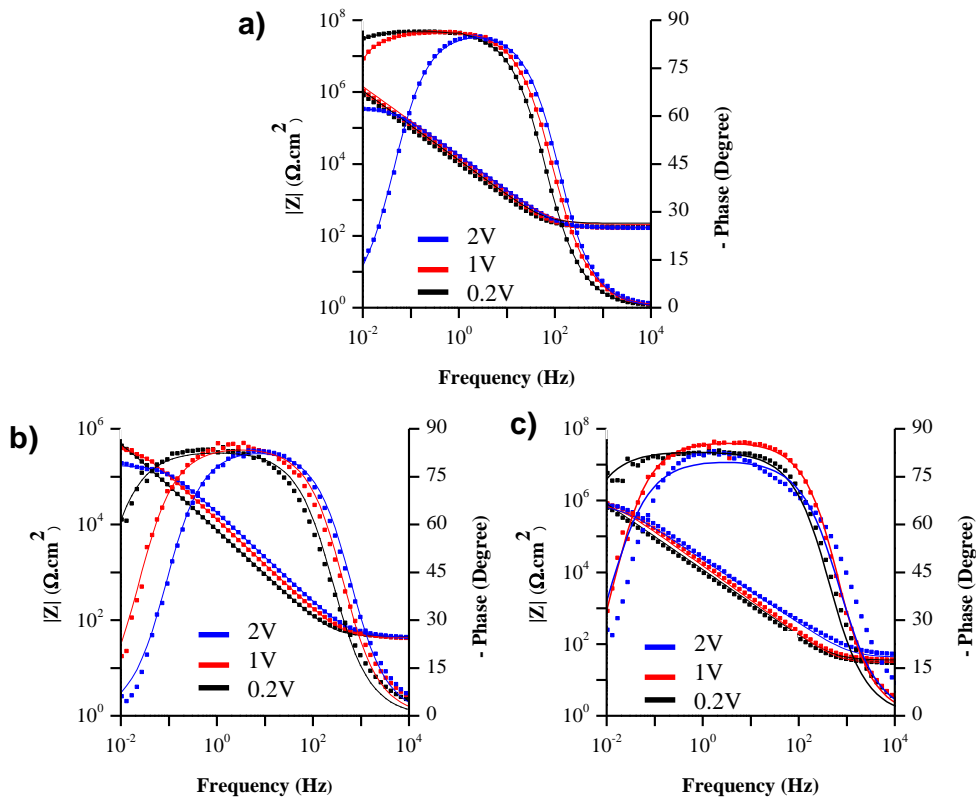


Figure 5.A1.4 Bode plots at 0.2, 1 and 2V of a) Ti, b) Ti6Al7Nb and c) Ti7Nb alloys in AS at 37°C .

The EEC used to model the experimental EIS is shown in **Figure 5.A1.5** and consists in a Randles circuit. The physical model for this equivalent circuit is the presence of a single layer on the metal surface described by a resistance as well as a capacitance for the double layer. The surface film is considered to be a parallel circuit of a resistor, due to the ionic conduction through the film, and a capacitor due to its dielectric properties. In order to validate these parameters, after doing the experimental data fitting to the EEC, two considerations were taken into account: the Chi-squared values (X^2) obtained with the fitting was suitable low ($X^2 \leq 10^{-4}$) and the errors associated with each element were lower than 5%.

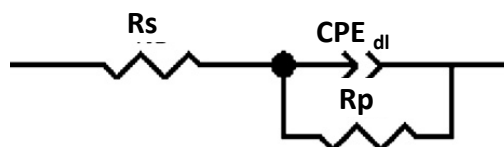


Figure 5.A1.5. Equivalent electrical circuit for the analysis of the impedance spectra. R_s is the solution resistance, R_p is the charge transfer resistance and CPE_{dl} is the CPE of the double layer.

A constant phase angle element (CPE) is introduced to replace the capacitor and to account for the non-ideal behavior of the capacitive elements due to different physical phenomena such as surface heterogeneity which results from surface roughness, impurities, dislocations or grain boundaries [15]. These inhomogeneities are present on a microscopic level under the oxide phase and at the oxide/electrolyte interface. CPE is defined in impedance representation as:

$$Z(\omega) = Z_0(i\omega)^{-n} \quad (1)$$

where Z_0 is the CPE constant, ω is the angular frequency (in rad/s), $i^2 = -1$ is the imaginary number and n is the CPE exponent. Depending on n , CPE can represent resistance ($n = 0$, $Z_0 = R$), capacitance ($n = 1$, $Z_0 = C$), or Warburg impedance ($n = 0.5$, $Z_0 = W$).

It is possible to determine the passive film thickness d_{Film} at each potential, using the film simulated capacitance through each model, according to the formula [16]:

$$d_{\text{Film}} = \varepsilon \cdot \varepsilon_0 \cdot A / C \quad (2)$$

where ε_0 is the permittivity of the vacuum and has a value of $8.85 \times 10^{-12} \text{ F.m}^{-1}$, ε is the relative permittivity and it was set to 30, A is the effective surface area of the sample (m^2) and C is the capacitance of the film (F).

In order to use the previous expression, the CPE has been converted into a pure capacitance (C) by means of the following equation [17]:

$$\text{CPE} = R^{n-1} \cdot C^n \quad (3)$$

Where R has been calculated according to Brug et al. [18], Eq. (4), from the solution resistance (R_s) and the charge transfer resistance of the passive film (R_p) for determining C :

$$1/R = 1/R_s + 1/R_p \quad (4)$$

The theoretical simulated impedance parameters for the tested alloys under different potentials are summarized in **Table 5.A1.3**

For each material, resistance (R_p) and capacitance (C_{dl}) of the passive film decrease with the applied potential. There is no significant difference in the C_{dl} values between all the materials under study. At all applied potentials, Ti exhibits the lowest values of R_p . On the contrary, Ti7Nb shows the highest R_p value and the lowest C_{dl} value, therefore it can be considered as the most resistant material to corrosion under the studied conditions.

The oxide film thickness of all materials increases with the applied potential. No clear influence of the alloying element is observed at 0.2 and 1V however at 2V the thickness of the passive film on Ti7Nb is increased by 91% and 151% when compared to Ti and Ti6Al7Nb respectively.

Table 5.A1.3 - Electrochemical parameters at different potentials from EIS fitting of Ti, Ti7Nb and Ti6Al7Nb sintered alloys in AS at 37 °C.

| Material | Potential (V) | R_s ($\Omega \cdot \text{cm}^2$) | R_p ($\text{K}\Omega \cdot \text{cm}^2$) | CPE ($\mu\text{F}/\text{cm}^2$) | n | C_{dl} ($\mu\text{F}/\text{cm}^2$) | d (nm) |
|----------|---------------|--------------------------------------|--|-----------------------------------|------|--|--------|
| Ti | 0.2 | 44 | 1608 | 24 | 0.74 | 13 | 3.1 |
| | 1 | 43 | 571 | 14 | 0.79 | 8 | 5.1 |
| | 2 | 45 | 262 | 10 | 0.8 | 6 | 7.1 |
| Ti7Nb | 0.2 | 33 | 2952 | 17 | 0.8 | 10 | 4.3 |
| | 1 | 30 | 1115 | 11 | 0.85 | 8 | 5.4 |
| | 2 | 42 | 876 | 8 | 0.66 | 3 | 13.6 |
| Ti6Al7Nb | 0.2 | 177 | 21600 | 15 | 0.82 | 12 | 3.7 |
| | 1 | 160 | 9403 | 13 | 0.82 | 10 | 4.2 |
| | 2 | 176 | 466 | 10 | 0.84 | 8 | 5.4 |

4. Discussion

The corrosion behaviour of all studied titanium alloys is very similar in the sense that all show very low active and passive dissolution rates with no clear influence of the alloying elements. Only an increase of approximately 30 mV in E_{corr} was observed for Ti7Nb with respect to Ti6Al and Ti6Al7Nb. Licausi et al [19] studied the electrochemical behaviour of powder metallurgy Ti6Al4V in artificial saliva and when comparing the reported electrochemical results (OCP= -267 mV. i_{corr} = 0.42 $\mu\text{A}/\text{cm}^2$. E_{corr} = -320 mV and i_p = 17.6 $\mu\text{A}/\text{cm}^2$ from [19]) to the Ti6Al7Nb, the latter appears to be more noble and shows higher corrosion resistance (lower i_{corr} and also lower i_p than the values reported for Ti6Al4V). Metikos-Hukovic [20] observed that Vanadium can diffuse to the surface of Ti alloys and is oxidized to form small amounts of V_2O_5 , VO_2 and V_2O_3 at the outermost surface. The formation of any of these vanadium oxides deteriorates the passivity of Ti6Al4V because they are not as protective as Ti oxides [20]. On the contrary the presence of Nb in the alloy generates an oxidized

product in the passive film which improves the resistance of the resulting alloy. Metikoš-Huković et al. [21] studied the structural integrity of the oxide film and have explained that alloying Ti with metals of higher valences results in the annihilation of anion vacancies in the crystal lattice of Ti oxide. Thus the presence of Nb^{5+} in the layer composition of Ti7Nb and Ti6Al7Nb (**Table 5**) increases the number of oxygen ions, which cancels out the anion vacancies and make the film less defective. The improved corrosion stability of Ti7Nb could also be associated with the presence of Nb_2O_3 in the passive TiO_2 layer which reduces the ingress of Cl^- ions within the oxide layer [22].

During the corrosion process of passive metal as titanium, metallic cations are generated. These ions can either contribute to the growth of the oxide layer or dissolve in the medium [23]. Therefore the total measured current (i_{pass}) can be divided into these two contributions [24]:

$$i_{pass} = i_{growth} + i_{diss} \quad (5)$$

where i_{diss} is the amount of current proportional to the metal dissolution and i_{growth} corresponds to the amount of current used for the formation of the passive oxide film.

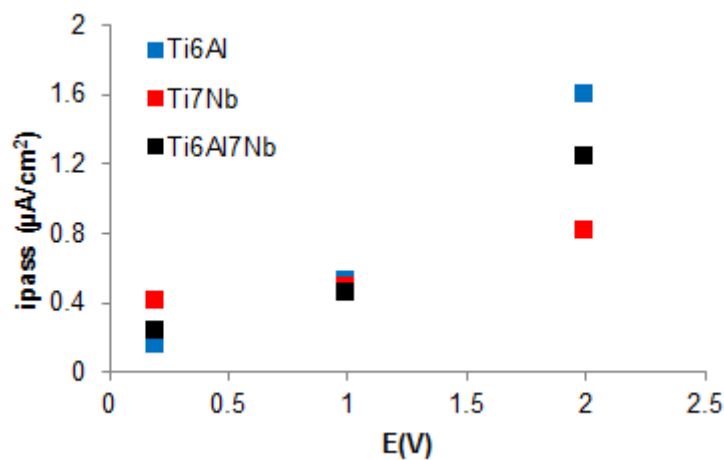


Figure 5.A1.6 Representation of passivation current density versus potential for the Ti alloys under study

The three alloys show an increase of the passivation rate with potential with similar low values at 0.2V and 1V, after what i_{pass} greatly increases for Ti6Al and Ti6Al7Nb (**Figure 5.A1.6**).

The increase of i_{pass} with potential has been associated with a more defective passive film. However the layer composition of Ti7Nb and Ti6Al7Nb is almost independent of the applied potential as previously observed by Milosev [25] for cast Ti6Al7Nb, therefore the latter does not explain the increase of current density with potential for Ti6Al7Nb.

The corrosion resistance of metallic materials is related to chemical stability of oxide layers. This increase could occur if the increase in potential is not accompanied by a corresponding thickening of the oxide film, therefore suggesting an increase of cation dissolution in the solution.

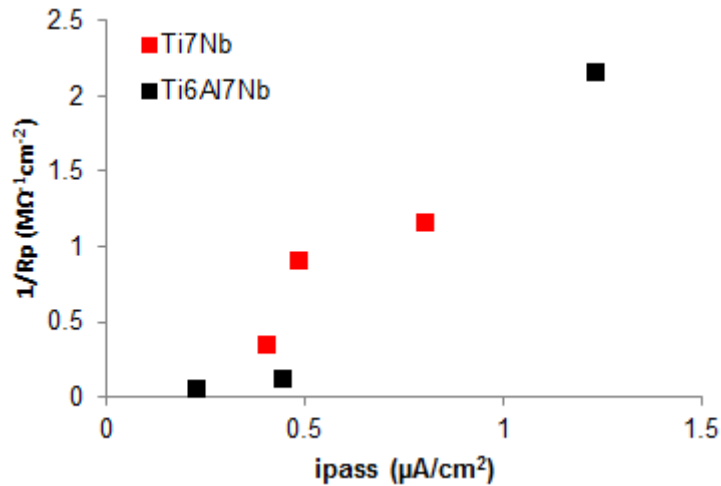


Figure 5.A1.7 Representation of the inverse of the polarization resistance versus the passivation current density for the Ti alloys under study.

The polarization resistance (R_p) represents the resistance to the passive dissolution and is therefore inversely proportional to i_{pass} . According to the High Field model (HFM) a high value of i_{pass} associated to a low value of R_p implies metallic cations dissolve into the electrolyte instead of contributing to the growth of the passive film. According to **Figure 5.A1.7** Ti7Nb shows relatively low values of $1/R_p$ at all potentials whereas in comparison Ti6Al7Nb exhibits lower values at 0.2 and 1V and a clear increase at 2V. Therefore the addition of Aluminium increases passive dissolution at potentials above 1V.

Table 5.A1.3 shows the values obtained for the oxide film thickness at selected potentials for Ti7Nb and Ti6Al7Nb as well as for pure Ti. The growth rate of Ti (2.2 nm/V), used as a reference, corresponds to the results obtained by Ohtsuka et al. [26]. They reported that the film thickness measured in situ by ellipsometry on titanium in phosphate solutions increases at a rate of 2.8 nm/V up to potentials of 7.3V_{Ag/AgCl}. Milosev et al. studied the oxide film formation on Ti6Al7Nb in physiological solution using a combination of electrochemical methods and XPS analysis [25]. They determined the film thickness as a function of the applied potential using the model of Hoppe and Strehblow [27] and from their results it increases from 5.8 nm at -0.25V_{Ag/AgCl} up to 9 nm at 2V_{Ag/AgCl}. These values correspond to a passive growth rate of 1.8 nm/V slightly higher than the

one obtained in this work, 0.95 nm/V. The passive behaviour of the Ti7Nb is different. The oxide film thickness on the Ti7Nb alloy exhibit similar values to those shown by Ti and Ti6Al7Nb at 0 V and at 1V and at higher potentials the film thickness shows an increase of 150% from 1V to 2V. This increase and the low i_{pass} shown in **Figure 5.A.1.6** indicate a higher resistance of the layer formed at 2V on the Ti7Nb. The passive film thickness of the Ti7Nb when compared to that of the Ti6Al7Nb could be explained by the lower solubility of Nb ions compared to Al, so that the passivation process is favoured in absence of Al [28]. These results are consistent with the passive current density values obtained as they follow the same trend.

5. Conclusions

The electrochemical behavior of Ti6Al, Ti7Nb and Ti6Al7Nb alloys obtained by powder metallurgy has been investigated by electrochemical techniques in artificial saliva. From the obtained results the following conclusions can be drawn:

- All studied titanium alloys show a high corrosion resistance, with very low passive dissolution rate in a wide range of potentials in artificial saliva. In all cases the corrosion resistance in the selected environment is higher than the pure titanium.
- At relatively low potentials (up to 1V), the effect of alloying elements Al and Nb in the titanium is negligible on the passive film thickness. However, at higher oxidising conditions, Nb significantly improves the passivating properties of the titanium, while the combine effect of Al and Nb in the Ti6Al7Nb is detrimental with respect to the Ti7Nb.

6. Acknowledgments

The authors wish to thank the Spanish Ministry of Economy and Competitiveness for the financial support of Research Project MAT2014-53764-C3-1-R, the Generalitat Valenciana for support through PROMETEO 2016/040, the European Commission via FEDER funds that have allowed the purchase of equipment for research purposes and for the Microscopy Service at the Polytechnic University of Valencia.

7. References

- [1] X. Liu, P. Chu, C. Ding. Surface modification of titanium, titanium alloys and related materials for biomedical applications. *Mater. Sci. Eng. R. Rep.* 47 (2004) 49-121
- [2] D. Scharnweber. *Metals as Biomaterials*. John Wiley and Sons Ltd. 1998
- [3] DL Sarandha, Sarandha D. L., Zakir. *Textbook of Complete Denture Prosthodontics*. Jaypee Brothers Medical Pub. 2008
- [4] Y. Okazaki, S. Rao, Y. Ito, T. Tateishi. Corrosion resistance, mechanical properties: corrosion fatigue strength and cytocompatibility of new Ti alloys without Al and V. *Biomaterials* 19 (13) (1998) 1197-1215.
- [5] S. Tamilselvi, R. Murugaraj, N. Rajendran. Electrochemical impedance spectroscopic studies of titanium and its alloys in saline medium, *Mater. Corrosion* 58 (2007) 113-120
- [6] M. Geetha, A.K. Singh, R. Asokamani, A.K. Gogia. Ti based biomaterials, the ultimate choice for orthopaedic implants - a review. *Prog. Mater. Sci.* 54 (2009) 397-425.
- [7] Hanawa T. A comprehensive review of techniques for biofunctionalization of titanium. *J Periodontal Implant Sci* 41(2011) 263-272
- [8] A. Zareidoost, M. Yousefpour, B. Ghaseme, A. Amanzadeh. The relationship of surface roughness and cell response of chemical surface modification of titanium. *J. Mater. Sci. Mater. Med.*, 23 (2012), 1479-1488
- [9] L. Bolzoni, E.M. Ruiz-Navas, E. Gordon. Evaluation of the mechanical properties of powder metallurgy Ti-6Al-7Nb Alloy. *Journal of the Mechanical Behavior of Biomedical Materials* 67 (2017) 110-116

- [10] F.X. Xie, X.B. He, S.L. Cao, X. Lu, X.H. Qu. Structural characterization and electrochemical behaviour of a laser-sintered porous Ti-10Mo alloy. *Corros. Sci.*, 67 (2013) 217-224
- [11] K.H.W. Seah, X. Chen. A comparison between the corrosion characteristics of 316 stainless steel, solid titanium and porous titanium. *Corros. Sci.* 34 (1993) 1841-1851
- [12] K.H.W. Seah, R. Thampuran, S.H. Teoh. The influence of pore morphology on corrosion. *Corros. Sci.* 40 (1998) 547-556
- [13] A.C. Alves, I. Sendão, E. Ariza, F. Toptan, P. Ponthiaux, A.M.P. Pinto. Corrosion behaviour of porous Ti intended for biomedical applications. *J. Porous Mater.* 23 (2016) 1261-1268
- [14] A. Dalmau, V. Guinón Pina, F. Devesa, V. Amigó, A. Igual Munoz. Influence of fabrication process on electrochemical and surface properties of Ti-6Al-4V alloy for medical applications. *Electrochimica Acta* 95 (2013) 102-111
- [15] F.B. Growcock, R.J. Jasinski. Time-Resolved Impedance Spectroscopy of Mild Steel in Concentrated Hydrochloric Acid. *Journal of the Electrochemical Society* 136 (1989) 2310-2320
- [16] C.-O.A. Olsson, D. Landolt. Anodization of Nb-Zr alloy. *Electrochimica Acta* 48 (2003) 3999-4001
- [17] N.P. Cosman, K. Fatih, S.G. Roscoe. Electrochemical impedance spectroscopy study of the adsorption behaviour of α -lactalbumin and β -casein at stainless steel. *Journal of Electroanalytical Chemistry*. *Journal of Electroanalytical Chemistry* 574 (2005) 261-271
- [18] G.J. Brug, A.L.G. van den Eeden, M. Sluyters-Rehbach, J.H. Sluyters. The analysis of electrode impedances complicated by the presence of a constant phase element. *Journal of Electroanalytical Chemistry* 176 (1984) 275-295
- [19] M.P. Licausi, A. Igual Munoz, V. Amigo' Borrás. Influence of the fabrication process and fluoride content on the tribocorrosion behaviour of Ti6Al4V biomedical alloy in artificial saliva. *Journal of the mechanical behavior of biomedical materials* 20 (2013) 137-148
- [20] I. Milosev, M. Metikos-Hukovic, H.-H. Strehlow. Passive film on orthopaedic TiAlV alloy formed in physiological solution investigated by X-ray photoelectron spectroscopy. *Biomaterials* 21 (2000) 2103-2113
- [21] M. Metikos-Huković, A. Kwokal, J. Piljac. The influence of niobium and vanadium on passivity of titanium-based implants in physiological solution. *Biomaterials*. 24 (21) (2003) 3765-3775

- [22] S.Y. Yu, J.R. Scully. Corrosion and passivity of Ti-13Nb-13Zr in comparison to other biomedical implant alloys. *Corrosion* 53 (1997) 965-976.
- [23] J.E.G. González, J.C. Mirza-Rosca. Study of the corrosion behavior of titanium and some of its alloys for biomedical and dental implant applications. *J. Electroanal. Chem.* 471 (1999) 109-115
- [24] C.O.A. Olsson, D. Hamm, D. Landolt. Evaluation of Passive Film Growth Models with the Electrochemical Quartz Crystal Microbalance on PVD Deposited Cr. *Journal of Electrochemical society* 147 (2000) 4093-4102
- [25] I. Milosev, T. Kosec, H.-H. Strehblow. XPS and EIS study of the passive film formed on orthopaedic Ti-6Al-7Nb alloy in Hank's physiological solution. *Electrochimica Acta* 53 (2008) 3547-3558
- [26] T. Ohtsuka, M. Masuda, N. Sato, Ellipsometric. Study of Anodic Oxide Films on Titanium in Hydrochloric Acid, Sulfuric Acid, and Phosphate Solution. *J. Electrochem. Soc.*, 132 (1985) 787-792
- [27] H.-W. Hoppe, H.-H. Strehblow. XPS and UPS examinations of Fe₅₃Ni and Fe₁₀Ni in 1 M NaOH and 0.005 M H₂SO₄. *Surf. Interface Anal.* 16 (1990) 271-277
- [28] H. B. Bomberger. Alloying to Improve Crevice Corrosion Resistance of Titanium. In: Presented at MATCON 74, ASM/TMS-AIME, Detroit, 22 Oct (1974)

-Article 2-

INFLUENCE OF THE ALLOYING ELEMENT (Al / Nb) AND THE POTENTIAL ON THE TRIBOCORROSION AND ELECTROCHEMICAL BEHAVIOR OF TITANIUM BIOMEDICAL ALLOYS OBTAINED BY POWDER METALLURGY

M.P. Licausi, A. Igual Muñoz, V. Amigó Borrás

(Manuscript)

**INFLUENCE OF THE ALLOYING ELEMENT (Al / Nb) AND THE
POTENTIAL ON THE TRIBOCORROSION AND
ELECTROCHEMICAL BEHAVIOR OF TITANIUM BIOMEDICAL
ALLOYS OBTAINED BY POWDER METALLURGY**

M.P. Licausi¹, V. Amigó¹, A. Igual Muñoz^{2*}

1- Universitat Politècnica de València, Institut de Tecnologia de Materials. Camí de Vera s/n, 46022València.

2- Universitat Politècnica de València, Instituto de Seguridad Industrial, Radiofísica y Medioambiental. Camí de Vera s/n, 46022València.

***Corresponding autor**

Abstract:

The tribo-electrochemical behaviour of Ti6Al, Ti7Nb and Ti6Al7Nb obtained by powder metallurgy has been investigated in artificial saliva. Additional electrochemical techniques and Scanning Electron Microscopy were applied to analyse both the influence of the alloying element and the electrochemical conditions on wear, and to elucidate the wear mechanisms. Aluminium improved wear resistance of Ti6Al and Ti6Al7Nb through solid solution strengthening, while Niobium increased material removal due to its inherent ductility. The effect of potential on wear was related to the properties of the passive film and mechanical wear increased until the applied potential was 1V while decreased from 1 to 2V. Ti7Nb shows the highest increase of wear under high oxidizing conditions.

Keywords: Titanium alloys, powder metallurgy, tribocorrosion.

1. Introduction

The design of dental implants consists of the coupling of different elements which are mechanically connected. Those designs cause the existence of several physical contacts between their components exposed to corrosive body fluids. Specifically, those contact zones appear between the implant/abutment and the abutment/ceramic. When a contact operates in a corrosive environment it leads to tribocorrosion deterioration which involves three different phenomena, corrosion, wear and wear accelerated corrosion [1]. The latter results from the removal of the passive film of the material through wear and causes the exposition of the underlying material to more severe corrosion. Therefore, tribocorrosion is a synergistic phenomenon which cannot be studied by evaluating corrosion and wear separately. The consequences of the tribocorrosion phenomenon is the generation of metal ions and/or solid particles, debris, which is of main concern as material loss not only can change the mechanical stability of the implant but may also result in harmful body reactions.

Ti cp was the material used for intraosseous applications [2], but it is a relatively soft material and fatigue may occur, particularly when it is used in small-diameter implants and mechanical stability is required to avoid overload and implant fracture [3]. Therefore Ti cp has been typically alloyed with aluminium to increase its strength and to decrease its density while Vanadium as a second alloying element has been added as an aluminium scavenger to improve the corrosion resistance [4]. Indeed, Ti6Al4V is the most commonly used titanium alloy for dental implants because it fulfils the primary requirements for artificial biomaterials. These include the high biocompatibility as well as high corrosion resistance of titanium alloys due to the 3–7 nm thick amorphous [5] or crystalline passive titanium oxide (TiO₂) [6] that spontaneously forms on its surface. However, one associated problem to these alloying elements is their possible toxicity [7] and their relatively high Young modulus. During recent years, new titanium alloys have been developed in order to decrease the possible cytotoxic adverse effects of Vanadium but also to lower the Young modulus to prevent the mechanical mismatch between the bone and the implant, thus the consequences of “stress-shielding”. This problem may appear due to comparatively higher elastic moduli of Ti6Al4V in comparison with that of the bone [8]. Therefore, adding Niobium as alloying element has gained great interest due its biocompatibility and ability to lower the Young modulus of the material. These newly developed alloys include Ti6Al7Nb, Ti15Zr4Nb2Ta (TNZT), Ti13Nb13Zr and Ti45Nb among others [9].

On the other hand, the good stability of dental implants not only depends on the biocompatibility of the material but on the surface morphology, which also plays a crucial role in osseointegration. For stable implant fixation, the bone tissues are expected to attach and to bond to the implant surface to

ensure an interface matrix, equivalent to that of the bone structure [10]. This process can be accelerated and improved by various surface modification methods such as acid etching or grit blasting to yield materials with micro-roughened surfaces [11]. Porous titanium alloys obtained by powder metallurgy can also be considered a method when aiming at enhancing and accelerating osseointegration.

The aim of this study is to characterize the tribocorrosion behavior and wear mechanisms of sintered TiAl7Nb, Ti6Al and Ti7Nb alloys (where numbers indicated %wt of the alloying elements) in artificial saliva and to determine the influence of the alloying element on their wear and corrosion response.

2. Experimental

2.1. Materials and electrolyte

The materials used as working electrodes were Ti6Al, Ti7Nb and Ti6Al7Nb sintered materials where the numbers indicate the weight percentage of the alloying elements. The sintered titanium material was fabricated by powder metallurgy according to the following procedure: powder compression, applying a compacting pressure of 400 MPa without the addition of any lubricant and sintering sequence consisting in a thermal cycle with specific heating and cooling ramps. The initial heating ramp consists in heating at 800 °C during 30 min in order to stabilize both the oven and the material at the same temperature and to avoid cracking due to thermal gradients. The sintering process lasts 2 hours at 1250 °C in a vacuum tube oven.

Before use, the sintered samples in form of disks 25 mm in diameter and 5 mm in thickness were cleaned with acetone in an ultrasonic bath in order to remove any existing particle from the pores and tested without any prior polishing.

The three different alloys were tested in the same electrolyte, a modified Fusayama Meyer artificial saliva (AS), which simulates the human saliva. The composition of this solution, which closely resembles natural saliva, was: 0,4 g NaCl, 0,4 g KCl, 0,6 g CaCl₂, 0,58 g Na₂HPO₄·12H₂O, 1 g urea, distilled water at 1 L. The pH of the solution was 6.5.

2.2. Material characterization

The Vickers hardness of the studied Ti alloys was measured by a microdurometer Duramin of Struers (Germany) applying 0.2 kg during 30 s. Elastic modulus was obtained using ultrasonic equipment Karl Deutsch – Digital Ecograph (Germany). Prior to this, test the samples were mirror polished: specimens were mechanically polished with 1000 grit with SiC paper followed by a polishing with a 9 μm diamond suspension. Measurements were repeated three times for checking the reproducibility

2.3. - Electrochemical Experiments

The electrochemical behaviour of the titanium alloys was studied using a three-electrode electrochemical set-up: a working electrode (the titanium sample), a reference electrode (Ag/AgCl 3M KCl) and a platinum coiled wire acting as a counter electrode. A potentiostat (solatronTM1286) was used for the electrochemical tests. All potentials are given with respect to the reference electrode (205 mV vs SHE).

Cathodic potentiodynamic polarization curves of the 3 different sintered alloys were performed from OCP to $-1.2 V_{\text{Ag/AgCl}}$ at a scan rate of 0.5 mV/s.

Potential step experiments during a short period, 1 second, were performed to assess passivation kinetics. Potential was kept at the cathodic potential of $-1 V$ for 5 min and then switched to the selected potentials ($-0.5, 0.2, 1, \text{ and } 2 V_{\text{Ag/AgCl}}$) in separated experiments. Instantaneous current and potential values were measured continuously at a sampling interval of 0.0001 s. Each experiment was performed three times. The passivation charge Q_{short} was then calculated by integrating the current density versus time.

2.4. Tribocorrosion Experiments

The tribocorrosion tests were carried out coupling the electrochemical cell to an unidirectional ball on disk tribometer with the reference electrode no more than 1 cm away from the wear track. Only the upper surface of the samples (2.04 cm^2) was exposed to the electrolyte and the lower part was insulated and electrically connected to the potentiostat. The computer-controlled tribometer applied a rotating motion to the working electrode and the static ball (alumina ball 6 mm in diameter). These tests were performed setting normal load, sliding velocity and sliding duration to 5 N (which corresponds to a maximum contact pressure of 960 MPa), 60 rpm (sliding velocity of 18 mm/s) and 1 h respectively.

For all materials, sliding tests were carried out both at Open Circuit Potential (OCP), and at an applied potential. The following applied potentials were used: $-1 V_{Ag/AgCl}$ in the cathodic domain and $-0.5, 0.2, 1$ and $2V_{Ag/AgCl}$ in the passive domain. The experimental sequence consisted in:

- Cathodic cleaning by applying a potential of -1.1 for 5 min
- Applied potential ($-1, -0.5, 0.2, 1$ and $2 V_{Ag/AgCl}$) during 60 min or allowing the system to stabilize at OCP during 60 min
- Start the sliding for 60 min while the polarization is maintained or the OCP is measured
- Sliding is stopped while the polarization or the OCP is maintained for 20 min.

All corrosion and tribocorrosion tests were carried out at $37^{\circ}\text{C} \pm 1^{\circ}\text{C}$, under aerated conditions and repeated three times for checking the reproducibility of the measurements.

At the end of the tribocorrosion tests the wear track and the alumina counterpart were examined using optical microscopy and Scanning Electron Microscopy (SEM). The wear track profile was measured by confocal microscopy (Olympus LEXT OLS3000).

3. Results

3.1. Material properties

Table 5.A2.1 shows the microhardness and the elastic modulus values of the titanium alloys. The Ti7Nb alloy shows the lowest hardness and the lowest elastic modulus when compared to the Ti6Al and the Ti6Al7Nb.

| Material | Ti6Al | Ti7Nb | Ti6Al7Nb |
|---------------------|---------|--------|----------|
| Microhardness (Hv) | 367±4 | 282±8 | 330±6 |
| Young Modulus (GPa) | 115±0.4 | 97±0.6 | 106±0.1 |

3.2. Electrochemical tests

Cathodic potentiodynamic test of the three alloys in the AS solution are shown in **Figure 5.A2.1**.

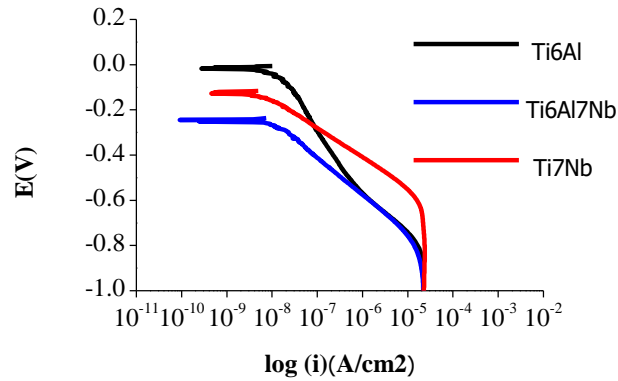


Figure 5.A2.1. Cathodic polarization curves of the titanium alloys in AS at $37\pm 1^\circ\text{C}$.

A linear relationship is observed between the logarithm of the current and the applied potential between -0.2 and $-0.7 \text{ V}_{\text{Ag}/\text{AgCl}}$, therefore in this potential domain the electrode reactions are limited by the rate of charge transfer at the electrode-electrolyte interface. Thus, in this potential domain a Tafel relationship, **Equation 1** can be obtained through the linear regression of the current versus the applied potential of the cathodic polarization curves

$$\eta = a_c - b_c \cdot \log(i) \quad (1)$$

where η is the overpotential ($E - E_{\text{corr}}$), a_c and b_c the Tafel coefficients and i the current density. By carrying out the linear regression, the Tafel constants were obtained and shown in **Table 5.A2.2**.

Table 5.A2.2. Tafel constants extracted from the linear regression of the cathodic polarization curves of the titanium alloys.

| Material | a_c (V/decade) | b_c (V/decade) |
|----------|------------------|------------------|
| Ti6Al | -2.30 ± 0.1 | 0.31 ± 0.1 |
| Ti7Nb | -1.20 ± 0.1 | 0.13 ± 0.1 |
| Ti6Al7Nb | -1.55 ± 0.1 | 0.16 ± 0.1 |

The current transients for the titanium alloys at different applied potentials are shown in **Figure 5.A2.2**. The passive current increases when increasing the potential for the Ti6Al, **Figure 5.A2.2a**. The same trend is observed for Ti7Nb and Ti6Al7Nb from 0.2 to 1V_{Ag/AgCl} but it decreases at 2V_{Ag/AgCl}. Passivation charge densities (Q_{short}) are given in **Table 5.A2.3**. At all potentials Ti7Nb shows the lowest values of Q_{short} while Ti6Al7Nb shows the highest values except at 2V_{Ag/AgCl}.

Table 5.A2.3. Passivation charge densities (Q_{short} (C/cm²)*10⁻³) of the studied alloys in AS at 37±1°C.

| Potential | Ti6Al | Ti7Nb | Ti6Al7Nb |
|-----------|-----------|-----------|-----------|
| -0.5V | 0.08±0.02 | 0.03±0.01 | 0.39±0.02 |
| 0.2V | 0.24±0.41 | 0.19±0.03 | 0.76±0.03 |
| 1V | 0.55±0.02 | 0.39±0.01 | 1.10±0.05 |
| 2V | 0.87±0.02 | 0.30±0.01 | 0.38±0.02 |

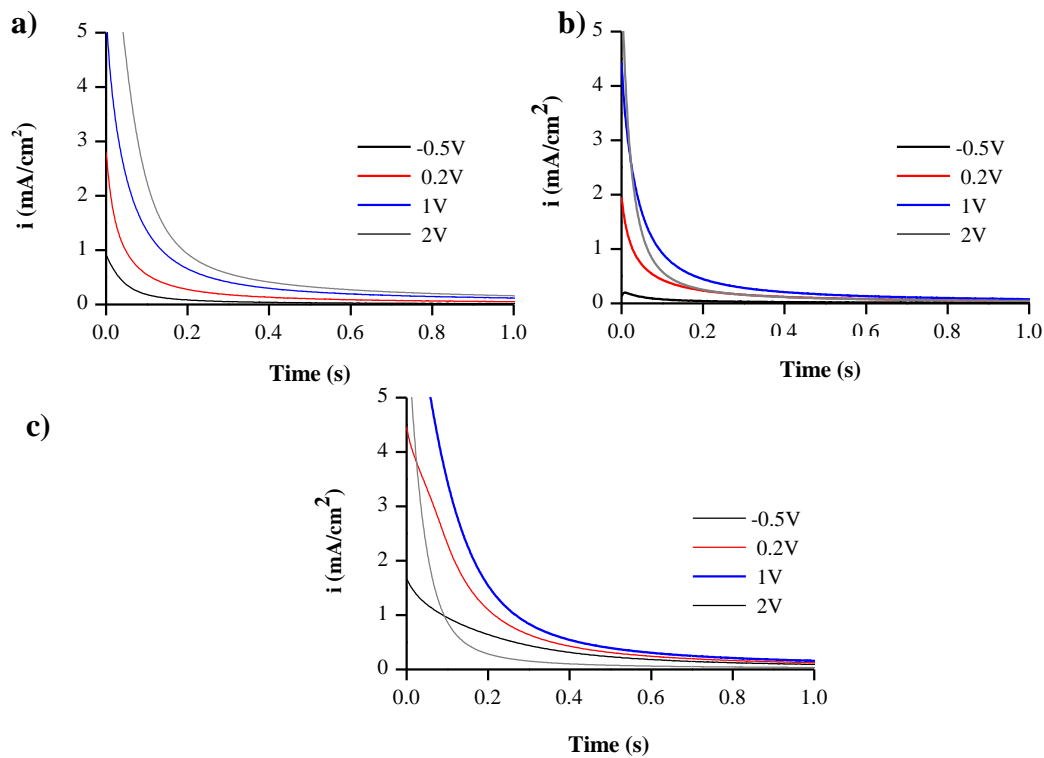


Figure 5.A2.2. Current transients at 0.2, 1 and 2 V_{Ag/AgCl} for a) Ti6Al, b) Ti7Nb and c) Ti6Al7Nb in AS at 37±1°C.

3.3. Tribocorrosion at OCP

The evolution of the open circuit potential (OCP) with time of the titanium alloys was monitored before, during and after the sliding and is shown in **Figure 5.A2.3**. Before the initiation of sliding, the measured OCP reflects the presence of a passive film on the alloys' surface in contact with the artificial saliva. An abrupt decrease in potential is observed immediately after the initiation of the sliding, indicating a depassivation of the surface induced by the mechanical removal of the passive film (depassivation), and the exposure of fresh active titanium to the electrolyte. During the sliding, the open circuit potential results from the galvanic coupling between the depassivated wear track (anode) and the passive unworn area (cathode). It remains constant around the same low value, indicating that a depassivated state prevails in the wear track and that the alloy is not able to recover its passive state while mechanical perturbation is taking place. Similar potentials were reached during sliding by all studied materials.

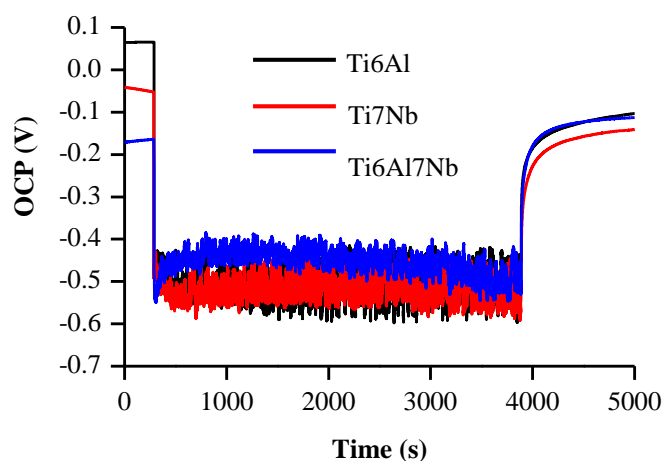


Figure 5.A2.3. OCP evolution with time during rubbing of a smooth alumina ball against Ti6Al, Ti7Nb and Ti6Al7Nb at OCP in AS at $37\pm 1^\circ\text{C}$.

During the sliding period the potential shows transitions, with an amplitude of around 0.05 V of a dynamic equilibrium between depassivation and repassivation mechanisms as a result of the periodic removal (depassivation) and growth (repassivation) of the passive film during the sliding. At the end the OCP exhibits an anodic shift, suggesting the occurrence of repassivation of the active area of the worn zone.

3.4. Tribocorrosion at an applied potential

Figure 5.A2.4 shows the evolution of the current during sliding for all the materials at $-1V_{Ag/AgCl}$. The registered current is negative for all samples, corresponding to the measurement of the cathodic reaction rate. At the onset of rubbing current increases (in absolute value) due to the stirring effect of the counterpart, which enhances mass transport and the mechanical removal of the passive film, which is known to inhibit the cathodic reaction. Slightly higher current was measured for Ti6Al7Nb.

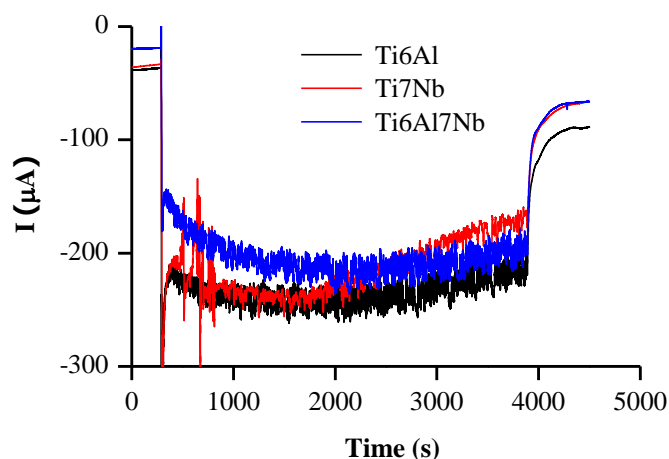


Figure 5.A2.4. Current evolution with time during sliding of a smooth alumina ball against Ti6Al, Ti7Nb and Ti6Al7Nb at $-1V_{Ag/AgCl}$ in AS at $37\pm 1^\circ C$

Figure 5.A2.5 shows the current evolution at -0.5 , 0.2 , 1 and $2V_{Ag/AgCl}$ for the Ti6Al7Nb and Ti7Nb alloys. At the applied anodic potentials, the whole titanium surfaces are initially passive and the anodic current (I_0) is low (below $4 \mu A$). When sliding starts, current exhibited a sharp increase due to the mechanical detachment of the passive film [20] and the steady state value was reached after a few seconds. After the initial increase in current, no significant variation in the current is observed during the tribocorrosion tests. When the sliding is stopped, the current sharply decreased again to the value observed at the beginning of the tests, which suggests the occurrence of repassivation of the worn area.

Table 5.A2.4 summarizes the average values of the current before and during the sliding in the tribocorrosion tests carried out at the different applied potentials. The current flowing from the wear track ($I_{sliding}$) was determined by subtracting from the current measured during sliding the value of the current measured before starting the sliding. The latter was assumed to correspond approximately to the current flowing through the area outside the wear track during sliding (the wear track are much smaller than the total electrode area).

For all materials, the current during sliding increases with potential from -0.5 to 1V_{Ag/AgCl}, however at 2 V_{Ag/AgCl} the I_{sliding} decreases to similar values to those measured at 0.2 V_{Ag/AgCl}.

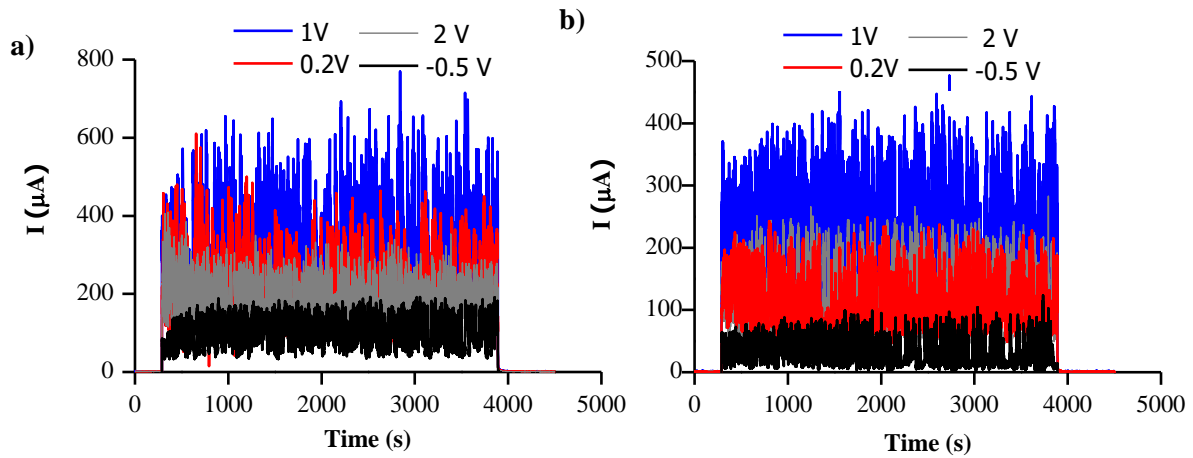


Figure 5.A2.5. Current evolution with time during sliding of a smooth alumina ball against (a) Ti7Nb and (b) Ti6Al7Nb -0.5, 0.2, 1 and 2V_{Ag/AgCl} in AS at 37±1°C

Table 5.A2.4 Average values of the current density measured before (I_0), during ($I_{sliding}$) and after sliding (I_{final}) of Ti6Al, Ti7Nb and Ti6Al7Nb in AS.

| Material | Potential (V _{Ag/AgCl}) | I_0 (µA) | $I_{sliding}$ (µA) | I_{final} (µA) |
|----------|-----------------------------------|-------------|--------------------|------------------|
| Ti6Al | -1 | -42.55±5.1 | -144±51.1 | -73.01±19.3 |
| | -0.5 | -6.08±3.5 | 39±10.6 | -6.15±4.7 |
| | 0.2 | 0.36±0.1 | 102±3.2 | 0.51±0.3 |
| | 1 | 1.89±1.1 | 168±23.2 | 34.82±15.1 |
| | 2 | 2.96±1.3 | 117±3.4 | 1.5±0.1 |
| Ti7Nb | -1 | -28.28±6.3 | -167±9.4 | -64.62±6.3 |
| | -0.5 | -5.98±2.3 | 81±11.2 | -6.81±3.2 |
| | 0.2 | -0.84±0.1 | 196±3.7 | 0.91±0.1 |
| | 1 | 1.21±0.4 | 273±24.5 | 0.97±0.1 |
| | 2 | 1.37±0.7 | 172±3.6 | 0.7±0.1 |
| Ti6Al7Nb | -1 | -29.46±10.1 | -170±13.3 | -70.54±1.5 |
| | -0.5 | -9.18±4.9 | 25±26.1 | -13.33±8.6 |
| | 0.2 | 0.45±0.1 | 135±9.2 | 0.59±0.2 |
| | 1 | 0.88±0.1 | 179±8.6 | 0.88±0.1 |
| | 2 | 1.22±0.1 | 136±1.9 | 0.6±0.1 |

3.5. Friction and wear quantification

The overall material loss in a tribocorrosion system can be expressed according to the following relationship:

$$V_{\text{tot}} = V_{\text{chem}} + V_{\text{mech}} + V_{\text{corr}} \quad (2)$$

Where V_{tot} is the total wear volume, V_{chem} is the volume loss caused by the wear accelerated corrosion, V_{mech} is the mechanical removal of particles in the wear track and V_{corr} is the material loss from the corrosion outside the wear track.

Since V_{corr} can be considered negligible for the titanium alloys (passive alloys), the overall material loss is simplified by the sum of the mechanical and wear accelerated corrosion volumes:

$$V_{\text{tot}} = V_{\text{chem}} + V_{\text{mech}} \quad (3)$$

The material loss removed by anodic oxidation in the wear track, V_{chem} was calculated from the measured current using Faraday's law:

$$V_{\text{chem}} = (I_{\text{sliding}} \times t \times M) / (n \times F \times \rho) \quad (4)$$

where M is the atomic mass of Ti6Al, Ti7Nb and Ti6Al7Nb (46.64, 51.05 and 49.79 g/mol respectively), n is the charge number for the oxidation reaction (valence of oxidation was assumed 4), F is the Faraday constant (96500C/mol), ρ is the density of the alloys equal to 4.25 g/cm³ and t is the duration of sliding, 3600 s.

The total wear volume, V_{tot} was determined geometrically by confocal microscopy. The area of an average cross section of the wear track multiplied by the length of the track gives one the V_{tot} . The wear track width was also measured using confocal microscopy at all potentials (**Figure 5.A2.6**). For all tested materials the wear track is larger at the lowest potentials (-1V) and gradually decreases when increasing potential. For all materials, the wear track is reduced by about 30% at 2 $V_{\text{Ag/AgCl}}$ when compared to the wear track width at -1 $V_{\text{Ag/AgCl}}$.

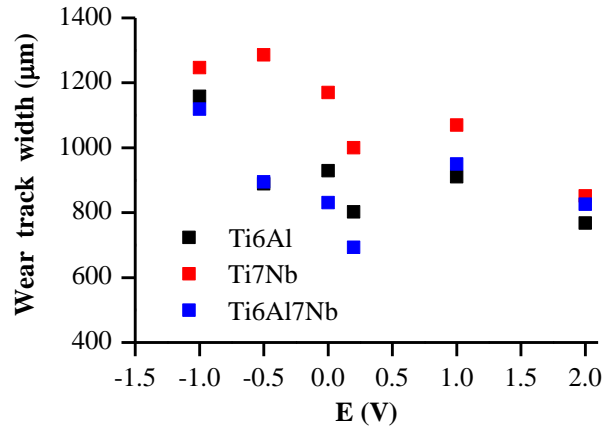


Fig.5.A2.6. Wear track width versus the applied potential and OCP, $E(V_{Ag/AgCl})$ for all studied titanium alloys at the end of the tribocorrosion tests.

The Wear accelerated corrosion contribution at OCP has been determined according to the galvanic model proposed by Vieira et al [12] and applied by Papageorgiou and Mischler [13], which takes into account the cathodic kinetics and the corrosion potential of the alloys, the potential during sliding and the anode to cathode ratio. From this model, the anodic current passing through the wear track (i_a) was calculated by using the following equation:

$$\log i_a = ((E_{\text{corr}} - E_c + a_c) / b_c) - \log (A_a / A_c) \quad (5)$$

where E_c is the potential measured during rubbing (OCP_{sliding}), E_{corr} is the corrosion potential, a_c and b_c are the Tafel constants extracted from the cathodic polarization curves by linear regression of the curve in **Figure 5.A2.1**. A_a corresponds to the wear track area obtained by the confocal profile at the end of the experiment, A_c corresponds to the cathode area which can be approximated by the sample area.

The contributions to total volume loss is represented in **Figure 5.A2.7**. All materials exhibit the lowest volumes at the cathodic potential of $-1 V_{Ag/AgCl}$. At this potential lying in the cathodic domain of the alloys no V_{chem} contribution is expected. Between -0.5 and $1 V_{Ag/AgCl}$ the total wear slightly increases or remains constant depending on the titanium alloy, while at $2 V_{Ag/AgCl}$ there is a decay in the wear volume for all studied alloys. The V_{chem} values increase with potential from -0.5 to $1 V_{Ag/AgCl}$ and then drop at $2 V_{Ag/AgCl}$ for all materials.

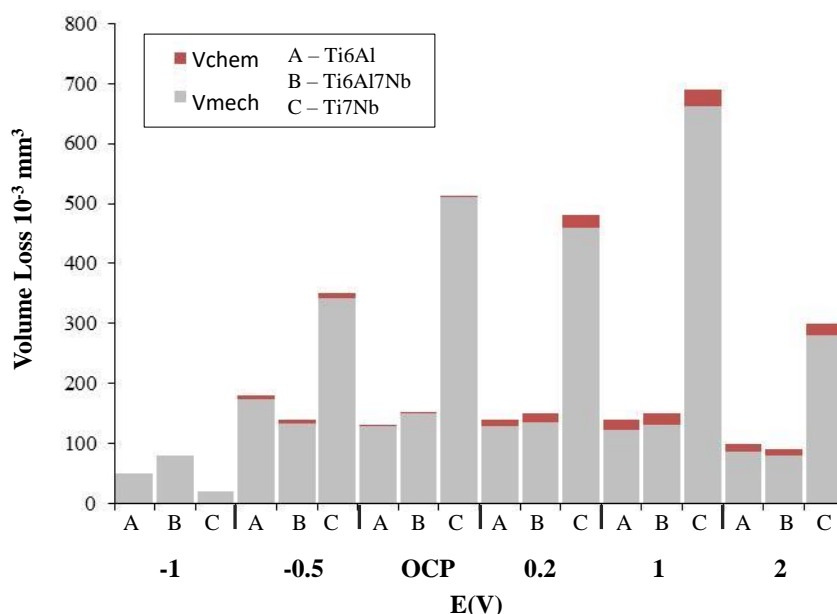


Figure 5.A2.7. Volume losses, V_{mech} and V_{chem} , with respect to the applied potential and OCP after the tribocorrosion tests for all studied titanium alloys.

Table 5.A2.5. shows the average values of the friction coefficients of all the studied alloys and at all considered potentials. The friction coefficients were registered simultaneously to the electrochemical signal and remained around a constant value during the whole tests. The values lie typically within the range 0.3–0.4. No influence of the potential on the coefficient of friction was observed. Slightly higher values of coefficient of friction were found in the Ti7Nb compared to the other alloys.

Table 5.A2.5 - Average values of the coefficient of friction measured during sliding of the studied alloys against an alumina ball at different potentials. Load 5N

| Potential | -1 V | -0.5V | OCP | 0.2V | 1V | 2V |
|-----------|-----------|-----------|-----------|-----------|-----------|-----------|
| Ti6Al | 0.32±0.01 | 0.33±0.01 | 0.33±0.02 | 0.36±0.02 | 0.35±0.01 | 0.38±0.01 |
| Ti7Nb | 0.42±0.01 | 0.39±0.02 | 0.39±0.02 | 0.40±0.01 | 0.40±0.01 | 0.40±0.01 |
| Ti6Al7Nb | 0.29±0.01 | 0.30±0.01 | 0.30±0.01 | 0.30±0.01 | 0.33±0.01 | 0.33±0.01 |

3.6. Wear morphology

Figure 5.A2.8 shows the SEM images of the wear tracks of Ti6Al, Ti7Nb and Ti6Al7Nb at 1V and 2V. At 1V the wear tracks show, for all materials, plastic deformation with fine abrasion lines. A few grooves are observed on the surface for the Ti6Al7Nb alloy. Similar wear characteristics were observed at -1, 0.5 and 0.2 $V_{Ag/AgCl}$. At 2 $V_{Ag/AgCl}$ a similar morphology is observed for Ti6Al and Ti6Al7Nb. However Ti7Nb wear track shows more severe plastic deformation with wide parallel grooves and severe delamination.

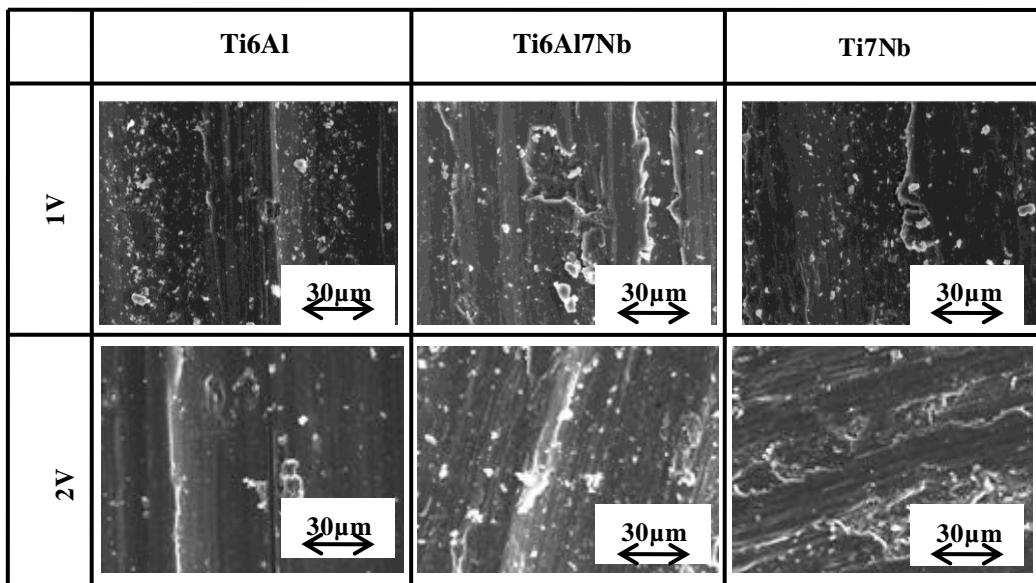


Figure 5.A2.8. SEM images of the wear track of Ti6Al, Ti7Nb and Ti6Al7Nb at the end of the tribocorrosion tests at different applied potentials in AS at $37\pm 1^\circ\text{C}$

Figure 5.A2.9 shows an example of an optical image of the alumina balls after the tribocorrosion tests. Similar images were obtained for all materials under the different applied potentials. In all cases material transfer from the titanium samples was observed.

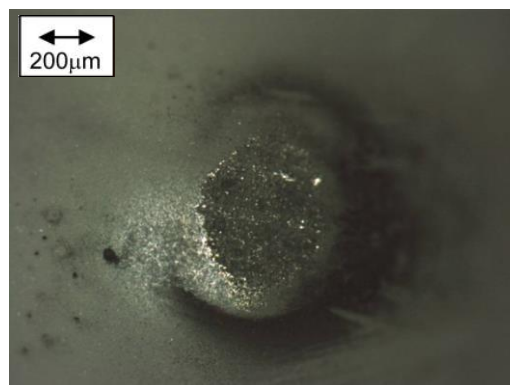


Figure 5.A2.9. Optical Image of the alumina ball at the end of the tribocorrosion tests of Ti6Al at 1V in AS at $37\pm 1^\circ\text{C}$

4 Discussion

4.1. Influence of the alloying element

Alloying titanium with aluminium has been commonly used in metallurgy because it is a substitutional solid *solution* strengthener. The addition of aluminium to titanium in the Ti6Al sample increases the microhardness of the resulting alloy by 11 % and 30 % when compared to the value of the Ti6Al7Nb and Ti7Nb respectively, **Table 5.A2.1**. Indeed, the obtained value of the hardness obtained for Ti6Al7Nb is similar to the one found by Semlitsch et al. [14] (350 HV) in the wrought alloy and in the wrought Ti6Al4V [15]. On the other hand, the hardness of the Ti7Nb is comparable to that specified for IMI 367 medical devices (290 HV) [16]

Alloying the pure titanium with aluminium and niobium, also changes the elastic modulus of the resulting material. The mean value of 106 ± 1 was obtained for the Ti6Al7Nb, corresponds to the typical value of 105 GPa of wrought Ti6Al7Nb [17]. Comparable measurements were published for powder metallurgy Ti6Al7Nb alloy by Bolzoni et al. [18]. The influence of adding Niobium, a known alloying element used to lower the elastic modulus of metallic biomaterials [15], can be observed as values decrease in the following order: Ti6Al > Ti6Al7Nb > Ti7Nb.

The effect of the alloying element on wear can be analysed in **Figure 5.A2.7** at different applied potentials. In the cathodic domain, at $-1V_{Ag/AgCl}$, no significant differences between wear volumes of the studied alloys were found. This is not surprising since at this potential the thin oxide layer formed on the alloys is very similar in chemical composition [19] thus the generated wear particles show the same properties and the surface also suffers the same plastic deformation. However, in the anodic domain, at the applied potentials between -0.5 and $2 V_{Ag/AgCl}$, higher material loss was measured in the Ti7Nb when compared to the Ti6Al and Ti6Al7Nb alloys. Even though a correlation between wear resistance and hardness has previously been reported [20], the later indicates that the increase in hardness (17% and 30% for Ti6Al and Ti6Al7Nb with respect to Ti7Nb respectively) cannot explain the increase of V_{tot} with potential for the Ti7Nb alloy, therefore suggesting a tribo-electrochemical mechanism as the responsible of the degradation rate of Ti7Nb. The detrimental effect of Nb on wear resistance of Titanium appears to be dependent on the weight percentage used for alloying. Under dry sliding and 2N loading, Xu et al [20] observed a smaller wear depth for Ti5Nb when compared to Ti15Nb. Guinon et al [21] studied the tribocorrosion behaviour of Ti30Nb in PBS under 5N and reported greater wear values $\sim 900 \cdot 10^{-3} \text{ mm}^3$ regardless of the potential applied (from -1V to 2V).

The composition of the passive oxide layer of Ti6Al7Nb as a function of the oxidation potential was studied in Hanks physiological solution [19]. It contains predominantly TiO₂ and the oxides of the minor elements, Al₂O₃, Nb₂O₅ (also smaller amounts of NbO and/or NbO₂) were all enriched and located on the top of the TiO₂ oxide layer. This enrichment at the top could be explained by the fact that the Gibbs free energy for the formation of TiO₂ (-765 kJ/mol) is higher than those of Al₂O₃ (-954 kJ/mol) and Nb₂O₅ [22]. Taking into account that Nb₂O₅ is a harder oxide than TiO₂, the increase in wear loss for Ti6Al7Nb and Ti7Nb could be related to the relative amounts of these two oxides. Furthermore, Al₂O₃ oxide particles are also known to act as a solid lubricant [23] according to the SEM images in **Figure 5.A2.8** which reveal a smoother surface in the two Aluminium-containing alloys.

However the chemical composition of the oxide layer in a previous study [19] is almost independent of potential and the oxide thickness between 0.2 and 1 V. The presence of oxides at the surface should not be regarded as the only factor that influences the wear characteristics as the repassivation capacity of the film during the wear process also needs to be taken into account. Landolt et al [24] suggested that at low anodic potentials the metallic particles formed by mechanical wear completely dissolved in the electrolyte, while at higher potentials the repassivation rate was sufficiently fast to allow them to repassivate and to form a third body. The presence of such debris in the wear track could change the contact and consequently affect wear. The increase in the passivation rate can indeed be observed from the shape of the transient current observed during one cycle (**Figure 5.A2.2**) and the wear track width (**Figure 5.A2.6**) shows a decrease with the applied potential. The latter implies that the pressure on the surface of the alloys tested increased with potential and was higher at 1 V than at 0.2 V which could explain the increase in wear loss with the applied potential. However Ti6Al and Ti6Al7Nb total wear shows only a slight increase with potential when compared to Ti7Nb which varies from 350mm³ (at -0.5V) to 700 mm³ (at 1V).

On the other hand, the lower wear volume of the Aluminium-containing alloys can be also related to the solution strengthening effect of aluminium as it hinders the motion of dislocations [25].

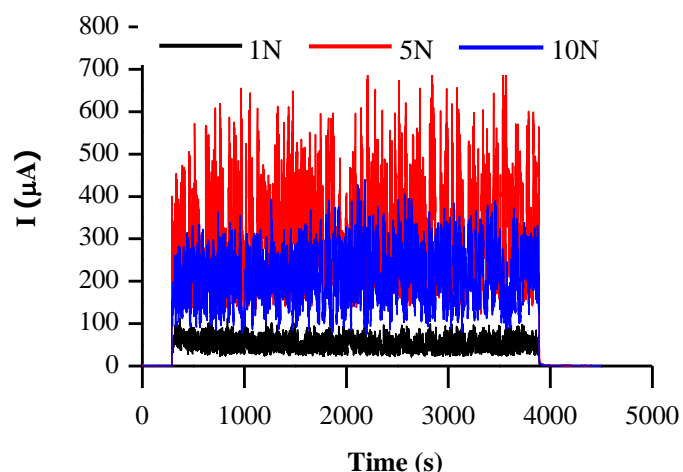


Figure 5.A2.10. Current evolution with time during sliding of a smooth alumina ball against Ti7Nb at 1V with varying load of 1, 5 and 10N in AS at $37\pm 1^\circ\text{C}$.

To gain greater insight into the Ti7Nb system, tribocorrosion tests were carried out at $1\text{ V}_{\text{Ag/AgCl}}$ applying 1 N and 10 N (**Figure 5.A2.10**) normal load on the Ti7Nb alloy. Under a load of 1 N the current density during sliding is extremely low as well as wear loss which implies that the average contact pressure, according to the Hertz formalism, is below the yield strength of the material. When applying 10 N the values of current during sliding as well as wear loss are similar to the ones obtained under 5N, however the cross section of the wear track exhibit clear ridges (**Figure 5.A2.11**). Applying the higher load of 10N causes microscopic movements in the metal occur allowing the material to plastically deform moving on the sides of the contact, confirming the high ductility of the material. This behaviour is caused by the increased amount of beta phase in the alloy as the high ductility of Niobium is inherent to BCC crystals with three slipping planes compared to Titanium with an HCP crystal lattice with only one slipping plane [26]. Therefore, Ti7Nb being a soft material, debris can easily grind into the surface removing large amounts of material and the phenomenon is emphasized when increasing the contact pressure.

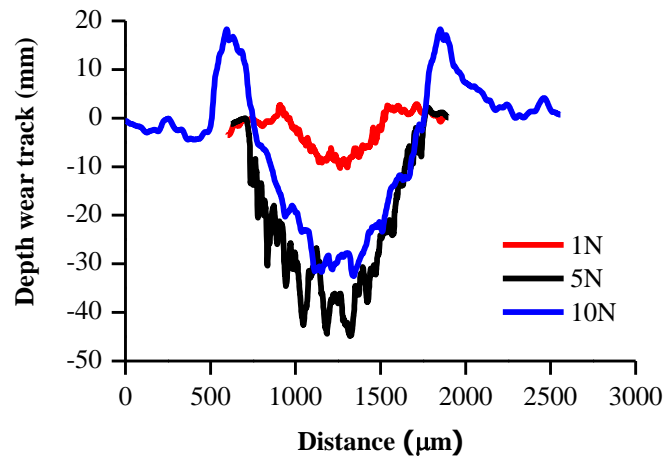


Figure 5.A2.11 Confocal 2D profile of the Ti7Nb wear tracks obtained after tribocorrosion tests under 1, 5 and 10 N in AS at $37\pm 1^\circ\text{C}$.

4.2. Influence of applied potential

Under all considered potentials, all studied materials show a passive behaviour, although three wear domains can be identified as a function of the prevailing electrochemical conditions. At cathodic potentials ($-1V_{\text{Ag}/\text{AgCl}}$), no metal oxidation takes place and total wear volume remains relatively low. According to Perret et al [27], at cathodic potentials emerging dislocations can be annihilated. When an oxide film covers the surface, dislocations trying to emerge are blocked and accumulate within the metal. The increased dislocation density results in strain hardened surface. At low applied passive potentials, from -0.5 to $1 V_{\text{Ag}/\text{AgCl}}$, V_{tot} shows a linear increase with the electrode potential. This increase of wear with potential has already been observed in passive alloys and can be explained by the presence of a passive film that blocks the dislocation annihilation while acting as a new source of dislocations.

At the highest potential of $2 V_{\text{Ag}/\text{AgCl}}$ however a decrease in total wear is observed for all materials, when compared to the value obtained at $1V_{\text{Ag}/\text{AgCl}}$. The deformation of the subsurface material could affect both the mechanical properties and the electrochemical responses. Stojadinovic et al [28] have observed a similar decrease in wear on tungsten due to the formation of a thick WO_3 tribolayer which protected the material against wear. Recently Oliveira et al [29] observed a gradient in the grain deformation from the surface down to the bulk material on Ti grade 2 following a tribocorrosion experiment at OCP in SBF. Such deformation was associated with an increased in hardness. The absence of tribolayer or grain refinement has been confirmed on the cross section of the wear track at 2V (**Figure 5.A2.12**) for the Ti7Nb which exhibits the greatest decrease in V_{tot} of about 50%.

The thickness of the oxide layer was determined to greatly increase from 5.4nm (at 1 V) to 13.6 nm (at 2V) after 1h immersion. It is reasonable to assume that the different physico chemical properties of the initial oxide film may modify the mechanical response of the alloy. It should be noted that a similar drop in total wear has been observed when studying the tribocorrosion behaviour of beta Ti45Nb in SBF. Wear values wear relatively constant and high ($\sim 800 \cdot 10^{-3} \text{ mm}^3$) from -1V to 0.3V followed by a decrease to $600 \cdot 10^{-3} \text{ mm}^3$ at 1.2 V [9].

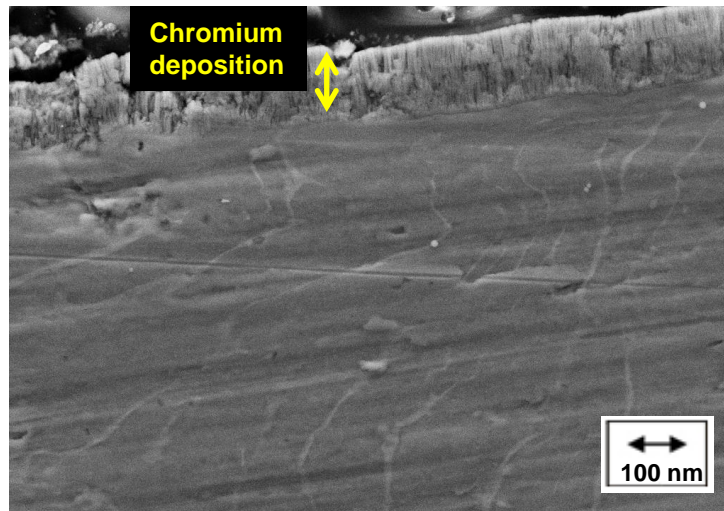


Figure 5.A2.12. FSEM image of Ti7Nb cross section of wear track obtained after tribocorrosion test at 2V.

4.3. Wear mechanism

The mechanical and chemical contributions to the total wear loss have been determined for all materials. The dominant deterioration mechanism is the mechanical detachment of particles as it represents $\sim 85\%$ of total material loss for both Ti6Al and Ti6Al7Nb and $\sim 95\%$ for Ti7Nb. The remaining percentage is due to the wear accelerated corrosion and represents a small contribution to the overall material loss. A correlation can be observed between the values of V_{chem} and the width of the wear track as I_{chem} is dependent on the number of contacting asperities, between the alumina ball and the surface, which depassivate by plastic deformation.

The poor wear resistance of Ti and its alloys is attributed to their low resistance to plastic shearing and low work hardening [30]. As a result the material weakly counteracts wear phenomena. The SEM examination (**Figure 5.A2.8**) shows the same wear appearances at all potentials. Indeed, Ti and its alloys are chemically active materials and have a high ductility, which result in the strong tendency to adhesion [31] and confirmed by the presence of transfer material on the alumina counterpart.

Under all applied potentials Ti6Al wear track exhibits mild adhesion with a relatively smooth surface and thin scratches. Repeated sliding results in the formation of debris which are formed of TiO_2 and Al_2O_3 a high strength, wear resistant oxide which may have induced abrasion [32]. Ti6Al7Nb also shows similar surface features regardless of the potential. The adhesion appears to be more severe as in addition to the fine abrasion lines, signs of smeared material are clearly visible. The higher amount of β phase in the alloy contributes to the increased plastic deformation as the inherent ductility helps the spreading of the metal particles on the surface of the wear track.

The Ti7Nb alloy shows similar wear track features to Ti6Al7Nb, with large plastic flow, up to 1 V. At the highest potential, the surface exhibits wide ($15\mu\text{m}$) parallel grooves and signs of material detachment within these grooves. The later could suggest delamination caused by large plastic strains. According to the theory of delamination, during sliding there is continuous mechanical mixing of the surface removed and debris, causing an increase in plastic deformation. Cracks will nucleate below the surface and propagate parallel to the surface when a critical value of the accumulated plastic strain is reached, resulting in flake like particles which will detach from the surface by adhesion to the alumina ball [33]. However no cracks were observed in the cross section observation (**Figure 5.A2. 12**). The high ductility associated to the lower young module of Ti7Nb allows to accommodate plastic strains generated at the subsurface of the alloy discarding the possibility of delamination. As it has previously been discussed in section 3.2, at 2V a transition in wear is observed which has been associated to the dynamic of debris during wear. The initial thickness of the passive film is very large causing large oxide debris to be incorporated into the film during rubbing. Under repeated loading these will break down into smaller particles due to the high brittleness of TiO_2 and detach from the worn surface resulting in the grooves observed on the SEM images of the wear scar.

5. Conclusions

The following conclusions can be drawn from the study of the electrochemical and tribocorrosion behavior of Ti6Al, Ti7Nb and Ti6Al7Nb in artificial saliva:

- Ti7Nb exhibits decreased tribocorrosion behaviour and wear resistance under passive potential due to high ductility of the material which facilitate material removal. Wear loss is dependent on the electrochemical condition and the dynamic of debris formation.
- Ti6Al and Ti6Al7Nb show similar electrochemical and tribocorrosion behavior. Aluminium improves tribocorrosion and wear resistance through solid solution strengthening.
- Wear damage is mainly due to mechanical action and wear accelerated corrosion which both depends on the prevailing electrochemical conditions. Ti7Nb shows higher sensitivity to electrochemical conditions on mechanical wear, showing an increase up to two orders of magnitude in mechanical wear in presence of passive film.
- When compared to Ti6Al4V the Ti6Al7Nb alloy shows a better corrosion resistance and similar tribocorrosion behaviour suggesting sintered Ti6Al7Nb is a promising biomaterial for implant applications

6. Acknowledgments

The authors wish to thank the Spanish Ministry of Economy and Competitiveness for the financial support of Research Project MAT2014-53764-C3-1-R, the Generalitat Valenciana for support through PROMETEO 2016/040, the European Commission via FEDER funds that have allowed the purchase of equipment for research purposes and for the Microscopy Service at the Polytechnic University of Valencia.

7. References

- [1] A.I. Munoz, N. Espallargas. Tribocorrosion mechanisms in sliding contacts, in: D Landolt, S Mischler (Eds.). Tribocorrosion of Passive Metals and Coatings. 2011
- [2] M. Quirynen, B. Al-Nawas, H.J.A.Meijer, A. Razavi, T.E. Reichert, M. Schimmel. et al.. Small-diameter titanium grade IV and titanium-zirconium implants in edentulous mandibles: three-year results from a double-blind, randomized controlled trial. *Clinical Oral Implants Research* (2014) 1-10
- [3] M. Jairo, V. Cordeiro, A.R. Barão. Is there scientific evidence favoring the substitution of commercially pure titanium with titanium alloys for the manufacture of dental implants? *Materials Science and Engineering C* 71 (2017) 1201-1215
- [4] DL Sarandha, Sarandha D. L., Zakir. Textbook of Complete Denture Prosthodontics. Jaypee Brothers Medical Pub, 2008
- [5] X. Liu, P. Chu, C. Ding. Surface modification of titanium, titanium alloys, and related materials for biomedical applications, *Material Sciences. Engineering: R. Reports*. 47 (2004) 49-121
- [6] D. Scharnweber. *Metals as Biomaterials*. John Wiley and Sons Ltd. England. 1998
- [8] Y. Shibata, Y. Tanimoto, N. Maruyama, M. Nagakura. A review of improved fixation methods for dental implants. Part II: biomechanical integrity at bone-implant interface. *Journal of Prosthodontic Research* 59 (2) (2015) 84-95
- [9] I. Hacisalihoglu, A. Samancioglu, F. Yildiz, G. Purcek. A. Alsaran. Tribocorrosion properties of different type titanium alloys in simulated body fluid. *Wear* 332-333 (2015) 679-686
- [10] E. Ziya, B. Ezgy. Surface characteristics and in-vitro behavior of chemically treated bulk Ti6Al7Nb. *Surface and Coatings Technology* 309 (2017) 829-839

- [11] X. Shi, L. Xu, K.B. Violin, S. Lu. Improved osseointegration of long-term stored SLA implant by hydrothermal sterilization. *Journal of the Mechanical Behaviour of Biomedical Materials* 53 (2016) 312-319
- [12] A.C. Vieira., L.A. Rocha, N. Papageorgiou, S. Mischler. Mechanical and electrochemical deterioration mechanisms in the tribocorrosion of Al alloys in NaCl and in NaNO₃ solutions. *Corrosion Science* 54 (2012) 26-35
- [13] N. Papageorgiou, S. Mischler, Electrochemical simulation of the current and potential response in sliding tribocorrosion. *Tribol. Lett.* 48 (2012) 271-283
- [14] M. Semlitsch, H. Weber, R. Steger, 1995. In: P.A. Blenkinsop, W.J. Evans, H.M. Flower. (Eds.). *Fifteen Years Experience with Ti-6Al-7Nb Alloy for Joint Replacements. Titanium '95: Science and Technology. Birmingham - UK, 1742-1759*
- [15] M.K. Dimah, F. Devesa Albeza, V. Amigo´ Borrás, A. Igual Muñoz. Study of the biotribocorrosion behaviour of titanium biomedical alloys in simulated body fluids by electrochemical techniques. *Wear* 294-295 (2012) 409-418
- [16] D. Henry. *Materials and Coatings for Medical Devices: cardiovascular.* ASM International. 2009
- [17] R. Boyer, G. Welsch, E.W. Collings. *Materials Properties Handbook: Titanium Alloys.* 1998
- [18] L. Bolzoni, E.M. Ruiz-Navas, E. Gordon. Evaluation of the mechanical properties of powder metallurgy Ti-6Al-7Nb alloy. *Journal of the Mechanical Behaviour of Biomedical Materials* 67 (2017) 110-116
- [19] I. Milosev, T. Kosec, H.-H. Strehblow. XPS and EIS study of the passive film formed on orthopaedic Ti-6Al-7Nb alloy in Hank's physiological solution. *Electrochimica Acta* 53 (2008) 3547-3558
- [20] L.J. Xu, S. Xiao, J. Tian, Y. Chen, Y. Huang. Microstructure and dry wear properties of Ti-Nb alloys for dental prostheses, *Transactions of Nonferrous Metals Society of China* 19(3) (2009) 639-644
- [21] V. Guinon Pina, A. Dalmau, F. Devesa, V. Amigo, A. Igual Muñoz. Tribocorrosion behavior of beta titanium biomedical alloys in phosphate buffer saline solution. *Journal of the mechanical behavior of biomedical materials* 46 (2015) 59-68

- [22] I. Milosev, M. Metikos-Hukovich, H.-H. Strehblow. Passive film on orthopaedic TiAlV alloy formed in physiological solution investigated by X-ray photoelectron spectroscopy. *Biomaterials* 21 (2000) 2103-2113
- [23] Yi Xu, Qiang Miao, Wenping Liang, Xiushui Yu, Qiong Jiang. Tribological behavior of Al₂O₃/Al composite coating on γ -TiAl at elevated temperature. *Materials Characterization* 101 (2015) 122-129
- [24] D. Landolt, S. Mischler, M. Stemp M, S. Barril. Third body effects and material fluxes in tribocorrosion systems involving a sliding contact. *Wear* 256 (5)(2004) 517-524
- [25] G. Luterjng, J.C. Williams. *Titanium*. Springer. 2003
- [26] R. Kieffer, H. Braun. *Vanadium, Niob, Tantal*. Springer Verlag, 1963
- [27] J. Perret, E. Boehm-Courjault, M. Cantoni, S. Mischler, A. Beaudouin, W. Chitty, et al., EBSD, SEM and FIB characterisation of subsurface deformation during tribocorrosion of stainless steel in sulphuric acid. *Wear* 269.(2010) 383-393
- [28] J. Stojadinovic', D. Bouvet, M. Declercq, S. Mischler. Effect of electrode potential on the tribocorrosion of tungsten, *Tribology International* 42 (2009) 575- 583
- [29] FG. Oliveira, AR. Ribeiro, G. Perez. Understanding growth mechanisms and tribocorrosion behaviour of porous TiO₂ anodic films containing calcium, phosphorous and magnesium. *Applied Surface Science* 341 (2015) 1-12
- [30] A. Molinari, G. Straffelini, B. Tesi, T. Bacci. Dry sliding wear mechanisms of the Ti6Al4V alloy. *Wear* 208 (1997) 105-112
- [31] H. Dong, T. Bell. Enhanced wear resistance of titanium surfaces by a new thermal oxidation treatment. *Wear* 238 (2000) 131-137
- [32] L. Benea, E. Mardare-Danaila, J.P. Celis, Increasing the tribological performances of Ti-6Al-4V alloy by forming a thin nanoporousTiO₂ layer and hydroxyapatite electrodeposition under lubricated conditions. *Tribology International* 78 (2014) 168-175
- [33] I. Cvijovic'-Alagic', Z. Cvijovic', S. Mitrovic', V. Panic', M. Rakin. Wear and corrosion behaviour of Ti-13Nb-13Zr and Ti-6Al-4V alloys in simulated physiological solution. *Corrosion Science* 53 (2011) 796-808

-Chapter 6-

Conclusions

and

Future lines of investigation

1. Conclusions

During their life span, implants are exposed to both the corrosiveness of body fluids and wear. Understanding the behaviour of biomaterials under wear-corrosion conditions is important to ensure the development of safe and reliable medical implants. The corrosion and tribocorrosion behaviour of powder metallurgy Ti6Al4V and Ti6Al7Nb alloys for dental implant application were analysed by electrochemical techniques (Open-Circuit measurements, potentiodynamic polarization curves, potentiostatic tests, Electrochemical Impedance Spectroscopy) and tribocorrosion (under Open Circuit Potential or applied potential and coupled to a Zero-Resistance Ammeter).

The results obtained in this thesis have been presented in two main chapters analysing several electrochemical and triboelectrochemical aspects of the degradation mechanisms of those titanium alloys. The specific conclusions have been outlined at the end of each chapter, and the major results of this work are summarized as follows:

- The fabrication process (cast or powder metallurgy) of titanium alloys has a small influence on the corrosion and tribocorrosion behavior of those biomedical alloys which degradation mechanism mainly depends on solution chemistry and electrode potential. Therefore the powder metallurgy process is a promising fabrication process for dental implant application.
- Ti6Al4V alloy, regardless of the fabrication process, spontaneously passivates independently of the fluoride content and pH in artificial saliva (AS). However, the deleterious effect of fluorides, due to the concentration of HF which forms soluble complexes with the titanium, is observed in presence of a threshold content of 1000 ppm of fluoride. Potentiostatic tests in AS show an increase of the passive dissolution of the alloy and in acidified saliva the material actively corrodes resulting in three orders of magnitude increase of the registered current in comparison to the fluoride free solution.
- Ti6Al7Nb processed by powder metallurgy exhibits similar mechanical properties (hardness and young modulus) as wrought Ti6Al7Nb.
- All studied titanium alloys show a high corrosion resistance. Below 2V the alloying element (Nb or Al) does not influence the passivating properties of the alloys, however Niobium considerably increases the film thickness above 1 V. The combined effect of Al and Nb in the Ti6Al7Nb is detrimental with respect to the Ti7Nb.

- The new ZRA technique for tribocorrosion allowed obtaining experimental values for the anodic current (wear accelerated corrosion during rubbing at different initial mechanical conditions) under Open Circuit Potential. For the lowest initial contact pressure of 540MPa, below the yield strength of the alloy, the highest current was registered. The ZRA technique has therefore allowed to detect when the wear mechanism of the alloy was mainly governed by the presence of the third body, as confirmed by SEM observation of debris on the wear track.
- The ZRA technique can be used to determine the evolution with time of the relationship between the depassivated area (anode) and the wear track area predicted by Archard wear law by measuring experimentally the potential and current evolution with time at OCP and applying the galvanic model. The prediction of the depassivated area has allowed to determine deviations of the wear mechanisms from Archard wear law at OCP.
- Tribocorrosion degradation mechanisms of the Ti alloys consist in 90% of mechanical loss while the remaining 10% is due to the chemical contribution independently on the AS pH. When the fluoride content is higher than 100 ppm in AS, higher anodic dissolution of titanium occurs, thus higher chemical contribution to wear. The latter is confirmed by the decreasing size and amount of wear debris with fluoride content. The addition of 1000 ppm in acidified saliva changes the main degradation mechanism to corrosion (90%), resulting in one order of magnitude higher total material loss compared to the fluoride free solution.
- The solid solution strengthening effect of Aluminium improved the tribocorrosion and wear resistance of Ti6Al and Ti6Al7Nb which show similar electrochemical and tribocorrosion behavior. Wear damage is mainly due to mechanical action which depends on the prevailing electrochemical conditions.
- High ductility of Ti7Nb decreased the tribocorrosion behaviour and wear resistance under passive potential due to increased material removal. Volume loss is mainly due to the mechanical contribution (90%). Wear loss of Ti7Nb is dependent on the electrochemical condition and the dynamic of debris formation, showing an increase up to two orders of magnitude in mechanical wear in presence of passive film.
- When compared to Ti6Al4V the Ti6Al7Nb alloy shows a better corrosion resistance and similar tribocorrosion behaviour suggesting sintered Ti6Al7Nb is a promising biomaterial for implant applications.

2. Future lines of investigation

The future research direction will be focused on the Ti6Al7Nb alloy processed by powder metallurgy as a new biomaterial for implant applications. The first main goal after this thesis is to assess the biocompatibility of the alloy by using cell culture on titanium alloy substrate, surface analysis and quantification of metal ion content. The following aspects will be considered:

- Determine the influence of the addition of cells to the electrochemical response of the alloy. The film/electrolyte interface should be investigated by different electrochemical techniques (EIS, EQCM) to study the influence of cells on the corrosion rate and passivity of Ti6Al7Nb. The influence of time should also be taken into account (couple days to weeks)
- Determine cell culture viability (apoptosis), when seeded on the surface of the alloy, depending on the applied potential.
- Determine the influence of the presence of cells on the tribocorrosion degradation mechanism of the alloy. The later could be investigated at OCP and applying potentials within the cell viability potential range previously investigated.
- Determine cell culture viability during tribocorrosion testing. Particular attention should be given to cells surrounding the wear track to observe influence of wear accelerated corrosion on their behavior.
- Determine the chemical composition of the passive film in presence of cells by X-Ray Photoelectron Spectroscopy and Auger Electron Spectroscopy.
- Identify and quantify released ions from the titanium alloy upon immersion in presence of cells under different oxidizing conditions.

-Glossaries-

LIST OF TABLES

Chapter 1

| | |
|---|---------|
| Table 1.1 - Mechanical properties of different biomaterials | 6 |
|---|---------|

Chapter 3

| | |
|--|----------|
| Table 3.1 - Impedance electrical symbols | 66 |
|--|----------|

Chapter 4

Article 1

| | |
|--|----------|
| Table 4.A1.1 - Electrochemical parameters for Ti6Al4V alloys in the studied solutions. | 91 |
|--|----------|

| | |
|---|----------|
| Table 4.A1.2 - shows the Q and ipass values obtained from the potentiostatic tests. | 93 |
|---|----------|

| | |
|---|----------|
| Table 4.A1.3 - Average values of the potential measured before (OCP_0), during ($OCP_{sliding}$) and after sliding (OCP_{final}) of the Ti6Al4V alloy sling against an alumina ball in different electrolytes. Normal force 5 N | 94 |
|---|----------|

| | |
|---|----------|
| Table 4.A1.4 - Average values of the current density measured before (I_0), during ($I_{sliding}$) and after sliding (I_{final}) against an alumina ball in different electrolytes. Normal force 5 N. | 96 |
|---|----------|

| | |
|--|----------|
| Table 4.A1.5 - Average wear volumes ($\times 10^{-3}$) expressed in mm^3 | 98 |
|--|----------|

Article 2

| | |
|--|-----------|
| Table 4.A2.1 - Electrochemical parameters for Ti6Al4V alloys in the studied solutions. | 117 |
|--|-----------|

| | |
|--|-----------|
| Table 4.A2.2 - Electrochemical parameters of the Ti6Al4V alloys in the studied solutions | 119 |
|--|-----------|

| | |
|--|-----------|
| Table 4.A2.3 - Average values of the potential measured before (OCP_0), during ($OCP_{sliding}$) and after sliding (OCP_{final}) of the Ti6Al4V alloy sling against an alumina ball in different electrolytes. Normal force 5N | 121 |
|--|-----------|

| | |
|---|-----------|
| Table 4.A2.4 - Average values of the current density measured before (I_0), during ($I_{sliding}$) and after sliding (I_{final}) of the Ti6Al4V alloy sliding against an alumina ball in different electrolytes. Normal force 5N. | 123 |
|---|-----------|

| | |
|---|-----------|
| Table 4.A2.5 - Average wear volumes expressed in $10^{-3} mm^3$. | 125 |
|---|-----------|

Article 3

| | |
|---|-----------|
| Table 4.A3.1 - Volume loss values (total, chemical and mechanical) after tribocorrosion tests at OCP using the ZRA set-up | 145 |
|---|-----------|

Chapter 5

Article 1

| | |
|---|-----------|
| Table 5.A1.1 - Electrochemical parameters of Ti6Al, Ti7Nb and Ti6Al7Nb in AS. | 168 |
|---|-----------|

| | |
|---|-----------|
| Table 5.A1.2 - Electrochemical parameters extracted from the potentiostatic tests of Ti6Al, Ti7Nb and Ti6Al7Nb in AS. | 170 |
|---|-----------|

| | |
|--|-----------|
| Table 5.A1.3 - Electrochemical parameters at different potentials from EIS fitting of Ti, Ti7Nb and Ti6Al7Nb sintered alloys in AS at 37 °C. | 173 |
|--|-----------|

Article 2

| | |
|---|-----------|
| Table 5.A2.1 Microhardness and Young modulus of the titanium alloys | 187 |
|---|-----------|

| | |
|---|-----------|
| Table 5.A2.2 - Tafel constants extracted from the linear regression of the cathodic polarization curves of the titanium | 188 |
|---|-----------|

| | |
|--|-----------|
| Table 5.A2.3 - Passivation charge densities ($Q_{short} (C/cm^2) * 10^{-3}$) of the studied alloys in AS at $37 \pm 1^\circ C$. | 189 |
|--|-----------|

| | |
|--|-----------|
| Table 5.A2.4 - Average values of the current density measured before (I_0), during ($I_{sliding}$) and after sliding (I_{final}) of Ti6Al, Ti7Nb and Ti6Al7Nb in AS. | 192 |
|--|-----------|

| | |
|--|-----------|
| Table 5.A2.5 - Average values of the coefficient of friction measured during sliding of the studied alloys against an alumina ball at different potentials. Load 5N potentials | 195 |
|--|-----------|

LIST OF FIGURES

Chapter 1

| | |
|--|----------|
| Figure 1.1. a) Endosteal and b) subperiosteal implants | 4 |
| Figure 1.2: basic phase diagrams for Ti alloys. The alloying elements affecting various phase diagrams are (a) Al, O, N, C; (b) Mo, W, V, Ta; (c) Cu, Mn, Cr, Ni, Fe. The dotted lines in (b) and (c) show the martensite starts (Ms) temperatures | 7 |
| Figure 1.3. Influence of the thermal-mechanical process on the microstructure of the titanium alloy | 8 |
| Figure 1.4. Simplified flowchart illustrating the sequence of operations in powder metallurgy | 10 |
| Figure 1.5. Sintering on a microscopic scale | 11 |
| Figure 1.6. Typical heat treatment cycle in sintering | 12 |
| Figure 1.7. Model tribocorrosion situation | 19 |
| Figure 1.8 Factors influencing the tribocorrosion | 20 |
| Figure 1.9. Illustration of the mechanistic approach | 21 |
| Figure 1.10. The third body approach | 22 |
| Figure 1.11. Cross-section scheme of the different regions beneath the worn surface of a metal-metal sliding contact | 23 |
| Figure 1.12. Scheme of body host reactions due to presence of metallic ions and debris | 31 |

Chapter 2

| | |
|---|----------|
| Figure 2.1. Scheme of the Doctoral Thesis structure | 46 |
|---|----------|

Chapter 3

| | |
|---|----------|
| Figure 3.1. A turbula mixer | 49 |
| Figure 3.2. Compaction system | 49 |
| Figure 3.3. Heating cycle used to obtain the sintered samples | 50 |
| Figure 3.4. Sintered samples | 50 |
| Figure 3.5. Flat electrochemical cell with electrodes | 52 |

| | | | |
|--|-----|-------|----|
| Figure 3.6. (a) Metal electrode in contact with its own ions (single electrode), (b) with aerated conditions (mixed electrode) and (c) passivation of the metal. | 54 | | 53 |
| Figure 3.7. Partial current densities ($i_{a,Me}$ and $i_{c,O_2/H_2O}$ in solid lines) and total current density (i in dotted lines) of mixed electrode near the corrosion potential. | 58a | | 54 |
| Figure 3.8. Evans diagram showing anodic and cathodic partial current densities and total current density of an electrode reaction on a logarithmic scale. Determination of i_{corr} from a $ I $ vs $\log i $ curve. | | | 57 |
| Figure 3.9. Evans diagram showing anodic and cathodic partial current densities and total current density of an electrode reaction on a logarithmic scale. | | | 58 |
| Figure 3.10. Experimental set up for potentiostatic measurements. Customized three electrode cell used for carrying out the electrochemical measurements. | | | 60 |
| Figure 3.11. (a) Nyquist diagram and (b) Bode plot of impedance data for a simple equivalent circuit (Randles circuit with solution resistance (R_s) of $100 \Omega cm^2$, double layer capacitance (C_{dl}) of $1 \cdot 10^{-6} F cm^{-2}$ and charge transfer resistance (R_{ct}) of $2000 \Omega cm^2$) | | | 64 |
| Figure 3.12. Experimental set up for impedance measurements using a transfer function analyser under potentiostatic control (a sinusoidal of weak amplitude $\Delta E = E - E_{st}$ is superimposed onto the steady state potential E_{st} of an electrode). | | | 64 |
| Figure 3.13 (a) Equivalent Electric Circuit (Randles) of the electrode-electrolyte interface and (b) Equivalent Circuit for the analysis of the impedance spectra of a Ti passive alloys. | | | 67 |
| Figure 3.14. Tribocorrosion set-ups. a) sliding and b) reciprocating configurations | | | 69 |
| Figure 3.15. Evolution of potential vs time during a tribocorrosion test at OCP | | | 72 |
| Figure 3.16. Schema of potentiostatic set-up for tribocorrosion experiments. | | | 72 |
| Figure 3.17. Evolution of current during a potentiostatic tribocorrosion test | | | 73 |
| Figure 3.18. Scheme of the electrochemical measurements carried out through a Zero-Resistance Ammeter (ZRA) where WE_A is the cathode (unrubbed sample), WE_B is the anode (rubbed sample) and RE is the reference electrode. | | | 75 |
| Figure 3.19. Schematic diagram of conventional optical microscope. a) simple microscope and b) compound microscope | | | 75 |
| Figure 3.20. Schematic diagram of Confocal microscope | | | 76 |
| Figure 3.21. a) 3D section obtained with confocal microscope and b) associated 2D profil | | | 77 |

| | |
|---|----------|
| Figure 3.22. Schematic diagram of scanning electron microscope with CRT display | 78 |
|---|----------|

Chapter 4

Article 1

| | |
|---|-----------|
| Figure 4.A1.1. Microstructure of the Ti6Al4V alloys; (a) casted and (b) sintered | 90 |
| Figure 4.A1.2. Potentiodynamic curves for Ti6Al4V alloys: (a) casting and (b) PM in the studied solutions at 37 °C. | 91 |
| Figure 4.A1.3 Potentiostatic curves E0.2 V for Ti6Al4V alloys: (a) casting and (b) PM in the studied solutions at 37 °C. | 92 |
| Figure 4.A1.4. OCP evolution with time during sliding of a smooth alumina ball against Ti6Al4V at OCP for (a) cast and (b) PM alloys. Arrows indicate the initiation and stop of sliding. | 93 |
| Figure 4.A1.5. Current evolution with time during sliding of a smooth alumina ball against Ti6Al4V alloys at imposed potential of 0.2 V for cast samples in (a) AS and MW, (b) AS+100F- and AS+1000F- and for sintered samples in (c) AS and MW, (d) AS+100F- and AS+1000F- | 95 |
| Figure 4.A1.6. SEM images of the center of the wear tracks in different electrolytes at OCP and E200. Normal load 5 N | 99 |
| Figure 4.A1.7. SEM images outside the wear tracks in different electrolytes at OCP and E200. Normal load 5 N. | 99 |
| Figure 4.A1.8. Optical images of the alumina balls sliding against the Ti6Al4V–F alloy in (a) AS and (b) AS+1000F- | 100 |
| Figure 4.A1.9. Equilibrium diagram of the species in the NaF solutions at 52 different pH values, where C is the molar concentration. | 102 |

Article 2

| | |
|---|-----------|
| Figure 4.A2.1. Potentiodynamic curves for Ti6Al4V alloys: (a) Cast, (b) Sintered in the studied solutions at 37°C | 116 |
| Figure 4.A2.2. Potentiostatic test at 0,2V for Ti6Al4V alloys: (a) Cast, (b) Sintered in the studied solutions at 37°C. | 118 |
| Figure 4.A2.3 Potentiostatic test at 0.2V for cast and sintered Ti6Al4V alloys in the AS-3-1000F ⁻ solution at 37°C. | 119 |
| Figure 4.A2.4. Evolution with time of the OCP during sliding of a smooth alumina ball against Ti6Al4V for (a) Cast and (b) PM alloys | 120 |
| Figure 4.A2.5. Evolution with time of the OCP during sliding of a smooth alumina ball against Ti6Al4V alloys in the AS-3-1000F ⁻ at 37 °C. | 121 |

| | |
|---|-----------|
| Figure 4.A2. 6. Evolution with time of the current during sliding of a smooth alumina ball against Ti6Al4V alloys at imposed potential of 0.2 V for (a) cast material, and (b) sintered material. | 122 |
| Figure 4.A2.7. Evolution with time of the current during sliding of a smooth alumina ball against Ti6Al4V alloys at imposed potential of 0.2 V in AS-3-1000F- at 37 °C. | 123 |
| Figure 4.A2.8. SEM images for cast and sintered alloys of the center of the wear tracks in different electrolytes at E200. Normal load 5N | 126 |
| Figure 4.A2.9. SEM images for cast and sintered alloys of the center of the wear tracks in AS-3-1000F- at OCP and E200. Normal load 5N | 126 |
| Figure 4.A2.10. Potentiodynamic curves for Ti6Al4V alloys: (a) Cast and (b) PM in AS and AS-3 with different fluoride content at 37°C. | 127 |

Article 3

| | |
|--|-----------|
| Figure 4.A3.1. Scheme of the electrochemical measurements carried out through a Zero-Resistance Ammeter (ZRA) where WEA is the cathode (unrubbed ample), WEB is the anode (rubbed sample) and RE is the reference electrode. | 141 |
| Figure 4.A3.2. Scheme of the a SiC pin and b alumina ball geometry used as counterpart for the tribocorrosion tests | 142 |
| Figure 4.A3.3. Cathodic curves of the Ti6Al4V alloy in artificial saliva at 37 °C. Two repetitions are shown in the figure for checking repeatability. | 143 |
| Figure 4.A3.4. (a) Potential and (b) current evolution with time for the Ti6Al4V alloy in artificial saliva at 37 °C. Only one test result is shown in the graphs for clarity however the repetition tests were successful. | 144 |
| Figure 4.A3.5. SEM images of the center of the wear tracks after tribocorrosion testing in artificial saliva at OCP: (a) against alumina ball at 3 N normal load (540 MPa), (b) against SiC pin at 2 N normal load (830 MPa) and (c) against SiC pin at 10 N normal load (1410 MPa). | 146 |
| Figure 4.A3.6. Optical image of the alumina counterpart after tribocorrosion testing in artificial saliva at 3 N normal load | 146 |
| Figure 4.A3.7. Experimental potential evolution with time for the Ti6Al4V against (a) Al ₂ O ₃ 540 MPa, (b) SiC pin 843 and (c) 1410 MPa measured by ZRA in artificial saliva at 37 °C. The model OCP (mathematical simulation) is superimposed in all figures according to equation 3 using i_a as fitting parameter. | 148 |
| Figure 4.A3.8. Potential and current evolution with time of the Ti6Al4V rubbed against (a-a') Al ₂ O ₃ ball at 540 MPa, (b-b') SiC pin at 830 MPa and (c-c') SiC pin at 1410 MPa in artificial saliva at 37 °C. The blue curve corresponds to the experimental data while the red one is the simulated response according to equations 3 and 4 | 150 |

Figure 4.A3.9. Evolution of the depassivated (A_a) and Hertzian (A_{contact}) areas versus time from the potential and current values measured by ZRA. Superimposed the wear track area (A_{wt}) obtained by the Archard wear law and the geometry of the counterpart 152

Figure 4.A3.10. (a) SEM image of the center of the wear track after tribocorrosion testing of a Ti6Al4V obtained by powder metallurgy in artificial saliva at OCP against alumina ball at 3 N normal load (540 MPa) and (b) current evolution with time measured by ZRA. 154

Chapter 5

Article 1

Figure 5.A1.1. Optical images of the microstructure of (a) Ti6Al, (b) Ti6Al7Nb and (c) Ti7Nb alloys 167

Figure 5.A1.2. Potentiodynamic curves in AS at $37 \pm 1^\circ\text{C}$ 168

Figure 5.A1.3. Long term potentiostatic tests at a) -1V and -0.5, 0.2, 1 and 2V for b) Ti6Al, c) Ti7Nb and d) Ti6Al7Nb alloys in AS at 37°C 169

Figure 5.A1.4. Bode plots at 0.2, 1 and 2V of a) Ti, b) Ti6Al7Nb and c) Ti7Nb alloys in AS at 37°C 171

Figure 5.A1.5. Equivalent electrical circuit for the analysis of the impedance spectra. R_s is the solution resistance, R_p is the charge transfer resistance and CPE_{dl} is the CPE of the double layer. 171

Figure 5.A1.6. Representation of passivation current density versus potential for the Ti alloys under study 174

Figure 5.A1.7. Representation of the inverse of the polarization resistance versus the passivation current density for the Ti alloys under study 175

Article 2

Figure 5.A2.1. Cathodic polarization curves of the titanium alloys in AS at $37 \pm 1^\circ\text{C}$ 188

Figure 5.A2.2. Current transients at 0.2, 1 and 2 $V_{\text{Ag}/\text{AgCl}}$ for a) Ti6Al, b) Ti7Nb and c) Ti6Al7Nb in AS at $37 \pm 1^\circ\text{C}$ 189

Figure 5.A2.3. OCP evolution with time during rubbing of a smooth alumina ball against Ti6Al, Ti7Nb and Ti6Al7Nb at OCP in AS at $37 \pm 1^\circ\text{C}$ 190

Figure 5.A2.4. Current evolution with time during sliding of a smooth alumina ball against Ti6Al, Ti7Nb and Ti6Al7Nb at $-1V_{\text{Ag}/\text{AgCl}}$ in AS at $37 \pm 1^\circ\text{C}$ 191

| | | |
|---|-------|-----|
| Figure 5.A2.5. Current evolution with time during sliding of a smooth alumina ball against Ti7Nb and (b) Ti6Al7Nb -0.5, 0.2, 1 and 2V _{Ag/AgCl} in AS at 37±1°C | | 192 |
| Fig.5.A2.6. Wear track width versus the applied potential and OCP, E(V _{Ag/AgCl}) for all studied titanium alloys at the end of the tribocorrosion tests. | | 194 |
| Figure 5.A2.7. Volume losses, V _{mech} and V _{wac} , with respect to the applied potential and OCP after the tribocorrosion tests for all studied titanium alloys | | 195 |
| Figure 5.A2.8. SEM images of the wear track of Ti6Al, Ti7Nb and Ti6Al7Nb at the end of the tribocorrosion tests at different applied potentials in AS at 37±1°C | | 196 |
| Figure 5.A2.9. Optical Image of the alumina ball at the end of the tribocorrosion tests of Ti6Al at 1V in AS at 37±1°C. | | 196 |
| Figure 5.A2.10. Current evolution with time during sliding of a smooth alumina ball against Ti7Nb at 1V with varying load of 1, 5 and 10N in AS at 37±1°C | | 199 |
| Figure 5.A2.11 Confocal 2D profile of the Ti7Nb wear tracks obtained after tribocorrosion tests under 1, 5 and 10 N in AS at 37±1°C | | 200 |
| Figure 5.A2.12. FSEM image of Ti7Nb cross section of wear track obtained after tribocorrosion test at 2V | | 201 |

LIST OF SYMBOLS

| | |
|-------------------------|--|
| A | Active area, cm^2 |
| A_a | Anodic area, cm^2 |
| A_c | Cathodic area, cm^2 |
| A_{wt} | Surface of the wear track after rubbing, mm^2 |
| a_a | Anodic Tafel constant, V |
| a_c | Cathodic Tafel constant, V |
| b_a | Anodic Tafel constant, V |
| b_c | Cathodic Tafel constant, V |
| C | Capacitance, F.cm^{-2} |
| C_{dl} | Double layer capacitance, F.cm^{-2} |
| d_{Film} | Film thickness, m |
| CPE | Constant phase element |
| E | Electrode potential, V |
| E_{corr} | Corrosion potential, V |
| E_{pp} | Passivation potential, V |
| E_{rev} | Equilibrium potential, V |
| f | Frequency of rubbing, Hz |
| F | Faraday's constant, C.mol^{-1} |
| F_n | Applied normal load, N |
| f_{eff} | Effective force, N |
| h_{min} | Micro hardness inside the wear track, GPa |
| i | Current density, A.cm^{-2} |
| i_a | Anodic partial current density, A.cm^{-2} |
| i_c | Cathodic partial current density, A.cm^{-2} |
| i₀ | Current parameter, A.cm^{-2} |
| i_{diss} | Ionic current density corresponding to metal-ion dissolution, A.cm^{-2} |

| | |
|--|---|
| i_{growth} | Current density leading to film growth, A.cm^{-2} |
| i_{corr} | Corrosion current density, A.cm^{-2} |
| i_{pass} | Passive current density, potentiostatic test, A.cm^{-2} |
| i_{pp} | Passivation current density, A.cm^{-2} |
| i_{p} | Passive current density, potentiodynamic curves, A.cm^{-2} |
| I | Overall measured current during rubbing, A |
| I_0 | Current prior to sliding of tribocorrosion test, A |
| I_{sliding} | Current enhancement due to rubbing (excess current), A |
| I_{chem} | Current generated in the wear track by wear accelerated corrosion, A |
| I_{final} | Current registered when sliding stops, A |
| j | Complex or imaginary number |
| K_{st} | Proportionality factor |
| K_0 | Proportionality factor for effective load |
| L | Inductance, H.cm^2 |
| m | Mass, g |
| M | Molar mass, g.mol^{-1} |
| n | Charge number for the oxidation reaction |
| n | CPE exponent |
| Q | Passivation charge density, C.mm^{-2} |
| R | Gas constant ($8.314 \text{ J.mol}^{-1}.\text{K}^{-1}$) |
| R_{dep} | Rate of generation of depassivated area (depassivation rate), $\text{mm}^2.\text{s}^{-1}$ |
| R_{ct} | Charge transfer resistance, $\Omega.\text{cm}^2$ |
| R_{s} | Solution resistance, $\Omega.\text{cm}^2$ |
| R_{p} | Polarization resistance, $\Omega.\text{cm}^2$ |
| R_{film} | Oxide film resistance, $\Omega.\text{cm}^2$ |
| t | Duration of rubbing, s |
| T | Temperature, $^{\circ}\text{C}$ |
| U_{tot} | Total wear rate, $\text{mm}^3.\text{s}^{-1}$ |

| | |
|-------------------------|---|
| U_{chem} | Chemical wear rate, mm ³ .s ⁻¹ |
| U_{mech} | Mechanical wear rate, mm ³ .s ⁻¹ |
| vs | Sliding velocity, mm. s ⁻¹ |
| V_{tot} | Total wear volume loss, mm ³ |
| V_{chem} | Volume of metal transformed by anodic oxidation, mm ³ |
| V_{mech} | Mechanical wear volume, mm ³ |
| V_{chem} | Metal volume removed by anodic oxidation in the wear track, mm ³ |
| Z | Impedance, Ω.cm ² |
| Z₀ | CPE constant |
| Z_{Re} | Real part of the Impedance, Ω.cm ² |
| Z_{Im} | Imaginary part of the impedance, Ω.cm ² |
| ρ | Density, g.cm ⁻³ |
| ω | Rotation rate, rpm |
| ε | Relative dielectric constant |
| ε₀ | Permittivity of the vacuum (8.85 10 ⁻¹⁴ F. cm ⁻¹) |
| η | Overpotential, V |
| φ | Phase, degrees |
| β_a | Anodic Tafel coefficient, V |
| β_c | Cathodic Tafel coefficient, V |
| α | Charge transfer coefficient (0-1) |

